MODELLING METALLURGICAL PHENOMENA

IN LADLE AND TUNDISH STEEL PROCESSING OPERATIONS

by

SANGHOON JOO

Department of Mining and Metallurgical Engineering

McGill University

Montreal, Quebec, Canada

December, 1989

A Thesis Submitted to
The Faculty of Graduate Studies and Research
in Partial Fulfilment of the Requirements
for the Degree of Doctor of Philosophy

Copy No.1 Ph.D. Thesis Dec. 14, 1989

Modelling Metallurgical Transport Phenomena in Ladle and Tundish Steel Processing Operations

Sanghoon Joo

Dept. of Mining & Metallurgical Engineering
McGill University

ABSTRACT

Cleanness and uniformity in steel properties are important for high quality steel. Physical and/or mathematical models can be used in order to achieve optimum conditions for the clean steel during steelmaking processes. In the present study, important metallurgical transport phenomena in steelmaking ladles and tundishes have been investigated using both mathematical and physical (water) models.

Through appropriate solutions of the Navier-Stokes equations, the intermixing of fluid within gas-stirred ladles can be modelled quite satisfactorily. It is shown that off-centered bubbling gives the most consistent results in terms of minimising mixing times, since angular velocity components intermix fluid across the width of a ladle Comparisons between mathematical and experimental data are presented

Fluid flow, heat transfer and inclusion flotation have been modelled mathematically for testing the behaviour of several tundish designs. Computations are presented to illustrate the importance of thermal natural convection currents in mixing the upper and lower layers of steel Particle removal rates are also experimentally studied with the aid of the novel E.S.Z. (Electric Sensing Zone) system, and compared with computational results.

RÉSUMÉ

La proprete et l'uniformite sont des proprietes importantes pour les aciers de haute qualite Des modeles physiques et/ou mathematiques peuvent être utilises afin d'atteindre les conditions optimales pour obtenir des l'aciers propre lors de traitements siderurgiques Dans l'ouvrage present, des phenomenes de transferts metallurgiques importants ont ete etudies pour des creusets et des separateurs siderurgiques, a l'aide de modeles mathematiques et physiques (d'eau)

A l'aide de solutions appropriees des equations de Navier-Stokes, le melange de fluids dans des recipients brasses par injection de gaz peuvent être assez bien modelise Il a ete demontre que l'injection decentree de gaz mene aux resultats les plus consistant pour minimiser les temps de melange, puisqe la composante angulaire de la vitesse melange le fluide transversalement dans le creuset Des comparaisons entre les donnees mathematiques et experimentales sont presentees

L'ecoulement des fluides, le transfert de chaleur et l'entrainement des inclusions ont ete etudie a l'aide de modeles mathematiques afin de tester le comportment de plusieurs designs de separateurs L'importance des courants de convection naturelle thermique sur le melange des couches superieure et inferieure d'acier liquide est illustre par la presentation de resultats provenant des calculs De plus, les taux d'elimination des particules sont etudies experimentalement, a l'aide d'une nouvelle technique E S Z (Electric Sensing Zone), et compares aux resultats provenant des modeles mathematiques

ACKNOWLEDGEMENTS

The author would like to thank his thesis supervisor, Prof R I L Guthrie, for his consistent and enlightening guidance during the doctoral course at McGill University Special thanks go to Mr Frank Sebo, a magic technician, who helped the author in preparing and carring out experimental part of this research program

The author also acknowledges the help of Mrs L Dumitru of Stelco Inc in work on the full scale water model tundish housed in their industrial research laboratories The support of Cray Research Inc in providing access to their 1S, XMP and YMP supercomputers is also gratefully acknowledged Particularly, the author appreciates the efforts of Dr H Greiss and Dr K Misergade in making a video film visualising flow fields, temperature distributions and inclusion movements within tundishes He also expresses gratitude to Dr C J Dobson for providing useful plant data of tundish operations in BHP Inc , Australia

The author is deeply indebted to Korean Ministry of Education for their scholarship for his Ph D program Finally, the author acknowledges that the love of his family encouraging him incessantly made the completion of his thesis possible

NOMENCLATURE

a	:	coefficients in discretization equations.
A	:	total surface area of reactor.
A_p	:	surface area of plug flow reactor.
A_b	:	surface area of well-mixed reactor
b	:	constant
C	:	mass fraction of inclusions/tracer.
C^*	:	stagnent boundary layer number density of inclusions.
C_1, C_2, C_μ	:	empirical turbulent constants (see Table 2-1).
C_p	:	mass fraction of inclusions at the node immediately next to the metal surface.
d	:	inclusion/particle diameter.
D	:	diffusion conductance in Part II.
	:	orifice diameter of probe in Part IV.
E	:	integration constant.
f	:	frequency of bubble formation
F	:	mass flow rate.
G	:	generation term of turbulence kinetic energy.
g	:	gravity accelation constant.
Gr	:	Grashoff number.
h_w	:	heat transfer coefficient on the side-wall.
H	:	height of vessel (ladle or tundish).
K	:	an empirial constant for determining mean plume velocity.
k	:	turbulent kinetic energy
L	:	characteristic length.
L_c	:	distance between inlet and outlet nozzles.
n''	:	particle absorption flux density into overlaying slag.
N_{in}	:	number density of inclusions at the inlet nozzle.
N_{out}	:	number density of particles at the outlet nozzle.
P	:	Peclet number
p	:	pressure
Q	:	volumetric flow rate of gas/liquid fluid.
Q_{cr}	:	critical flow rate.
q_w''	:	specific heat loss from tundish side-walls.
R	:	ladle radius in Part III.
		residual ratio of (inclusion) particles in Part IV.
r	:	radial coordinate.
$r_{av,p}$	.	average plume radius.
R_p	:	radius of particle
Re	:	Reynolds number
R_ϕ	:	residual source of ϕ.
ΔR	:	resistance change
S	:	source term
T	:	temperature.
t	:	time
T_a	:	ambient temperature.
T_w	:	tundish side wall temperature.
ΔT	:	characteristic temperature difference
u	:	time averaged axial component of velocity.
u^+	:	dimensionless velocity.

U_p	:	mean plume velocity.
u_s	:	Stokes rising velocity of particles/inclusions.
u_t	:	friction velocity.
v	:	time averaged radial component of velocity.
V_b	:	bubble volume.
V_d	:	volume fraction of dead volume zone.
V_{dp}	:	volume fraction of dispersed plug flow zone.
V_m	:	volume fraction of backmix flow zone.
V_p	:	volume fraction of plug flow zone.
w	:	time averaged circumferential component of velocity.
y	:	distance from the solid wall.
y^+	:	local Reynolds number (dimensionless distance).
z	:	axial coordinate.

Greek characters

α	:	volume fraction of gas in the gas/liquid plume
β	:	volumetric expansion coefficient.
ε	:	dissipation rate of turbulent kinetic energy.
ε_w	:	emissivity of tundish sidewalls.
ϕ	:	variables.
γ	:	specfic gravity of alloys in Part I.
	:	plug flow volume fraction in Part IV.
Γ_e	:	effective diffusivity
κ	:	von Karman constant.
μ	:	laminar viscosity.
μ_{eff}	:	effective turbulent viscosity.
μ_t	:	turbulent viscosity
θ	:	circumferential coordinate.
ρ	.	density of fluid (water/molten steel).
$\Delta\rho$	:	density difference between fluid and particle.
ρ_G	:	density of gas.
ρ_L	:	density of liquid.
ρ_S	:	density of slag.
ρ_p	:	density of particle
σ	:	laminar Schmidt/Prandtl number in Part III
		Stephan-Boltzman constant in Part IV.
σ_k	:	Prandtl Number for *k*
σ_t	:	turbulent Schmidt/Prandtl number.
τ_m	:	95% mixing time.
τ_w	:	wall shear stress.

LIST OF FIGURES

Part I

Part II

Part III

Part IV

LIST OF TABLES

TABLE OF CONTENTS

PART II. COMPUTATIONS OF FLUID FLOWS, HEAT AND MASS TRANSFER FOR THREE DIMENSIONAL TURBULENT FLOWS

PART III MODELLING MIXING IN STEELMAKING LADLES

PART IV PREDICTION OF FLUID FLOW, INCLUSION SEPARATION, AND HEAT TRANSFER IN TUNDISH PROCESSING OPERATIONS

PART I

GENERAL INTRODUCTION

Chapter 1

Introduction

Cleanness and uniformity in steel properties have become an increasingly important issue with the marked increase in demand for high quality steel. For producing higher quality steel, secondary processing is commonly carried out in order to remove harmful residual elements (i.e. S, P, O, N, H, etc.) to parts per million levels. For instance, arctic oil rig platforms require that the ductile/brittle transformation temperature be lowered as far as possible, and certainly to -20 °C. The special properties sought can be approached by reducing the concentration of residual elements within the steel bath, prior to teeming into the continuous casting machine. This reduces the number of inclusions, while the remainder must be converted into harmless refractory type spheroids prior to hot rolling, so that they do not subsequently form elongated stringers For plate, pipe, rail steels, and other thick sections, dissolved hydrogen retained within the matrix can precipitate at discontinuities within the steel (e.g. inclusions), and lead to hydrogen induced cracking (HIC)

Since the early 1970's, there have been numerous studies on ladle metallurgy as a secondary refining process for steelmaking operations.Typical ladle metallurgy procedures used in order to donate superior properties to the final steel product are shown in Figure 1-1 There, the particular process routes currently in operation at Sumitomo Metals, in Japan, are shown (1). Thus hot metal is first dephosphorised with soda ash in a torpedo car/ladle, and is then decarburised in a combination blown converter employing top and bottom blowing of oxygen After tapping the steel, any oxidising converter slag, which carries over to the ladle, is removed. Second stage refining is then conducted using an RH vacuum degassing unit in order to remove dissolved hydrogen nitrogen, oxygen and carbon.

A ladle furnace is fitted with an arc heating unit to provide steel reheating capability together with alloy/slag injection procedures for desulphurising. The use of vacuum ($\sim$1 Torr) in the RH degasser allows initial levels of hydrogen of 4-5 ppm (say), to be lowered to 2ppm, nitrogen from 40 to 32 (say), and oxygen from about 300 ppm to perhaps 10 ppm (total oxygen), over a fifteen minute processing period. The oxygen is removed through the nucleation of dissolved carbon and oxygen to form carbon monoxide, the reaction proceeding at the interfaces of ascending bubbles of argon injected into the 'up-leg' of the RH degasser, and the steel/vacuum interfaces of the bath surface and splashing droplets. Initial carbon levels of 200-300 ppm, can typically be reduced to 'ultra low levels' of 20 ppm, for 'interstitial free' steels, by degassing This cursory glance at primary and secondary ladle metallurgy operations illustrates a wealth of procedures and phenomena to which mathematical and/or physical modelling can be applied.

For alloy additions and/or deoxidation, aluminum and/or ferroalloys in lump form are generally added prior to, or during furnace tapping operations into ladle. Thus gas bubbling, through a lance set deep within the liquid steel or through a porous plug bubbler set in the bottom of

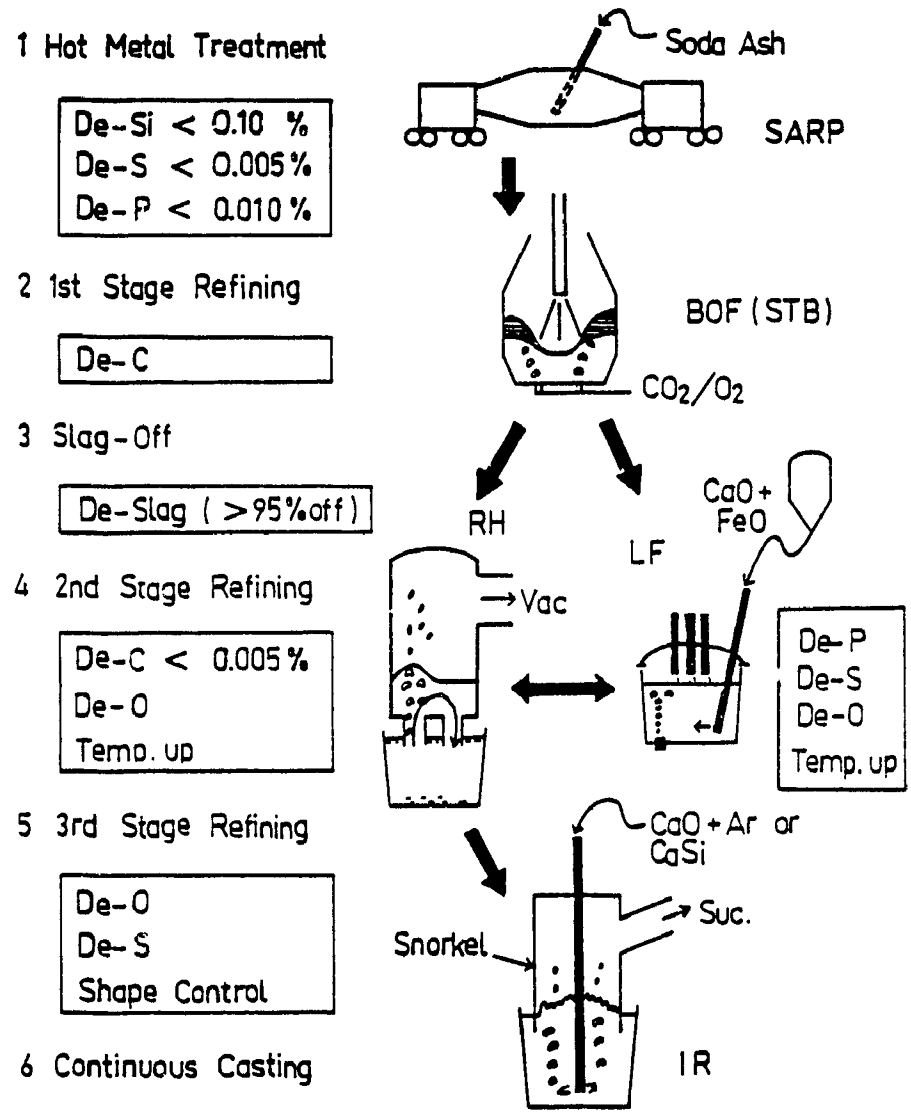

Figure 1-1 An Example of current processes for making clean steels (Sumitomo Metals Industry, Kasima Works).

the ladle, has now become standard practice in most steel shops Over the correct range of flows, this practice can eliminate chemical and thermal gradients within the steel by thoroughly mixing the vessel's contents, while minimising slag entrainment and heat loss. The procedure can also rinse the liquid steel of condensed oxide inclusions, which nucleate following aluminum or ferroalloy additions to the steel. However, in this processing, reoxidation due to variable slag carryover, and air entrainment can play havoc with alloy recoveries and in turn induce unacceptable variability into the final product chemistry Hence, less crude alloy addition procedures are subsequently made at alloy trimming stations (e.g. wire feeding, submerged powder injection, CAS process, etc.) in order to achieve closer control of the final product chemistry

Following ladle processing operations, the liquid steel is then cast into ingots, slabs, blooms, or billets. The continuous casting process shown in Figure 1-2 can produce slabs, blooms, or billets directly from molten steel. Its great advantage over an ingot pouring operation is on melt-shop yields, energy costs, improvements in steel quality, etc During the era of the 1980's, the ratio of steel produced via the continuous casting process versus total steel production has increased significantly in most major steel product countries, except for Eastern Europe It has been reported that the percentage of crude steel produced by continuous casting in 1987, reached 93.3 % in Japan, 81 1 % in Western Europe, 58 8 % in U S A , 49 % in Canada, 58 5 % in South America, and 86.4 % in Asian developing country (R. of Korea and Taiwan) (2). However, Eastern Europe is reported to have a mean continuously cast steel ratio of 16.7 % and U S S.R 14.9 %

Figure 1-2 An illustration of a continuous slab caster.

Direct rolling of slabs represents a further hurdle in the quest for continuous steelmaking Energy savings associated with direct rolling are significant and in the order of 0.5 GJ/tonne. These represent a 3.6% decrease from current best steel work practices of 13 8 GJ/tonne (from pellets to hot band) and bring steelmakers one step closer towards the minimum thermodynamic value of about 6.5 GJ/tonne for the production of steel from iron ore. These savings are brought about by the elimination of inspection procedures on cold slabs and subsequent slab reheating.For these benefits to be realised, the quality of steel entering hot mills must be assured in terms of chemistry, temperature and other physical characteristics, such as integrity (freedom from cracks, center-line porosity, scale, etc.) and metal cleanness (minimum levels of exogeneous inclusions).

In recent years, the tundish, which is an the intermediate vessel between the ladle and the mould of a continuous casting machine, has been recognized as an important metallurgical processing reactor for clean steel. Therefore, several operational techniques for tundish processing operations have been developed for the improvement of steel quality For instance, submerged inlet nozzles shrouded by an inert gas are generally used in order to avoid air and slag entrainment into liquid steel. Flow modification devices, such as weirs, dams, baffles, perforated dams, etc., can be employed for improving flow patterns so as to eliminate a greater portion of inclusions from the melt. Currently, ceramic filters are being tested for steel casting. They are commonly used for casting molten aluminum.

This section has provided a general review of subject matter relevant to ladle and tundish metallurgy In chapter 2, ladle metallurgy is reviewed in terms of furnace tapping, gas stirring, alloy addition, and ladle teeming operations. Chapter 3 provides a description of tundish metallurgy. There, the origin of nonmetallic inclusions, fine particle flotation, and current physical and mathematical models are briefly introduced. Finally, the last chapter describes the objectives and scope of the present study.

Chapter 2

Ladle Metallurgy

2.1 Furnace Tapping

Ladle processing operations begin with tapping steel from an electric, or basic oxygen, steelmaking furnace (B.O.F.), into the type of steelworks ladle shown in Figure 1-3. During the course of this tapping, alloy additions in lump form can be fed through chutes set above the filling ladle, so that they fall into the churning bath of molten steel. The additions melt and/or dissolve into the steel bath, so that the bath chemistry can hopefully be adjusted to that specified for the grade of steel being produced.

2.1.1 Turbulent flow in a filling ladle

Salcudean and Guthrie [3,4] were the first to predict flow patterns and velocity in an idealized filling ladle, where the jet of liquid steel was assumed to enter vertically into the center of a cylindrical ladle. There, using the k-ε turbulent model, the highest values of turbulent viscosities were to be found at the juncture of the penetrating jet and the recirculating bulk of steel, turbulent viscosities some 10^3-10^4 times laminar values being predicted. These predictions with respect to turbulent kinetic energy levels were later confirmed experimentally by Sahai and Guthrie [5].

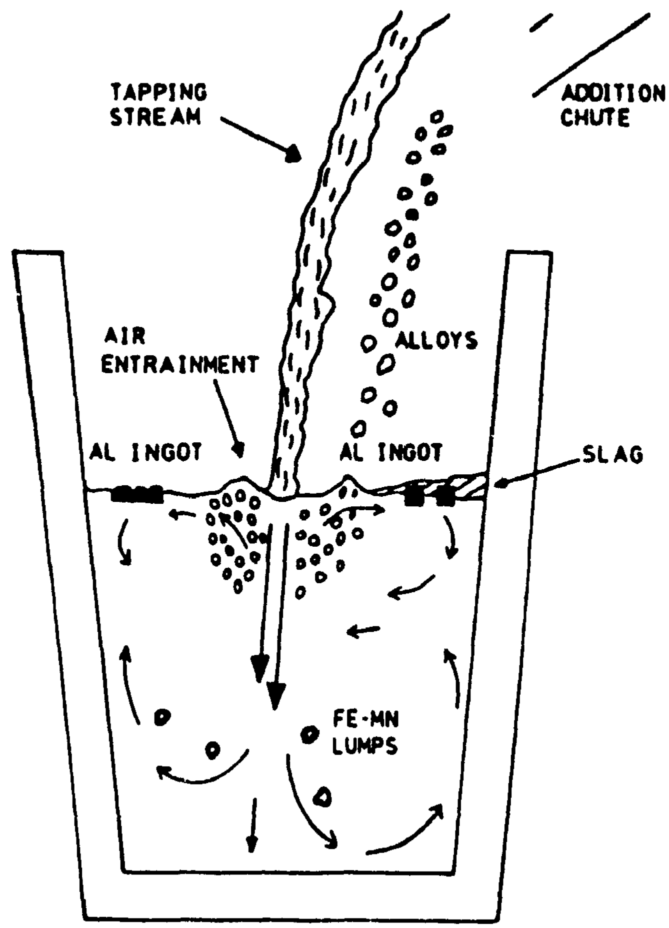

Figure 1-3 Schematic of tapping a furnace into a steelworks teeming ladle, showing alloy additions and slag carryover.

Figure 1-4 shows the velocity fields predicted by Sahai and Guthrie for a 250 tonne steel ladle filled to a height of 2.75 m with an incoming jet velocity at entry of 8.4 m/s [5]. It is clear that the recirculating flow will have a marked influence on the trajectory of alloy additions made to the melt during primary conditioning procedures.

2.1.2 Alloy trajectories in a filling ladle

An important aspect of getting ferro-alloys and aluminum to melt in molten steel in a reliable manner, is to try and ensure that they melt and disperse subsurface, out of harms way of any oxidising slags, or interactions with air. Guthrie et al. [6] demonstrated that gravitational, buoyancy, drag, and 'added mass' forces were needed for adequate representation of subsurface trajectories for large particles dropped vertically into stagnant liquid. Based on these simplifications, M. Tanaka [7] predicted the trajectories of entrained large particles.

Figure 1-5A shows computations and experimental data using a smaller scale water model simulation, wherein the correct density ratio between addition and liquid was maintained. Thus, wooden spheres with a specific gravity of 0.4 (roughly corresponding to spheres of aluminum, $\gamma = 2.3/7.0 = 0.33$, and ferrosilicon, $\gamma = 4.0/7.0 = 0.57$), are predicted to resurface almost immediately after projection into any part of such recirculating flows. On the other hand, heavier particles, ($\gamma = 0.8$), (roughly corresponding to the apparent densites of ferro-manganese, silico-maganese, etc., additions), have a chance of being drawn downwards into the recirculating flow, provided they are projected into the bath, reasonably close to the plunging jet. Figure 1-5B shows predictions for a ladle of 4 meters diameter, at a filling height of

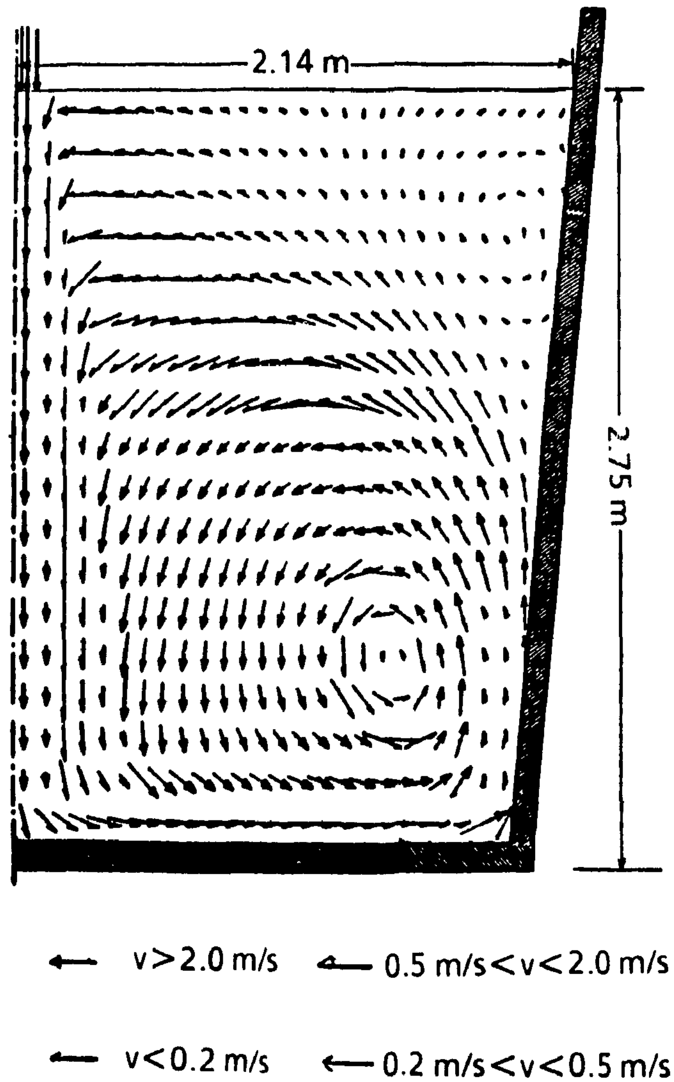

Figure 1-4 Predicted flow field for an idealized furnace tapping operation into a 250 tonne teeming ladle.

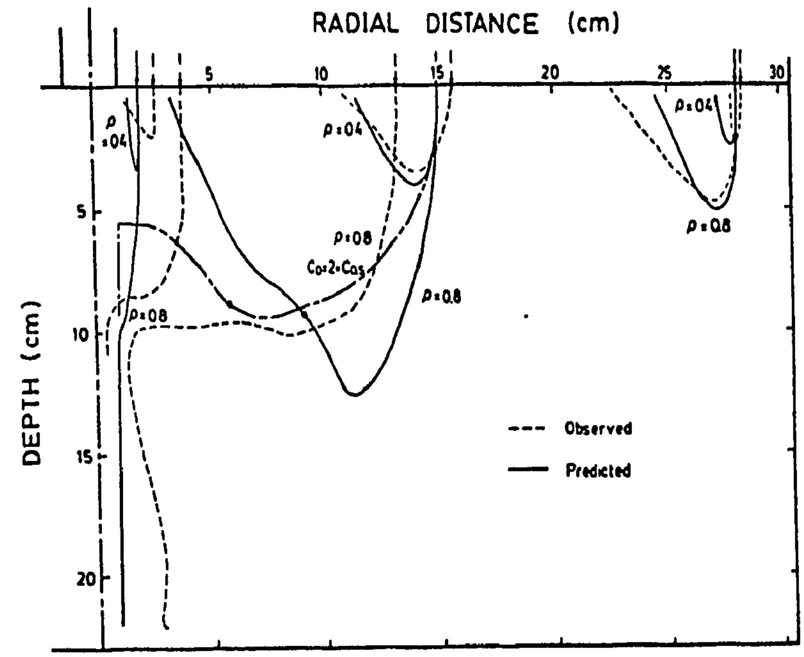

Figure 1-5A Trajectories of 10 mm diameter wooden spheres in a 0.15 scale model of a 250 tonne teeming ladle, during idealized furnace tapping operations.

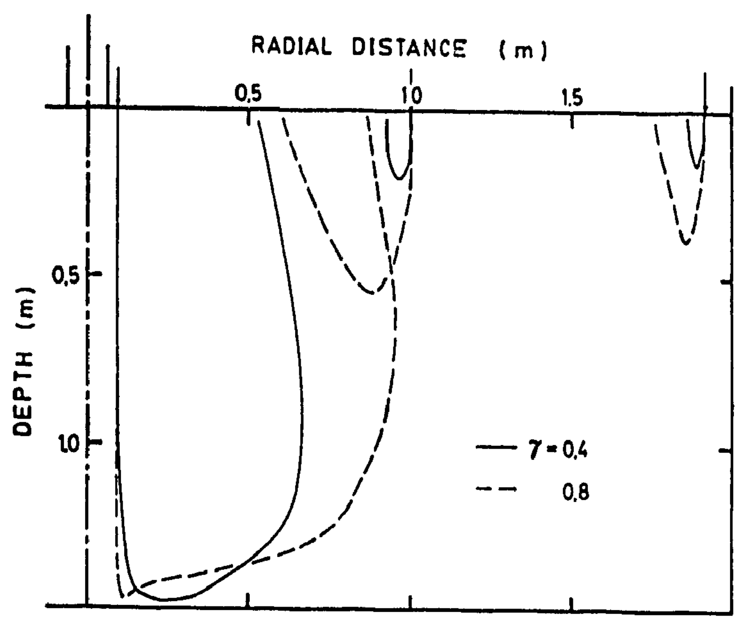

Figure 1-5B Predicted mean trajectories of 67 mm lumps (spheres) of alloy additions ($\gamma = 0.4$ and 0.8).

1.5 metres. It is worth noting that these predictions do not allow for air becoming entrained as the plunging jet enters the liquid bulk.

It is equally important to note that while predicted trajectories of alloy additions in such flow fields would be relatively similar,that once any entrained objects lost the 'protection' of their surrounding shells of steel, dispersion of their contents would be critically dependent on turbulent diffusion phenomena.

2.1.3 Slag carryover and air entrainment

While these simulations point to the deficiences of current alloy addition making procedures, the most critical problem in practice, is the variable amount of slag carryover from the furnace into the ladle, and air entrainment from the filling stream.

Towards the end of tapping operations, some steelmaking slag lying on top of the raw steel within the furnace is almost inevitably carried over into the ladle, due to overflowing the furnace lip or vortexing As this slag is oxidising, any steel deoxidation procedures will be affected by its presence. Slag carryover can also be a potential source of exogeneous inclusion material. Cramb and Byrne (8) argued that very small slag droplets might remain in suspension within liquid steel, being finally entrained into the product. Their work was based on EPMA (electron probe microanalysis) results of slab samples which were presented for a combined ladle and tundish slag tracer experiment. S.Tanaka (9) has demonstrated that rising gas can disrupt a slag layer, and entrain slag droplets into the liquid steel during combined blowing BOF steelmaking process. This fine dispersion of slag droplets in liquid steel within the furnace, can also be a source of slag carryover during metal tapping operations.

Most converter shops are now practising slag separation in one way or another. Typical methods are 1) to use refractory balls whose specific gravity has been adjusted to be between the slag and the molten steel, 2) to apply high pressure air jets sideways to the tapping hole so as to blow the slag away, and 3) to physically monitor the onset of slag vortexing in order to stop tapping when this occurs. Through these practices, the carryover of furnace slag into the ladle, which used to amount to more than 100 mm in thickness, can typically be decreased to less than 30 mm (10).

Air entrainment caused by the steel stream plunging into the filling ladle is also of interest during tapping operations. Brower et al. (11) proposed a qualitative mechanism for air entrainment by highly turbulent jet. They argued that it is the wavy shape of the penetrating stream that causes air to be entrained, resulting in a cloud of bubbles being drawn into the bath. Similarly, as the distance of the nozzle from the bath surface increases, such an irregular turbulent jet begins to disintegrate into droplets at its fringe. These droplets can then tend to form cavities as they enter the bath which subsequently collapse into entrained bubbles.

Several equations describing the volumetric ratio of entrained gas to liquid, Q_g/Q_l, have been proposed by different researchers who used a variety of experimental conditions (12-14). M.Tanaka (7) demonstrated with a physical water/air model that the volume flow rate of air entrained was of approximately same order as the melt tapping rate, for conventional furnace tapping operations.

2.2 Gas Stirring

Once teeming ladles have been filled with molten steel, the next step is to stir the vessel's contents for chemical and thermal homogeneity. The main point in gas stirring operations is to identify procedures and equipment for achieving minimum mixing times, and maximum recoveries of alloy additions at optimum gas flow rates. In order to reasonably predict these phenomena, detailed information on flow patterns, fluid velocities, and turbulent properties is needed: these have been the subject of study via ongoing mathematical and physical models over the last decade.

2.2.1 Gas dispersions in liquid metal

(a) bubble formation

The normal injection of gas into liquid metals is accompanied by the formation of very large bubbles. It is important to note that these bubbles are inevitably of the "spherical cap" variety owing to the high surface tension of liquid metals and the non-wetting characteristics of refractories.

The behaviour of bubble formation can generally be classified into three regimes of gas flow rates (15). At low gas flow rates, bubbles with a constant volume form periodically (single bubble regime). Irons and Guthrie (16) suggested the consecutive steps taking place for the isothermal formation of bubbles at nozzles in the single bubble regime. Thus, for an upward-facing nozzle, the bubble initially forms on the inner diameter of the nozzle, increasing in size towards a hemisphere. Owing to non-wetting and inertial phenomena, the bubble then tends to spread across the substrate, moving away from the inner diameter of the nozzle. Should the bubble reach the outside diameter, it can continue to grow by changing the observed contact angle in accordance with the Gibb's inequality. It does not spread down the nozzle since the considerable buyancy forces would oppose such movement. When the buoyancy of the bubble is balanced by the surface tension forces holding it to the outer, rather than inner, diameter of a nozzle, the bubble is released. The bubble formation/release mechanisms for an downward-facing or sideways-pointing nozzle are modified versions of this growth sequence.

At higher flowrates (e.g. 0.1 to 10 liters per second), inertial factors begin to outweigh surface tension factors, and a constant frequency regime is entered. In this regime, the frequency of bubble formation remains constant at about 10 per second, the volumes of the bubble forming and releasing becoming larger and larger, and the distance between the succesively forming bubbles becomes shorter with increase in gas flow rate [17]. Due to the suction effect of the previous bubble, the following bubble forms more quickly. They can then coalesce while rising up. The bubble volume in a constant frequency regime can simply calculated from

$$V_b = Q/f \simeq 0.1Q \tag{1-1}$$

However, these large bubbles or gas envelopes forming at nozzles, orifices, or porous plugs tend to exhibit hydrodynamic instability. Thus, they must consequently shatter a shorter way above the nozzle into an array of smaller bubbles.

With a further increase of the gas flow rate, the bubbles coalesce directly at the nozzle. Finally, a continuous gas jet forms at the nozzle (continuous jet regime). Since gas flow rates for gas stirring in ladle processing operations remain within a constant frequency regime, the jet will be out of consideration for ladle metallurgy.

(b) plume

The characteristics of the gas/liquid mixture region, or *plume,* during gas bubbling in ladles plays a key role in the generation of recirculating flows for the mixing of chemical and physical components. Figure 1-6 provides a schematic of the gas/liquid mixture [18]. As a driving force of recirculation in bath, two-types of force can be taken into account, the kinetic force and the buoyancy force. However, it has been recognized that the kinetic energy of the incoming gas into stirred ladle is quickly dissipated in the vicinity of the tuyere opening, and does not significantly affect the remainder of the bath [19,20]. The buoyancy force , thus, is the essential driving force for the motion of gas/liquid mixture system.

The general progress of forming the plume and consequently generating recirculating flows in the ladle can be suggested as follows: As the gas envelopes or large bubbles are discharged from the orifice, or the porous plug, into the surrounding heavier liquid, they expand quickly due to the sudden pressure drop and temperature change within a very short time (0.1~0.3 second) [19]. However, these large bubbles rising are hydrodynamically unstable due to a continuous drop in pressure within surrounding liquid. Combined with the fast, turbulent, movement of bubbles, large gas envelopes soon shatter into different sizes of smaller bubbles. Since each bubble entrains adjacent liquid during rising-up, gas/liquid mixture regime tends to expand with vertical distance above the orifice, forming a cone-shaped two-phase region. Each bubble exerts a drag force on liquid proportional to its buoyancy.

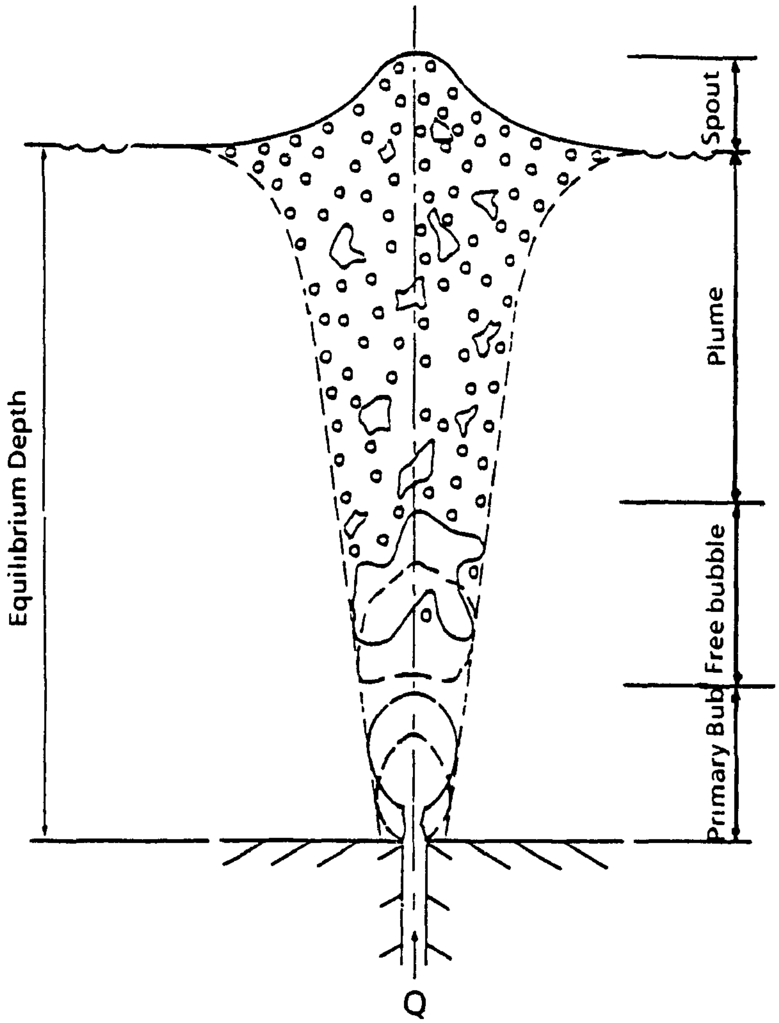

Figure 1-6 A schematic of complete gas dispersion in liquid.

The liquid around the bubbles inside the plume is, therefore, accelerated and generally moves upward with them. At the surface of the liquid, the gas bubbles disengage from the two-phase flow region, the liquid moves outwards from the plume. Thus the motion is transfered to the liquid bulk by both convective force and turbulent fluctuations. This progress of energy exchange between the injected gas and the liquid results in mixing of the liquid in bath.

Recently, several plume models, which evaluate plume velocities and/or gas voidge in plume, have been proposed (18, 19, 21, 23). Sahai and Guthrie (21) have shown that the mean rising velocity within a gas/liquid plume approximates the expression (*SI* unit) :

$$U_p = 4.17\left(\frac{H^{\frac{1}{4}}\,Q^{\frac{1}{3}}}{R^{\frac{1}{3}}}\right) \tag{1-2}$$

where Q is the flow of gas at mean ladle height and temperature (m^3/s), H is the depth of liquid steel (m), and R is the mean radius of the ladle (m).

2.2.2 Flow fields in stirred ladles

Szekely, Wang and Kiser (24) were the first to attempt hydrodynamic modelling of an argon stirred ladle. Through solution of Navier-Stokes equation (stream function/volticity method) and k-W two equation model of turbulence, they predicted flow fields and turbulence energy fields in water model of the system. However, as a deficit of this work, boundary velocity values were experimentally obtained by hot wire anemometry measurements. Szekely, Lehner, and Chang (25) employed the same shear stress model for an argon stirred ladle, but boundary velocity values and shear stress adjacent to the cylindrical core of gas were estimated from a plume rise relationship. Nonetheless, their results were proven unrealistic because of the crude representation of the plume.

More recently, Debroy and Majumdar (23) and ,at the same time, Grevet, Szekely, and El-Kaddah (26) proposed more developed computational schemes wherein the gas/liquid mixture contained within the plume region was represented by a fluid of the variable density. They solved the turbulent Navier-Stokes equation, in conjunction with the k-ε two equation model of turbulence, with consideration for the buoyancy force of lighter fluid (plume) in the u-momentum equation. They found that theoretically determined and experimentally measured velocity profiles were in good agreement.

Concurrently, Sahai and Guthrie (21, 22) developed a mathematical model for gas stirred ladles through the solution of turbulent Navier-Stokes equation and k-ε turbulence model.Their numerical procedure was based on the SIMPLE procedure of Patankar and Spalding (27). The gas/liquid, two-phase, region was treated by the GALA (Gas And Liquid Analyser) method of Spalding (28). The velocity boundary condition at the axis of symmetry and gas voidge in the plume zone were calculated from their plume model. Their approach is simple and correctly emphasizes the importance of buoyancy, versus shear, forces in gas driven recirculating flows. It has been confirmed through many experiments to be an effective way of treating such problems. Nonetheless, the approach requires that the plume dimensions and gas voidage be specified "a priori".

Figure 1-7 illustrates the computed flow fields generated in a 250

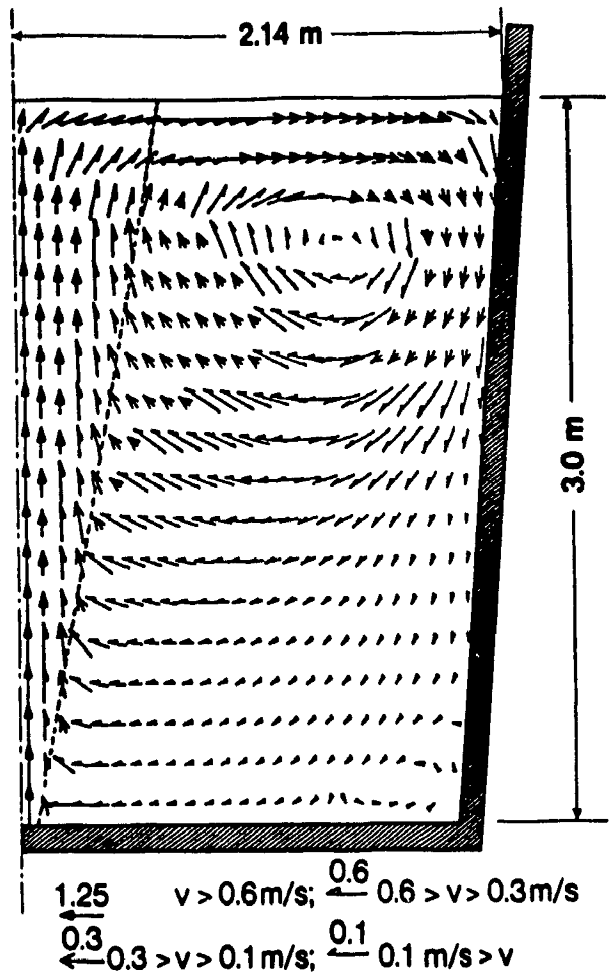

Figure 1-7 Predicted velocity field in a 250 tonne ladle of steel with central gas injection at 0.25 Nm^3/min.

tonne ladle with 5 degree inclination of sidewalls from the vertical, when a gas flow of 0.25 Nm^3/min is injected axially through a porous plug [5]. Plume velocities were predicted to be in the range of 1.0~1.5 m/sec, and steel flow down the sidewalls to be ~0.2 m/sec.

2.2.3 Mixing behaviour in stirred ladles

The purpose of agitation in gas stirred ladles is to promote the dispersion of ladle additions and to attain uniform properties (e.g. temperature) within the bath. Agitation can also be used to promote the coalescence and flotation of inclusion particles. Hence, mixing mechanisms of physical and/or chemical elements in recirculating flow vessels is an important issue for ladle metallurgy practices.

Mazumdar [29] demonstrated that mixing in a gas stirred ladle can be expected to be controlled by a combination of eddy diffusion and bulk convection, both mechanisms contributing in roughly equal proportions. Joo and Guthrie [30] further illustrated that the mixing would occur in different ways, depending on a plug's locations, the number of plugs, and the tracer addition point. For instance, when the tracer is added at a sidewall of axisymmetrically stirred ladle (center bubbling), mixing appears to occur largely by eddy diffusion, rather than by the bulk circulation of liquid. This is caused by the fact that center gas bubbling has no angular momentum associated with it. By contrast, for the off-center gas bubbling or multi-plug gas bubbling, momentums in the three-polar directions become comparable so that mixing occurs more rapidly versus center bubbling, and the contributions of bulk circulation and eddy diffusion should be weighted about equally.

In order to represent quantitatively the state of agitation in the chemical and metallurgical processing vessels, the concept of a mixing time has been introduced. The mixing time is defined as the time which elapsed between the addition of a tracer to the bath and the moment when its concentration reaches the final, homogenised, concentration over the bath. However, in measuring and/or computing mixing times, it is important that there be a clear definition of what is meant by mixing time. It has been suggested (29) that the 95 % mixing time be used as a suitable standard, and that it be defined as that time at which all the local concentrations of tracer addition have reached 95 % of the bulk well-mixed value.

Mixing times tend to decrease exponentially with an increase in gas flow rate. Thus, Nakanish, Fuji, and Szekely (32) plotted mixing time data against the global rates of specific energy dissipation (or input stirring energy) for an argon stirred ladle, an induction stirred ASEA-SKF system and a water model ladle, then suggesting a relationship given by (*SI* unit) :

$$\tau_m = k\varepsilon_m^{-n} \tag{1-3}$$

where *k* and *n* were given to be 800 and 0,4, repectively, in their work. Then, followed by many theoretical and physical studies on mixing behaviour in stirred ladles, it has been proven that the value of *n* in Equation (1-3) is 0.33 without consideration of upper slag layer (29,33,34), and ~0.4 with liquid-phase slag layer (19,32,35,36). But, the constant *k* varies depending on vessel shape and size, gas bubbling location, the number of porous plugs, etc..

Màzumdar and Guthrie [37] provided that the 95% mixing-in time for a neutrally buoyant addition (or tracer) added to the surfacing plume of liquid in an axisymmetrically stirred ladle, could be approximated by the empirical expression (*SI* units).

$$t_m = 25.4 \frac{R^{7/3}}{\left(\beta Q\right)^{1/3} H} \tag{1-4}$$

where β is the fractional depth of lance submergence (β = 1 for bottom porous plugs).

Mixing behaviours including mixing times can be studied by numerically solving the turbulent mass transport equation with incorporation of fluid flow fields calculated *a priori*. (This will be covered in Part III of this thesis).

2.2.4 Effects of a slag layer

The pouring of liquid steel from a furnace into a ladle, or vice-versa, generally leads to uncontrolled amounts of slag carryover. Being lighter, this slag separates to form an upper phase of variable thickness and viscosity. While its insulating properties are generally beneficial for maintaining steel temperatures, its chemical characteristics are often detrimental. For instance, steel deoxidation efficiencies can be significantly lowered through chemical reduction of the iron oxide component of any carryover slag. This mass transfer reaction with residual dissolved silicon and/or aluminum deoxidant within the steel can be exacerbated when disturbances of the slag layer during gas bubbling are sufficient to cause slag entrainment. Nonetheless, stirring procedures for eliminating thermal stratification, inclusion removal and uniform mixing in alloy additions have now become standard practice for all concast operations (the Strong Stir Station).

With the presence of a liquid phase slag layer on the steel melt, mixing during gas sirring operations is known to be significantly delayed. Mazumdar, Nakajima and Guthrie [38] have illustrated that the overlying liquid phase slag dissipates a part of the input energy, which in turn, causes the speed of metal recirculation and levels of turbulence to be significantly decreased, thereby delaying mixing. Their experimental work showed that it is the deformation of the overlaying liquid phase slag, into the lower melt bath around the perimeter of the surfacing plume, that is primarily responsible for the energy deficit in the recirculating liquid.

The behaviour of the gas/liquid mixture plume often causes slag/metal interfacial turbulence, resulting in the acceleration of mass transfer between slag and metal and/or the entrainment/dispersion of slag droplets into the melt [9, 38]. In addition, it has been reported that the desulfurization rate of steel by a synthetic slag in a plant scale ladle showed a sudden increase at a critical flow rate [39,40].

Figure 1-8 provides a typical example of an abrupt increase in mass transfer rates [41]. It was obtained from a 0.14 scale water model of a 200 tonne steelmaking ladle, where the liquid phase slag was simulated by paraffin oil, and β-naphthole ($C_{10}H_8O$) was used as the transfered tracer. At low gas flow rate, the mass transfer rate increased slowly with the increase of gas flow rate. At a critical flow rate, Q_{cr} (6.5 liters/min in Figure 1-8), the

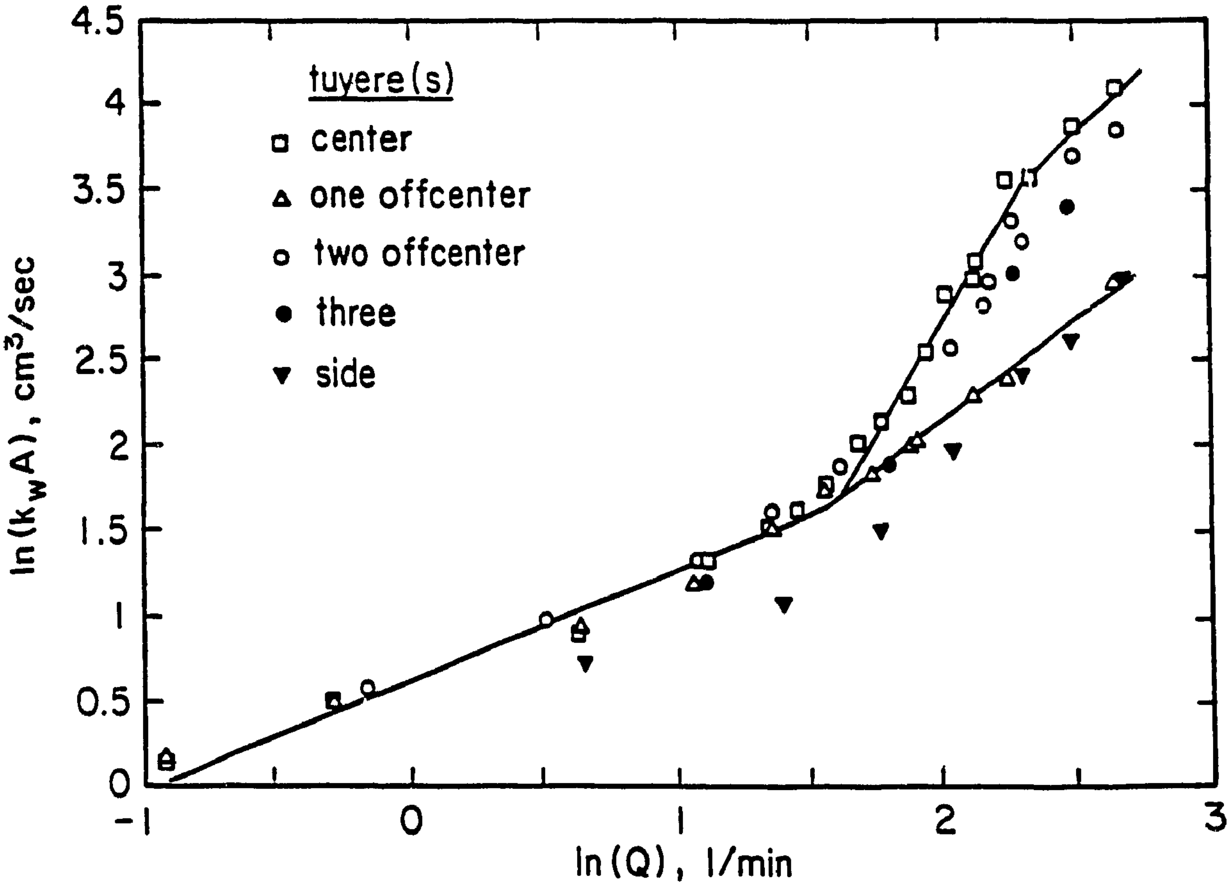

Figure 1-8 Relationship between mass transfer coefficient (k_wA) and gas flow rate (Q) for four different tuyer patterns.

change rate of mass transfer coefficient versus gas flow rate abruptly increased, the slope being a strong function of flow rate. It was observed that this phenomenon is caused by the break-up of liquid the slag layer in the plume region, and the attendant entrainment of slag droplets into the metal bath.

Using dimensional analysis and a physical model experiment, an empirical expression for predicting the critical gas flow rate through a plug that causes liquid slag start to be entrained into an underlying steel bath has been formulated. It is given by (C.G.S. unit) :

$$Q_{cr} = 6.7 \times 10^{-2} H^{1.81} \left(\frac{\sigma \, \Delta\rho}{\rho_s^{\,2}} \right)^{0.35} \tag{1-5}$$

where Q_{cr} (cm^3/s) represents the critical flow rate, H (cm) the height of ladle, σ (dyne/cm) the interfacial surface tension, $\Delta\rho$ (gr/cm^3) the density difference between slag and metal, and ρ_s the slag density.

2.3 Alloy Additions

Following tapping, mixing and rinsing procedures, many plants transfer the ladle to an alloy addition trimming station. There, special alloy additions, wire feeding of aluminum or cored wires containing calcium silicide or rare earths, and powder injection of calcium silicide or calcium oxide can be used for precise trimming of alloying elements or inclusion modification, in order to meet the steel's specifications.

2.3.1 Alloy melting/dissolution

Guthrie (42) proposed four main possible route of melting when a cold addition is placed or immersed in a bath of molten steel, depending on the precise heat and mass transfer conditions involved. They are, in schematic form, illustrated in Figure 1-9. The first three refer to additions having melting points lower than the steel bath (e.g. aluminum, ferro-silicon, ferro-manganese, silico-manganese, etc.), the fourth refers to additions having melting ranges higher than the bath (e.g. ferro-molybdenum, ferro-tungsten, ferro-niobium, ferro-vanadium, etc.). Immediately following immersion, in all cases, a solid steel shell freezes around the object due to the cold surface temperature and interfacial thermal resistance at the solid addition (43, 44).

If the melting range of the addition is then below the bath's freezing point, it is quite likely for internal melting to begin and in many cases to be completed before the enclosing shell melts back (Path 1). Provided that the alloy's solubility limit is not exceeded, this molten core will dissolve very rapidly into the steel bath The second path (Path 2) shows the case of an addition which, after freezing the customary chill layer around it, is reexposed to the bath before complete internal melting has occured. Conditions favoring such behaviour include high superheat temperatures (e.g. 50~100 °C), large diameters, and alloy with low thermal conductivities (<~0.01 cals / cm·°C·sec). Path 3 shows a second smaller shell of steel which has formed around the remaining unmelted portion of the addition after dispersion of the outer alloy liquid has occured. This takes place if the amount of heat being convected into the first shell surface is below the heat demand from the colder interior. Finally, the last path (Path 4) refers to those additions having melting ranges above that of the steel bath. Once more, a steel shell will first

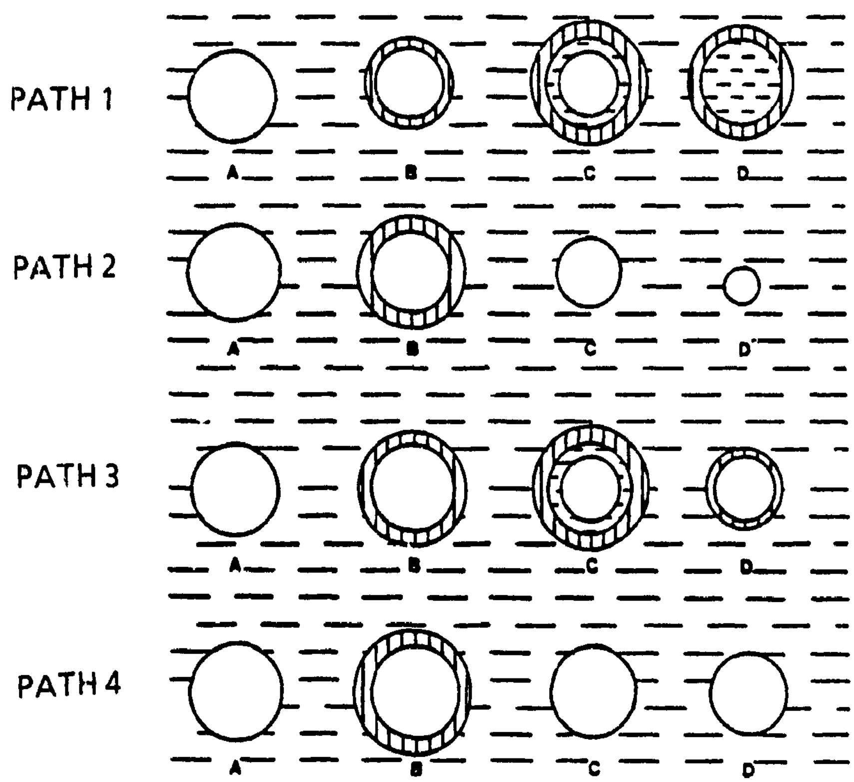

Figure 1-9 Four kinetic paths for alloy additions melting and/or dissolving in molten steel.

form, only to melt back as the addition approaches the steel bath temperature. Thereafter, the rate of dissolution will be physical or chemical mass transfer limited and heat transfer becomes of secondary importance.

Therefore, melting kinetics of alloy additions and dissolution time tend to depend largely on the given conditions of specific alloy-bath system, such as addition properties, superheat, size and shape of additions, intensity of bath agitation, and so on. While it is useful to be able to predict the accurate melting time, the task is complex on account of the numerous factors involved (i.e. determination of melting route, multi-phase heat convection/conduction, moving boundary problems, precise thermal data, etc.).

Guthrie went on to suggest a simple way to evaluate approximate melting time, for Class 1 ferroalloys. Thus, supposing that the melting time is equal to the total heat requirement of the addition devided by the rate at which heat is being supplied from the bath, i.e.

$$t_{melt} \approx \frac{\Delta H \rho_a V_a}{q'' A_a} \tag{1-6}$$

where ρ_a, V_a, and A_a are the density, the volume, and the surface area of addition, repectively. ΔH represents the total heat required for melting alloy addition, and q'' the heat flux flowing through the steel shell/alloy addition.

2.3.2 Motion of alloy additions

Before alloy additions disperse into the steel within the ladle they remain as discrete objects, and are therefore subject to Newton's laws of motion. For additions such as aluminum and ferro-manganese, a chilled layer of steel forms over a molten core of alloy. Figure 1-10 schematically demonstrates the forces acting on a sperical object, there, both the object and fluid being supposed to be in motion. F_G and F_B represent the gravitational force and the buoyant force respectively, and as such are parallel to gravity. The Stokes drag force, F_D, is taken to be parallel to the relative velocity of the particle in the fluid. The "added mass" force, F_A, which originates from the acceleration of the surrounding fluid by the particle, is taken to be parallel to the acceleration vector of the object.

Thus, ignoring changes in mass for such additions, an appropriate force balance on a particle within the fluid is (6):

$$\frac{4}{3} R_p^3 \rho \frac{d\mathbf{U}_p}{dt} = \frac{4}{3} R_p^3 g \left(\rho_p - \rho \right) - \frac{C_D}{2} R_p^2 \rho \mathbf{U}_r \left| \mathbf{U}_r \right| - C_A \frac{4}{3} R_p^3 \rho \frac{d\mathbf{U}_p}{dt} \tag{1-7}$$

where,

$$\mathbf{U}_p = \frac{d\mathbf{x}}{dt} \tag{1-8}$$

In Equation 1-8, U_p is the instantaneous velocity vector of the particle while U_r, is the relative velocity between the particle and the bulk fluid. It is through the drag term (i e , $F_D \propto U_r^2$) that the liquid's motion within the vessel exerts an influence on the trajectory of submerged particles. Consequently, the distribution of flow parameters within the vessel must first be specified, before subsurface trajectories can be predicted via Equations 1-7

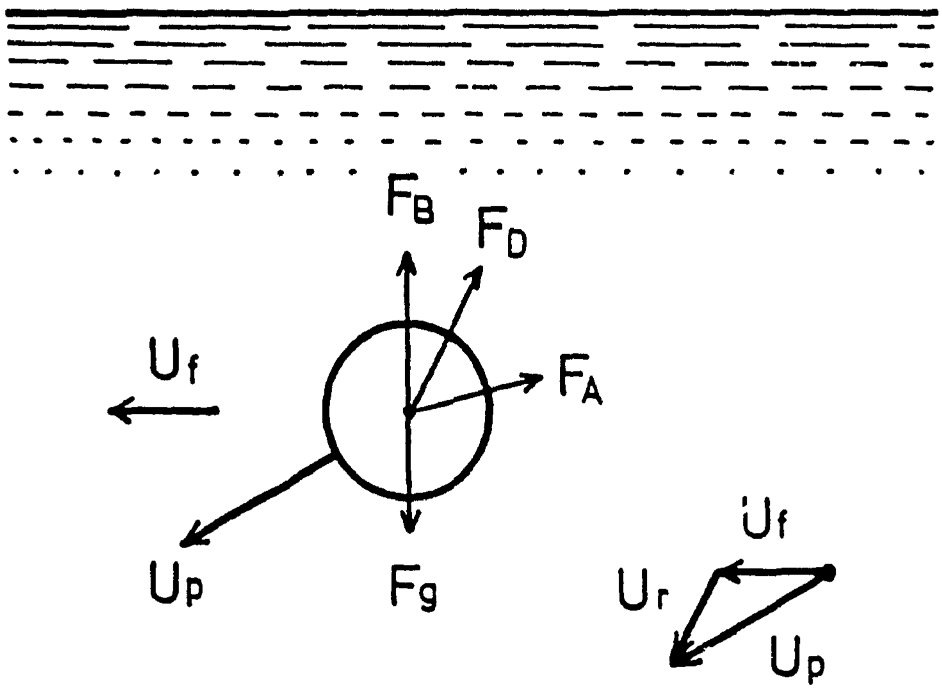

$$F_D \parallel U_r, \quad F_A \parallel \frac{dU_p}{dt}, \quad F_g, F_B \parallel g$$

Figure 1-10 The forces acting on a spherical particle in a moving bath.

and 1-8.

2.3.3 Alloy trimming stations

Figure 1-11 provides schematic illustrations of several alloy trimming stations for the improvement of alloying efficiency [10]. Thus, Muzumdar and Guthrie [45] have analysed the motion of the melt and alloy additions for the C.A.S. (Composition Adjustment by Sealed argon bubbling) process developed by Nippon Steel Corporation [46], through the use of physical and mathematical models

Figure 1-12A shows computed flow fields, following somewhat ad-hoc adjustments to two of the k-ε model's coefficients (i.e. $C_1 = 1.58$, $C_2 = 1.75$, instead of standard values). These solutions correctly modelled the strong recirculatory flow beneath the cylindrical baffle, and the much slower anticlockwise vortex in the main bulk of the ladle. Subsequently, Schwarz et al. [47] found that correct flows could be obtained using standard turbulent constants provided a two-phase flow simulation techique was employed. They also showed that the 'interphase slip' between the gas and liquid phases within the plume greatly affects computations of flow patterns.

Figure 1-12B predicts the trajectory of ferro-alloy additions and aluminum after being projected into steel within the central baffled region of a 150 ton ladle As seen, the light additions (Al and Fe-Si) will remain within this region, while the more dense additions ($\gamma > 1$) will sink to the bottom of the ladle, and then only gradually disperse. Consequently, additions such as ferro-niobium, which dissolves comparatively slowly compared to the release times of Class 1 (low melting point) additions [48,49] need to be finely crushed

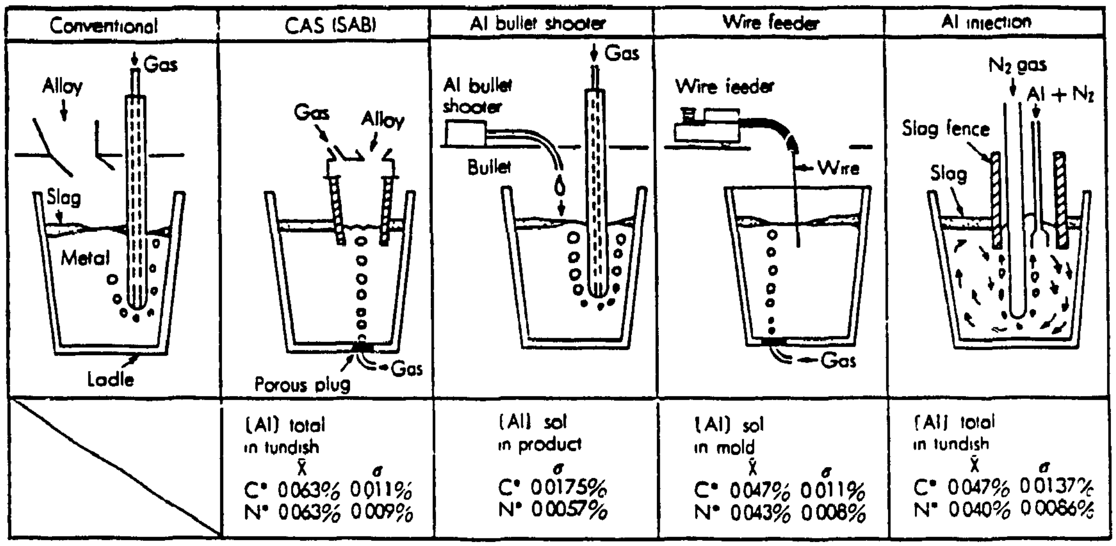

C*, Conventional, N*, New practice, X̄: Average, σ Standard deviation

Figure 1-11 Typical alloy trimming stations at industrial steel shops for low carbon aluminum killed steel.

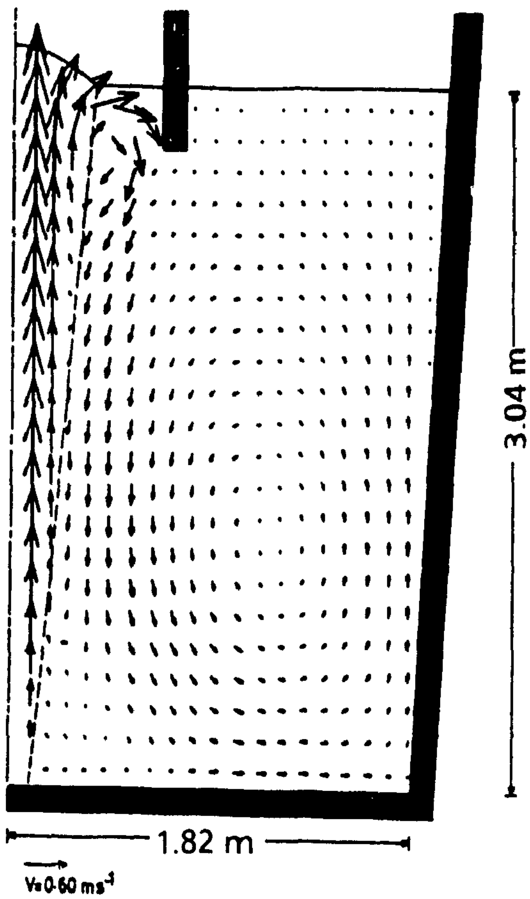

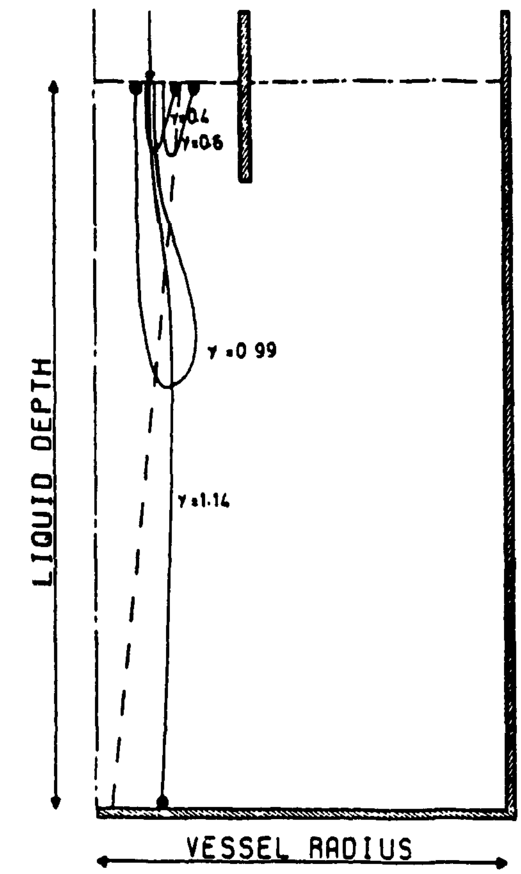

Figure 1-12A

Predicted velocity field in a 150 tonne steel ladle with a baffle at the center of ladle (CAS process).

Figure 1-12B

Predicted trajectories of four typical spherical alloy additions in a 150 tonne ladle during CAS alloy addition operation.

A

B

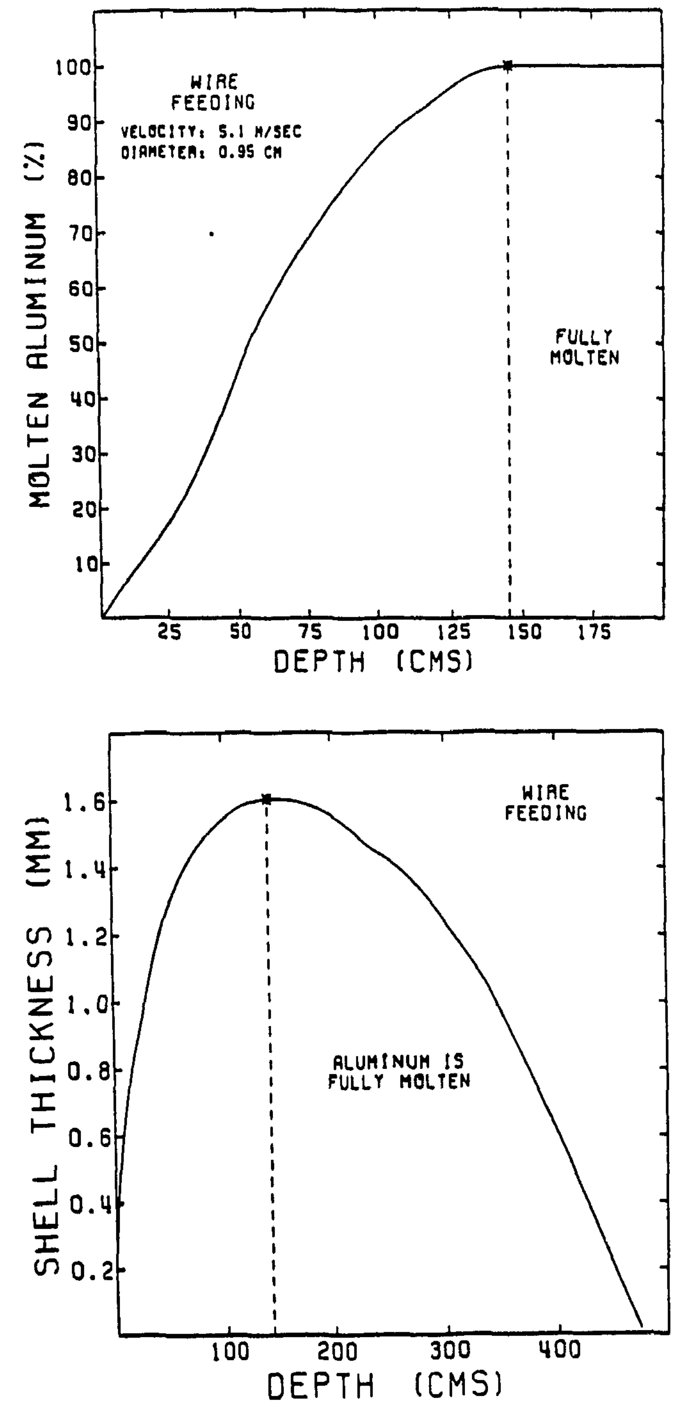

Figure 1-13 Thermal simulation of a 0.95 cm aluminum wire fed at 5.1 m/s into a steel bath with a superheat of 30 °C. (A) % aluminum molten vs. depth of wire in bath. (B) Steel shell thickness vs. depth of wire in bath.

(d<2 cm) if they are to dissolve completely within a reasonable length of time.

A way of ensuring subsurface melting is the wire feeding technique. In such cases, the relative motion is provided by the rapid entry of wire into argon stirred ladles. Figure 1-13A and B provide some predictions(50) for an industrial process in which 0.95 cm diameter aluminum wire is fed at 5.1 m/sec. As seen, a ladle depth of 1.4 m would almost match predicted shell melt-back times. Here, the heat transfer coefficient was computed as 4.4 (cals / $cm^2 \cdot °C \cdot s$) on the basis of forced convection heat transfer corelations. It have been observed that the mixing time is fastest when wire feeding takes place near the bottom of the ladle and within the plume during off-center bubbling rather than center bubbling (51).

2.4 Ladle Teeming

After mixing, and/or alloy addition trimming, the ladle moves to the ingot or tundish for continuous casting operations, and molten steel is drained through the ladle's outlet nozzle. An interesting (though distressing) metallurgical phenomenon during ladle teeming is slag carryover during the last stages of ladle draining.

Recently, a few reports have appeared (52-56) on this matter. Andrzejewsk et al (53) have observed that slag carryover during ladle teeming can take place by the "*vortex sink*" and/or "*drain sink*" mechanisms. The vortex sink can be generated by residual angular momentum within the fluid bulk. Conservation of angular momentum then requires a high velocity of revolution of metal above a centrally placed outlet. This leads to the formation of a hollow core, with slag being carried through the core. Such vortices can be suppressed using tactics such as filter brakes, gas injection, or simply eccentric positioning of the outlet (53-55).

Andrzejewski et al. go on to show that the drain sink flow mechanism during the last stages of ladle emptying is the more important cause of slag carryover. This drain sink phenomenon is characterized by a precursing hydraulic jump above the outlet, followed by the development of a hollow core at some critical flow velocity in the outlet nozzle. As with the vortex sink, there is a great amount of slag drainage through the core of the drain sink. Furthermore, any slag carryover resulting from drain sink flow is a more or less sudden, and perhaps, inevitable event.

Chapter 3

Tundish Metallurgy

3.1 Non-metallic Inclusions in Steel

Steel products inevitably contain various types of nonmetallic inclusions in the form of oxides, sulphides, nitrides, etc.. These inclusions sometimes give detrimental effects on steel quality, if they are not properly controlled. In the steelmaking process, the non-metallic inclusions are naturally categorized by two groups, those of indigeneous, and those of exogeneous, origin. The indigeneous inclusions are formed as a product of reactions taking place in the molten or solidifying steel bath, whereas the exogeneous inclusions result from mechanical incorporation of slags, refractories or other materials with which the molten steel comes in contact.

The possible origins of nonmetallic inclusions for continuously casting machine are illustrated schematically in Figure 1-14 (1). Thus, indigeneous inclusions are principally composed of oxides and sulphides, and the reactions forming them may occur by alloy and/or powder additions to the steel for deoxidation, desulfurization, inclusion shape control purposes. Alternatively, changes in solubility during the cooling and freezing of the steel may be responsible for their formation.

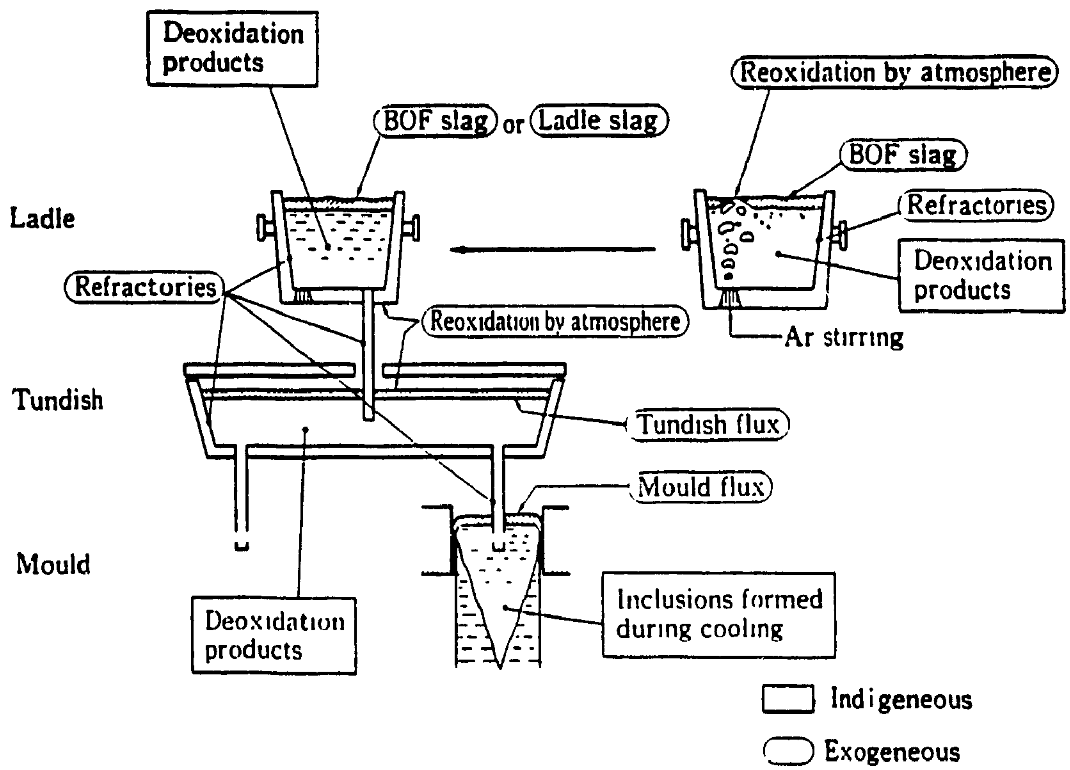

Figure 1-14 Schematic illustration of possible origins of oxide inclusions.

Exogeneous inclusions are usually composed of oxides, and are a result of alloying additions and exogeneous materials such as slags, refractories and fluxes. Their characteristic features include a generally larger size inclusions of sporadic occurence, together with irregular shapes and complex structure [57]. These exogeneous inclusions are often extremely harmful to a steel's properties, and must therefore be avoided or eliminated from steel processing procedures.

3.2 Inclusion Flotation in Liquid Steel

In tundish metallurgy, inclusion particle behaviour is of great interest for the study of inclusion separation from the steel. Non-metallic inclusions in steel are usually lighter than liquid steel. Therefore, if a lighter particle, at rest, begins to rise up under the action of buoyancy, its velocity is increased initially over a period of time. The particle is subjected to the resistance of the fluid medium through which it ascends. This resistance increases with particle velocity until the accelerating and resisting forces are equal. From this point on, the solid particle continues to rise at a constant maximum rising velocity, u_s.

For the Stokes law range (Re<2), the terminal rising velocity of a monosize spherical particle, u_s, can be written

$$u_s = \frac{(\rho - \rho_p) g d^2}{18\mu} \tag{1-9}$$

where ρ and ρ_p is the density of the fluid and of the particle, respectively. g is the acceleration due to gravity, d the particle diameter, and μ the viscosity of the fluid.

Within the intermediate range of Reynolds number ($2<Re<500$), the empirical relationship for a particle's rising velocity becomes [58]

$$u_s \simeq 0.78 \frac{(\rho-\rho_p)^{0.715} d^{0.43}}{\rho^{0.285} \mu^{0.43}} \tag{1-10}$$

and, similarly, for particles within the range of Newton's law ($Re>500$)

$$u_s \simeq 5.46 \left\{ \frac{(\rho-\rho_p) d}{\rho} \right\}^{0.5} \tag{1-11}$$

Though inclusion particles larger than 200 µm in diameter can sometimes be observed in a steel product, most inclusion particles are distributed within less than ~150 µm in diameter [59]. Considering this fact, the maximum particle size for which velocity follows Stokes law can be established by substituting $\mu Re/d\rho$ for the rising velocity in Equation (1-9), and setting Re equal to 2, i.e.

$$d_{max} = 1.56 \left\{ \frac{\mu^2}{(\rho-\rho_p)\rho} \right\}^{1/3} \tag{1-12}$$

Taking $\rho = 7000$ Kg/m^3, $\rho_p = 3000$ Kg/m^3, and $\mu = 0.0068$ Kg/m s, the maximum particle size is estimated to be 185 µm. Hence, it is reasonable to assume that inclusions typically encountered in molten steel should follow Stokes law.

3.3 Physical modelling for tundish metallurgy

3.3.1 Inlet nozzle shrouding

When the steel stream flowing from the ladle into the tundish is exposed to atmosphere, the molten steel can be reoxidized by air entrainment. Consequently, argon gas sealing, and/or submerged nozzles are currently used in order prevent reoxidation during metal transfer operations to the tundish.

Figure 1-15 compares total oxygen contents for argon shrouded and non-shrouded streams (60). As seen, the total oxygen content was significantly decreased when the stream was shrouded by a sealing gas. Submerged nozzles between ladles and tundishes are also very useful for avoiding the entrainment of slag droplets into the liquid steel: these are associated with open pouring of steel stream which plunge through an upper slag layer (61).

3.3.2 Flow modification - Improvement in inclusion separation

Many studies have been carried out for improving inclusion separations from tundish melts by using flow modification devices (62-67). Kemeney et al. (62) were early pioneers to investigate flow patterns in tundishes. For their studies, they injected a dye tracer ($KMnO_4$) into the ladle teeming stream, and measured minimum retention times for several different configurations of flow control devices (i.e. weirs and/or dams). They found that retention time profiles could be used to interpret flows in a tundish in terms of a mixed flow model. They were able to suggest the fractions of backmixed flow, plug flow, and dead volume within the tundish. According to

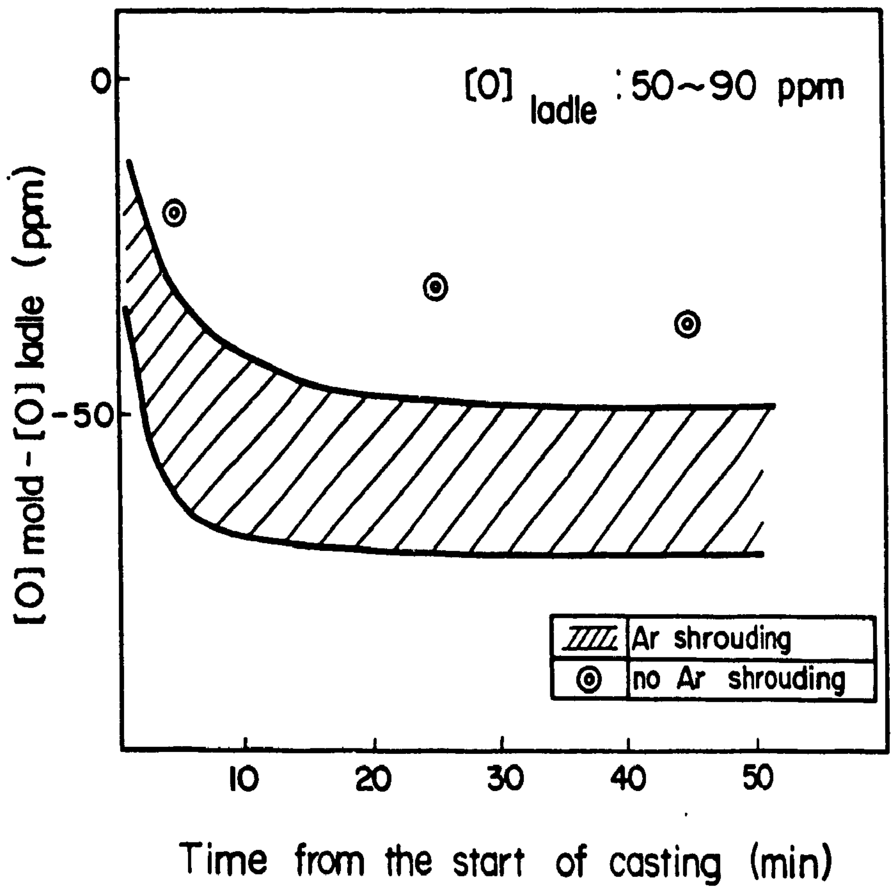

Figure 1-15 The effect of argon gas shrouding on change in oxygen content during casting.

these authors, the weir and dam arrangements greatly improved the tundish flow patterns (i.e. plug flow volume fraction increased). Further, minimum retention time were also markedly increased, thereby enhancing the separation of nonmetallic inclusions from liquid steel. Figure 1-16 shows some schematic flow patterns in a tundish with, and without, flow control devices observed by them.

D. Harris and J. Young, on the basis of industrial plant experiments, were the first to confirm (63) the benifit of the weir and dam arrangement for inclusion separation . However, they found that the refractory property of the flow control device used also significantly affected the results of inclusion separation.

The depth of steel in a tundish as well as its casting rate are also considered to be major factors determining inclusion separation behaviour. As the bath depth is increased, the number of inclusions into the mould decreases (9, 60). Similarly, inclusion separation is significantly improved with decreasing steel casting flow rate (1, 9).

3.3.3 Tank reactor model

S.Tanaka (9) has presented data and argued that the inclusion residual ratio, which defines inclusions still present in the effluent stream expressed as a fraction of those entering, is seen to correlate with rising velocity of inclusion particles following an equation of the form :

$$R = \frac{N_{out}}{N_{in}} = exp\,(-\,k\,u_s) \qquad (1\text{-}13)$$

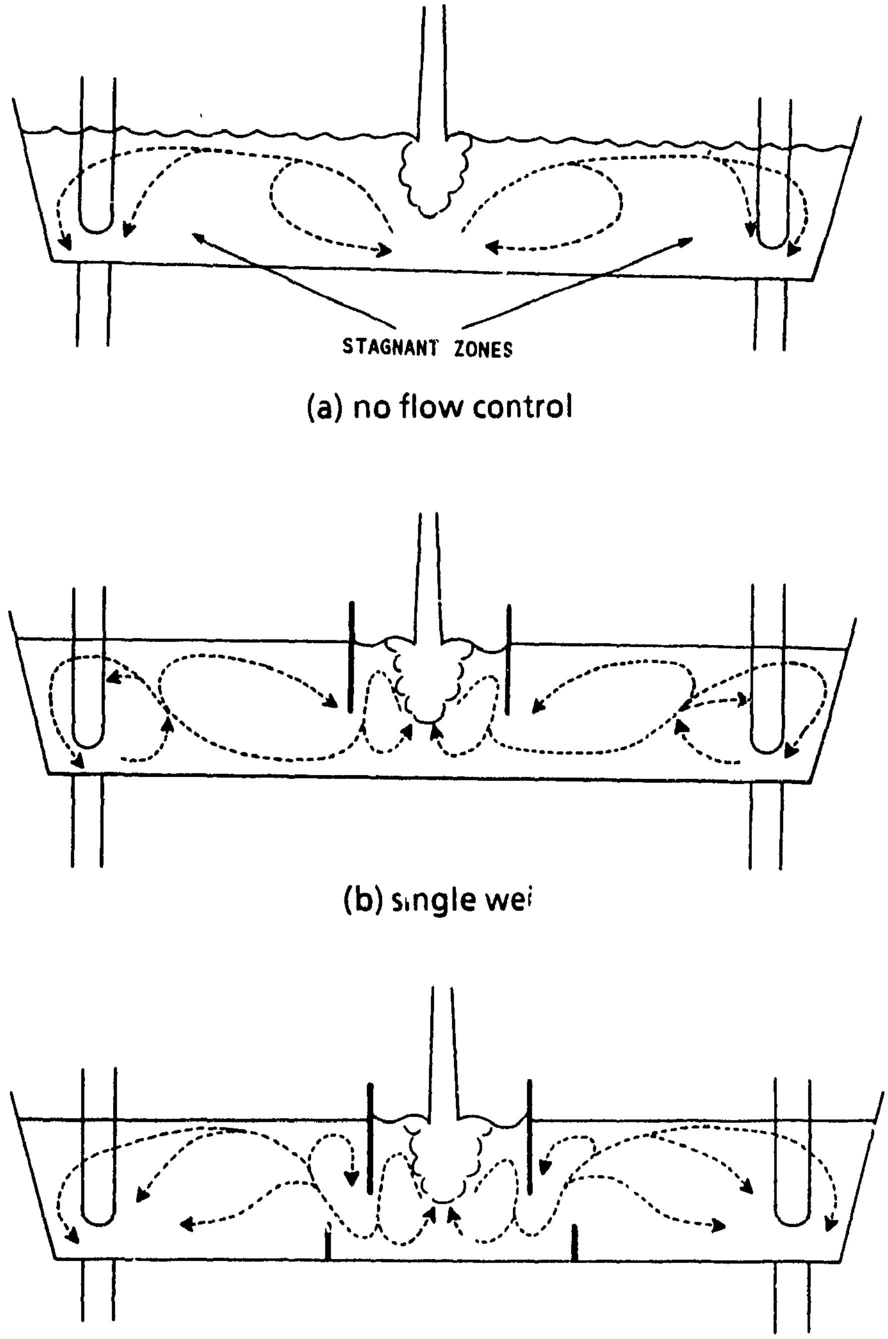

(a) no flow control

(b) single wei

(c) weir/dam arrangement

Figure 1-16 A schematic of flow patterns observed in a tundish with (a) no flow control (b) single weir (c) weir and dam arrangement.

where k is a constant, and u_s is Stokes rising velocity of a particle expressed in Equation (1-9). If the flow within tundish is assumed to be pure plug flow, the constant, k, becomes

$$k = \frac{t_n}{H} = \frac{A_p}{Q} \tag{1-14}$$

where t_n is the nominal mean residence time, and Q is the input stream flow rate. H and A_p represent the height and the surface area of the reactor, i.e. tundish. However, he found that this simple plug flow model tended to underestimate the inclusion residual ratio (i.e. inclusion entrainment rate).

Nakajima (1) has also developed a hybrid model, which allows for some plug flow, backmix flow reactors, and some dead volume. Figure 1-17 provides a schematic of the hybrid model for a single port tundish. According to this hybrid model, the resultant inclusion residual ratio is given by

$$R = \frac{N_{out}}{N_{in}} = \frac{1}{(1 + A_b u_s/Q)} \exp\left(-\frac{A_{dp} u_s}{Q}\right) \tag{1-15}$$

where A_b and A_{dp} represent the surface areas for the backmix flow components of the reactor and the plug flow dipersed plug flow part, respectively.

This expression is useful for crude estimates of inclusion entrainment for single, or axisymmetric twin ported tundish, but the volume fraction of each reactor has to be determined *a priori*. Consequently, the method is semi-empirical Further, the concept of tank reactor models must be

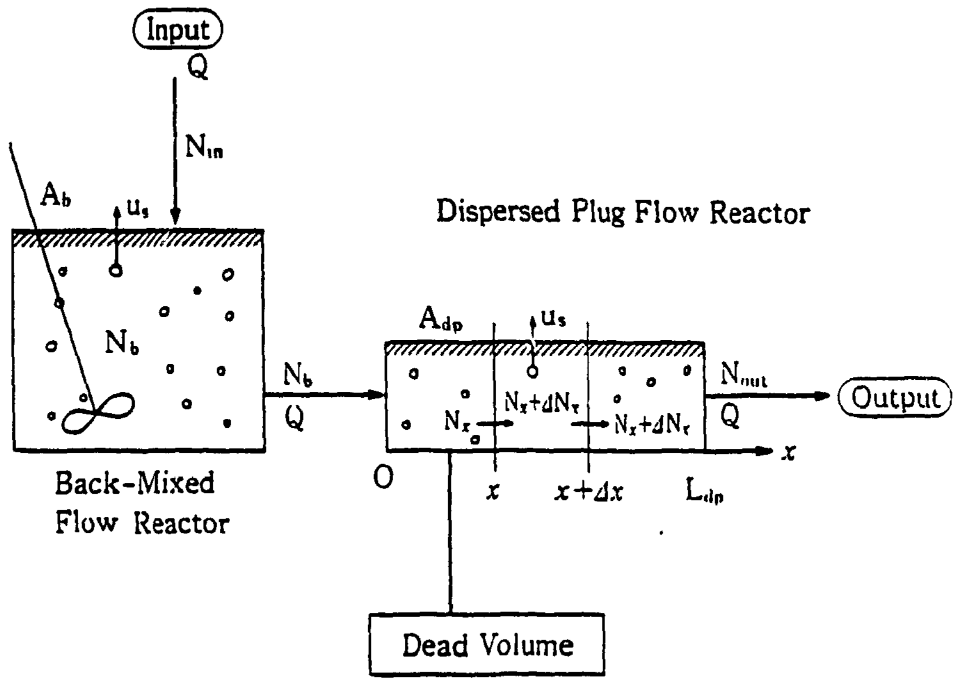

Figure 1-17 The hybrid model for calculating inclusion separation ratios.

restriced to simple systems, being inappropriate for complex geometry or multiported tundishes.

3.3.4 Tundish temperature

In tundish processing operations, there is generally a significant drop in steel temperature between inlet and outlet nozzles (68). Tundish temperature has been shown to be an important factor in determining solidification conditions in the mould. It also has an effect on slab surface quality. McPherson (64) has suggested that tundish temperatures should remain within the range of 1550 °C to 1560 °C for achieving good surface quality of slabs.

Figure 1-18 demonstrates how significantly tundish temperatures can influence steel quality (69). As seen, while the amount of inclusions entrained into the effluent stream to the caster is decreased with increasing tundish temperature, (or superheat), the extent of central segregation in slabs is also increased with such temperature increases. Improvements in inclusion separation at higher steel superheat temperatures are a reflection of decreases in the molecular viscosity of steel with temperature. This decrease enhances the Stokes rising velocities of particles in molten steel within the tundish bath, thereby accelerating inclusion float-out from the melt. By contrast, higher mould superheat lead to a columnar, rather than equiaxed, microstructure, and provides solutes (e.g. S,C, etc.) has more time to segregate to the liquid phase during solidification procedures in the mould. Thus, it has been suggested that for typical operating conditions on slab and billet casters, the optimal temperature of steel in the tundish is 1555 °C to 1560 °C, in order

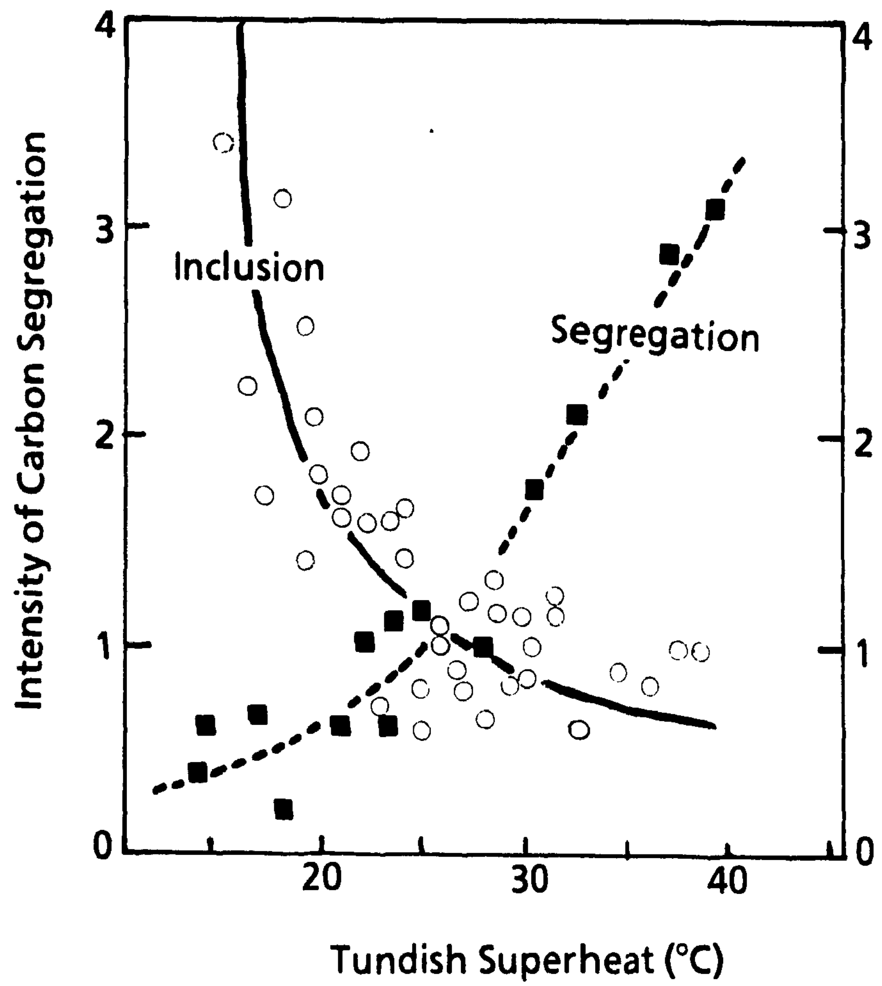

Figure 1-18 Relationship between tundish temperature and steel quality.

to balance the conflicting advantages of optimising inclusion separation and central segregation.

3.3.5 Nozzle clogging

Nozzle clogging can occur as a result of non-wetting solid inclusions accumulating on the inside walls of a nozzle outlet from a tundish. Clearly, partial or complete blocking will cause serious operation difficulties during casting operations. Further, the build-up of inclusion agglomerates in the ports of the tundish-to-mould shrouds represents a potential source of large exogeneous inclusions. This accretion problem is especially serious when the alumina composition of shroud nozzle becomes high ($\geqq \sim 75$ %) (61, 70).

Byrne and Cramb (61) have suggested a mechanism of port clogging in submerged shrouds based on visual observation and EPMA studies. Thus, when liquid steel is cast through the tundish-to-mould shroud nozzle, they propose that a thin solidified metal shell coats the inner surface of the colder nozzle. For the submerged shroud surface which is immersed in the steel of the mould, a thin coating of mould slag can occur, as a result of slag creep over the shroud surface. Solid nonmetallic inclusions can then attach to the shroud surface and start to dissolve in the slag layers, causing an increase in the thickness of the clogging deposits. In clean steel, where there are lower levels of alumina inclusions, the layer will assimilate any contacting alumina particles causing the matrix to become more viscous and thicker. This thickening film of viscous slag slowly clog the ports as it builds up. When the steel contains many more alumina in inclusions, the coating layer helps initiate the attachment of the build-up to the shroud, so that an alumina-type build-up will begin to grow. This nozzle clogging can be diminished by gentle gas bubbling through insert nozzle (70) or through the use of tundish stopper rod (63).

3.4 Mathematical Modelling for Tundish Metallurgy

A mathematical model can be a very useful tool for the study of fluid flow characteristics in tundishes and for their optimal design. Thus, detailed information on velocity fields and turbulence parameters allows one to predict, in a quantitative sense, inclusion dispersion and separation characteristics as well as temperature fields, during tundish processing operations. Mathematical modelling of tundish metallurgy involves solution of a complex three-dimensional turbulent form of the Navier-Stokes equations.

El-Kaddah and Szekely (71) reported a mathematical model describing three-dimensional tundish fluid flow using the commercial PHOENICS code. They also predicted tracer dispersion curves at the outlet nozzle of the tundish, and showed that they were in very good agreement with measurements by Kemeney et al. (62). Concurrently, Lai et al. (72) calculated tundish flow fields numerically via the three-dimensional turbulent Navier-Stokes equations, incorporating the k-ε turbulence model. There, predicted flow fields were compared with experimental measurements obtained via Laser-Doppler anemometry and flow visualization techniques.

Y. He and Sahai (73) performed computations of fluid flows in tundishes under the condition of sloping sidewalls, comparing the effects of these with vertical walls in terms of flow patterns and retention time distribution curves. They concluded that the inclination of tundish sidewalls has a significant effect on the fluid flow, and hence on the residence time distribution in tundishes. Tacke and Ludwig [74] solved a transport equation for monosized particles, taking into account their specific buoyancy, convection, and turbulent dispersion, again using the PHOENICS code. However, their computations for particle separation contradict those from physical modelling.

More recently, Joo and Guthrie [75, 76] recognised the fundamental importance of natural convection on flows and inclusion behaviour in tundishes, due to slight temperature variations within tundish baths. In their work, the entrainment rates of inclusion particles were first computed via a three-dimensional mass transport equation, incoporating the turbulent Navier-Stokes equations for fluids under isothermal conditions for comparison with full scale water model data. The experimental measurements in the full-scale water model tundish which paralleled these computations, used an on-line particle measurement technique. They were able to report that predictions agreed well with their measurements. Their mathematical analysis was then extended to the description of such transient, 3D, flow systems, and associated heat and mass transfer phenomena of industrial tundish processing operations. They demonstrated the importance of thermal natural convection phenomena in tundishes and the role of flow modification devices with providing quantitative information on flows, temperatures, and inclusion concentrations by mathematical modelling. (This will be described in Part IV in this thesis).

Chapter 3

Scope of Present Study

Before the mid 1970's, a metallurgist's need for understanding fluid flows in actual steelmaking reactors were often met by performing water model experiments. However, these experiments, while providing useful qualitative descriptions of flows, had two major limitations: first, they were often expensive and time consuming, and second, it was impossible to achieve all the physical conditions providing in a real metallurgical process.

In the absence of direct measurements and experiments on full scale operations, a more recent recourse is to calculate flow fields and turbulence levels in such processes, by solving a set of partial differential equations governing the transport of momentum, mass, energy, and other properties of the flow. Moreover, since a major feature of industrial steelmaking process vessels (e.g. ladles and tundishes) is their three-dimensional character (e.g , off-center bubbling and multi-plug gas bubbling in ladle process operations, and complex fluid flow / inclusion movements in tundish operations, etc.), a relevant three-dimensional turbulent flow model is needed if such metallurgical transport phenomena are to be properly studied.

In the present investigation, a general purpose computer code, which can solve three-dimensional turbulent flow, heat and mass transfer phenomena in metallurgical processing vessels, has been developed for both rectangular and cylindrical polar coordinate systems.

The objectives of the present research were to investigate and to analyse important metallurgical transport phenomena in steelmaking ladles and tundishes. These includes such items as mixing behaviour during gas bubbling in ladles, the dispersion / separation behaviour of nonmetallic inclusions in tundishes and associated tempera .ure variations. These heat and mass transfer phenomena are directly and strongly influenced by particular flows, such as those generated by gas bubbling in ladles or those when a ladle teeming stream enters a tundish. The present work emphasizes the role of mathematical models for predicting and visualizing the complex metallurgical phenomena involved. Simultaneously, physical experiments in parallel with the mathematical model were carried out, so that the results of one could be compared.

This thesis consists of four different parts. The first part introduced general aspects of ladle and tundish metallurgy, and then reviewed recent important research works concerned with ladle and tundish processing operations. Part II describes the numerical methods of solution used for coding of the computer program. Part III describes the modelling of mixing in steelmaking ladles. There, mixing phenomena are studied particularly for off-center and multi-plug gas bubbling. The last part of this work is devoted to the illustration of fluid flows, temperature distributions, and particle/inclusion float-outs. Consequently, this part emphasizes the importance of thermal natural convection on flows and inclusion separation in industrial tundishes, which can not properly be modelled by using physical water models.

REFERENCES

1) H. Nakajima, Ph.D. thesis, Department. of Mining & Metallurgical Engineering, McGill University, 1986.

2) Int. Iron & Steel Institute, Iron & Steelmaker, July, 1988, p 4.

3) M. Salcudean and R.I.L. Guthrie, 1978, Met. Trans., Vol. 9B, pp. 673-680.

4) M. Salcudean and R.I.L. Guthrie, 1978, Vol. 9B, pp. 151-154.

5) Y. Sahai and R.I.L. Guthrie, Advances in Transport Processes, Vol. IV, Ed. A. S. Majumdar and R.A. Mashelkar ,Wiley Eastern Limited, New Delhi, India, 1986, pp 1-48.

6) R.I.L. Guthrie, R. Clift and H. Henein, Met. Trans., Vol. 6B, 1975, pp. 321-329.

7) M. Tanaka, Ph.D. thesis, Department. of Mining and Metallurgical Engineering, McGill University, 1979.

8) A.W. Cramb and M. Byrne, Steelmaking Proceedings, ISS-AIME, Vol. 67, 1984, pp. 5-13.

9) S. Tanaka, Ph.D. thesis, Department. of Mining and Metallurgical Engineering, McGill University, 1986.

10) The Iron & Steel Institute of Japan, Trans. ISIJ, Vol. 25, No.7, 1985, p. 666.

11) T.E. Brower, J.W. Bain and B.M. Larsen, Trans. TMS-AIME, Vol. 188, 1950, pp. 851-861.

12) Y. Oyama, Y. Takeshima and H. Idemura, Kagaku Kenkyusho Hokoku, Vol. 29, 1953, pp. 344.

13) J. Szekely, Trans. TMS-AIME, Vol. 245, 1969, pp. 341-344.

14) J.B. Henderson, M.J. McCarthy and N.A. Molloy, Proc. Chemica '70, Butterworths, Melbourne, 1970, pp. 86-100.

15) L. Davidson and E. Amick, A. I. Ch. Eng. J., Vol. 2, No. 3, 1956, pp. 337-342.

16) G.A. Irons and R.I.L. Guthrie, Can. Met. Quart., Vol. 19, No. 4, 1980, pp. 381-387.

17) E.O. Hoefele and J.K. Brimacombe, Met. Trans. B, Vol. 56, 1979, pp. 631-648.

18) P.E. Agnabo, J.K. Brimacombe and A.H. Castillejos, Int. Sym. on Ladle Steelmaking and Furnaces, CIM, 1988, Montreal, Canada, pp. 29-46.

19) T.C. Hsiao, T. Lehner and B. Kjellberg, Scand. J. Metallurgy, Vol. 9, 1980, pp. 105-110.

20) M. Sano and K. Mori, Trans. ISIJ, Vol. 23, 1983, pp. 169-175.

21) Y. Sahai and R.I.L. Guthrie, Met. Trans.B, Vol. 13B, No. 2, 1982, pp. 193-202.

22) Y. Sahai and R.I.L. Guthrie, Met. Trans. B, Vol. 13B, No. 2, 1982, pp. 203-211.

23) T. DebRoy and A.K. Majumdar, J. Metals, Nov. 1983, pp. 42-47.

24) J. Szekely, H.J. Wang and K.M. Kiser, Met. Trans. B, Vol. 7B, 1976, pp. 287, 295.

25) J. Szekely, T. Lehner and C.W. Chang, Ironmaking & Steelmaking, Vol. 6, PP. 285-293.

26) J.H. Grevet, J. Szekely, and N. El-Kaddah, Int. J. Heat Mass Transfer, Vol. 25, No. 4, 1982, pp. 487-497.

27) S.V. Patankar and D.B. Spalding, Int. J. Heat Mass Transfer, Vol. 15, 1972, pp. 1787.

28) D.B. Spalding, Heat Transfer in Turbulent Buoyant Convection, Ed. D.B. Spalding and N. Afgan, Hemisphere Publishing Corporation, New York, 1977, pp. 569.

29) D. Mazumdar, Ph.D. Thesis, Department of Mining & Metallurgical Egineering, McGill University, Montreal, Canada, 1985.

30) S. Joo and R.I.L. Guthrie, Int. Sym. on Ladle Steelmaking and Furnaces, CIM, 1988, Montreal, Canada, pp. 1-28.

31) S. Joo, R.I.L. Guthrie and J. Kamal, Steelmaking Proceedings, ISS-AIME, Vol. 72, Chicago, 1989, pp517-528.

32) K. Nakanishi, T. Fujii and J. Szekely, Ironmaking and Steelmaking, No. 3, 1975, pp. 193-197.

33) T. Lehner, Symp. of Ladle Treatment of Carbon Steel, CIM, Hamilton, Canada, May 1979.

34) S. Asai, T. Okamoto, J.C. He and I. Muchi, Tetsu-to-Hagane, Vol. 68, No. 3, 1982, pp. 426-434.

35) O. Haida, T. Emi, S. Yamada and F. Sudo, Scaninject II, Lulea, Sweden, June 1980, Paper #20.

36) Q. Ying, L. Yun and L. Liu, Scaninject III, Lulea, Sweden, June 1980, Paper #21.

37) D. Mazumdar and R.I.L. Guthrie, Met. Trans. B., Vol. 17B, 1986, pp. 725-733.

38) D. Mazumdar, H. Nakajima and R.I.L. Guthrie, Met. Trans. B.,Vol. 19B, 1988, pp. 507-511.

39) J. Ishida, K. Yamaguchi, S. Sugoura, N. Demukai and A. Notoh, Denki Seiko, Vol. 52, No. 1, 1981, pp. 2-8.

40) G. Carlsson, M. Bramming and C. Wheeler, 5th Int. Iron & Steel Congress, Washington D.C., April 1986, Vol. B, Paper #1.

41) S. Kim, Ph.D. Thesis, Carnegie-Mellon University, U.S.A. ,1987.

42) R.I.L. Guthrie, Electric Furnace Proceedings, 1977, pp. 30-40.

43) S. Argyropoulos, M Eng. Thesis, Department of Mining and Metallurgical Engineering, McGill University, 1977.

44) F. Mucciardi, M Eng Thesis, Department of Mining and Metallurgical Engineering, McGill University, 1977.

45) D. Mazumdar and R.I.L. Guthrie, Applied Mathematical Modelling, Vol. 10, 1986, pp. 25-32.

46) K. Takashima, K. Arima, T. Shozi, and H. Mori, U.S. Patent 3971655, 1976.

47) M.P. Schwartz and W. J. Turnal, Appl. Mat. Modelling, Vol. 12, June, 1988, pp. 273-279.

48) S.A. Argyropoulos and R.I.L. Guthrie, Steelmaking Proceedings, Vol. 65, Pittsburgh, 1982, pp. 156-167.

49) L. Gourtsoyannis, R.I.L. Guthrie and G. Ratz, Proceedings of the Electric Furnace Conference, A.I.M.E., Vol. 42, Toronto, 1984, pp. 119-132.

50) F. Mucciardi and R.I.L. Guthrie, 105th AIME Annual Meeting, LasVegas, U.S.A., February, 1976.

51) B. Kulunk, M. Eng. Thesis, Department of Mining & Metallurgical Engineering, McGill University, 1986.

52) B.T. Lubin and G.S. Springer, J. Fluid Mech., Vol. 29, Part 2, 1987, pp. 385-390.

53) P. Andrzejewski, A. Diener, and W. Pluschkell, Steel Research, Process Metallurgy, Vol. 58, No. 12, 1987, pp. 547-552.

54) R. Sankaranarayanan, Doctoral Candidate, Department of Mining and Metallurgical Engineering, McGill University, unpublished research.

55) P. Hammerschmid, K.H. Tacke, H. Popper, L. Weber, M. Dubke, and K. Schwerdtfeger, Ironmaking and Steelmaking, No. 6, 1984, pp. 332-339.

56) D. Sucker, J Reinecke, H. Hage-Jewasinki, Stahl und Eisen, Vol. 105, No. 14/15, 1985, pp. 765-769.

57) R. Kiessling, "Nonmetallic Inclusions in Steel", The Metal Society, London, 1978, Part IV, p1.

58) D.S. Azbel and N.P. Cheremisinoff, "Fluid Mechanics and Unit Operations", Ann Arbor Science, 1983, pp 516-518.

59) H. Ichihashi, Y. Kawashima, T. Ikeda, K. Nishida and A. Kawami, Tetsu to Hagane, Vol 71, 1985, A25.

60) M. Hashito, M. Tokuda, M. Kawasaki and T. Watanabe, 2nd Process Technology Conference, Chicago, 1981, pp. 65-73

61) M. Byrne, T.W. Fenicle and A.W. Cramb, Iron & Steelmaker, June, 1988, pp. 41-50.

62) F. Kemeney, D.J. Harris, A. McLean, T.R. Meadowcroft and J.D. Young, 2nd Process Technology Conference, Chicago, 1981, pp. 232-245.

63) D.J. Harris and J.D. Young, Continuous Casting Vol. I, ISS-AIME, 1983, pp. 99-112.

64) N.A. McPherson, Steelmaking Proceedings, ISS-AIME, Vol. 68, Detroit, 1985, pp13-25.

65) E. Martinez, M. Maeda, L.J. Heaslip, G. Rodriguez and A. Mclean, Trans. ISIJ, Vol. 26, 1986, pp. 724-731.

66) D.O. Wilshynski, D.J. Harris and L. Heaslip, Proceedings of CIM 23rd Annual Conference of Metallurgist, August, 1984.

67) C.J. Dobson, R. Serje and K. Gregory, 4th Continuous Casting Conference, Brussess, 1987.

68) Y. Maruki, S. Shima and K. Tanaka, Trans ISIJ, Vol. 28, 1988, Technical Note.

69) Y. Miztani, Aichi Steel Works Ltd., Japan, Private Communications, 1989.

70) K. Ebato, I. Wakasugi and Y. Suzuki, Taikabutsu Overseas, Vol. 3, No. 2, 1987, pp. 21-25.

71) N. El-Kaddah and J. Szekely, 114th AIME Annual Technical Meeting, New York, 1985.

72) K. Lai, M. Salcudean, S. Tanaka and R.I.L. Guthrie, Metal. Trans. 17B, 1986, pp. 449-459.

73) Y. He and Y. Sahai: Metal. Trans. 18B, 1987, pp. 81-92.

74) K.H. Tacke and J.C. Ludwig: Process Metallurgy, Steel research, Vol. 58, No.6, 1987, pp262-269.

75) R.I.L. Guthrie, S. Joo and H. Nakajima, Int. Sym. on Direct Rolling and Direct Charging of Strand Cast Billet, CIM, Montreal, Canada, !988, Paper 51-5.

76) S. Joo, R.I.L. Guthrie and C.J. Dobson, Steelmaking Proceedings, ISS-AIME, Chicago, !989, pp401-408.

PART II

COMPUTATIONS OF FLUID FLOWS, HEAT AND MASS TRANSFER FOR THREE-DIMENSIONAL TURBULENT FLOWS

Chapter 1

Introduction

The flow of liquid metal in steelmaking operations (e.g. furnace tapping, gas stirring, flows in tundish and mould, etc.) is characteristically turbulent such that velocities, temperatures, and pressures are subject to fluctuations. These are both spatially and time dependant. For turbulent flows, the conservation of momentum, energy, and mass transport can be expressed through partial differential equations, in terms of time-averaged mean values of properties.

Numerical methods of solution are then used extensively in practical applications to determine flow velocity fields, temperature distributions and mass transfer in the systems having complicated geometries, boundary conditions, etc. A commonly used numerical scheme is the finite-difference method. In this approach, the partial differential equations for momentum, energy, and mass conservations are approximated by a set of algebraic equations in a number of finite volume elements placed within the region of interest.

Thus, in the present study, a general purpose computer code, *METFLO*, capable of predicting three-dimensional turbulent flows in systems of rectangular and cylindrical geometry, was written by the author using the finite difference method. The first step for this was to establish the appropriate partial differential equations for continuity, momentum, turbulent parameters, and those for energy and mass conservation. The second step is the transformation into a set of algebraic equations, or discretization, of the differential equations. The final step is to design a specific solution procedure for the discretization (or finite-difference) equations constructed

This part is comprised of four chapters. Chapter 2 provides the fundamental mathematical formulae governing continuity, momentum, energy, chemical species and fine particles conservation. It also explains the concept of wall function method for treating the flow properties (e.g. shear stress, turbulent kinetic energy and energy dissipation rate) in the near wall region. Chapter 3 describes how to discretize the non-linear differential equations for computations by using the finite difference method, and then introduces the solution strategy and boundary conditions. In chapter 4, the structure of the computer code and computational procedures are briefly overviewed. In order to verify *METFLO*, some case studies were carried out, and these are described

Chapter 2

Theory

2.1 Fluid Flow

In turbulent flow, the motion of fluid elements are irregular, time-dependent, and accompanied by fluctuations in velocity. In order to solve this complex turbulent flow, the equations of continuity and motion are averaged over a short time interval to get the *time-smoothed* equations. These equtions describe the time-smoothed velocity and pressure distributions. Figure 2-1 illustrates the concept of the instantaneous velocity, v_z, the velocity fluctuation, v_z', and time-averaged velocity, $\overline{v}_z$. The only difficulty is that the time-smoothed equation of motion contains turbulent momentum fluxes, which is usually referred to as the *Reynolds stresses* $(-\rho u_i' u_j')$.

For the use of the time-smoothed equations to obtain velocity profiles, some expressions for the Reynolds stress terms have to be inserted. In the present study, Boussinesq's eddy viscosity model(1) was imposed on the time-smoothed momentum equations. This approach writes

$$-\rho u_i' u_j' = \mu_t \left(\frac{\partial u_i}{\partial x_j} + \frac{\partial u_j}{\partial x_i} \right) \tag{2-1}$$

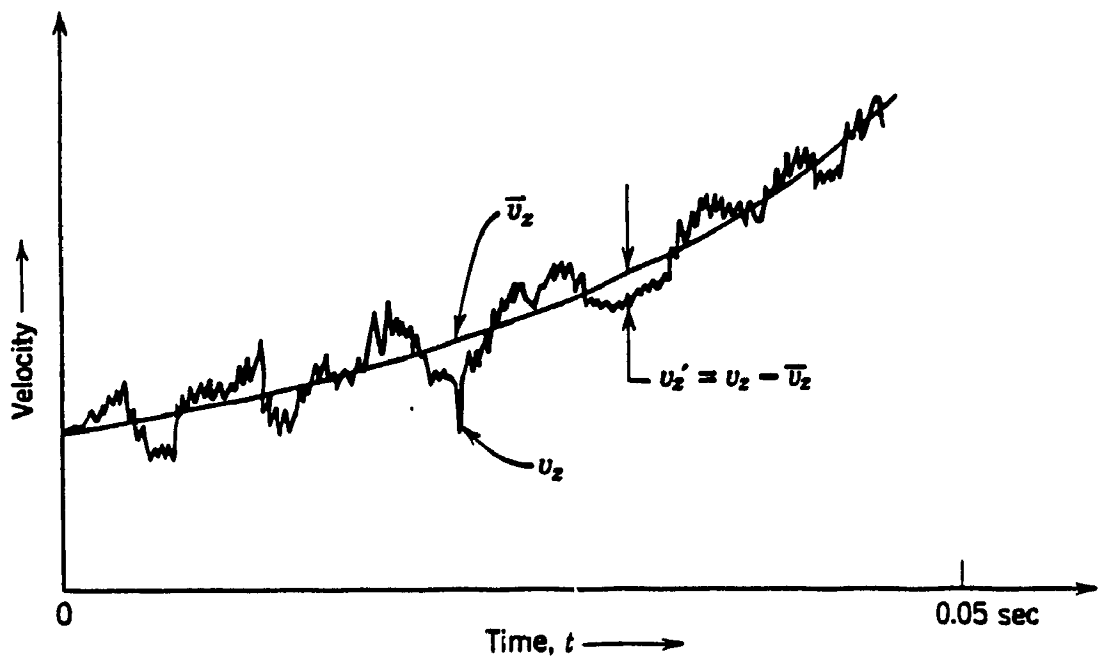

Figure 2-1 Oscilation of velocity component about a mean value.

by analogy with Newton's law of viscosity. μ_t represents a *turbulent coefficient of viscosity* or *eddy viscosity*, and usually depends strongly on the local position of fluid.

Thus, the differential equations for steady state, turbulent flow can be written in three-dimensional, incompressible, and ensemble-averaged form for both rectangular and cylindrical coordinates as follows. There, λ is set to unity for cylidrical polar coordinates. For rectangular coordinates, λ is set to zero and r is replaced by unity, $d\theta$ by dx, and dr by dy. It is appropriate to note that u is velocity in the axial direction , v in the radial direction , and w in the angular direction for cylindrical polar coordinates, respectively.

Continuity Equation

$$\frac{\partial}{\partial z}\left(\rho u\right)+\frac{\partial}{\partial r}\left(\rho v\right)+\frac{1}{r}\frac{\partial}{\partial \theta}\left(\rho w\right)+\lambda\frac{\rho v}{r}=0 \qquad (2\text{-}2)$$

Momentum Conservation Equation

Axial direction :

$$\frac{\partial}{\partial z}\left(\rho uu\right)+\frac{1}{r}\frac{\partial}{\partial r}\left(r\rho vu\right)+\frac{1}{r}\frac{\partial}{\partial \theta}\left(\rho wu\right)-\frac{\partial}{\partial z}\left(\mu_{eff}\frac{\partial u}{\partial z}\right)$$

$$-\frac{1}{r}\frac{\partial}{\partial r}\left(r\mu_{eff}\frac{\partial u}{\partial r}\right)-\frac{1}{r}\frac{\partial}{\partial \theta}\left(\mu_{eff}\frac{1}{r}\frac{\partial u}{\partial \theta}\right)=-\frac{\partial P}{\partial z}+S_u \qquad (2\text{-}3)$$

where

$$S_u=\frac{\partial}{\partial z}\left(\mu_{eff}\frac{\partial u}{\partial z}\right)+\frac{1}{r}\frac{\partial}{\partial r}\left(r\mu_{eff}\frac{\partial v}{\partial z}\right)+\frac{1}{r}\frac{\partial}{\partial \theta}\left(\mu_{eff}\frac{\partial w}{\partial z}\right)-\rho g \qquad (2\text{-}4)$$

The *turbulent effective viscosity*, μ_{eff}, is defined as

$$\mu_{eff} = \mu + \mu_t \tag{2-5}$$

Radial direction :

$$\frac{\partial}{\partial z}\left(\rho u v\right) + \frac{1}{r}\frac{\partial}{\partial r}\left(r\rho v v\right) + \frac{1}{r}\frac{\partial}{\partial \theta}\left(\rho w v\right) - \frac{\partial}{\partial z}\left(\mu_{eff}\frac{\partial v}{\partial z}\right)$$

$$-\frac{1}{r}\frac{\partial}{\partial r}\left(r\mu_{eff}\frac{\partial v}{\partial r}\right) - \frac{1}{r}\frac{\partial}{\partial \theta}\left(\frac{\mu_{eff}}{r}\frac{\partial v}{\partial \theta}\right) = -\frac{\partial P}{\partial r} + S_v \tag{2-6}$$

where

$$S_v = \frac{\partial}{\partial z}\left(\mu_{eff}\frac{\partial u}{\partial r}\right) + \frac{1}{r}\frac{\partial}{\partial r}\left(r\mu_{eff}\frac{\partial v}{\partial r}\right) + \frac{1}{r}\frac{\partial}{\partial \theta}\left[r\mu_{eff}\frac{\partial}{\partial r}\left(\frac{w}{r}\right)\right]$$

$$+\lambda\left[\frac{\rho w^2}{r} - \frac{2\mu_{eff}}{r^2}\left(v + \frac{\partial w}{\partial \theta}\right)\right] \tag{2-7}$$

Angular direction :

$$\frac{\partial}{\partial z}\left(\rho u w\right) + \frac{1}{r}\frac{\partial}{\partial r}\left(r\rho v w\right) + \frac{1}{r}\frac{\partial}{\partial \theta}\left(\rho w w\right) - \frac{\partial}{\partial z}\left(\mu_{eff}\frac{\partial w}{\partial z}\right)$$

$$-\frac{1}{r}\frac{\partial}{\partial r}\left(r\mu_{eff}\frac{\partial w}{\partial z}\right) - \frac{1}{r}\frac{\partial}{\partial \theta}\left(\frac{\mu_{eff}}{r}\frac{\partial w}{\partial \theta}\right) = -\frac{1}{r}\frac{\partial P}{\partial \theta} + S_w \tag{2-8}$$

where

$$S_w = \frac{\partial}{\partial z}\left(\frac{\mu_{eff}}{r}\frac{\partial u}{\partial \theta}\right) + \frac{1}{r}\frac{\partial}{\partial r}\left[\mu_{eff}\left(\frac{\partial v}{\partial \theta} - \lambda w\right)\right] + \frac{1}{r}\frac{\partial}{\partial \theta}\left[\frac{\mu_{eff}}{r}\left(\frac{\partial w}{\partial \theta} + \lambda 2 v\right)\right]$$

$$+\lambda\left[\frac{\mu_{eff}}{r}\left(\frac{\partial w}{\partial r} + \frac{1}{r}\frac{\partial v}{\partial \theta} - \frac{w}{r}\right) - \frac{\rho v w}{r}\right] \tag{2-9}$$

2.2 Turbulence Model

Unlike laminar viscosity, the turbulent eddy viscosity is not a property of the fluid. Its value will vary from point to point in the flow, being largely determined by structure of the turbulence at the point in question. There are several tasks of expressing the turbulent viscosity in terms of known or calculable quantities(2-7)

In the present study, the k-ε model of turbulence proposed by Jones and Launder(7), was used to determine the value of the local turbulent viscosity. In this model, the governing transport equations for turbulence kinetic energy, k, and its dissipation rate, ε, can be represented by :

Equation of Turbulent Kinetic Energy

$$\frac{\partial}{\partial z}(\rho u k) + \frac{1}{r}\frac{\partial}{\partial r}(r\rho v k) + \frac{1}{r}\frac{\partial}{\partial \theta}(\rho w k) - \frac{\partial}{\partial z}\left(\frac{\mu_t}{\sigma_k}\frac{\partial k}{\partial z}\right)$$

$$-\frac{1}{r}\frac{\partial}{\partial r}\left(\frac{\mu_t}{\sigma_k}\, r\,\frac{\partial k}{\partial r}\right) - \frac{1}{r}\frac{\partial}{\partial \theta}\left(\frac{\mu_t}{\sigma_k}\frac{\partial k}{r\partial \theta}\right) - G + \rho C_D \varepsilon = 0 \qquad (2\text{-}10)$$

where

$$G \equiv 2\mu_t \left[\left(\frac{\partial u}{\partial z}\right)^2 + \left(\frac{\partial v}{\partial r}\right)^2 + \left(\frac{\partial w}{r\partial \theta} + \lambda\frac{v}{r}\right)^2\right]$$

$$+\mu_t \left[\left(\frac{\partial u}{\partial r} + \frac{\partial v}{\partial z}\right)^2 + \left(\frac{\partial w}{\partial z} + \frac{\partial u}{r\partial \theta}\right)^2 + \left(\frac{\partial v}{r\partial \theta} + \frac{\partial w}{\partial r} - \lambda\frac{w}{r}\right)^2\right] \qquad (2\text{-}11)$$

Equation of Energy Dissipation Rate

$$\frac{\partial}{\partial z}(\rho u\varepsilon) + \frac{1}{r}\frac{\partial}{\partial r}(r\rho v\varepsilon) + \frac{1}{r}\frac{\partial}{\partial \theta}(\rho w\varepsilon) - \frac{\partial}{\partial z}\left(\frac{\mu_t}{\sigma_\varepsilon}\frac{\partial \varepsilon}{\partial z}\right)$$

$$- \frac{1}{r}\frac{\partial}{\partial r}\left(\frac{\mu_t}{\sigma_\varepsilon} r \frac{\partial \varepsilon}{\partial r}\right) - \frac{1}{r}\frac{\partial}{\partial \theta}\left(\frac{\mu_t}{\sigma_\varepsilon}\frac{\partial \varepsilon}{r\partial \theta}\right) - C_1 G\frac{\varepsilon}{k} + C_2\rho\frac{\varepsilon^2}{k} = 0 \qquad (2\text{-}12)$$

The turbulent eddy viscosity, μ_t, is given by

$$\mu_t = \frac{C_\mu \rho k^2}{\varepsilon} \qquad (2\text{-}13)$$

The five values of constants, set according to the recommendation of Launder and Spalding(8), are given in Table 2-1.

Table 2-1 Recommended values of constants for k-ε two-equation model of turbulence

C_1	C_2	C_μ	σ_k	σ_ε
1.44	1.92	0.09	1.0	1.3

2.3 Dispersion of Alloy Additions/Tracer

In the pesence of a steady state flow field, to which a tracer is added at time zero, the appropriate statements for conservation of mass, in terms of cylindrical polar coordinates, as it spreads through the system is :

$$\frac{\partial}{\partial t}\left(\rho C\right) + \frac{\partial}{\partial z}\left(\rho u C - \Gamma_{e,C}\frac{\partial C}{\partial z}\right)$$

$$+ \frac{1}{r}\frac{\partial}{\partial r}\left[r\left(\rho v C - \Gamma_{e,C}\frac{\partial C}{\partial r}\right)\right] + \frac{1}{r}\frac{\partial}{\partial \theta}\left(\rho w C - \Gamma_{e,C}\frac{1}{r}\frac{\partial C}{\partial \theta}\right) = 0 \qquad (2\text{-}14)$$

where the effective exchange coefficient, $\Gamma_{e,C}$, is defined by

$$\Gamma_{e,C} = \frac{\mu}{\sigma} + \frac{\mu_t}{\sigma_{t,C}} \qquad (2\text{-}15)$$

where σ and $\sigma_{t,C}$ represents the laminar and turbulent Schmidt number, respectively, and $\sigma_{t,C}$ is assumed to have a value of unity.

2.4 Dispersion of Fine Particles

Stokes law provides that the terminal rising velocity, u_s, of a spherical particle in steel is related to size, buoyancy and steel viscosity according to

$$u_s = \frac{\Delta\rho g d^2}{18\mu} \qquad (2\text{-}16)$$

where $\Delta\rho$ is the density difference between the fluid and the particle, g is the acceleration due to gravity, d is the particle diameter and μ is the viscosity of the fluid.

The mathematical model for predicting inclusion population distributions employed a standard mass conservation equation describing spatial distributions in terms of the mass fraction of fine particles within a fluid control volume. Thus, in the presence of a steady flow field, the mass fraction of particles of a specific size can be expressed according to a species conservation equation for cartesian coordinates:

$$\frac{\partial}{\partial t}\left(\rho C\right)+\frac{\partial}{\partial x}\left[\rho\left(u-u_{s}\right)C-\Gamma_{e,C}\frac{\partial C}{\partial x}\right]$$

$$+\frac{\partial}{\partial y}\left(\rho v C-\Gamma_{e,C}\frac{\partial C}{\partial y}\right)+\frac{\partial}{\partial z}\left(\rho w C-\Gamma_{e,C}\frac{\partial C}{\partial z}\right)=0 \qquad (2\text{-}17)$$

Since the flotation of micron size fine particles in metallurgical processing vessels would seem to be subject to Stokes law, their dispersion within such a system can be described via a three-dimensional convection-diffusion type mass transport equation. The solution of such equations requires that the distribution of flow variables (u, v, and w) and turbulence variables be known *a priori*. The possibility of inclusions directly affecting the flow within the tundish is discounted.

2.5 Energy Conservation Equation

Under steady flow conditions, the general energy conservation equation for incompressible, non-viscous liquid flow can be expressed as :

$$\frac{\partial}{\partial z}\left(\rho u T - \Gamma_{e,T}\frac{\partial T}{\partial z}\right) + \frac{1}{r}\frac{\partial}{\partial r}\left[r\left(\rho v T - \Gamma_{e,T}\frac{\partial T}{\partial r}\right)\right]$$

$$+ \frac{1}{r}\frac{\partial}{\partial \theta}\left(\rho w T - \Gamma_{e,T}\frac{1}{r}\frac{\partial T}{\partial \theta}\right) = 0 \qquad (2\text{-}18)$$

The effective diffusivity concept was used to represent the combined effect of molecular and turbulent thermal diffusion The exchange coefficient, $\Gamma_{e,T}$, is given by

$$\Gamma_{e,T} = \frac{\mu}{\sigma} + \frac{\mu_t}{\sigma_{t,T}} \qquad (2\text{-}15)$$

where σ and $\sigma_{t,T}$ represents the laminar and turbulent Prandtl number, respectively, and $\sigma_{t,T}$ is assumed to have a value of unity

2.6 Wall Function Method

For the turbulence model, it is assumed that the characteristic Reynolds number for a given flow is sufficiently large (e g. 2 1×10^3 for the flow in circular tube) to ensure turbulent, rather than laminar conditions. However, in the immediate neighborhood of the wall, the fluctuations in the parallel direction to the wall are greater than those in vertical direction to the wall, and all fluctuations approaching zero at the wall itself.

In order to treat the flow near the wall boundary, generally, a one-dimensional Couette flow analysis is made close to walls[9,10]. The layer is assumed to be one of constant shear stress and constant heat flux. These conditions are true only for an impermeable wall with zero or negligible streamwise pressure gradient. The momentum equation is, then, reduced to a particularly simple non-dimensional form.

The region close to the wall is one where the local Renolds number changes considerably. Hence, the approach adopted is dependent upon the value of local Reynolds number, y^+, based on the distance, y, from the wall and the friction velocity, u_τ. These are respectively defined as[10] :

$$y^+ = \rho u_\tau y/\mu \tag{2-20}$$

where

$$u_\tau = \sqrt{\tau_w/\rho} \tag{2-21}$$

Although the change of fluctuations (or intensity of turbulence) increases continuously with distance from wall, it has become customary to think of three arbitrary zones based on the local Reynolds number : the *viscous sublayer* ($0<y^+<5$), in which Newton's law of viscosity is used to describe the flow ; The *buffer layer, or transient, zone* ($5<y^+<30$), in which both laminar and turbulent effects are important ; and the *inertial sublayer, or turbulent layer* ($y^+>30$), in which the flow seems to be completely turbulent, but being still close to the wall, suggests that the shear stresses are approximately the same as those for wall shear stress.

To study velocity distributions in turbulent flow, the following dimensionless velocity, u^+, was also introduced.

$$u^+ = u/u_\tau \tag{2-22}$$

Therefore, in the viscous sublayer, the shear stress, τ_w, is taken in the form $\tau_w = \mu\, \partial u/\partial y$. The integration of this expression for constant τ_w with $u = 0$ for $y = 0$ leads to the following result

$$u^+ = y^+ \tag{2-23}$$

In the turbulent sublayer, the laminar shear stress is negligible in comparison to the turbulent shear stress. By utilizing the mixing length concept(2) and assuming that the mixing length varies linearly with the distance from the wall in the form, $l = \kappa y$, it can be shown that velocity distribution in the turbulent layer has a logarithmic profile of the form

$$u^+ = \frac{1}{\kappa}\, ln(Ey^+) \tag{2-24}$$

where κ is the von Karman constant, with a value of 0.4187. E is an integration constant depending on the magnitude of the variation of shear stress across the layer and on the roughness of the wall. The value of E is given by 9 793 for impermeable smooth walls with a constant shear stress(8). Figure 2-2(10) shows a correlation of the velocity distribution law with Nikuradse's(11) measured data for turbulent flow inside smooth pipes.

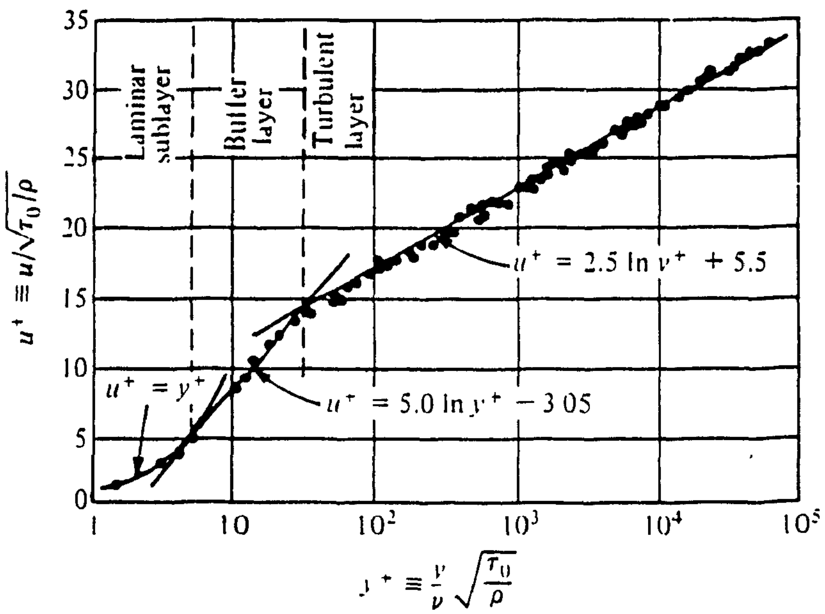

Figure 2-2 Logarithmic velocity distribution law and Nikuradse's[11] experimental data for turbulent flow inside smooth pipe.

In many engineering calculations, the buffer zone is disposed of by defining an algebraically averaged point $y^+ = 11.63$, below which the flow is assumed to be purely viscous (i.e. viscous sublayer) and above which it be purely turbulent (i.e. turbulent layer)

Hence, the analysis shows that the local Reynolds number near the wall, y^+, can be given by

$$y^+ = \frac{\rho y C_\mu^{1/4} k^{1/2}}{\mu} \tag{2-25}$$

When y^+ is less than 11.63, it is assumed that the flow can be described by Newton's viscosity law, and hence the shear stress becomes

$$\tau_w = \mu \frac{\partial u}{\partial y} \tag{2-26}$$

In the turbulent layer (i.e. $y^+ > 11.63$), the shear stress is written by

$$\tau_w = \frac{\rho \kappa C_\mu^{1/4} k^{1/2} u}{ln(E y^+)} \tag{2-27}$$

The incorporation of the wall boundary condition for the turbulent kinetic energy, k, requires special attention. The usual k-balance is used but, since the turbulence energy goes to zero at a wall, there is no flux contributed from the wall. The generation term G (Equation 2-11) in the k-equation reduces to a simplified form as follows,

$$\mu_t\left(\frac{\partial u_j}{\partial x_i} + \frac{\partial u_i}{\partial x_j}\right)^2 \simeq \tau_w \frac{u}{y} \tag{2-28}$$

and

$$C_D \rho \varepsilon \simeq C_D \rho C_\mu^{3/4} k^{3/2} u^+ / y \tag{2-29}$$

Unlike the turbulence kinetic energy, k, which falls to zero at wall, the energy dissipation rate, ε, reaches its highest value at the wall. This makes an ε-balance for a cell extending up to a wall very difficult since one cannot know how to modify it in such cases. For this reason, a fixed value for ε is adopted irrespective of y^+ The energy dissipation rate in the wall boundaries can generally be expressed as(16)

$$\varepsilon = \frac{C_\mu^{3/4} k^{3/2}}{\kappa y} \tag{2-30}$$

The value represented in this equation is fixed at every node next to the wall.

Chapter 3

Numerical Treatment

3.1 General Differential Equation

The differential equations of interest to this study are the equations of continuity, momentum, kinetic energy of turbulence and its rate of dissipation, together with equations for the conservation of mass and energy transport. These differential equations have been described in Chapter 2 and can be cast in the generalized form :

$$\frac{\partial}{\partial t}\left(\rho\phi\right)+\frac{\partial}{\partial x_j}\left(\rho u_j\phi\right)=\frac{\partial}{\partial x_j}\left(\Gamma\frac{\partial\phi}{\partial x_j}\right)+S \qquad (2\text{-}31)$$

where ϕ denotes the dependent variable (e.g. u, v, w, k, ε, T, etc.), Γ is the diffusion coefficient, and S is the source term. The four terms in the general differential equation are the unsteady transient or time dependent term, the convective term, the diffusive term, and the source term For steady flows, the first term (i.e. unsteady term) can be set equal to zero.

When the source S depends on ϕ, it can, if necessary, be decomposed into a linear form, according to :

$$S = S_C + S_P \phi \tag{2-32}$$

Physical reality requires that the values of certain dependent variables always remain positive. These are the kinetic energy of turbulence, its rate of dissipation, the mass fractions of chemical species, liquid metal temperatures, and so on If the source of such "always-positive" variables is not properly handled, they may, in actual computations, acquire erroneous negative values wrecking further calculations and iterations. Hence, a strict requirement ensuring no negative values of always-positive variables is that S_C must always be positive and S_p always negative.

3.2 Grid and Control Volumes

A numerical solution to a differential equation consists of a set of numbers from which the dependent variable, ϕ, can be constructed. In other words, a numerical method treats the value of the dependent variable at a finite number of locations, that is, grid points, as its basic unknowns in the calculation domain, and solves for this dependent variable as a function of space and time (for transient flows).

Thus, the first step in deriving the finite difference equations is to establish a suitable grid and choice of storage locations for variables. A typical two-dimensional grid and control volume is shown in Figure 2-3. The scalar control volume is shown by the dashed lines, while the velocity control volumes are represented by dotted lines. While the scalar variables (P, C, k, ε, T, etc.) are located at the intersection of grid nodes, the velocity components

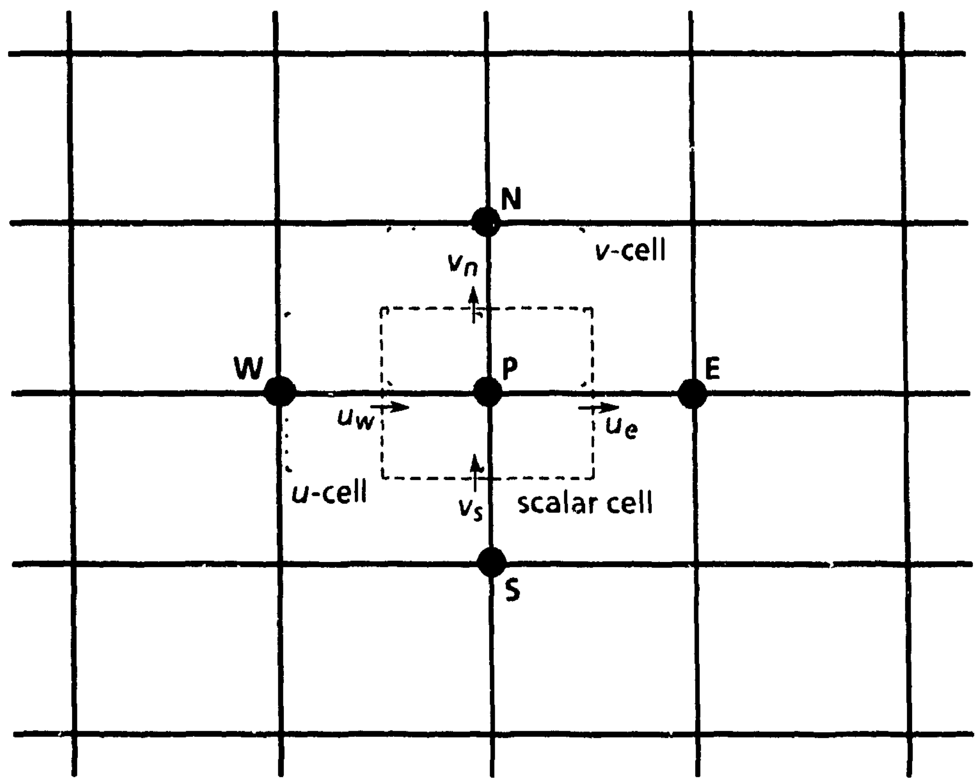

Figure 2-3 Control volume for the two-dimensional situation

are located at the boundaries of the scalar cells (control volumes).

Such a displaced or "staggerred" grid for the velocity components was first proposed by Harlow and Welch(17) in their MAC method. As seen in Figure 2-?, an immediate consequence of the staggered grid is that the mass flow rates across the scalar control volume faces can be calculated without any interpolation for the relevant velocity component. Similarly, for the velocity control volume, the pressure difference between two adjacent scalar grid points now becomes the natural driving force for the velocity component, this again requiring no interpolation for the pressure at the face of the velocity control volume. These procedures lead to improved stability in numerical integration procedure(12).

The three-dimensional control volumes for the scalar variables in the present work are illustrated in Figure 2-4 (a) and (b), for rectangular and cylindrical polar coordinates systems, respectively It is appropriate to note that the control volume faces were placed midway between grid points in a *Type A* grid arrangement.

3.3 Discretization Equation

In order to solve a differential equation using a computer, equivalent algebraic equations known as discretization equations, which incorporate the unknown values of ϕ at chosen grid points, have to be constructed. Such a discretization equation is derived from the differential equation governing ϕ, and thus expresses the same physical information as the differential equation. In a given discretization equation, only neighboring

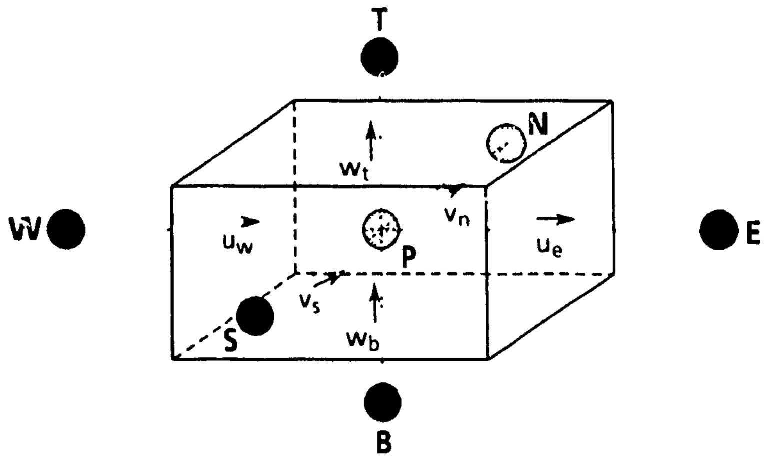

(a) rectangular system

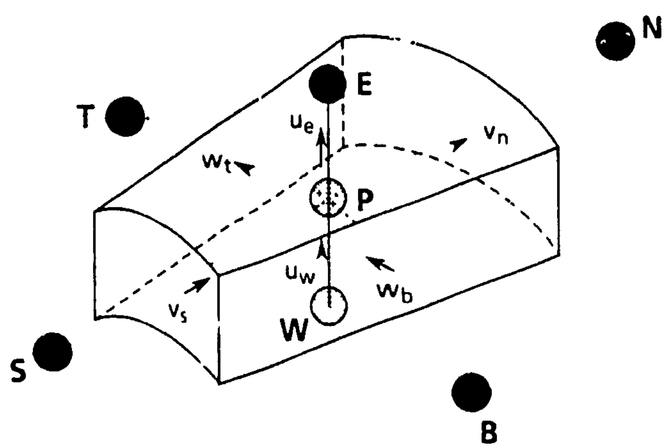

(b) cylindrical system

Figure 2-4 Three-dimensional scalar control volume for (a) rectangular coordinates and (b) cylindrical polar coordinates systems.

grid points participate as a consequence of the piecewise nature of the profiles chosen As the number of grid points becomes very large, the solution of the discretization equations is expected to approach the exact solution of the corresponding differential equation.

Two alternative versions of the discretization method are generally used in typical computational practices by engineers They are finite-difference and finite-element methods In the present study, the discretized equations were derived using the integral control volume approach (i.e. finite-difference method). In this procedure, the calculation domain is divided into a number of non-overlapping control volumes such that there is one control volume surrounding each grid point. Integrating a differential equation over a control volume, and choosing the appropriate interpolation formulae (e g piecewise linear profile or stepwise profile), one can obtain a discretized equation containing the values of ϕ for a group of grid points. (More detailed information on these procedures is presented by Patankar, 1980 [12].)

The discretization equation obtained in this manner expresses the principle of conservation for ϕ for a control volume of finite proportions, just as its counterpart differential equation expresses this principle for an infinitessimal control volume. Referring to Figure 2-4, the final discretization equation based on the general differential equation can be expressed as [12]:

$$a_P\Phi_P = a_E\Phi_E + a_W\Phi_W + a_N\Phi_N + a_S\Phi_S + a_T\Phi_T + a_B\Phi_B + b \qquad (2\text{-}33)$$

where

$$a_E = D_e A(|P_e|) + max(-F_e, 0)$$

$$a_W = D_w A(|P_w|) + max(F_w, 0)$$

$$a_N = D_n A(|P_n|) + max(-F_n, 0)$$

$$a_S = D_s A(|P_s|) + max(F_s, 0)$$

$$a_T = D_t A(|P_t|) + max(-F_t, 0)$$

$$a_B = D_b A(|F_b|) + max(F_b, 0)$$

$$a_P{}^{\circ} = \frac{\rho_P{}^{\circ} V}{\Delta t}$$

$$b = S_C V + a_P{}^{\circ} \phi_P{}^{\circ}$$

$$a_P = a_E + a_W + a_N + a_S + a_T + a_B + a_P{}^{\circ} + S_P V \qquad (2\text{-}34)$$

where V represents the metric volume of a *control volume*. F indicates the mass flow rate, D the diffusion conductance, and P is the local Peclet number They are defined as follows :

$$F_i = (\rho u)_i A_i$$

$$D_i = \Gamma_i A_i / (\delta x)_i \qquad (2\text{-}35)$$

$$P_i = F_i / D_i$$

The symbol *max(A,B)* is defined to denote 'the greater of *A* and *B*' The function $A(|P|)$ for various schemes is listed in Table 2-2. In the present study, the hybrid scheme was adopted based on economic grounds, since it gives physically realistic and reasonable solutions even for somewhat coarse grids versus central difference and upwind schemes.

Table 2-2. The function A(|P|) for different schemes

Scheme	Formula for $A(\|P\|)$
Central difference	1-0 5|P|
Upwind	1
Hybrid	max(0, 1-0 5|P|)
Power law	max(0, $(1\text{-}0\ 1\|P\|)^5$)

3.4 Calculation of the Flow Field

As described earlier, the momentum equations governing the velocity components are also particular cases of the general differential equations for ϕ (e.g. $\phi = u$, $\Gamma = \mu_{eff}$, etc. for the u-momentum equation). However, these equations need special procedures. The major difficulty arises from the fact that the momentum equations incorporate unspecified pressure gradient terms (i.e. $\partial P/\partial x_i$), and no obvious equations exist for obtaining the pressure field.

The pressure field, then, is specified indirectly via the continuity equations. Unless the correct pressure field is employed, the resulting velocity field will not satisfy the continuity equation. As a consequence, special numerical procedures have been developed in which the continuity and momentum equations are solved by coupling them via a pressure correction equation (13). Two of the 'sub-algorithms' for solving the flow field are SIMPLE (semi-implicit method for pressure linked equations) and SIMPLER (semi-implicit method for pressure linked equations-revised) (12).

The operations of SIMPLE algorithm, used in this work, are as follows; an initial pressure field is first guessed and the implied flow field is then calculated from the discretized momentum equations. The discretized continuity equation is then tested with the proposed velocity field. If that flow field does not satisfy the continuity, pressure corrections are calculated using a pressure correction equation. Adjustment are therefore made for velocity and pressure fields throughout the flow domain. The discretization equations for other variables (i.e. turbulence quantities and temperature), if necessary, are then solved, since they influence the flow field through fluid properties, source term, etc. Employing the newly proposed pressure field, the momentum equation is re-solved. Again the resulting flows are checked for local continuity, etc These procedures are successively repeated until a converged solution is obtained.

3.5 Solution Method

In constructing the discretization equations, we need a particular method for their solution. It is useful to consider the derivation of the equations and their solution procedure as two distinct operations, and there is no need for the choice of one to influence the other. In a computer program, the two operations can be conveniently performed in separate sections. Further, either section can, when desired, be modified independently

One of the solution methods for the multi-dimensional discretization equations is an iterative method, the so-called 'line-by-line' method. This is a combination of the TDMA (Tri-Diagonal Matrix Algorithm) for one-dimensional situations used in conjunction with the Gauss-Seidel method. In this procedure, one chooses a grid line (say, the y-direction), assume that the ϕ's along the neighboring lines (i.e. the x-and z-direction neighbors of the points on the chosen line) are known from their *guessed* or *latest* values, and then solve for the ϕ's along the chosen line using the TDMA algorithm. One follows this procedure for all lines of nodes in one coordinate direction and then repeats the procedure by successive sweeps, until one obtains converged solutions. Thus, in the present work, the set of discretized equations of those variables of interest were solved using the SIMPLE algorithm with this line-by-line iterative procedure.

In the process of the iterative solution procedure, a criterion determining 'convergence' is needed. Convergence is defined as the property of the iteration scheme to proceed from a set of initial values to an acceptible solution of the discretized equations. In the present computational work, the acceptibility of the converged solution was measured by the "residual sources", R_ϕ. This is defined as

$$R_\phi = a_P \phi_P - (\sum a_{nb} \phi_{nb} + b) \tag{2-36}$$

Physically, the R_ϕ represents the net flux imbalances for the cells of ϕ. This will approach zero as the prevailing ϕ field reaches convergence. Thus, when the sum of residual sources reaches a very small reference value, $R_{\phi,ref}$, it can be assumed that the discretization equations have been solved. In this work, $R_{\phi,ref}$, was set to 0.01 for velocity field and 0.001 for mass concentration, Sufficiently small grid space and time intervals (for transient cases) are also important factors for the accuracy of the solution. Thus, it is necessary to ensure that the solution is invariant to further reduction in these intervals.

Sometimes, *under-relaxation* can be employed in order to avoid divergence in the iterative solution of strongly nonlinear equations. Equation 2-33 can be written as

$$\phi_P = \frac{\sum a_{nb}\phi_{nb} + b}{a_P} \tag{2-37}$$

or

$$\phi_P = \phi_P^* + \left(\frac{\sum a_{nb}\phi_{nb} + b}{a_P} - \phi_P^* \right) \tag{2-38}$$

where ϕ_P^* is the value of ϕ_P from the previous iteration. This change can be modified by the introduction of a relaxation factor, α, so that

$$\phi_P = \phi_P^* + \alpha \left(\frac{\sum a_{nb}\phi_{nb} + b}{a_P} - \phi_P^* \right) \tag{2-39}$$

or

$$\frac{a_P}{\alpha}\phi_P = \sum a_{nb}\phi_{nb} + b + (1-\alpha)\frac{a_P}{\alpha}\phi_P^* \tag{2-40}$$

As seen in Equation 2-40, under-relaxation can be performed by modifying a coefficient and the source term. In the present computational work, the under-relaxation factor, α, was set to 0.5 for velocities, 0.7 for turbulence parameters and temperature, and 1.0 for pressure and mass fraction (i.e. no under-relaxation).

Chapter 4

Overview of Computer Code (*METFLO*)

4.1 Overall Structure

Figure 2-5 provides a schematic structure of the code, *METFLO,* developed for computational predictions of three-dimensional transport phenomena in metallurgical vessels. It shows the various subroutines, their functions and interrelations The core of the program is the main subprogram, here called *MAIN*: its functions are controlling the progress of the calculation, and producing and saving resultant variable fields (i e. u, v, w, P, k, ε, μ_{eff}) and other information at intermediate and final stages.

Subroutine *USER* contains several entry routines, which carry out the initial specification of the grid, the control parameters, constants of the problems, fixed boundary values, and any other relevant initial specifications required.

Subroutine *INIT* calculates the grid coordinates, inter-node distances, cell dimensions, etc., and assigns the starting points of the calculation domain The iteration procedures are performed and controlled by *ITER*. It also gives intermediate outputs of the number of iteration, residual sources, and the value of variables at a specific grid point being monitored so as to enable one to check the progress of iterations and convergence.

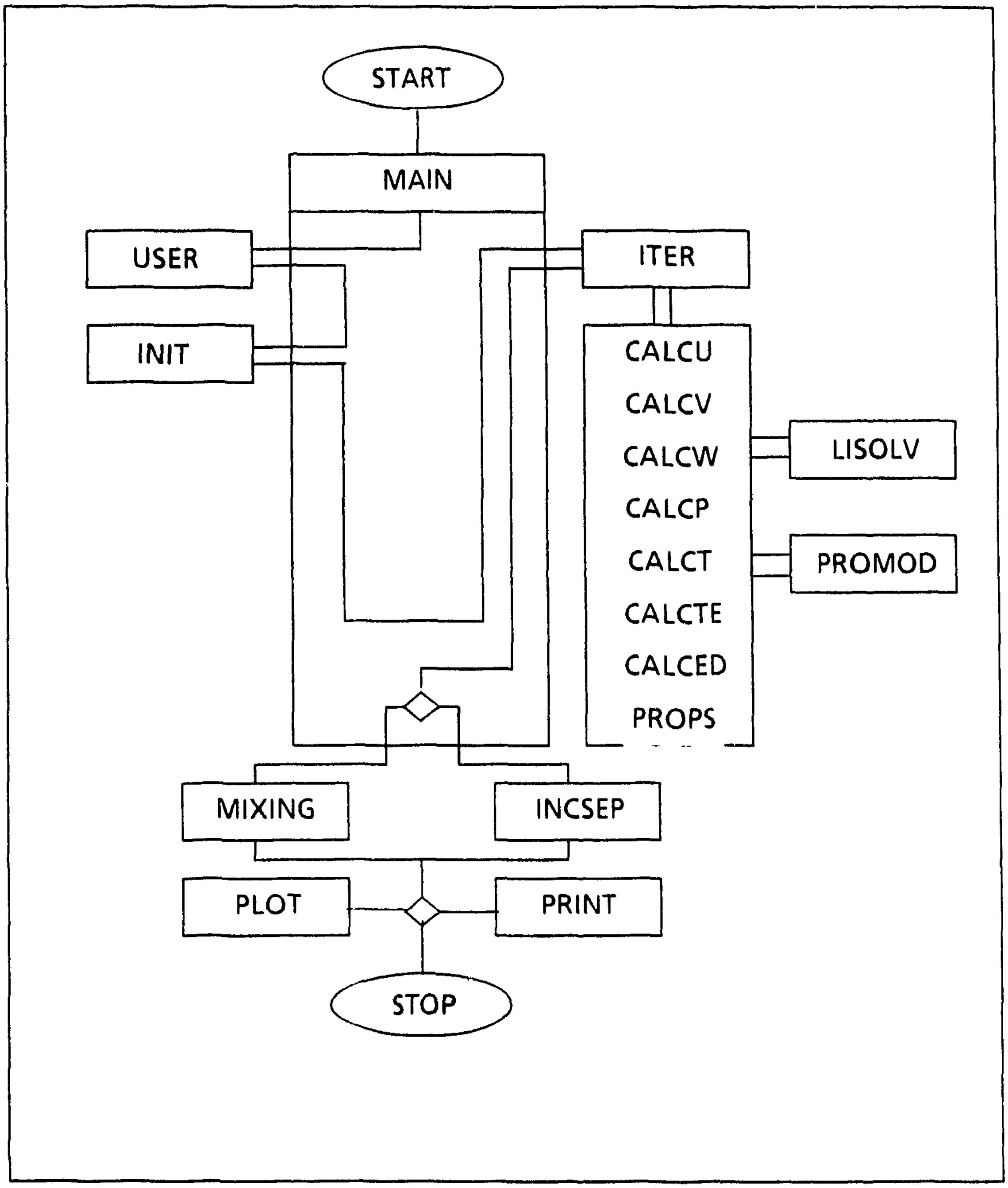

Figure 2-5 Structure of the METFLO code.

All of the *CALC*ϕ subroutines have the same structure with exception of *CALCP*. Being entered from *ITER* and also exited to *ITER*, each of these subroutines calculates the coefficients over the entire field, and makes a call to *MOD*ϕ in *PROMOD* in order to modify the sources and boundary coefficients for the particular problem. All the coefficients are then gathered, and the residual source is calculated from the values of ϕ in the previous iteration. Finally, a call is made to *LISOLV* for the application of the line-by-line procedure, before returning to *ITER*. Subroutine *CALP* has almost the same structure as the above, but, after *LISOLV* is called, a correction for velocities and pressure is carried out, and the pressure corrections set to zero. Subroutine *PROPS* evaluates fluid properties (e.g. density, turbulent viscosity, thermal diffusivity, etc.) based on formulae provided.

The line-by-line iteration is performed in subroutine *LISOLV*. The subroutine *PRINT* performs the printing of the dependent variables, if desired, while *PLOT* performs plotting of the velocity profiles, and iso-value contours. Subroutine *PROMOD* consists of several entries of *MOD*ϕ. It plays the most important role as it is the major area where the sources and boundary conditions can be modified to suit the individual problem.

INIT, *ITER*, *LISOLV*, *PRINT*, and the set of *CALC*ϕ subroutines are independent of problem type. Modification for specific case is required only in *MAIN*, *USER*, *PROMOD*, and sometimes *PROPS* and *PLOT*.

If required, other subroutines can be created and easily linked into this program. For instance, subroutine *MIXING* was created and incorporated for the study of mixing behavior within ladles during gas stirring operations, and *INCSEP* was developed for the study of inclusion separation in tundishes.

4.2 Computational Procedures

Figure 2-6 shows a flow chart of the computational procedures used in the present study. To begin, information such as the grid size, vessel dimensions, fluid properties, control parameters, type of coordinate system, etc., is input through a data block. The grid arrangement is then set up with the grid size and the number of grids given. Some fixed boundary values are also imposed with respect to the problem *<USER>*.

Using the input data of vessel dimensions and grid size, the cell dimensions for the variables are calculated and some parameters are determined by the type of coordinates. The variable fields are then initialized *<INIT>*. At this stage, it is ready to start iteration procedure of variables *<ITER>*.

The calculation of variables proceeds as follows: first, the *u*-momentum equation is solved. Calculating cell areas and volumes, the coefficients and source terms are set up for all cells in the domain. Special boundary conditions are imposed for the walls, symmetry planes, free surface and blocked region *<MODPRO>*. After performing under-relaxation, the discretization equations at all *u*-cells are solved by means of TDMA *<LISOLV>*. This procedure is carried out in the subroutine *CALCU*. Other variables (i.e. v, w, T, P', k, ε) are solved sucessively using the same procedures just described *<CALCV, CALCW, CALCT, CALCP, CALCTE, CALCED>*.

Fluid properties are calculated and updated by new values of the dependent variables *<PROPS>*. The steps from *CALCU* to *PROPS* are repeated until a converged solution is obtained. The results are saved on a disk, and, if

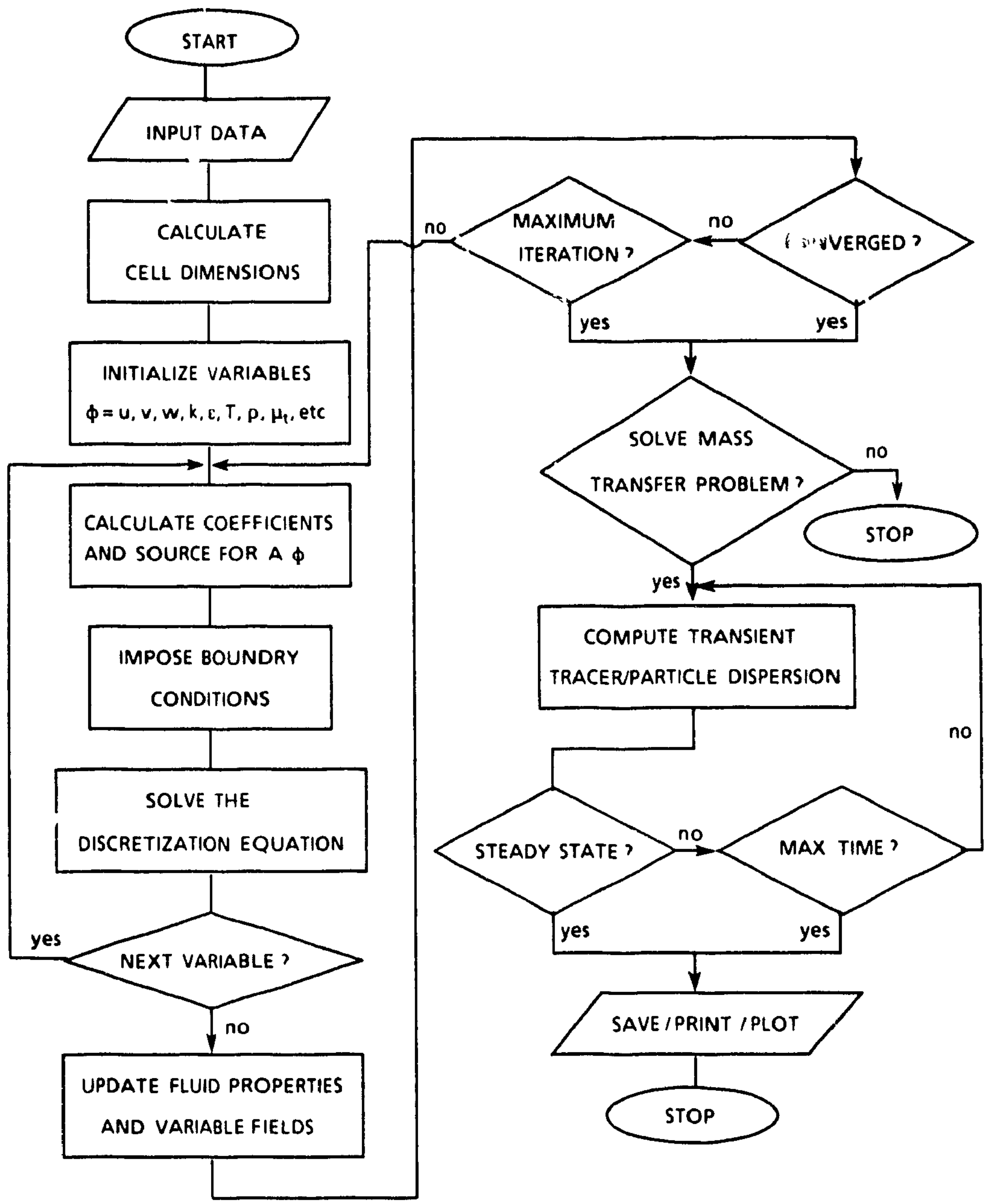

Figure 2-6 A flow chart of the computational procedures in METFLO code.

necessary, printed and plotted, following convergence or reaching a maximum number of iterations.

Using the variable fields computed and/or saved, associated transport phenomena in metallurgical processing vessels (e.g. mixing procedures, and inclusion separation) can be solved <*MIXING, INCSEP,* >. When the criterion for steady state is satisfied or the maximum transient time is reached, the results are also saved, printed and plotted.

4.3 Code Verification

In order to verify the code, two case studies were carried out. One is to solve an axisymmetric gas stirring problem in a steelmaking ladle (this is actually two-dimensional problem) using the three-dimensional code. Figure 2-7, hence, shows an isometric surface flow fields when a gas flow rate of 30Nl/min is centrally injected through a single porous plug into a one-third scale water model of 100 ton ladle. Axisymmetrical flow patterns to the vertical center axis can be seen from the figure. It was also observed that the values of the local flow velocities was exactly the same as those solved using two-dimensional code.(14)

The other computation was carried out for a rectangular 1/6 scale water model tundish(15), measured 1.167m in length, 0.167m wide, and a filled height of 0.214m. The water flow rate was 19 liters/min. Thus, Figure 2-8 illustrates an isometric view of flow vectors for a quadrant of the tundish.

Comparisons between predictions and observations of the flow patterns in some selected planes of the central longitudinal plane (plane A),

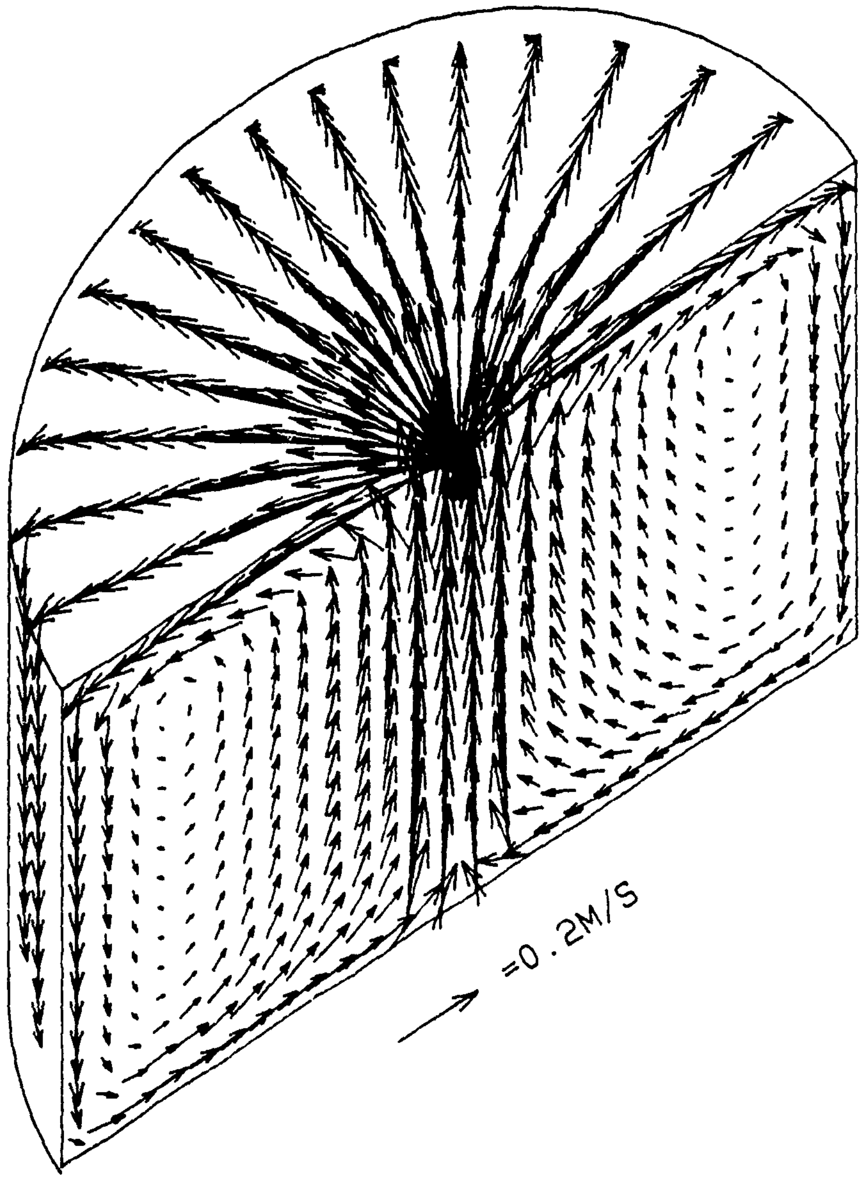

Figure 2-7 Computations illustrating flow patterns developed by submerged gas injection through a single porous plug located at center of vessel. (This figure shows the two-dimensional characteristic of center gas bubbling.)

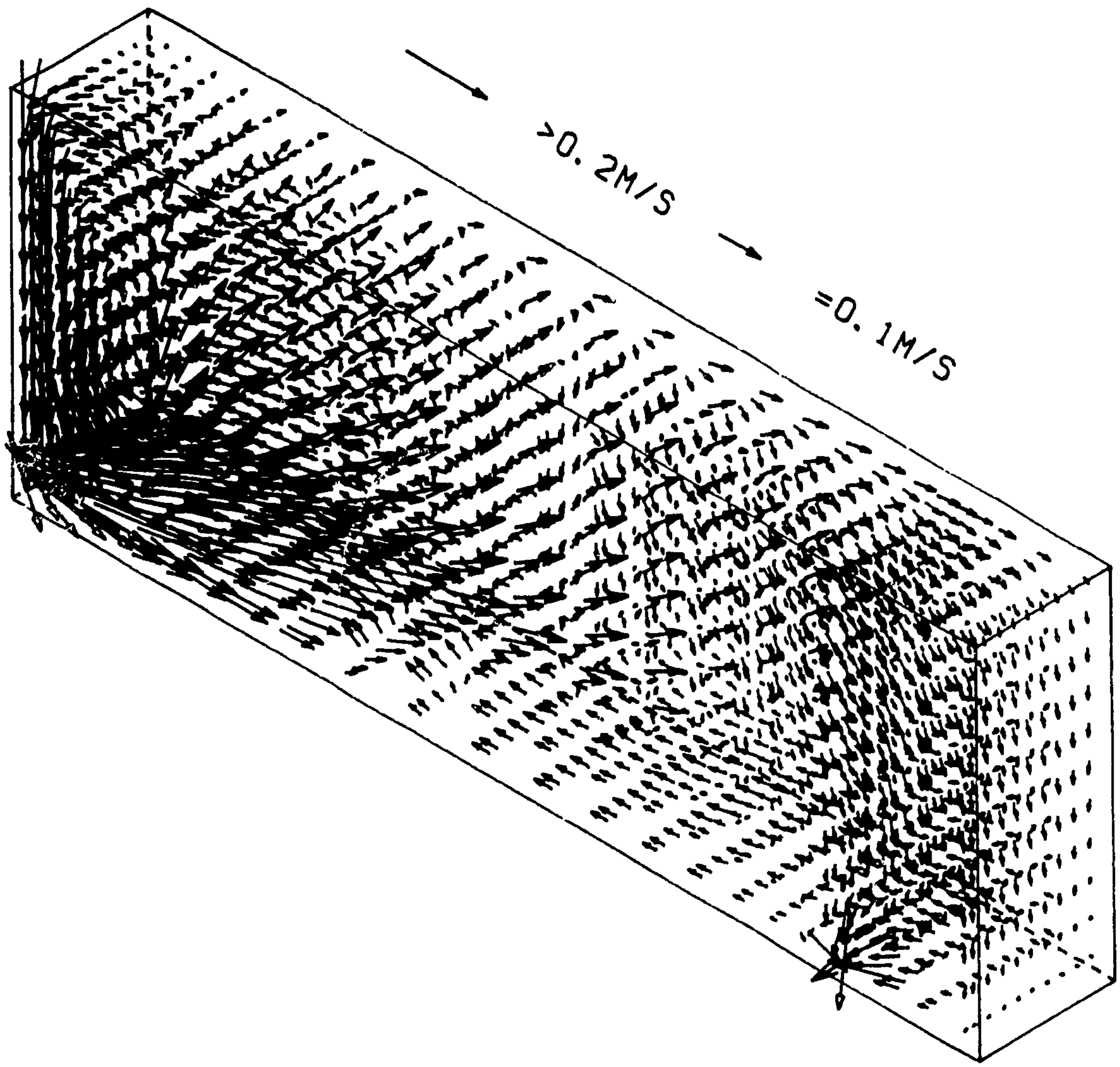

Figure 2-8 An isometric view of flow fields predicted for a 1/6 scale water model of a twin slab casting tundish. (Only a quadrant of tundish was taken into account for computation)

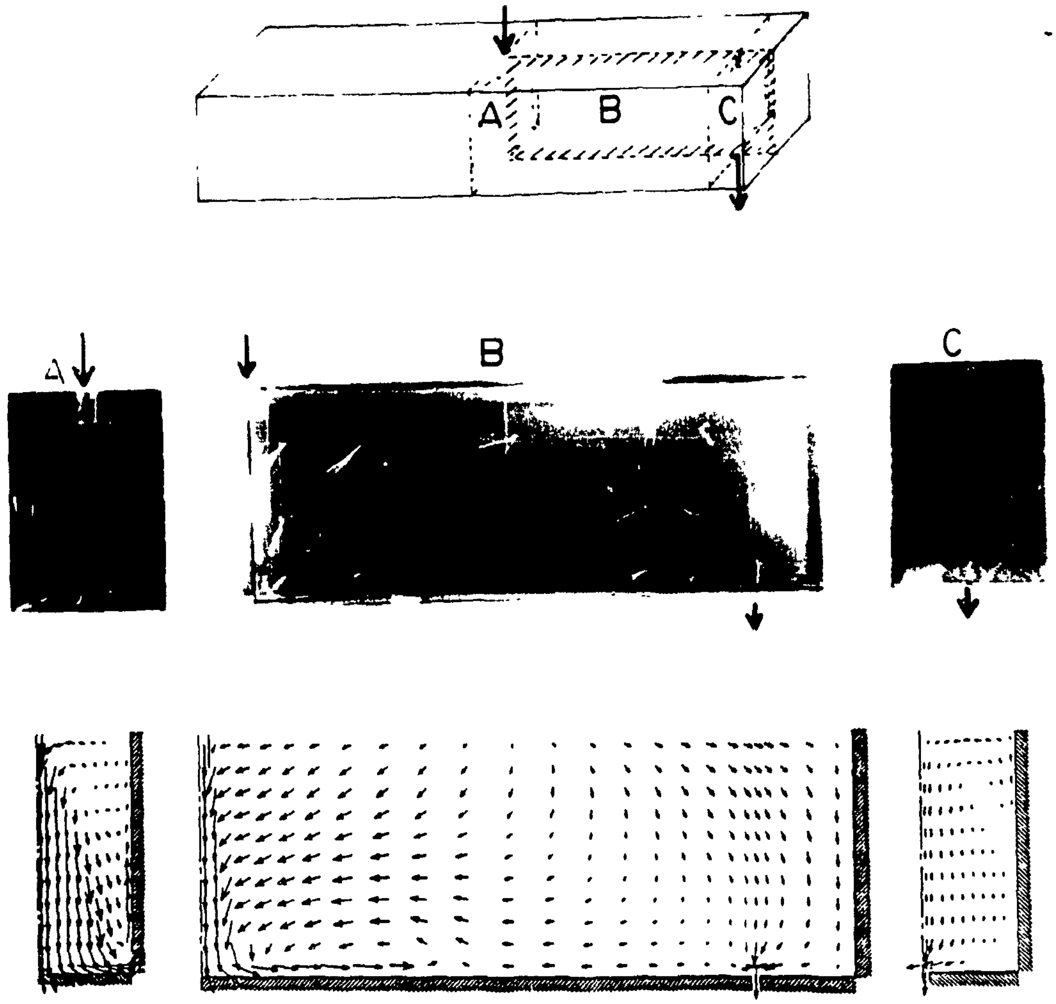

Figure 2-9 Comparison of predicted flow vectors and flow visualization with silk tuft.

the inlet vertical plane (plane B), and the outlet vertical plane (plane C), are given in Figure 2-9. As seen, the predicted flow patterns agreed well with the observations. It is appropriate to note that the mean speed of flows within the tundish was predicted to be 4.8 mm/s, while the measured mean flow speed was reported to be about 5 mm/s.

These and other case studies show that the code, *METFLO*, is correctly programmed and that it provides reasonable predictions for fluid flows in ladle and tundish steelmaking vessels.

4.4 Summary and Concluding Remarks

In this part of the thesis, a computational method for three-dimensional turbulent flows used in the prediction of transport phenomena in metallurgical vessels, has been briefly described. This outline is schematically summarized in Figure 2-10.

Thus, the laws of fluid dynamics can be combined and expressed into differential equations, which can then be transformed into finite difference forms for the calculation using a con.puter machine. A solution algorithm is necessary to achieve solutions for the finite difference equations. Since such an algorithm involves thousands of operations, it is embodied in a computer program in order to take advantage of the capability of the computer. Finally, the computer program can yield solutions to the set of equations and can provide predictions, that are consistent with physical reality provided the differential equations, finite difference equations and computer code have been adequately established, and the problem is well set.

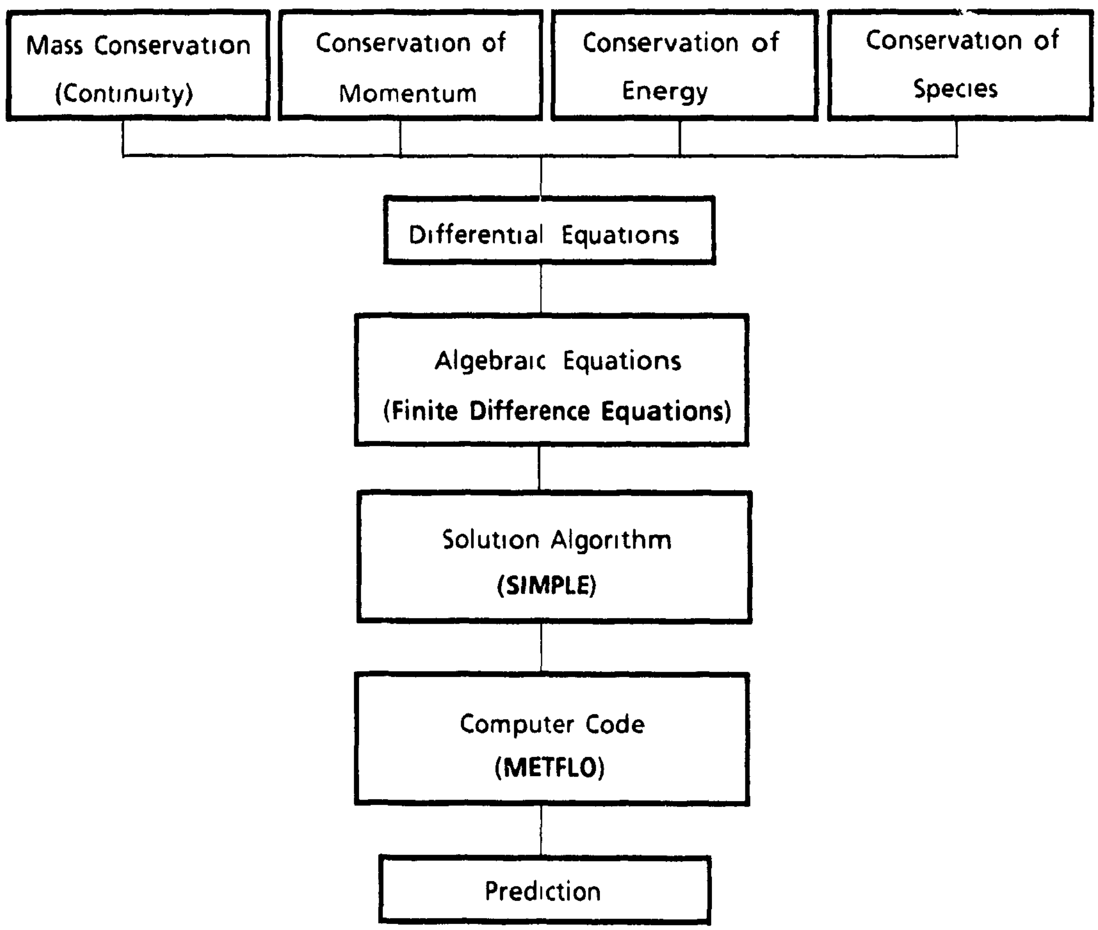

Figure 2-10 A computational prediction procedure for simulating transport phenomena.

Using METFLO, the computer program developed in the present study, one can predict fluid flow, mixing behaviour, inclusion flotation or settling and their population distributions, energy transport and temperature distributions in metallurgical processing vessels. With the larger storage capacities of today's computers and their faster processing times (e.g. Cray super-computers), many complex metallurgical problems expressed in three-dimensional differential equations are now amenable for study, at reasonable cost and time.

REFERENCES

1) T.V. Boussinesq, Mém. Pré. Acad. Sci., Third Edition, Paris, Vol 23, 1877, pp46

2) L. Prandtl, "Bericht über Untersuchüngen zur ausgebildeten Turbulenz", ZAMM, vol 5, 1925, pp136

3) L. Prandtl, "Über ein neues Formelsystem für die ausgebildete Turbulenz", Nachrichten von der Akad. der Wissenchaft in Göttingen, 1945.

4) P. Bradshaw, D.H. Ferriss and N.P. Atwell, J. Fluid Mech., Vol.28, 1967, pp593

5) K. Hanjalic and B.E. Launder, J. Fluid Mech., Vol 52, 1972, pp609

6) A.D. Gosman, W.H. Pun, A.K. Runchal, D.B. Spalding and M. Wolfshtein, "Heat and Mass Transfer in Recirculating Flows", Academic Press, London

7) W.P. Jones and B.E. Launder, Int. J. Heat Mass Transfer, vol. 15, 1972, pp 301-304

8) B.E. Launder and D.B. Spalding, Computer Methods in Appl. Mech. & Eng., Vol. 3, 1974, pp269

9) S.V. Patankar and D.B. Spalding, "Heat and Mass Transfer in Boundary Layers", 2nd Ed., Intertext Books, London, 1970

10) M.N. Özisik, "Heat Transfer - A Basic Approch", McGraw Hill, New York, 1985

11) J. Nikuradse, Forch. Arb. Ing. Wes., No. 346, 1932

12) S.V. Patankar, "Numerical Heat transfer and Fluid Flow", McGraw Hill, 1980

13) S.V. Patankar and D.B. Spalding, Int. J. Heat Mass Transfer, Vol. 15, 1972, pp1787

14) D. Mazumdar, Ph.D. Thesis, Department. of Mining & Metallurgical Engineering, Mcgill University, Montreal, Canada, 1985

15) S. Tanaka, Ph.D. Thesis, Department. of Mining & Metallurgical Engineering, Mcgill University, Montreal, Canada, 1986

16) A.D. Gosman and F.J.K. Ideriah, "A General Computer Program for Two-Dimensional, Turbulent, Recirculating Flows", Dept. of Mechanical Engineering, Imperial College, London, 1976.

17) F.H. Harlow and J.E. Welch, Phys. Fluids, Vol. 8, 1965, p2182

PART III

MODELLING MIXING IN STEELMAKING LADLES

Chapter 1

Introduction

For higher quality steelmaking, gas bubbling in ladles is used to obtain chemical and thermal homogenization, as well as to accelerate the absorption of harmful non-metallic inclusions into an overlaying slag. The main point in gas stirring operations is to identify procedures and equipment needed for achieving minimum mixing times and maximum recoveries of alloy additions at optimum gas flow rate. In order to reasonably predict these phenomena, detailed information on flow patterns, fluid velocities and turbulent properties is needed. These have been the subject of study via on-going physical and mathematical models over the last decade.

Szekely et al [1] were the first to attempt modelling the hydrodynamic behaviour of liquid metal in an argon stirred ladle. Velocity and turbulence energy fields were predicted through the solution of the turbulent Navier-Stokes equations in conjunction with the k-W two equation model of turbulence. However, the boundary conditions (e.g. velocity and shear stress), adopted for an "interface" between the bulk fluid and the plume, proved unrealistic. Deb Roy et al.[2] and Grevet et al [3] recognized the role of buoyancy in the gas/liquid mixture, and proposed that the gas/liquid mixtures could be represented by a pseudo-one-phase fluid of variable density. Sahai and Guthrie[4,5] went on to develop mathematical and algebraic models to describe the interaction of a plume with its surrounding liquid, enabling plume dimensions, voidage, and center line velocities to be specified, and the whole flow field analyzed. Their results matched pilot scale water model results.

These mathematical models were developed for axisymmetric gas stirring. In such systems, flows can be described via the two-dimensional continuity and momentum equations, expressed in cylindrical polar coordinates. While many flows within ladles can be idealized by assuming axisymmetric conditions, a major feature of industrial operations is their three-dimensional character (e.g. off-centered gas bubbling, multi-plug gas bubbling, off-centered alloy/tracer additions, the RH degassing process, etc.). However, few studies on three-dimensional turbulent flows in gas stirred ladles have been reported to date.[6-8]

The concept of mixing time, τ_m, has commonly been used to represent the state of agitation in the chemical and metallurgical processing vessels. Since Nakanishi et al.[9] first correlated mixing times to stirring energy input, many empirical relationships of the type $\tau_m = k\varepsilon^{-n}$, have been reported[9-14], assuming that mixing times are independent of the experimental conditions. However, in general, the values of k and n varies with respect to the experimental situations studied by investigators. The fact that there are various empirical values for them reveals that the measured mixing times could be dependent on experimental conditions, such as vessel geometry, tracer injection point, monitoring point, gas bubbling location, and the existence of a slag layer.

Mazumdar (14) observed that the measured mixing time depends on the points of tracer injection and monitoring . He further demonstrated that mixing in gas injection ladle metallurgy operations can be expected to be controlled by a combination of eddy diffusion and bulk convection, both mechanisms contributing in roughly equal proportions. Asai et al (10), Kim(13), and Dobson et al.(21) reported that mixing times decreased as the plug's location became more off-centred. On the other hand, Marujama et al.(15) reported that rapid mixing was achieved with gas injection at the mid-radius of the vessel, where both wall effects and relative stagnation zones could be minimized.

The purpose of the present research was to study realistic industrial situations in order to analyse mixing behaviour and mixing mechanisms as a function of porous plug location, tracer injection point and ladle monitoring point. For this, mathematical and physical models were used.

Chapter 2

Mathematical Model

2.1 Governing Equations

In order to describe fluid flow, turbulent properties and alloy/tracer dispersion in steelmaking ladles, the relevent partial differential equations requiring (numerical) solution are the equations of continuity, momentum and mass conservation, expressed in cylindrical polar coordinates. These are aleady described in PART II (e.g. Equations 2-2 to 2-15), and need no repetition. Hence, in the following sections, a plume model, boundary conditions and solution procedures used for the present study will be described

2.2 Treatment of Plume

In the numerical solution procedures for this study, gas injection was treated as a pseudo-one-phase flow phenomenon, in which the gas-liquid metal plume is characterized by a region of lower density steel. The gas voidage, α, within a rising gas-liquid plume was accounted for by introducing a buoyancy term, $\rho_l g \alpha$, on the right side of Equation 2-4 for S_u, the 'source term' for the u-momentum equation. The gas voidage, α, can be calculated by applying the principle of volume continuity as follows:

$$\alpha = Q/\pi r^2_{av,p}\ U_p \tag{3-1}$$

Sahai and Guthrie[4] have provided a simple algebraic equation to calculate the plume rising velocity, U_p, such that

$$U_p = K\,\frac{Q^{1/3}L^{1/4}}{R^{1/3}} \tag{3-2}$$

where the constant K is estimated as 4.17 in SI units, . The density of the plume can then be obtained by

$$\rho = \alpha\,\rho_G + (1-\alpha)\,\rho_L \tag{3-3}$$

The approach is simple and correctly emphasizes the importance of buoyancy, versus shear forces, in gas driven recirculating flows. It has been confirmed through many experiments to be an effective way of treating such problems[5,14].

2.3 Boundary Conditions

Impermeable and adiabatic conditions were assumed at all boundaries. All variables (i.e. u, v, w, k, ε) at solid walls were set to be zero. At the node adjacent to solid boundaries, the wall shear stress and the energy dissipation rate were calculated using the wall function method described in Part II. The plume was assumed to be a vertical cylinder of lower density liquid. At the free surface, the boundary was assumed to be flat, and normal velocity components and normal gradients of all variables were set equal to zero.

2.4 Numerical Procedures

A general purpose code for three-dimensional turbulent flow in metallurgical processing vessels, dubbed with the acrouymn, *METFLO*, was developed, as described in Part II. In this modelling program, discretisation equations derived from Equations 2-2 through 2-19 were solved using an implicit finite difference procedure, referred to as the SIMPLE algorithm of Patankar and Spalding[18], for both rectangular and cylindrical polar coordinates. For analysis of the gas-liquid region, the GALA[19], procedure was incorporated into the SIMPLE algorithm. In this, the physical properties of fluid mixture in a cell in the two-phase region were averaged on a volumetric basis. This required that the conventional mass continuity equation be replaced by a volume continuity equation, such that the volume of fluids entering a volume element equalled the total volume of fluids leaving.

The numerical time step integration in the mass conservation equation (viz., Eq. 2-14) was approximated by a fully implicit marching integration procedure, while for the representation of total flux (i.e., convection + diffusion), an hybrid differencing scheme was adopted.

Equation 2-14, though a linear differential equation, was solved iteratively, using a line-by-line solution scheme.

Following grid independence studies, the domain was divided into a uniform grid of 18 (axial) x 16 (radial) x 16 (angular) in the three polar directions. The computations were performed on a personal computer equipped with a DSI (Definicon System Inc.) micro coprocessor (68020 coprocessor system) which magnifies RAM size up to 8 megabytes and increased clock speeds to 20 megahertz. About 600-1000 iterations were needed to reach converged values of the velocity fields, the actual time being taken amounting to about 12-18 hours.

Chapter 3

Experiment

3.1 Experimental Procedures

Experimental work was carried out in a one-third scale water model of a 100 tonnes ladle planned for Stelco's McMaster Works. Part of this model appears in Figure 3-1 The model had a bottom diameter of 0.864 m, a top diameter of 1.00 m, and a filled height of 0.787 m This corresponded to actual (internal) dimensions of 2 60 m, 3.00 m, and 2.36 m respectively for the McMaster Works ladle

Figure 3-2 provides a schematic diagram of experimental equipment for the measurement of mixing times Air was injected into the water through porous plugs set in the bottom of the cylindrical tank. In order to measure mixing times for single porous plug bubbling, a tracer (20% HCl solution) would be injected into the surface of the plume zone, and concentration changes at a point near the bottom wall and the plume, monitored versus time. The 95% bulk mixing time criterion was then used as a suitable standard mixing time. This is defined as that time when all the local concentrations of tracer addition have reached 95% of the bulk well-mixed value. For double bubbler configurations, tracer was injected into the center, and mixing times were measured at a point near the bottom wall and the plume.

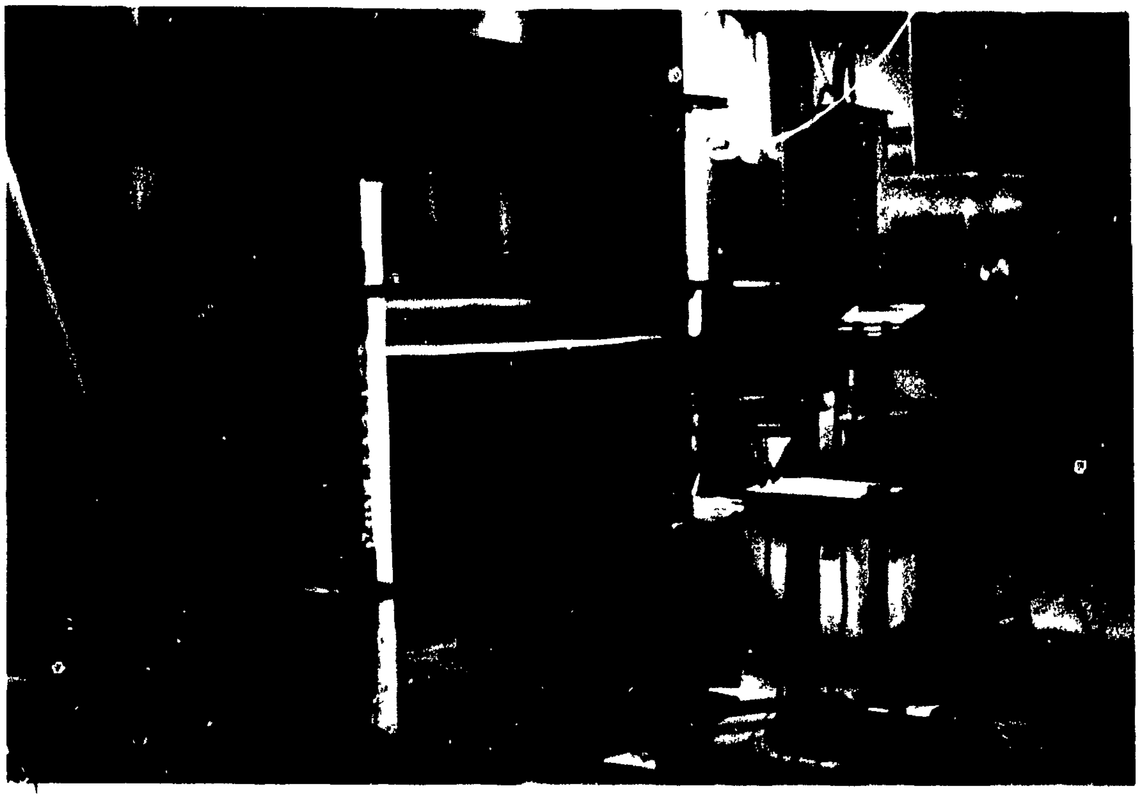

Figure 3-1 Photograph of experimental equipment for mixing time mesurements.

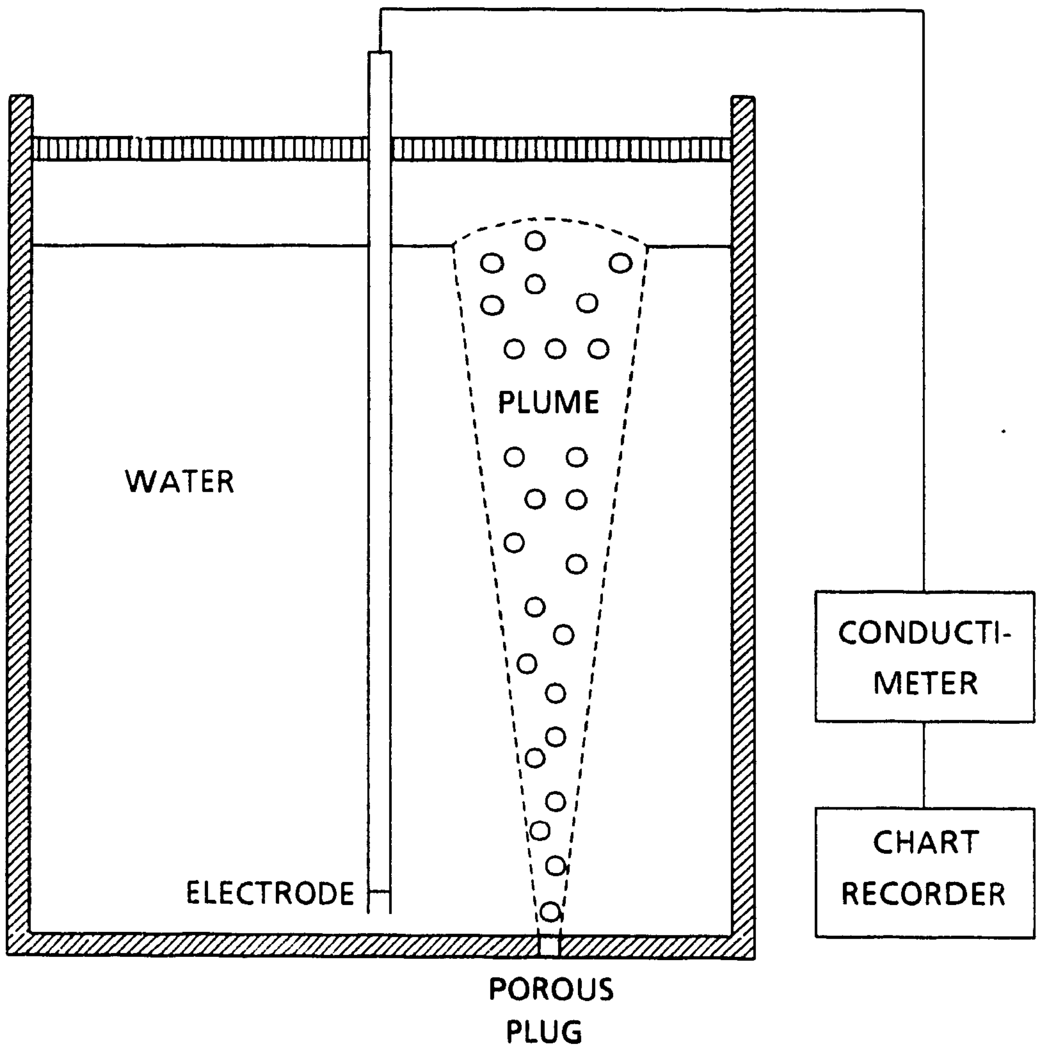

Figure 3-2 Schematic diagram of experimental set-up for mixing time measurements.

Mixing times were measured five to six times for a given set of experimental conditions, the mean value then being reported as the measured mixing time. It is appropriate to note that individual mixing times fell within ± 10% of the mean values reported here.

3.2 Experimental Results

Figure 3-3 shows how mixing times decreased with gas flow rate. As seen, the mixing time decreases exponentially with increasing gas flow rate. This work on a single porous plug gas bubbler confirms the relationship that mixing times decrease according to the one-third power of the gas flow rate.

Figure 3-4 presents some of the data already shown in Figure 3-3, in terms of mixing times versus radial placement of the plug, for various gas flow rates. As seen, mixing rates within the bulk of the liquid are increased, and mixing times shortened, as the plug is moved away from the centre towards the half radius. Beyond a minimum mixing time, reached at half radius, plugs set closer to the ladle sidewalls tended to give slightly longer mixing times for equal flows of gas. Consequently mid-radius bubbling gave a reduction of 15-30 % in mixing times over the range of gas flow rates studied.

It is occasionally necessary to bubble an industrial ladle with two or more plugs, in order to achieve gentle but rapid mixing, as well as to promote slag/metal intermixing, and to avoid explosive degassing effects under vacuum. A specific example is the tank degasser unit being operated by Dofasco (Hamilton, Canada) as an alternative to an RH degasser unit.

Figure 3-5 shows the effect of having two bubblers. There, experimental mixing times are plotted versus net flow of gas. As seen, for two bubblers placed at mid-radius, and diametrically opposite each other ($\theta = \pi$), the mixing time for a nett flow of 40 liters/min. is about 28 seconds, versus 33 seconds for a single bubbler. This represents a 15 to 20 % reduction in mixing times versus the optimum single bubbler configuration. Figure 3-6 confirms the fact that two bubblers, placed diametrically opposit each other, will exhibit minimum mixing times when operating at half radii. By moving both plugs out to 2/3 radii, mixing times are practically doubled at the higher flow rate (i.e. 40 liters/min).

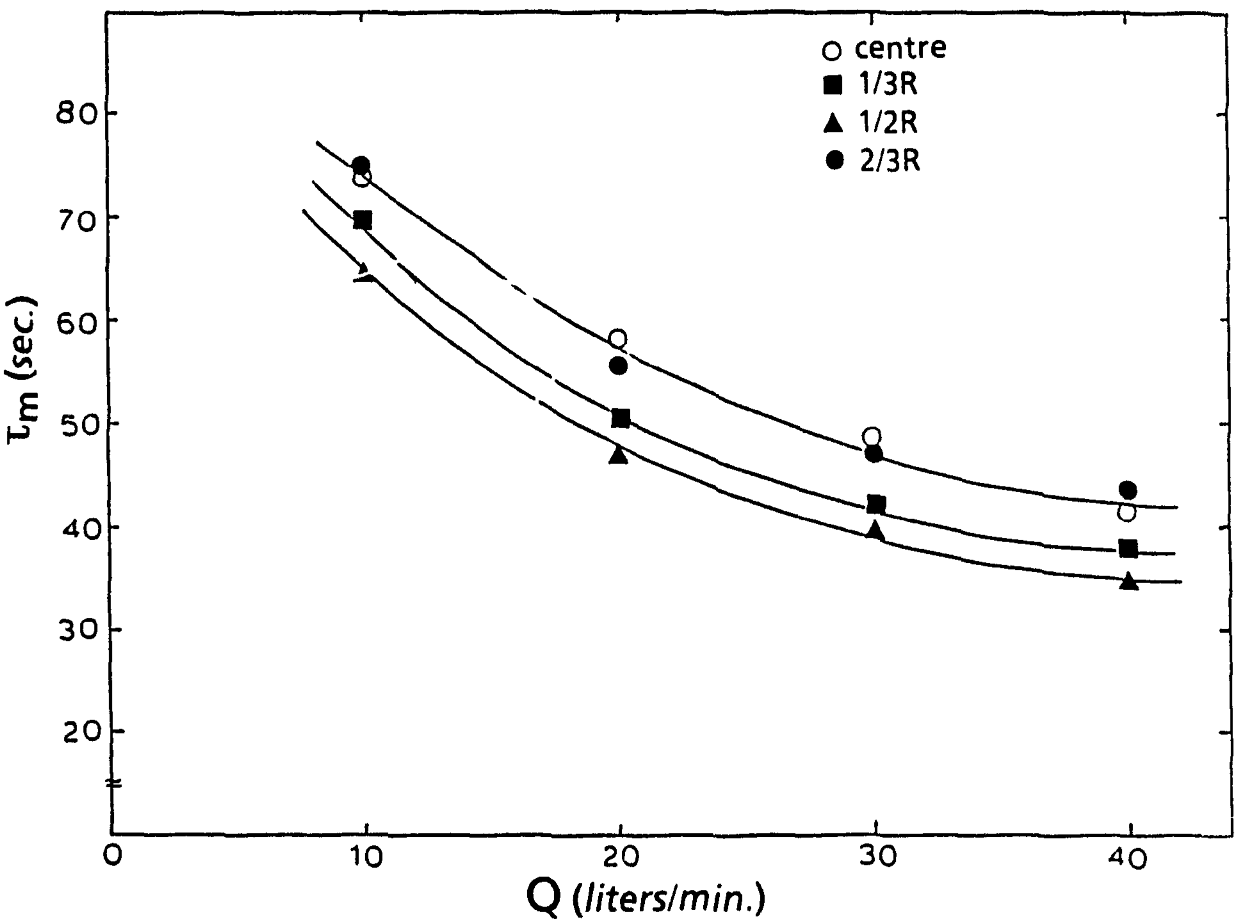

Figure 3-3 Variation in 95% mixing times with gas flow rate for plugs placed at: centre, one-third, half, and two-thirds radius of ladle base.

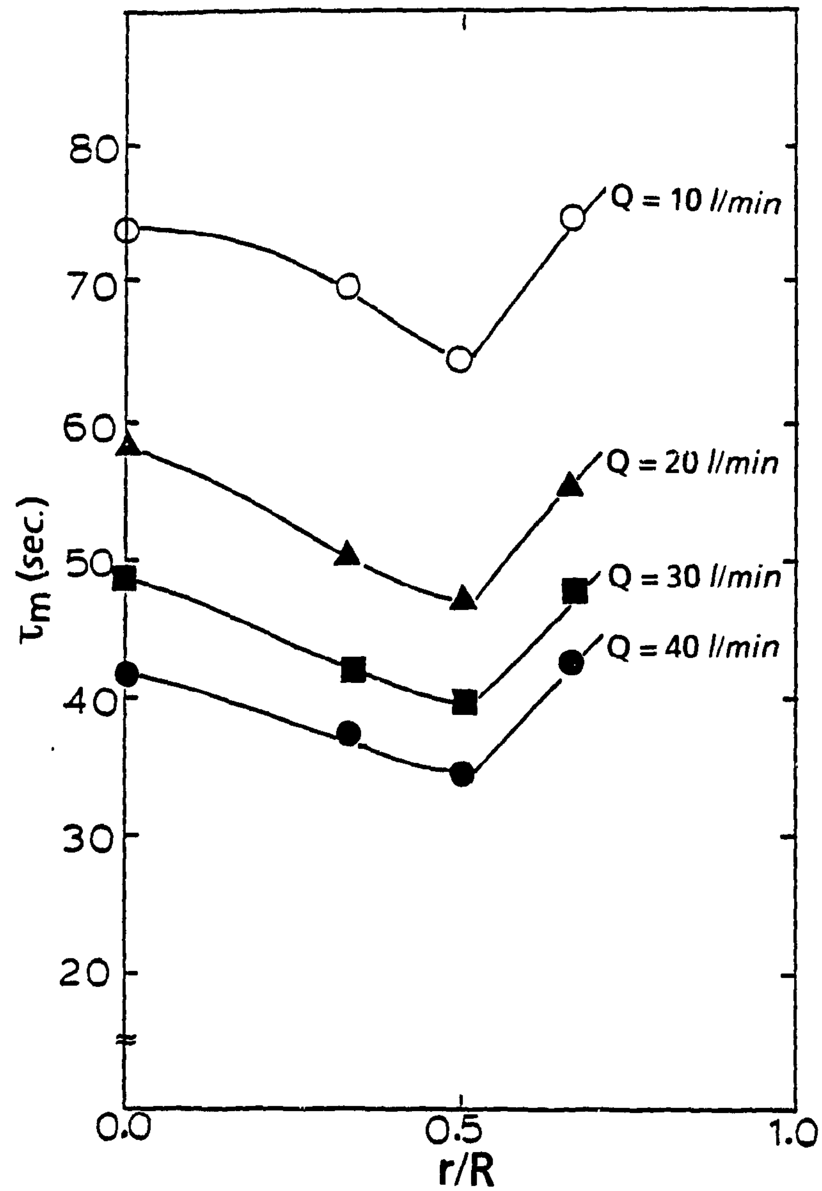

Figure 3-4 A plot of mixing time versus radial position for a single plug for various flow rates.

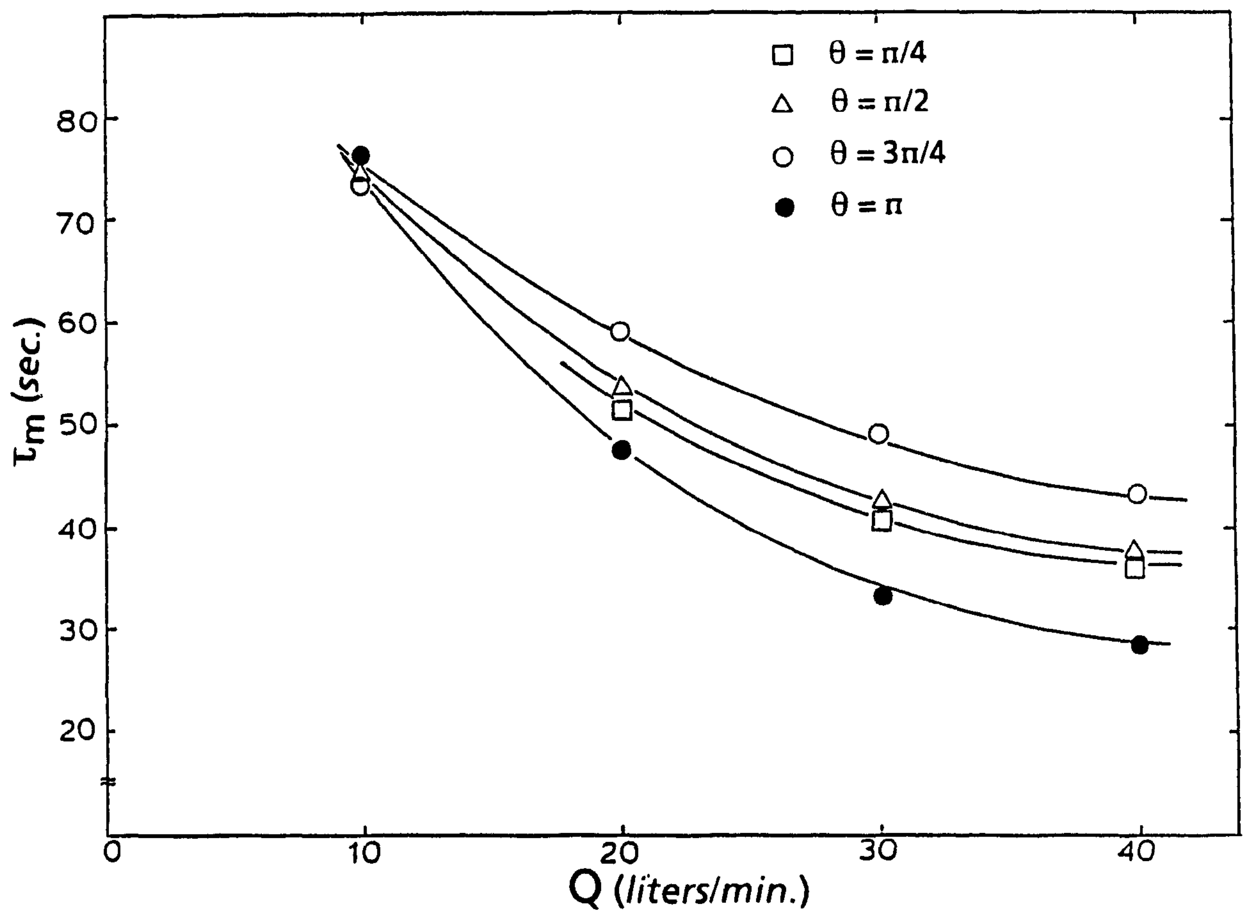

Figure 3-5 Variation in 95% mixing times with gas flow rate for double plug arrangements, placed at mid-radius. The effect of the angle, θ, subtended between the two plugs is illustrated.

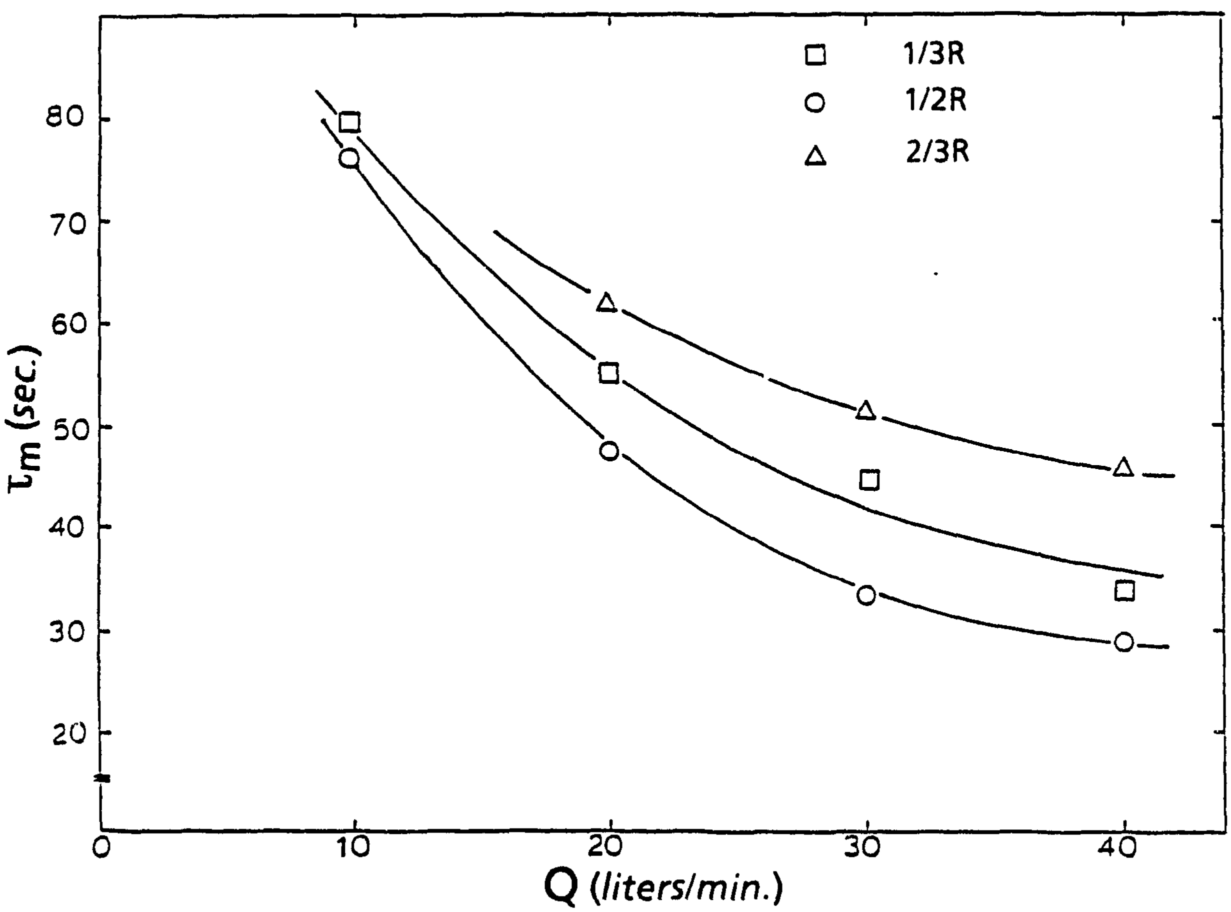

Figure 3-6 Variation in 95% mixing times with symmetrical changes in the radial positions of two opposing plugs ($\theta = 180°$).

Chapter 4

Computational Results and Discussions

In order to study mixing behaviour during such gas stirring operations in steelmaking ladles, computations were performed to predict flow patterns, transient mixing procedures and the final mixing time for a vertical, cylindrical ladle of equivalent scale to that studied, using the *METFLO* code already described, in conjunction with gas-liquid mixture models developed previously by Sahai and Guthrie[4], and Mazumdar and Guthrie[20].

4.1 Flow Patterns

Figure 3-7 illustrates some predicted three-dimensional surface flow fields when a gas flow of 30 Nl/min is injected through a single porous plug. In these modelling predictions, the position of the porous plug was changed from the centre to 2/3 radius in order to investigate the effect of plug location and tracer input location on mixing time. Figure 3-8 provides detailed two-dimensional flow fields in some selected vertical (a, b, and c) and horizontal (d, e, and f) planes for half radius placement of the plug. There, velocity vectors in vertical planes through the plume (a), at 45 degrees to the plume (b), and at right angles to the plume (c), have been provided. Similarly,

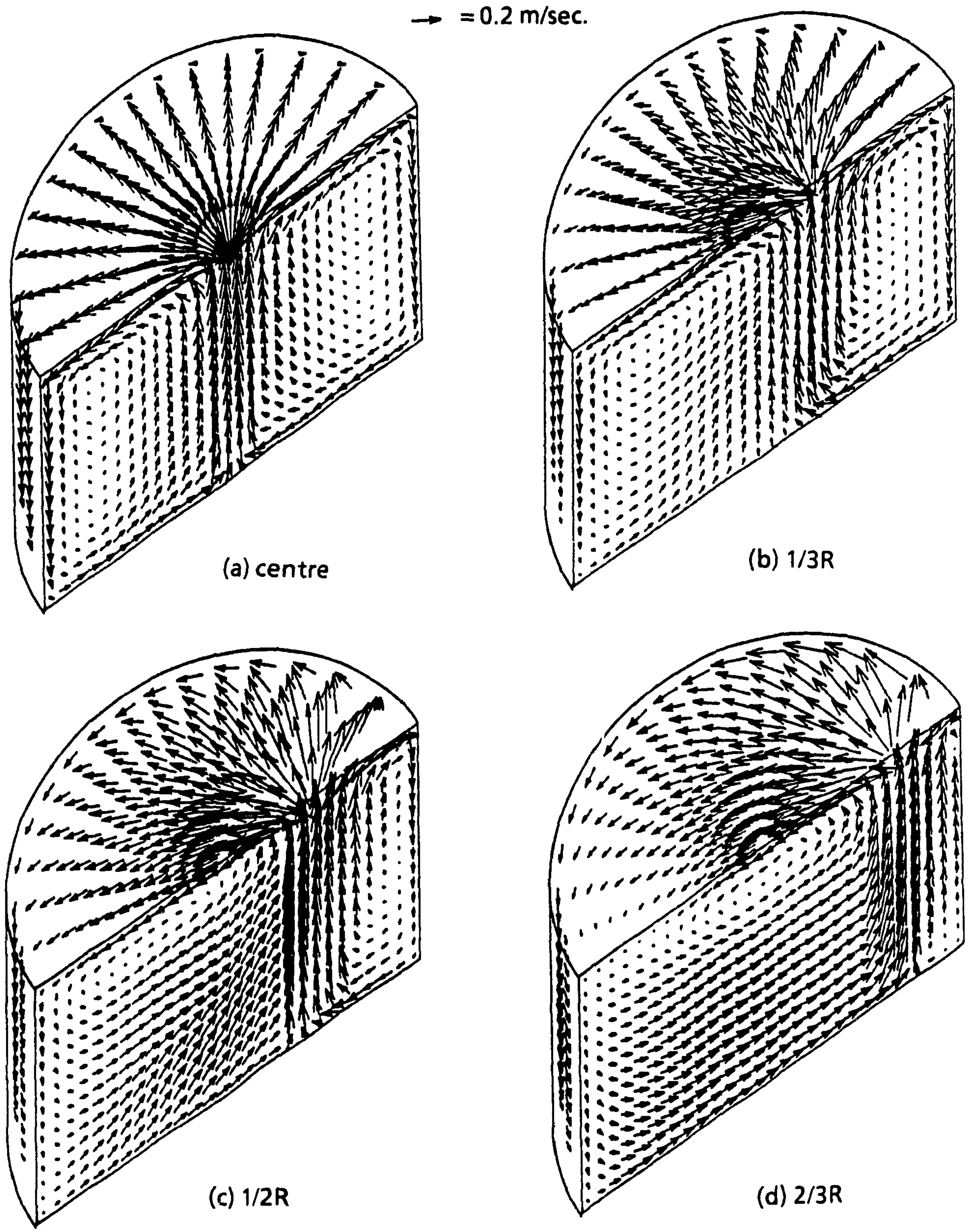

Figure 3-7 Computations illustrating flow patterns developed by submerged gas injection through a single porous plug located at center, one third, half, and two thirds radius, respectively.

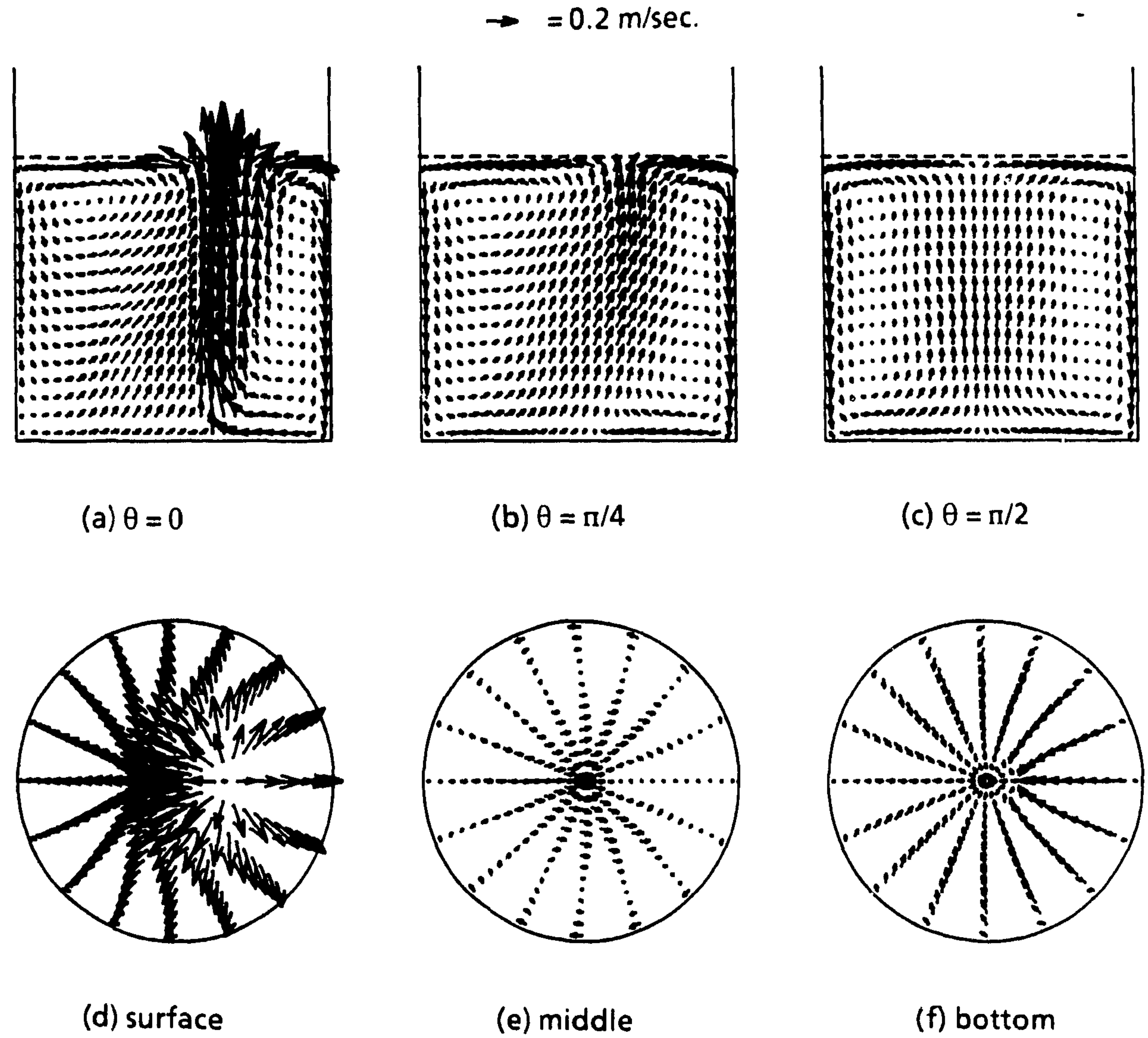

Figure 3-8 Two-dimensional velocty vectors in some selected vertical and horizontal planes for half radius placement of a single plug.

horizontal components of the fluid flow across the surface (d), at mid-level (e), and along the bottom of the ladle (f), are presented. The average recirculating flow speed was predicted to be 0.1 m/s.

The key features to note are the angular velocities which significantly affect tracer dispersion rates (as discussed later). It can be seen that as the plug's position is moved off center, the angular momentum of fluid motion increases remarkably. Predicted mean speeds within the ladle, versus change in porous plug location are presented in Table 3-1. It can be seen that the mean angular velocity increases and that the mean axial and radial velocities decrease, as the plug is moved away from the centre.

Flow patterns for twin plug injection, diametrically placed one to the other, are provided in Figure 3-9. There, diametrically opposed porous plugs were placed at 1/3, 1/2, and 2/3 radii, respectively. The two-dimensional plots in some selected planes are illustrated in Figure 3-10 for diametrically opposed plugs at half radius location. The mean recirculating flow speed was

Table 3-1 Predicted mean speeds of axial, radial and angular directions in a 1/3 scale water model of a 100 tonne ladle for various plug positions (Q = 30Nl/min., unit = m/s)

	$\overline{\lvert u \rvert}$	$\overline{\lvert v \rvert}$	$\overline{\lvert w \rvert}$	$\overline{\lvert U_{rec} \rvert}$
Centre	0 1094	0.0464	0.0000	0.1391
1/3R	0.0687	0.0346	0.0311	0.1008
1/2 R	0.0658	0.0368	0.0421	0.1025
2/3 R	0 0529	0.0355	0.0533	0.1028

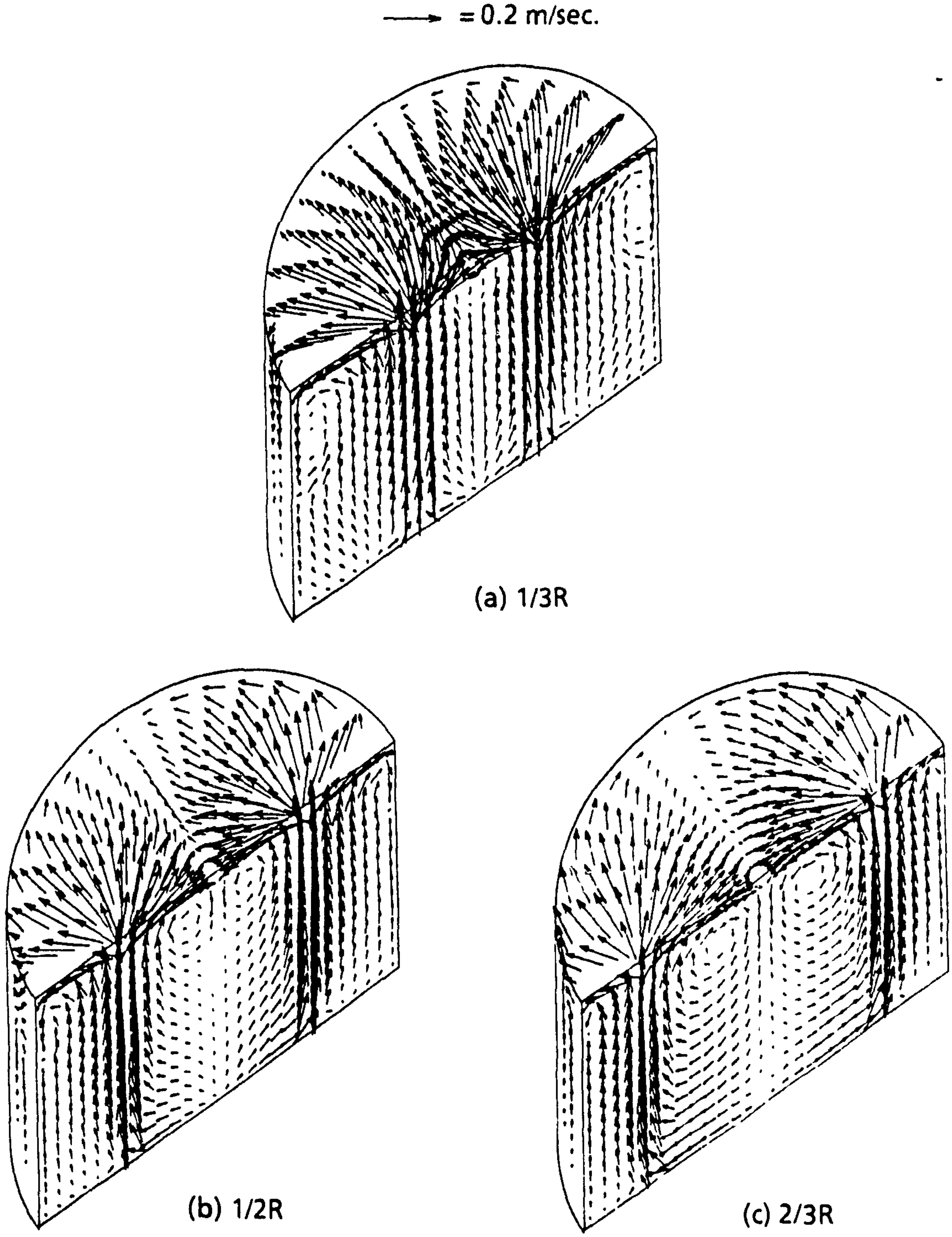

Figure 3-9 Isometric views of flow vectors predicted for double porous plug gas bubbling diametrically opposed at one-third, half, and two-third radii, respectively.

→ = 0.2 m/sec.

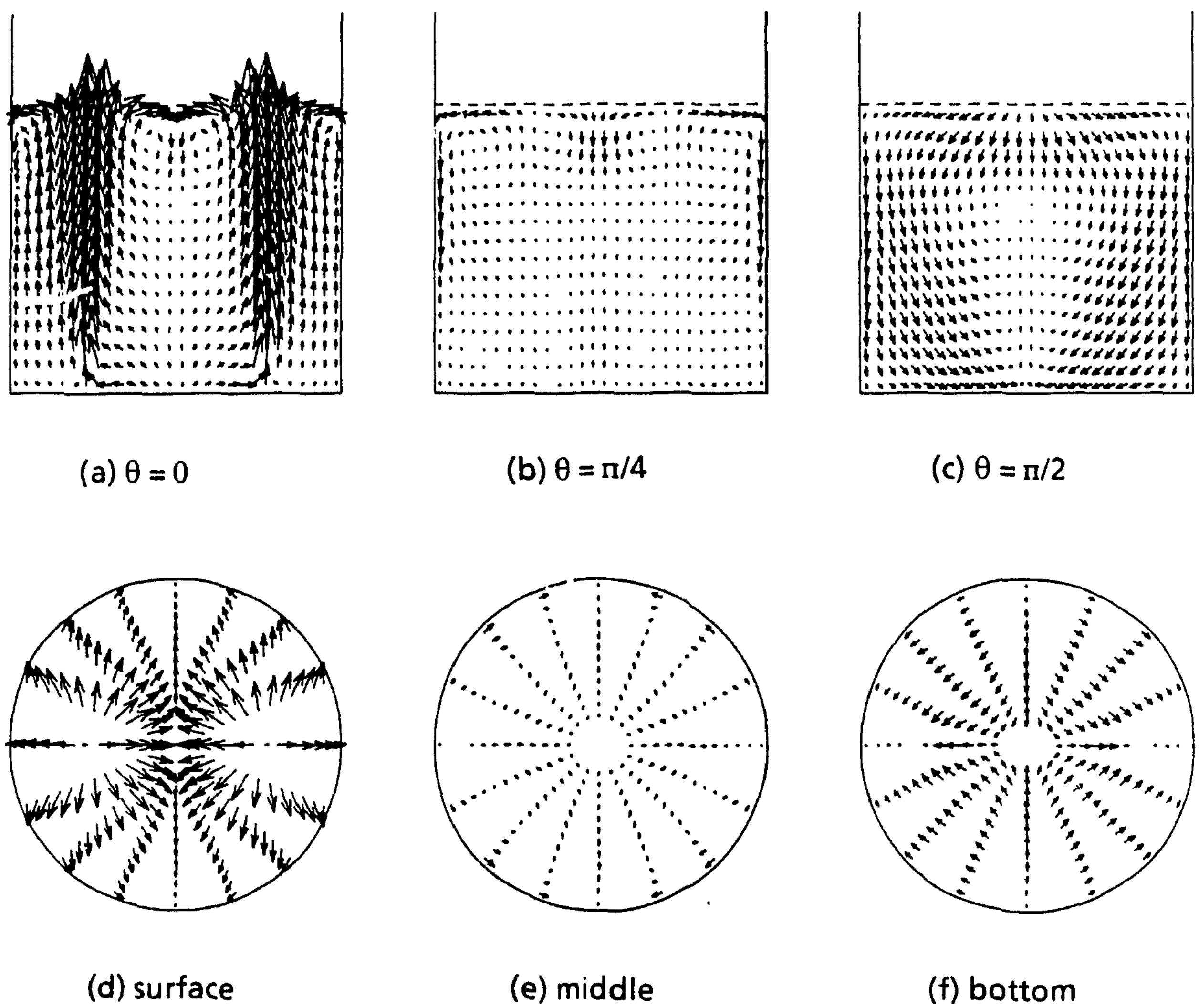

Figure 3-10 Two-dimensional velocity components in some selected vertical and horizontal planes for diametrically opposed porous plugs at half radii.

predicted to be 0.09 m/s for such cases, this being 10 % less than that for single plug bubbling with the equivalent gas flow rate. The meen speed in axial ($\bar{u}$), radial ($\bar{v}$), and angular ($\bar{w}$) directions were predicted to be 0.068 m/s, 0 020 m/s, and 0.028 m/s, respectively. It can again be seen that the angular momentum of fluid motion increases as the plug's position is moved off the center.

4.2 Mixing Procedures

Using the numerical procedures already outlined, the combined effects of tracer addition point and bubbler location on mixing times were studied mathematically. Figure 3-11 (a) shows the four different locations chosen for tracer input with respect to the plume's eye, for single plug bubbling. Figure 3-11 (b) gives three different locations of tracer input chosen for twin plug bubbling.

Thus, Figure 3-12 provides mixing times predicted for tracer input to a 1/3 scale water model of a 100 tonne ladle with single plug bubbling. The marked squares represent the experimentally measured mixing times for comparison with mathematical predictions. As seen, when the tracer was added exactly into the eye of the plume (Case A), center gas bubbling proved to have the shortest bulk mixing time. This was followed by increases as the bubbler position approached the ladle sidewall. However, since the flow characteristics of real plumes in the gas stirred ladles are turbulent, unstable, and time-dependent, with vertical plume axes that tend to precess, this 'theoretical' experiment proved to be difficult to reproduce in practice.

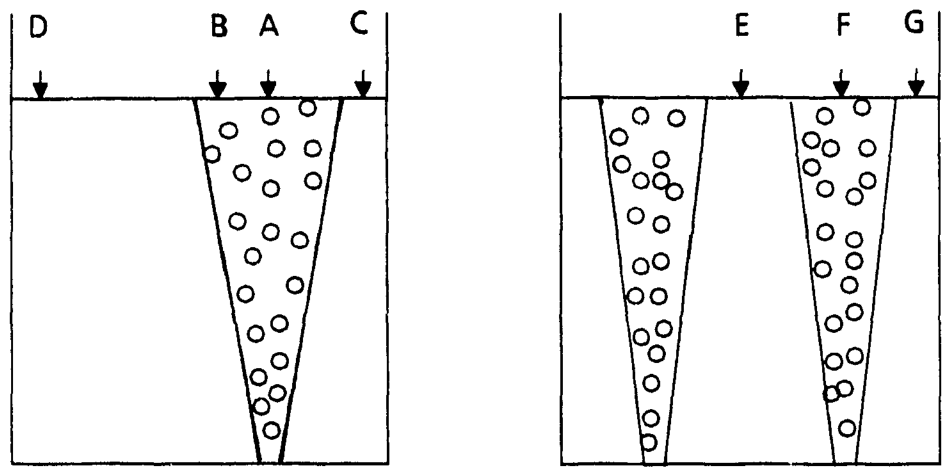

(a) single porous plug (b) twin porous plugs

Figure 3-11 Location of tracer additions with respect to center line of rising gas-liquid plume for (a) single porous plug bubbling and (b) twin porous plug bubbling..

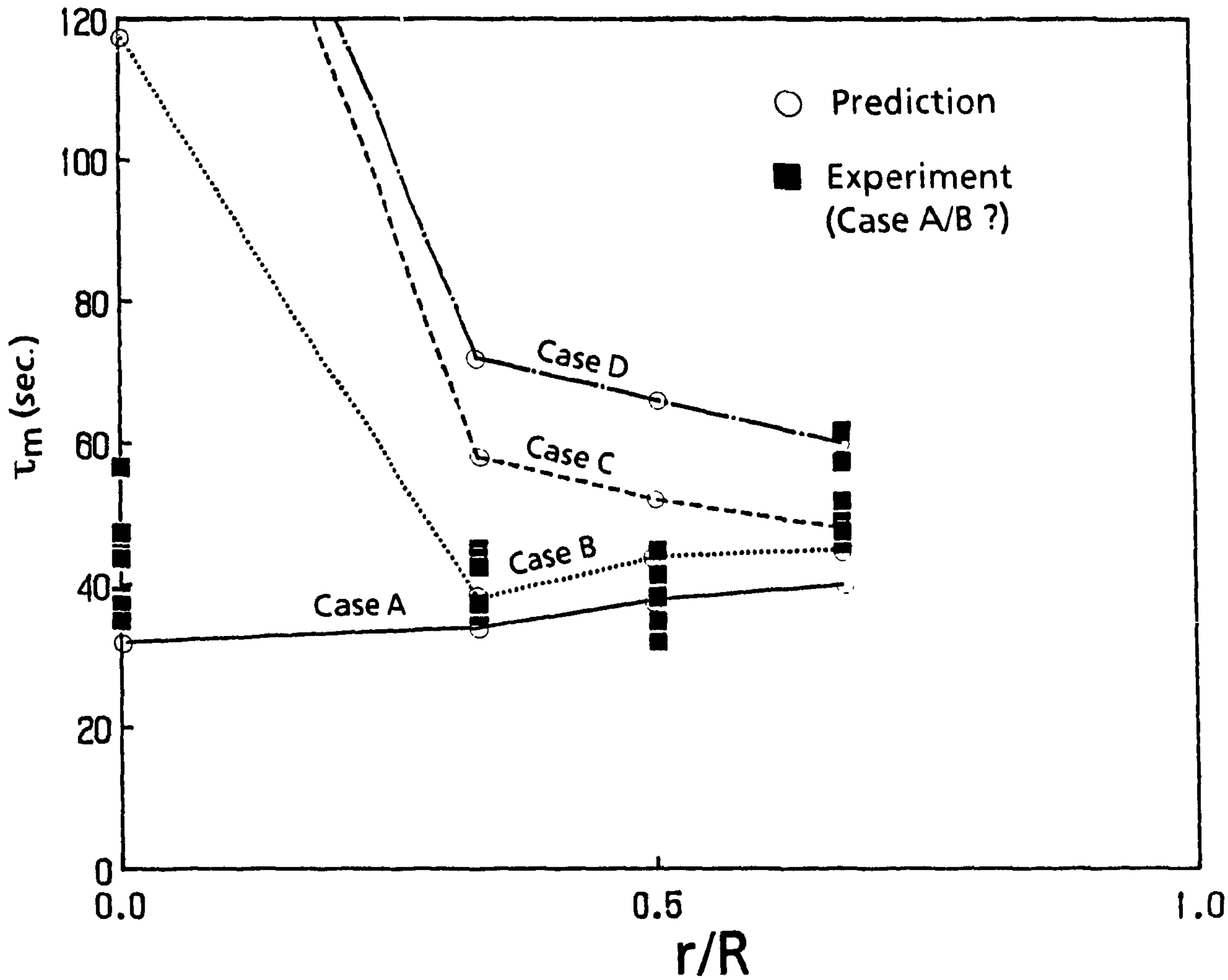

Figure 3-12 Illustration of predicted 95% bulk mixing times in a 1/3 scale water model of a 100 tonne ladle for various plug positions and tracer addition points. (Square marks represent measured mixing times.)

It is more realistic to suppose that the tracer will inevitably be added slightly off-center to a plume's eye (Case B). Predicted mixing times for off-center-plume additions were therefore studied and these exhibit very different characteristics versus center-plume additions. In this case, the 95% bulk mixing times for center bubbling were greatly extended, and moreover an off-plume addition close to a ladle sidewall (Cases C and D) leads to much longer mixing times. For side-wall additions, 95% mixing times for center bubbling proved to be the longest, and decreased significantly as the plug was moved towards the side-wall. Asai et al.[10] and Dobson et al.[21], using physical models, studied mixing behaviour under the conditions of Case C.

As discussed in previous research work[14], mixing of steel in ladles occurs by a combination of both convective transport and turbulent eddy diffusion, both mechanisms contributing in roughly equal proportions. Figures 3-13A and 3-13B illustrate the transient mixing processes for centre bubbling computed for Case A and Case B tracer addition respectively . The shaded region represents the zone wherein 95% bulk mixing times are reached. Since center gas stirring has no angular momentum associated with it, angular mixing can only take place by eddy diffusion processes should the tracer not be added precisely into the eye of the plume. As noted, the consequence of missing the 'bull's eye' leads to tremendous increases in mixing times.

Per contra, as the plug is moved away from the centre towards the side-wall, solute transport by angular momentum increases, yielding faster mixing even though the tracer is injected at the sidewall. Figure 3-14A and B illustrate the transient mixing processes for a plug placed at half radius, when

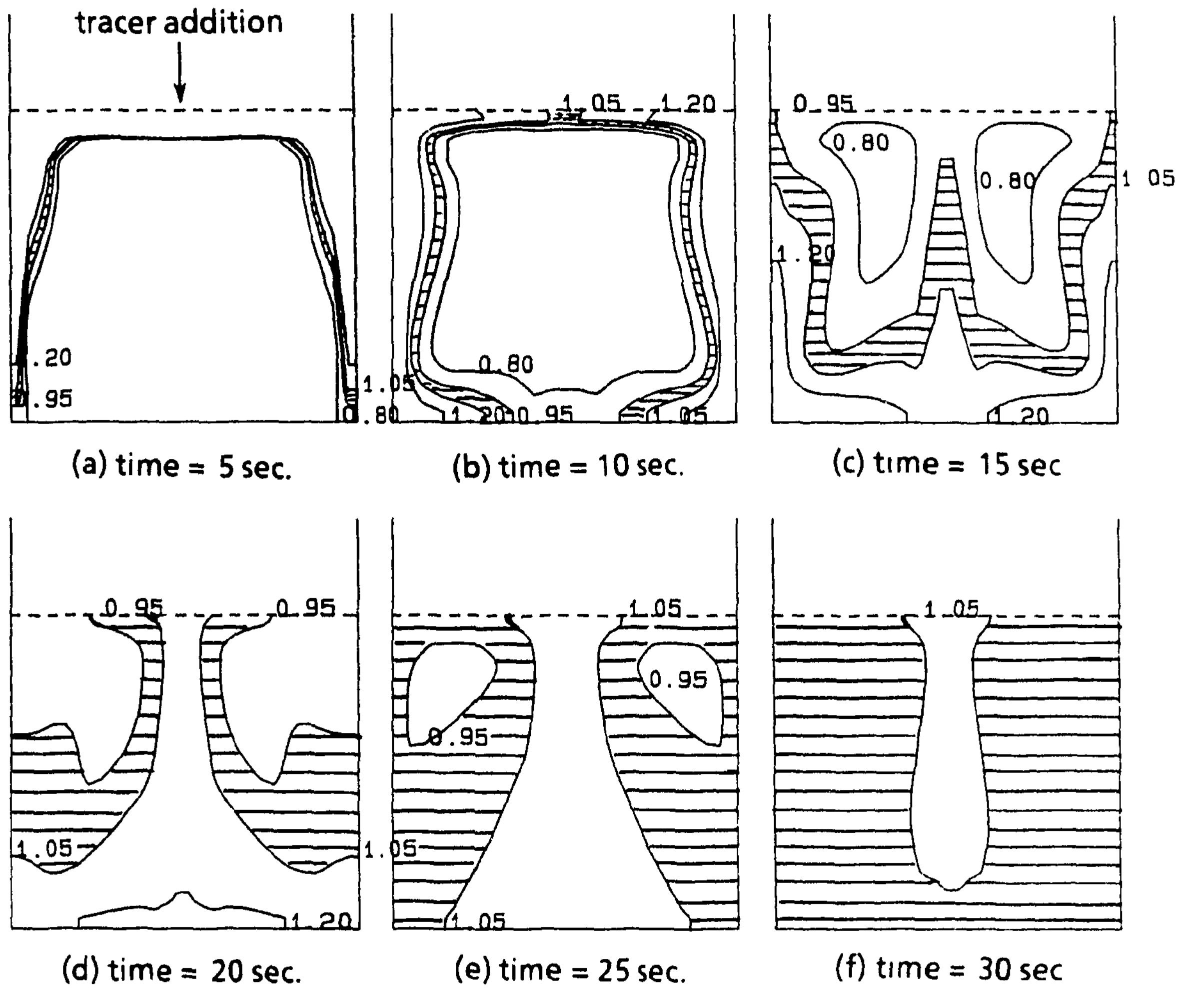

Figure 3-13A Illustration of transients in iso-concentrations following center-plume additions of a tracer, during center gas bubbling. (Case A in Figure 3-11 (a))

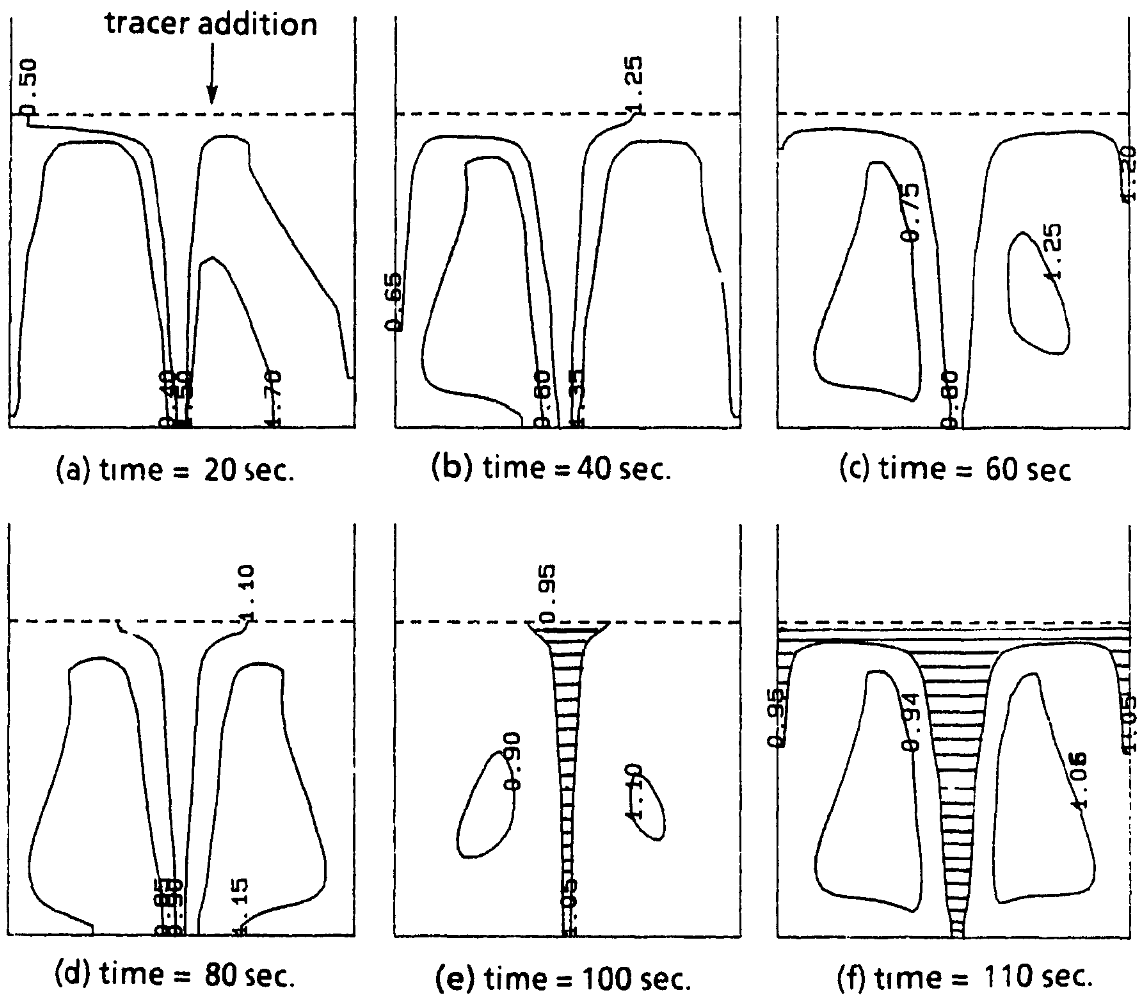

Figure 3-13B Illustration of transients in iso-concentrations following a tracer addition just off-center to the gas/liquid plume, during center gas bubbling. (Case B in Figure 3-11 (a))

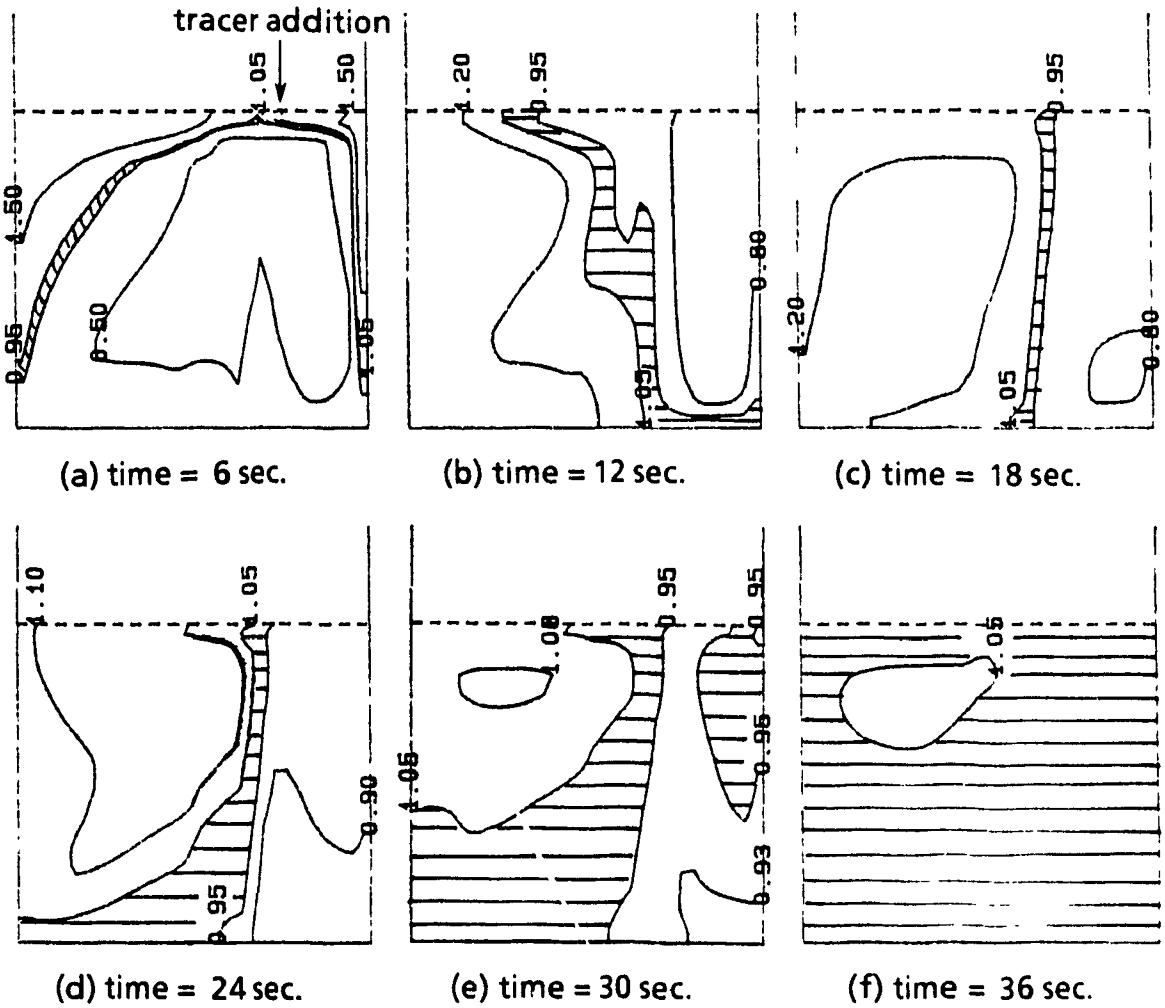

Figure 3-14A Illustration of transients in iso-concentrations following center-plume additions of a tracer, for a off-center porous plug placed at half radius. (Case A in Figure 3-11 (a))

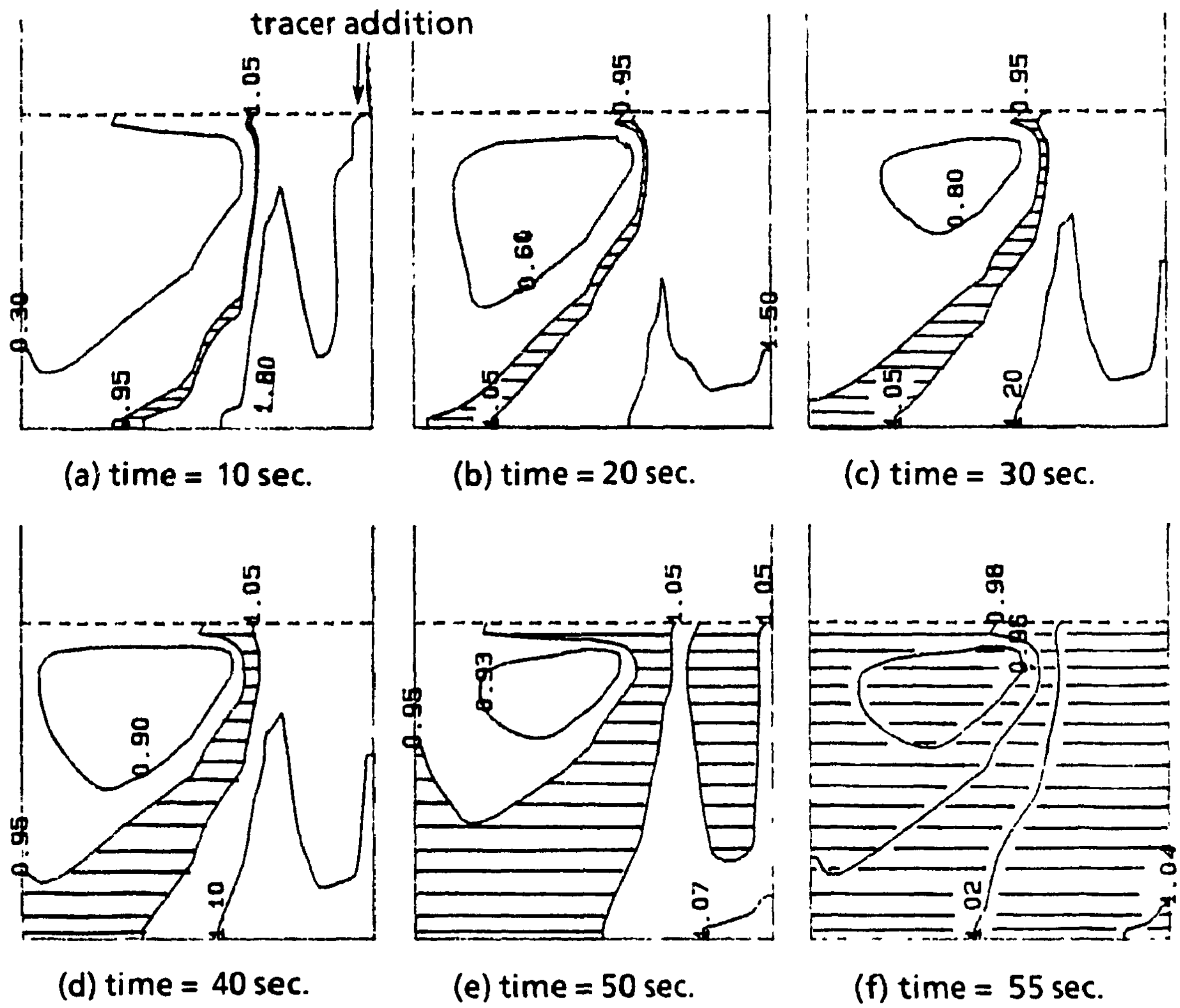

Figure 3-14B Illustration of transients in iso-concentrations following a side-wall tracer addition for half radius plug bubbling. (Case C in Figure 3-11 (a)) tracer was injected into the center-plume (Case A) and into liqiuid at the side-wall (Case C), repectively. As seen, for the center-plume addition, tracer is dispersed rapidly, reaching 95% bulk mixing at the left side and bottom of plume after 24 seconds, and then at the upper right side-wall to plume after 30 seconds. The 95% bulk mixing time was predicted to be 38 seconds for such a case. Dispersion aspects for the side-wall additions was seen to be similar but to take much longer time (55 seconds) for complete 95% bulk mixing.

In summary, since center gas bubbling has no angular momentum, mixing is dominated by eddy diffusion, resulting in delayed mixing times for off-center-plume additions. As the plug is moved away from the center towards the side wall, momentums in the three polar directions become comparable. Owing to concurrent increases in angular momentum, mixing times become relatively insensitive to the tracer addition point. This can be interpreted for the industrial steelmaking ladle process such that off-center gas stirring is relatively insensitive to the location of thermal and chemical segregation in ladle.

Figure 3-15A, B, and C illustrate tracer dispersion behaviour for twinly opposed porous plugs, at half radii for (1) a center-ladle addition (Case E in Figure 3-11), (2) a plume addition (Case F), and (3) a side-wall addition (Case G). Mixing times were predicted to be 38 seconds for Case E, 58 seconds for Case F, and 70 seconds for Case G. It is interesting to note that for the center-ladle addition, 95% bulk mixing levels are first reached in the two plume zones, expanding the mixing area to each side-wall, while for Case F and Case G, it is first reached at the center of the vessel. It can be seen from Figures 3-13, 3-14, and 3-15 that the last mixing point is dependent on the tracer injection point and plug locations.

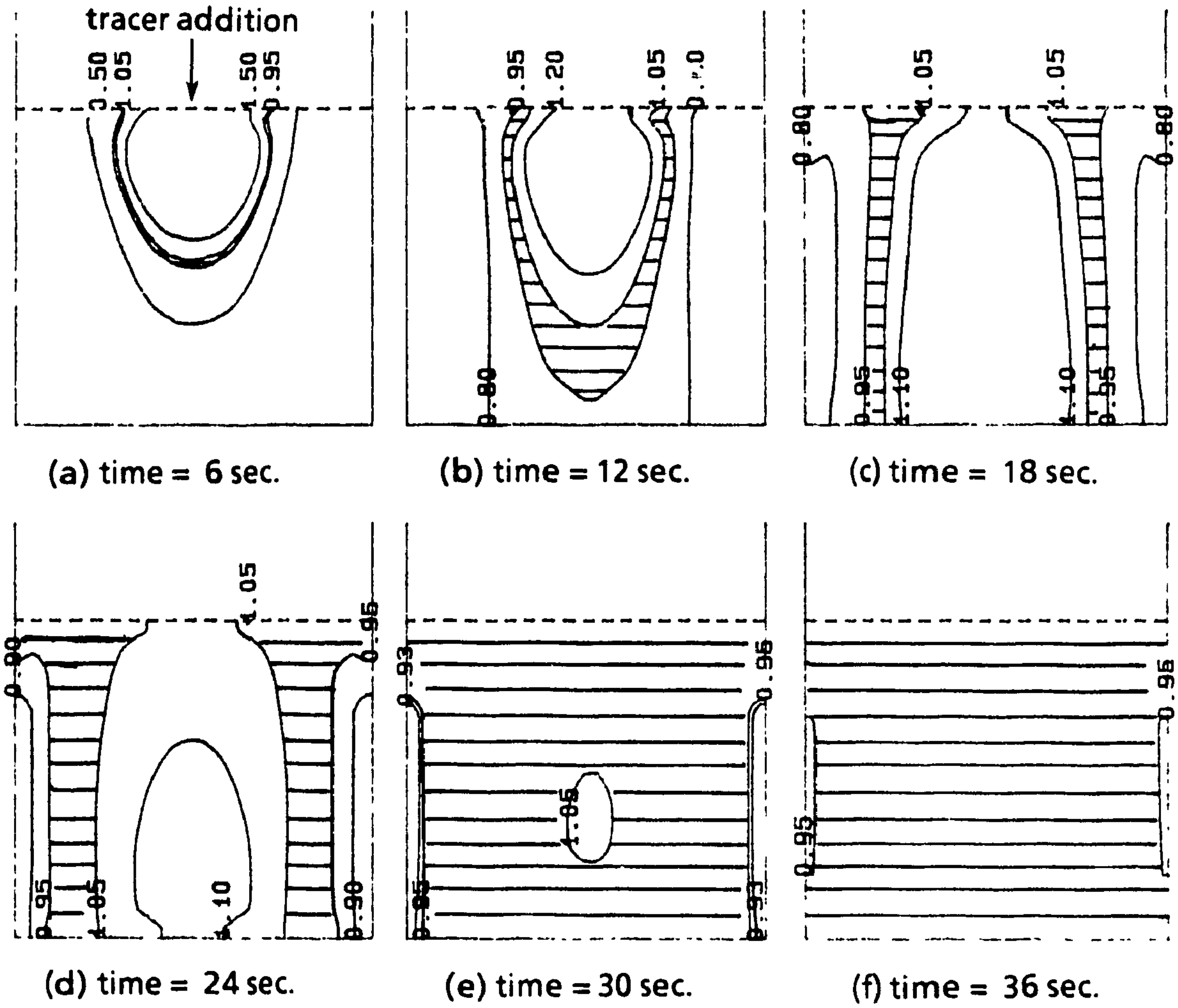

Figure 3-15A Illustration of transients in iso-concentrations following center-tank additions of a tracer, for double porous plug gas bubbling diametrically placed at half radii. (Case E in Figure 3-11 (b))

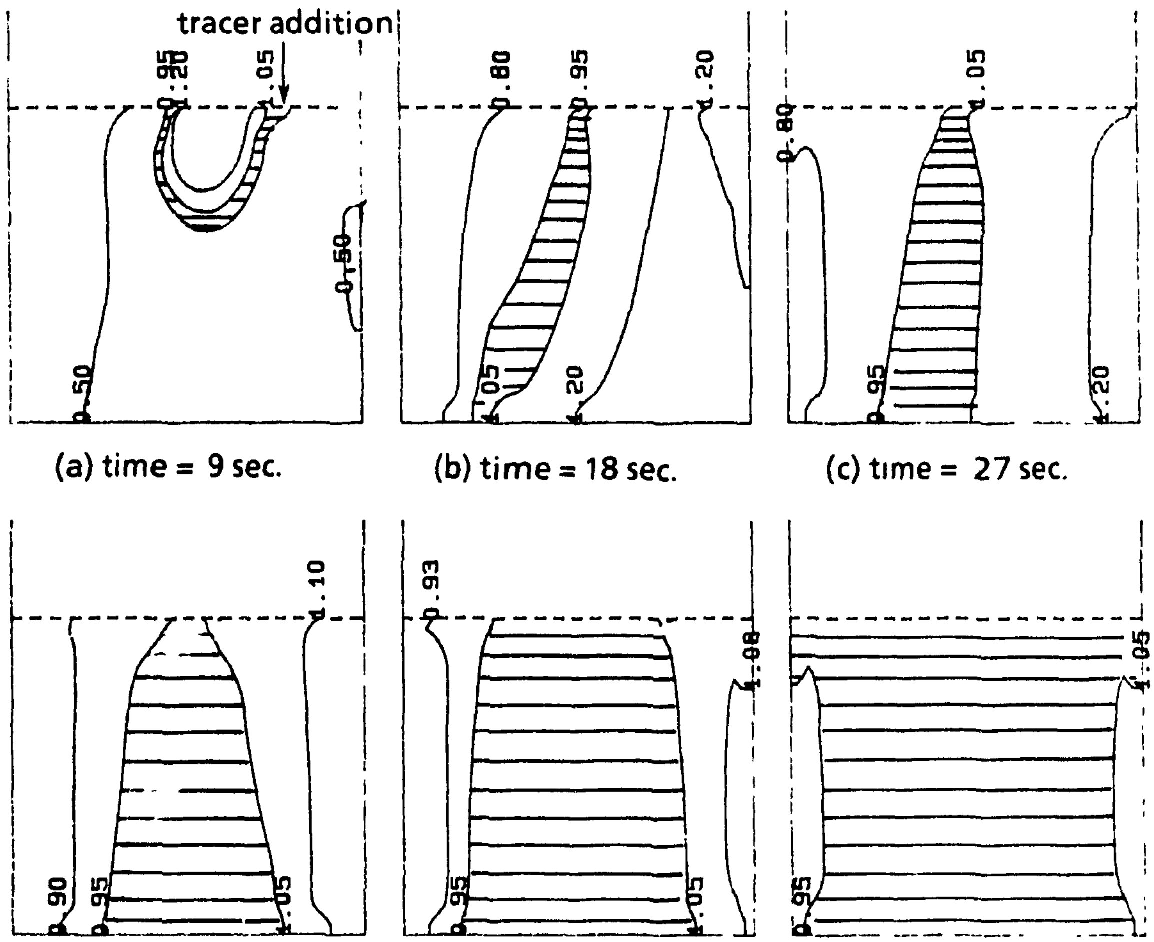

(a) time = 9 sec. (b) time = 18 sec. (c) time = 27 sec.

(d) time = 36 sec. (e) time = 45 sec. (f) time = 54 sec.

Figure 3-15B Illustration of transients in iso-concentrations following a plume addition of a tracer, for double porous plug gas bubbling diametrically placed at half radii. (Case F in Figure 3-11 (b))

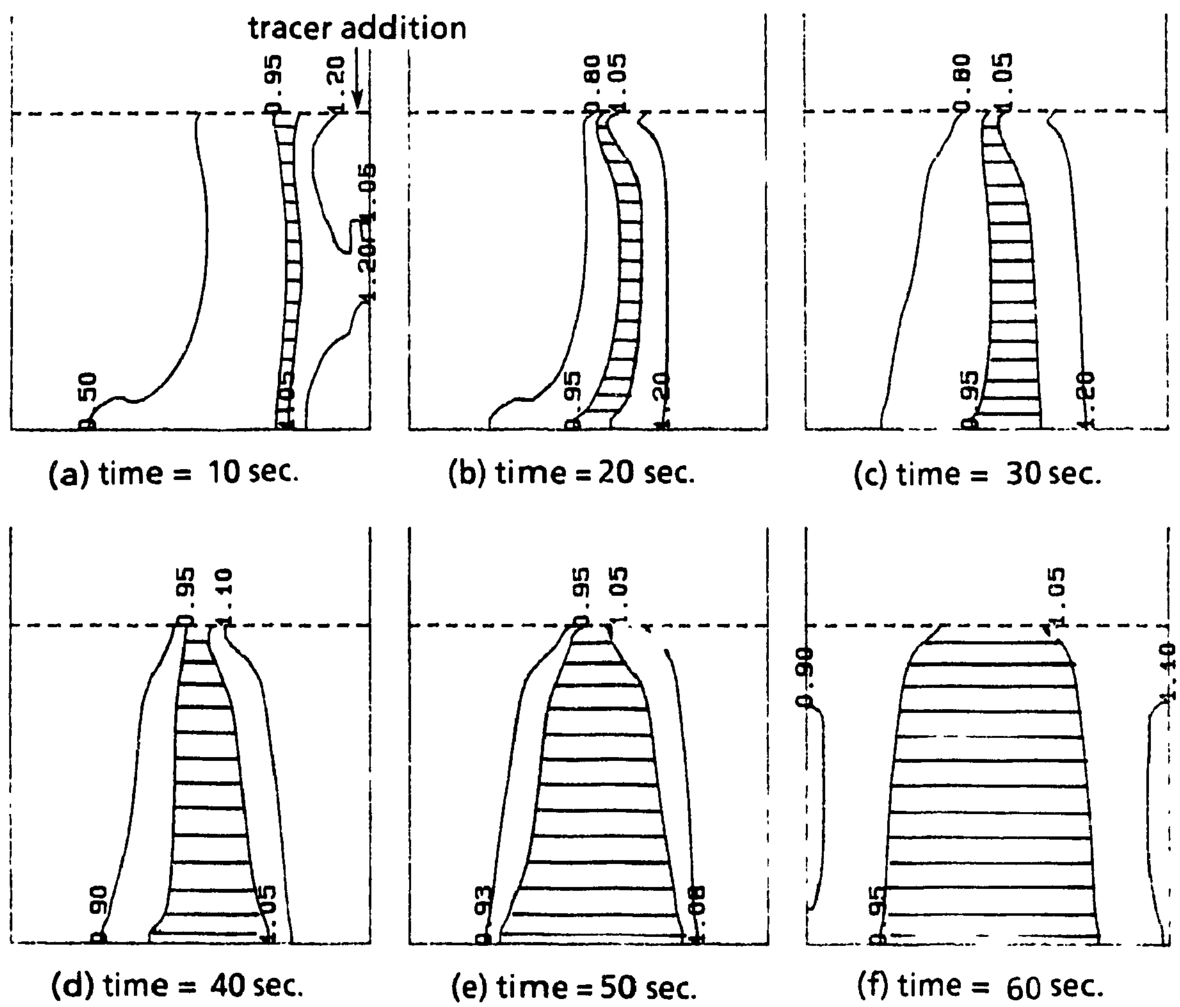

Figure 3-15C Illustration of transients in iso-concentrations following a side-wall addition of a tracer, for double porous plug gas bubbling diametrically placed at half radii. (Case G in Figure 3-11 (b))

4.3 Plume Distortion and Wall Effects

The results of the computations just described provide a convincing argument for mixing times becoming shorter as the plug is moved away from the ladle's center. However, since slippage and wall friction effects were not taken into account in the present computational model for plugs located near the side-wall, the experimental observation that mixing at 2/3R was again somewhat delayed could not be properly predicted.

Figure 3-16 illustrates pictorially the characteristics of a single plume rising through water, for plugs set at the ladle's center, one third, one half and two third's radii, respectively One should note that the flow field can distort the plume so as to not rise vertically, this being a function of cross-flows within the ladle

For a plug located at two thirds radius, its associated plume is distorted towards the sidewall, resulting in contact of the plume with the sidewall This might cause a part of the buoyancy force of the bubbles to be lost by slippage, together with an increase in drag force (shear stress) up the side-wall Furthermore, the large shear stress on the wall will increase the potential for hydrodynamic erosion of the ladle's refractories. However, plume distortions were not observed with weak gas bubbling (i e <10 liters/min in this water model system)

An alternative, but more computationally demanding procedure, by Boysan et al [8], can predict those conditions for which the plume is 'bent' inwards, or outwards, as a result of interactions with the bulk flow fields. There, a flow field is first deduced using the Eulerian scheme Successive bubbles are then introduced into the system, using a Lagrangian framework

(a) center

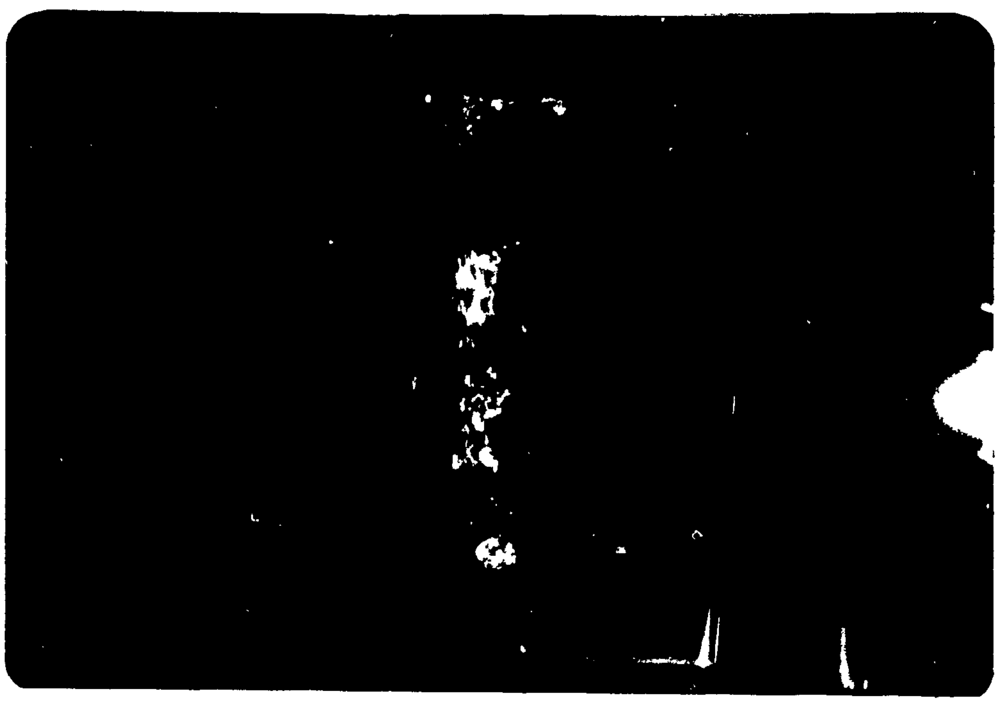

(b) 1/3 R

Figure 3-16 Photographs of model ladle illustrating the distortion of the plume during single plug bubbling at (a) center and (b) 1/3 R.

(c) 1/2 R

(d) 2/3 R

Figure 3-16 Photographs of model ladle illustrating the distortion of the plume during single plug bubbling at (c) 1/2 R and (b) 2/3 R.

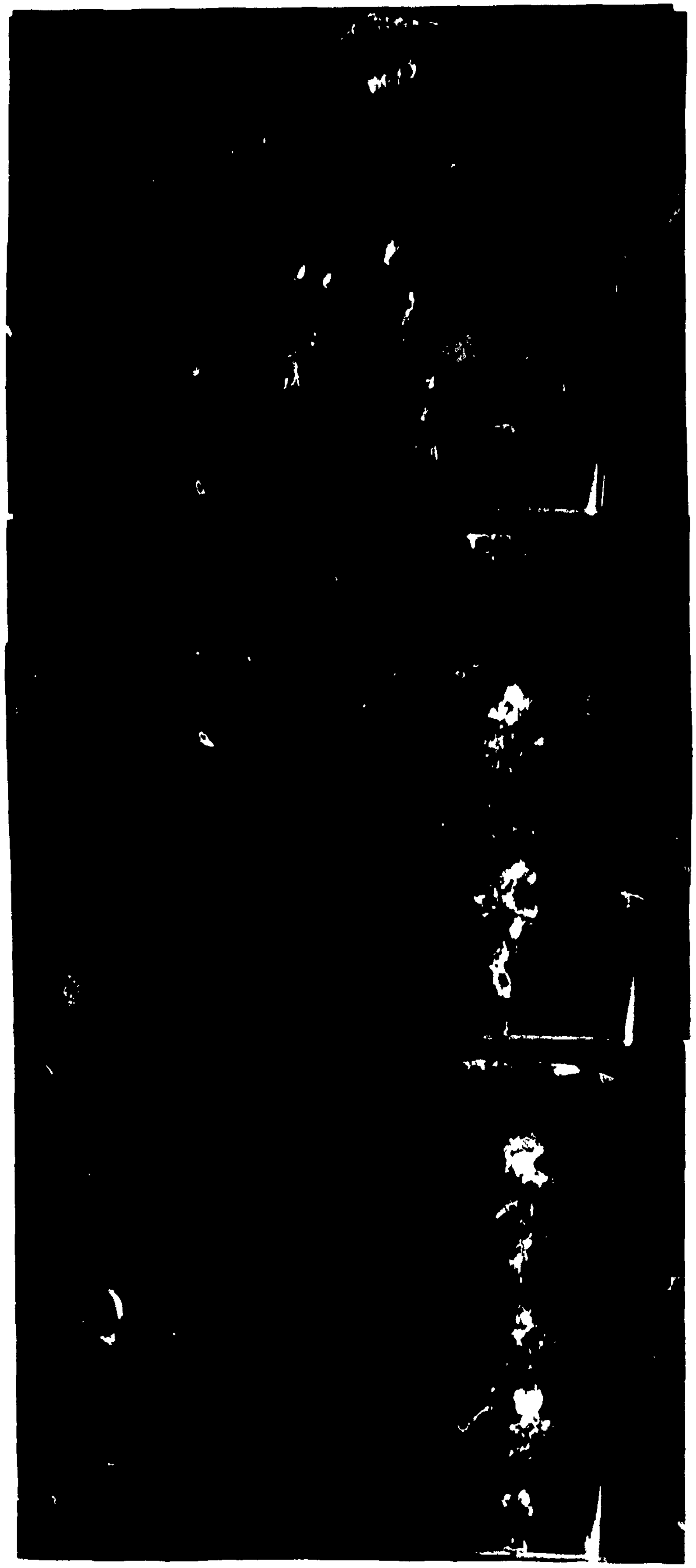

(a) 1/3R

(b) 1/2R

(c) 2/3R

Figure 3-17 Photographs of model ladle illustrating the distortion of the plume during double plug bubbling.

This allows spatial variations in plume voidage to be computed as a function of bulk flow patterns. Through successive iterations between Eulerian and Lagrangian frames of reference therefore, plume geometries can be deduced as part of the numerical solution procedures.

Figure 3-17 shows plume interactions for two plug arrangements. As seen, when two plugs are closely placed, the plumes coalesce, diminishing the effect of double gas bubbling. Similarly, when two plugs are located near the side-walls, this will increase wall shear stresses and the potential of hydrodynamic erosion of the refractories.

It is therefore concluded that the placement of porous plugs at half radius is an optimum location. There, the portion of momentum in each direction is of the same order and wall effects are minimal.

4.4 Industrial Applications

Proper stirring of the liquid steel is very important during steelmaking processes. For instance, there are metallurgical reactions which require strong mixing of metal and slag. Stirring for decarburization, desulfurization and dephosphorization belong to this case. On the other hand, stirring for deoxidation, alloy homogenization, or inclusion removal require gentle mixing at the metal/slag interface and maintenance of an unbroken slag layer.

For gas stirring in the teeming ladle, the need for gentle mixing can be intensified due to improper control of slag carryover The presence of a liquid slag layer on the metal surface can cause significant delay in mixing times since the breakage and deformation of the slag layer consumes part of the stirring input energy. Moreover, strong turbulent flows at the slag/metal interface activates interfacial mass transfer and slag droplet entrainment., leading to steel reoxidation by entrained slag droplets, and oxygen and nitrogen pick-up from the free metal surface exposed at the atmosphere in the "plume's eye".

The critical flow rate for slag/metal mixing expressed by Equation 1-5 could be used as a criterion for the determination of gentle stirring. The analysis indicates the flow rate should be quite low, typically 100-150liters/min for a 150 tonne ladle (22). The critical flow rate for slag/metal mixing is mainly related to slag layer break-up and slag droplet entrainment caused by strong up-rising momentum energy of the plume. Therefore, if high flow rates combined with gentle but fast mixing is needed, multi-plug gas bubbling could be appropriate as a technical solution, since it would distribute input stirring energy over the bath with a low plume velocity from each bubbler.

Chapter 5

Conclusions

Mixing phenomena in steelmaking ladles have been studied using mathematical and physical models (water modelling) for an one-third scale of a 100 ton ladle. It was concluded that :

1. Flow patterns are strongly dependent on the number and positions of the bubblers. As the bubblers are moved off-center, angular momenta increase, reducing mixing times significantly.

2. Measured mixing times are sensitive to monitoring point, as well as to bubbler location.

3. When a porous plug bubbler is close to a ladle side-wall, flows will distort the plume towards that sidewall, increasing drag force on the wall. This increases the mixing time needed for alloy homogenisation and increases the potential for hydrodynamic erosion of the ladle's refractories.

4. For double porous plug bubbling, more gentle flow and equivalent mixing times versus single off-center bubbling were predicted using equal net flows of gas into the ladle.

5. A mid-radius placement of a porous plug represents an optimum location for single plug bubbling, while diametrically opposed, mid-radius placement of bubblers is recommended for double plug bubbling.

6. The last point within the bulk of the liquid to become mixed depends on the tracer addition point and plug arrangements.

7. The pseudo-one-phase model used in the present study has limited application, since it cannot take into account plume distortion/ coalescence and wall slippage/friction effects. In order to account for such phenomena properly, a two-phase model would seem to be needed.

REFERENCES

1) J. Szekely, H.J. Wang and K.M. Kiser, Met. Trans. B, Vol 7B, June 1976, pp287-295.

2) T. Deb Roy and A.K. Majumdar, J. of Metals, November 1981, pp42-47.

3) J.H. Grevet, J. Szekely and N. El-Kaddah, Int. J. Heat Mass Transfer, Vol. 25, No. 4, 1982, pp487-497.

4) Y. Sahai and R.I.L. Guthrie, Met. Trans. Vol. 13B, No. 2, 1982, pp 193-202.

5) Y. Sahai and R.I.L. Guthrie, Met. Trans. Vol. 13B, No. 2, 1982, pp. 203-211.

6) M. Salcudean, C.H. Low, A. Hurda and R.I.L. Guthrie, Chem. Eng. Comn., Vol. 21, 1982, pp89-103.

7) M. Salcudean, K.Y.M. Lai, R.I.L. Guthrie, Canadian J. of Chem. Eng , Vol. 63, February, 1985, pp 51-61.

8) F. Boysan and S.T. Johansen, 'Mathematical Modelling of Gas Stirred Reactor', Int'l Seminar on Refining and Alloying of Liquid Aluminium and Ferroalloys, Ed, T.A. Engh, S. Lyng, H.A. Oye, N.I.T Trondheim, 1985, Aluminum-Verlag, Dusseldorf.

9) K. Nakanishi, T. Fujii and J. Szekely, Ironmaking and Steelmaking, 1975, No. 3, pp. 193-197.

10) S. Asai, T. Okamoto, J.C. He and I. Muchi, Trans. ISIJ, Vol. 23, 1983, pp. 43-50.

11) M. Sano and K. Mori, Trans. ISIJ, Vol. 23, 1983, pp169-175.

12) O. Haida, T. Emı, S. Yamada and F. Sudo, Scaninject II, #20, MEFOS and Jernkontoret, June 1980, Lulea, Sweden.

13) S. Kim, Ph.D. Thesis, Dept. of Metallurgical Engineering and Materials Science, Carnegie-Mellon University, USA, 1987.

14) D. Mazumdar, Ph.D. Thesis, Department of Mining and Metallurgical Egıneering, McGill University, Montreal, Canada, 1985.

15) T. Marujama, N. Kamishıma and T. Mizushina, J. Chem. Eng. Japan, Vol. 17, No. 2, 1984, pp120-126.

16) W.P. Jones and B.E. Launder, Int. J. Heat Mass Tranfer, Vol.15, 1972, pp301-314.

17) B.E. Launder and D.B. Spalding, Computer a Methods in Applied Mechanics and Engineering, Vol. 3, 1974, pp. 269 .

18) S.V. Patankar and D.B. Spalding, International Journal of Heat and Mass Transfer, Vol. 15, 1972, pp. 1787.

19) D.B. Spalding, Heat Transfer in Turbulent Buoyant Convection, Eds. D.B. Spalding and N. Afgan, Hemisphere Publishing Corporation, New York, 1977, pp. 569.

20) D. Mazumdar and R.I.L. Guthrie, Met. Trans. B., Vol. 16B, March 1985, pp. 83-90.

21) C.J. Dobson and M. Robertson, 'Model Studies of Gas Stirred Ladles', Internal B.H.P. Report, C.R.L. Australia, September 1986.

22) R.J. Fruehan, Int. Symp. on Ladle Steelmaking and Furnaces, CIM ,, Montreal, Canada, August. 1988, pp92-110.

PART IV

PREDICTION OF FLUID FLOW, INCLUSION SEPARATION AND HEAT TRANSFER IN TUNDISH PROCESSING OPERATIONS

Chapter 1

Introduction

Tundishes act as distributors of liquid metal between the ladle and the molds of continuous casting machines. They can also act as removal tanks for non-metallic inclusions within liquid steel. To study such matters, detailed velocity and turbulence fields are required, these being specific to a given tundish design, metal flowrate, etc..

There have, in recent years, been a number of studies on fluid flow and/or inclusion separation behaviour for tundish arrangements, using physical (water) models[1-6] and/or mathematical models[7-12]

Using a full scale water model tundish, Kemeney et al[1] carried out a simple fluid dynamic analysis of tundish flows with the aim of improving steel cleanness by maximising fluid retention times They observed that the flow patterns were improved using combinations of dams and weirs and that the minimum retention time could be increased. Tanaka[5] developed a probe based on a Coulter counter technique[13] to detect non-metallic inclusions in aqueous system. Nakajima[6] extended such a probe for both water and molten steel systems. Both authors analysed the separation behaviour of inclusion particles in terms of a 'tank reactor' model.

Lai et al[8] carried out both computational and physical modelling of three-dimensional fluid flow in a symmetric twin strand tundish, and compared one to the other El-Kaddah and Szekely[7] also numerically predicted three dimensional tundish fluid flows and the retention time distribution (RTD) curves with and without flow control devices (weir/dam arrangements), using the commercial PHOENICS code. Y. He and Sahai[9] performed a computation of fluid flows in tundishes under the condition of sloping sidewalls, comparing the effect of these with vertical walls in terms of flow patterns and RTD curves. Tacke and Ludwig[11] solved a transport equation for particles, taking into account their specific buoyancy, convection and turbulent dispersion, again using the PHOENICS code. There, particle concentration fields and the percentage of particles removed were calculated. However, none of the authors seem to have recognised the fundamental importance of natural convection on flows and inclusion behaviour in tundishes. Similarly, the application of mathematical models to tundish design with respect to geometry of tundish, location of flow control devices and their numbers, etc. has not yet been tackled.

Most major steel companies study the change of fluid flow and inclusion particle behaviour with, or without, flow control devices using isothermal physical modelling in large plexiglass water models. Flow visualization with dye, residence time distribution studies and detection of inclusion particles in such physical models provide useful information. Nevertheless, such full-scale physical modelling often requires expensive equipment and significant time and effort.

On the other hand, computations of three-dimensional fluid flow are becoming less expensive and are widely applicable to tundish performance. These can provide detailed flow information, enabling one to predict inclusion flotation together with temperature distributions within tundishes. The prediction of such phenomena in a tundish vessel by mathematical modelling is useful for determining the best design of vessel with respect to size, shape and the placement of flow control devices (e.g weir/dam arrangements, baffles, etc.) for a given set of operating parameters (e.g. metal flow rate, input temperature, etc.). However their validity have not yet been clearly demonstrated through physical models, nor from actual plant data. It is therefore necessary that such predictions continue to be paralleled by proper experiments, and the results compared with each other.

In the present experimental work, particle removal rates could be studied thanks to the development of the novel E.S Z (Electric Sensing Zone) system(14). This was capable of detecting inclusions on-line and in-situ, and provided number densities and size distributions of inclusions within the fluid A full scale water model of a multi-purpose tundish (i.e. single strand for slab casting and double strands for bloom casting), at Stelco Research Centre, Burlington, Ontario was therefore used to test experimental data against computations. It will be described in Chapter 2

In order to predict mathematically inclusion separation, two different approaches are possible, these being the description of the tundish in terms of reactor theory (i.e. tank reactor model), the other through a full computational description of fluid flow and inclusion movement through numerical solutions of continuity, turbulent Navier-Stokes equation and mass conservation equation for fine particles (i.e. differential equation model). Tank reactor models will be discussed in Chapter3, the differential equation model being fully described in Chapter 4 and Chapter 5.

The purpose of the present study was to validate the mathematical and computational methods developed, and to conceive, design, and evaluate the efficiency, of various configurations of flow control devices (i.e. weir/dam combinations) so that steelmaking tundishes might be optimized in terms of steel cleanness, temperature distribution and product uniformity. In order to perform such a study, Stelco's Hilton Work tundish, Canada (single or double port tundish), Dofasco's Hamilton Work tundish, Canada (axisymmetric twin strand tundish), and BHP's Port Kembla Work tundish No.1 (trough-shaped twin port tundish) and No.2 (wedge-shaped single port tundish) in Australia were taken into account for computations. Their configurations are schematically illustrated in Figure 4-1A~D, while Table 4-1 provides the key dimensions and capacities of tundish vessels considered.

Table 4-1 The physical characteristics of tundishes

	Volume (m^3)	Weight (tons)	Thruput (tons/min)	Res. Time (min)	U_{plug} (mm/s)
Stelco (single slab)	5 0	35	3	12.0	7 2
Stelco (double bloom)	5.0	35	2 (1 0 each)	17.5	5 8
Dofasco (twin slab)	10.3	72	9 (4 5 each)	8.0	11.2
B H.P. #1 (twin slab)	6.0	42	3 (1 5 each)	14 0	8.1
B.H.P. #2 (single slab)	7.3	50	4	12.5	5.5

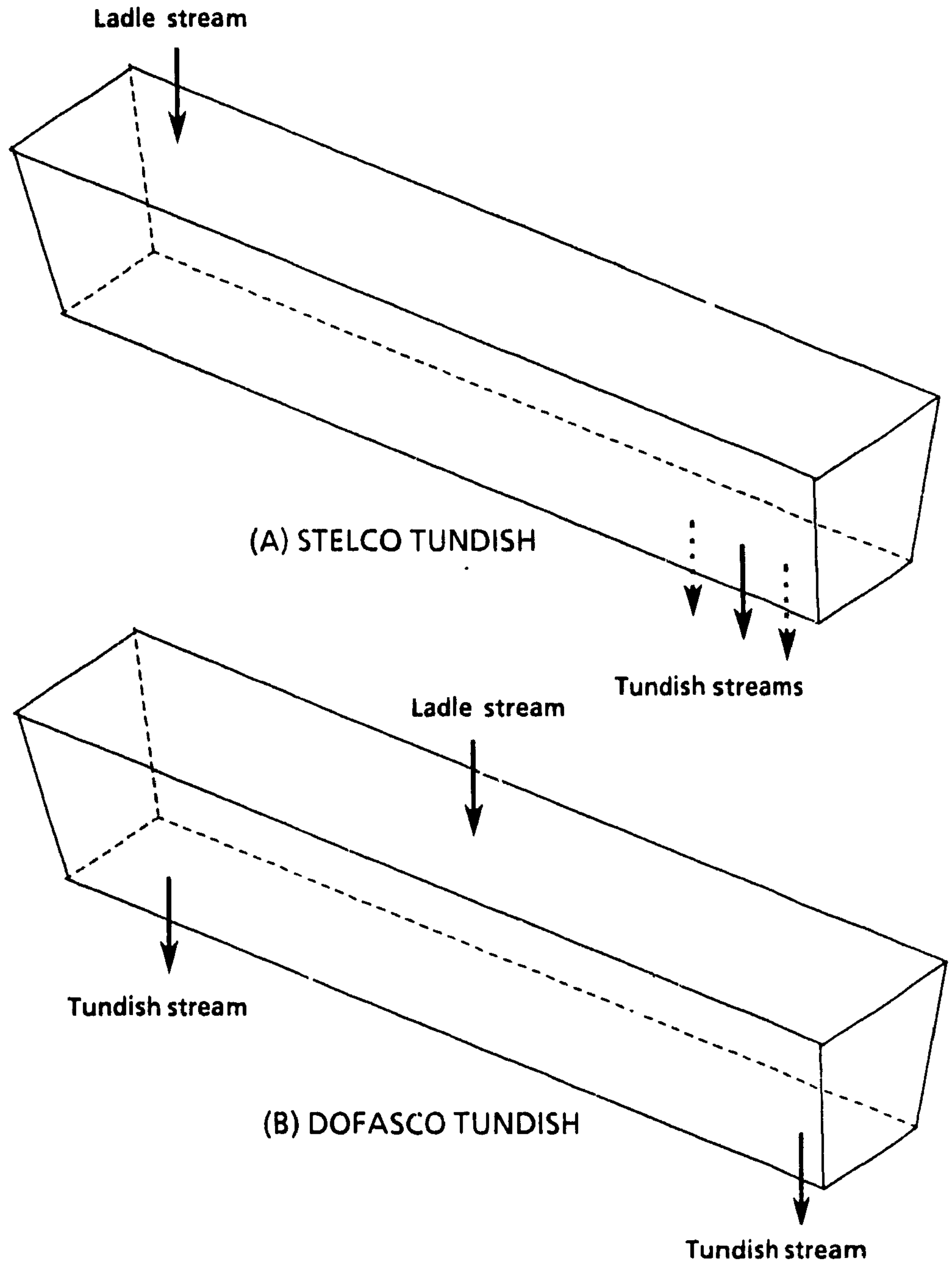

Figure 4-1 Schematics of (A) Stelco's Hilton Work Tundish. (B) Dofasco's Hamilton Work tundish.

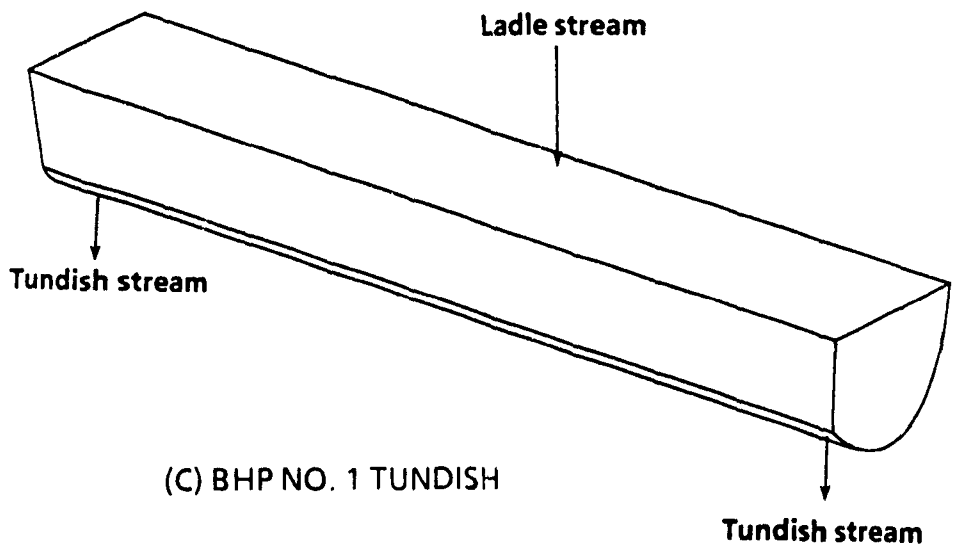

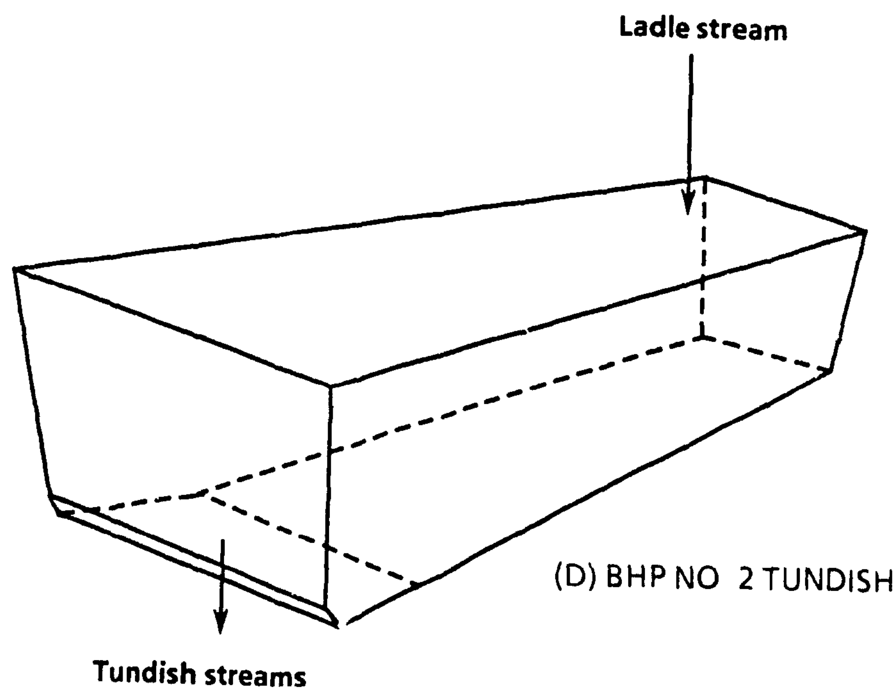

Figure 4-1 Schematics of (C) BHP's Port Kembla tundish No. 1 (D) BHP's Port Kembla tundish No 2.

Chapter 2

Experiment

2.1 Experimental Equipment

2.1.1 Full-scale water model system

The full-scale model tundish at Stelco's Hilton Works was constructed of transparent plexiglass, its walls being outwardly inclined at an angle of 10 degrees to the vertical. Filled to a height of 1.1 m, the tundish measures 5 19 m in length, 0 68 m wide at the bottom and 1 07 m at the free surface. A photograph of model tundish used is shown in Figure 4-2 Then, Figure 4-3 illustrates the experimental arrangement used for inclusion detection studies. It consisted of the full-scale plexiglass tundish, a ladle, and slurry injection system supplying particles (inclusions) at a constant rate of feeding, together with the novel E S.Z system for their detection and counting, and a personal computer to record the data sets acquired, and to provide particle frequency versus size distribution curves.

For simulating actual inclusions in molten steel, hollow glass microspheres, with an appropriate number density of 10^8 particles/m^3, over the size range 20-110 µm, were fed continuously at a feeding rate of 0 5 liters/min into the tundish through the inlet shroud The specific density of the glass microspheres was 295 kg/m3. The important parameters and properties of this full scale model tundish are summarized in Table 4-2.

Table 4-2 Important parameters and properties of model and prototype.

		Model	Prototype
Geometry	Tundish Length	5.19m	5.19m
	Tundish Depth	1.10m	1.10m
	Bottom Width	0.68m	0.68m
	Surface Width	1.07m	1.07m
Fluid Properties	Liquid	Water	Steel
	Temperature	15°C	1580°C
	Density	1000 Kg/m3	7000 kg/m3
	Viscosity	1.14×10^{-3} kg/m3	6.7×10^{-3} kg/m s
	Volumetric Flowrate	6.9×10^{-3} m3/s	6.9×10^{-3} m3/s
Inclusion Properties	Inclusions	Glass microspheres	Al_2O_3 and/or SiO_2
	Size Range	20~110μm	-
	Density	295 kg/m3	≈3000 kg/m3

Figure 4-2 A photograph of a full-scale water model tundish at Stelco's Hilton Work.

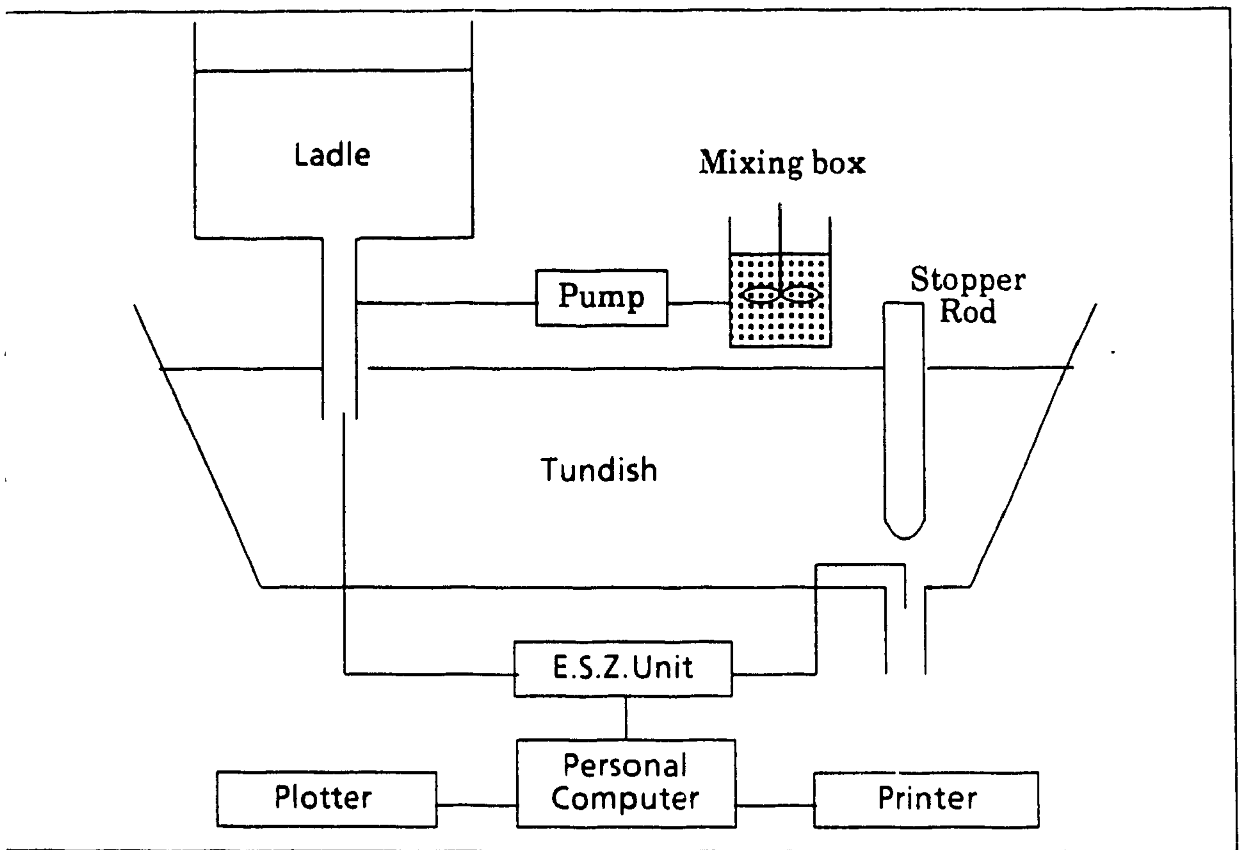

Figure 4-3 Schematic diagram of experimental arrangement.

2.1.2 Principle of E.S.Z. technique

It is appropriate to briefly describe the principle, illustrated in Figure 4-4, of particle detection by the Electric Sensing Zone (E.S.Z) method, which began with the invention of *Coulter* counters(21). When small non-conducting particles pass through an electrically insulated orifice, the electrical resistance of a fluid electrolyte flowing through this orifice increases in direct proportion to a particle's volume. Voltage pulses generated in the presence of an electrical current can then be measured, and then both the number and size of particles counted.

The signal produced consists of a steady voltage baseline with a bell shaped transient related to a particle's passage through the Electric Sensing Zone. The change in resistance, ΔR, caused by the introduction of a non-conducting particle into an orifice is given by DeBlois(24).

$$\Delta R = \frac{4\rho d^3}{\pi D^4} F\left(\frac{d}{D}\right) \tag{4-1}$$

where ρ is the fluid's electrical resistivity, d is the particle diameter, D is the orifice diameter and $F(d/D)$ is a geometric correction factor It has been proposed by DeBlois that this correction factor be expressed as :

$$F\left(\frac{d}{D}\right) = \left[1 - 0.8\left(\frac{d}{D}\right)^3\right]^{-1} \tag{4-2}$$

As most of the time only particles smaller than 40 % of the orifice diameter can be analysed without frequent orifice blockage, the error involved in ignoring this correction factors is, in the worst case, in the order of

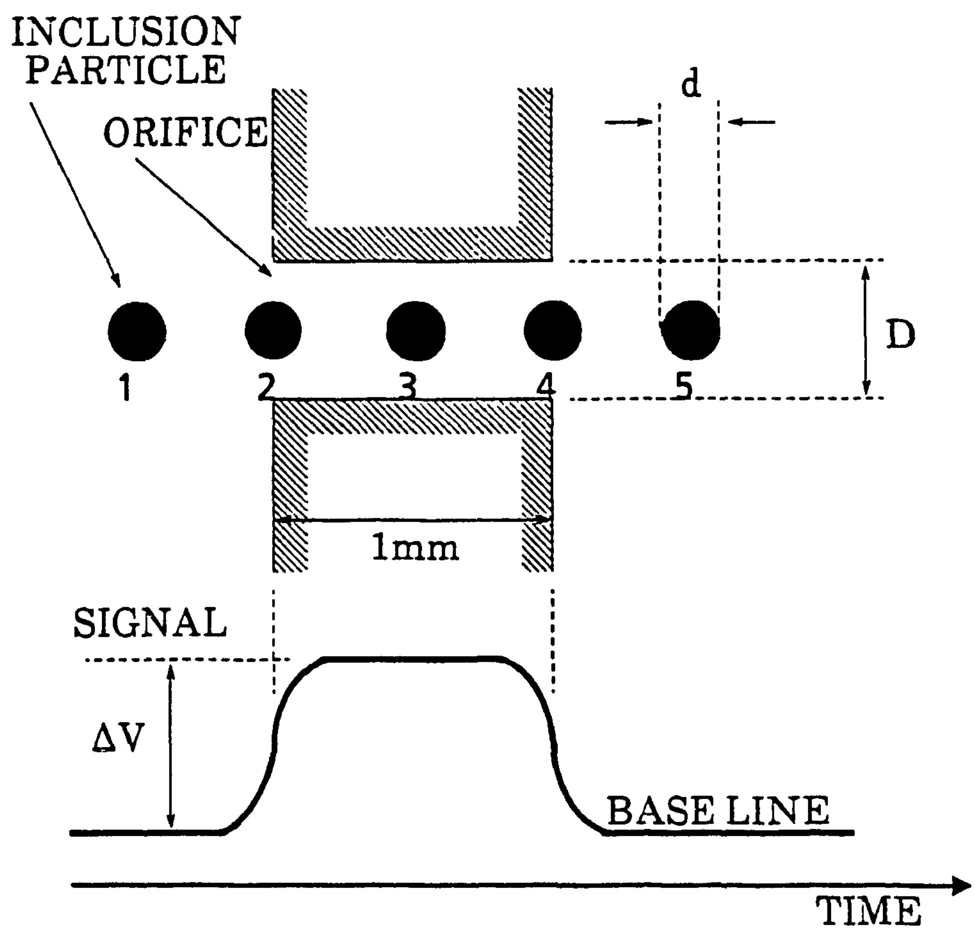

Figure 4-4 Principle of particle detection by the Electric Sensing Zone (E.S.Z) technique

5%. Consequently, *F(d/D)* is often taken as unity This method was adapted to aqueous systems[5], non-ferrous metallic melts[22], and is in the development stage for liquid steel[6,23] at McGill University.

2.1.3 <u>E.S.Z device</u>

The E.S.Z. device itself is shown schematically in Figure 4-5. It consists of a glass probe for the sampling, a current feeding circuit and signal processing analysis equipment. A high pass filter (HPF) removes the DC content of the signal taken at R_b and is first linearly amplified to bring the signal amplitude to a suitable level and then logarithmically amplified to increase detection efficiency of small particles. A peak detector device recognises pulses, triggers notify the pulse height analyzer (PHA) to measure, sort, and count them, thereby providing particle size distribution data A micro-computer, connected to the PHA, is used for data acquisition control and for storage

Taking the difference of the potentials across R_b between the case of no particle within the ESZ (resistivity of the orifice = $R_{orifice}$) and that when a particle is present (resistivity of orifice = $R_{orifice} + \Delta R$) and noting that:

$$\Delta R << (R_b + R_{orifice})$$

it can easily be shown that the variation of potential at R_b relative to a change in orifice resistivity is given by[6] :

$$\Delta V = \frac{R_b}{R_{orifice} + R_b} I.\Delta R \qquad (4\text{-}3)$$

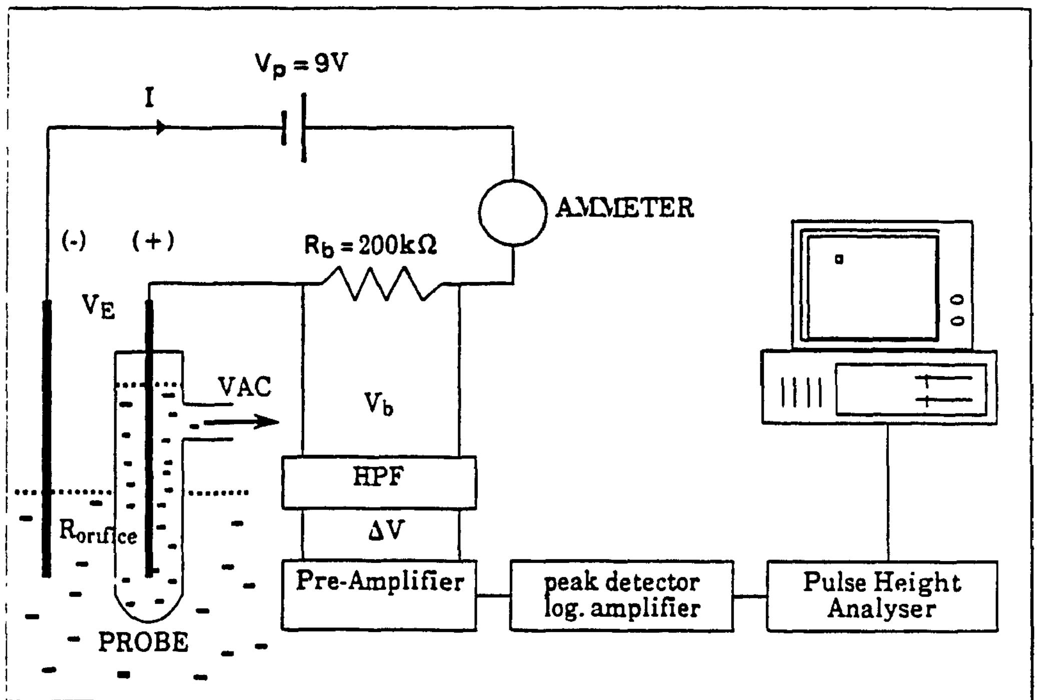

Figure 4-5 Schematic diagram of the E.S.Z. system for aqueous systems.

where R_b is the ballast resistance at which the potential is taken, $R_{orifice}$ is the resistivity of the E.S.Z. with no present particle, I is the current through the orifice, while ΔR is given by Equation 4-1

The glass probes located at the inlet and outlet nozzles are shown in Figure 4-6.The probes were shielded with a stainless steel flexible hose in order to eliminate environmental noise which can 'drown' signals deriving from particles. The probe readily contains a smooth orifice, which is exchangable. In the present study, sensing zone orifices of 480 µm diameter were used.

A photograph of experimental arrangements for the detection of the present study is provided in Figure 4-7 (a).There, an oscilloscope, pre-amplifier, swich changer, logarithmic amplifier, multi-channel analyser and personal computer are shown in the order of the left to the right. Figure 4-7 (b) provides particularly the signal processing analysis equipment.

The system operates as follows: the voltage difference between the two electrodes is carried to an oscilloscope (Tektronics #5223), which allows one to observe electrical signals (i e. voltage pulses) and also serves as a pre-amplifier. Figure 4-8 shows the typical pulses observed in the oscilloscope The pre-amplified signals are then carried to a logarithmic amplifier (Tracer-Northern #TN1246), which is used as a peak detector The pulse height analyzer is a multi-channel analyzer (Tracer-Northern #TN7200), which can provide a 512 channel histogram of particle size distribution. An example of a size distribution is given in Figure 4-9 These data, acquired over preseleted time periods, are then transferred to an IBM compatible personal computer and saved on the disk

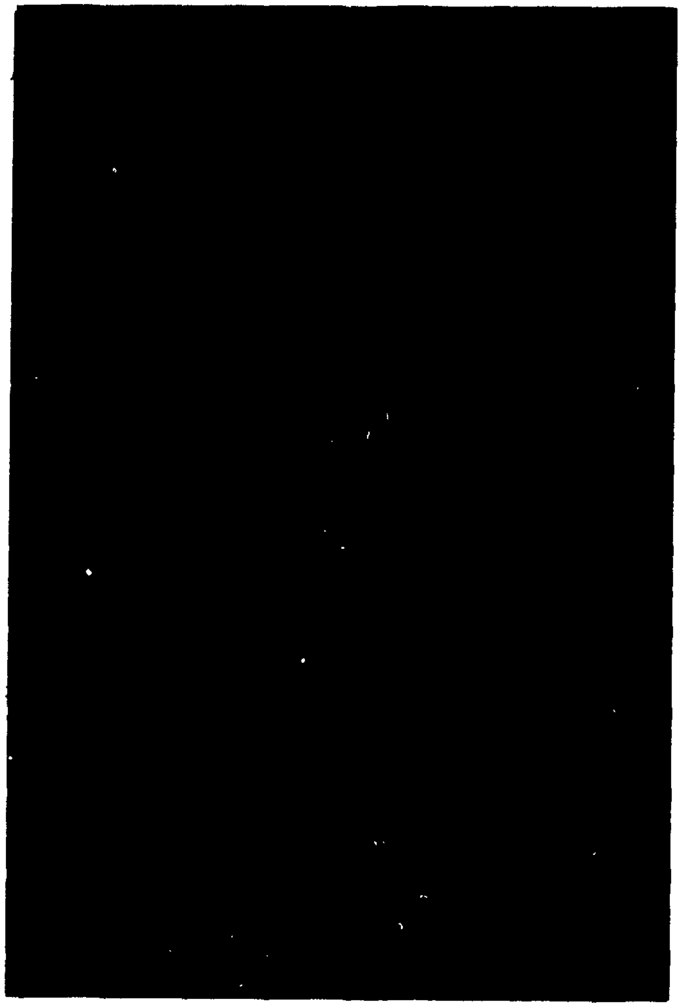

Figure 4-6 The E.S.Z. probe for aqueous system.

A

B

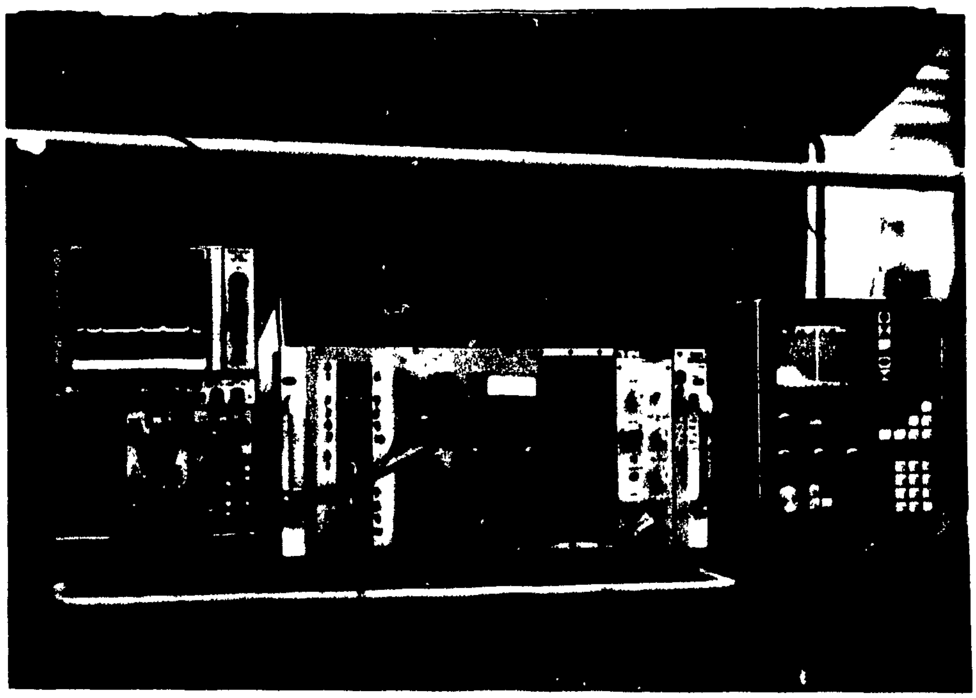

Figure 4-7 Photographs of the experimental arrangements for particle detection in the full-scale water model tundish While Photo. A shows the overall experimental arrangements, Photo B illustrates particularly the signal processing analysis equipment

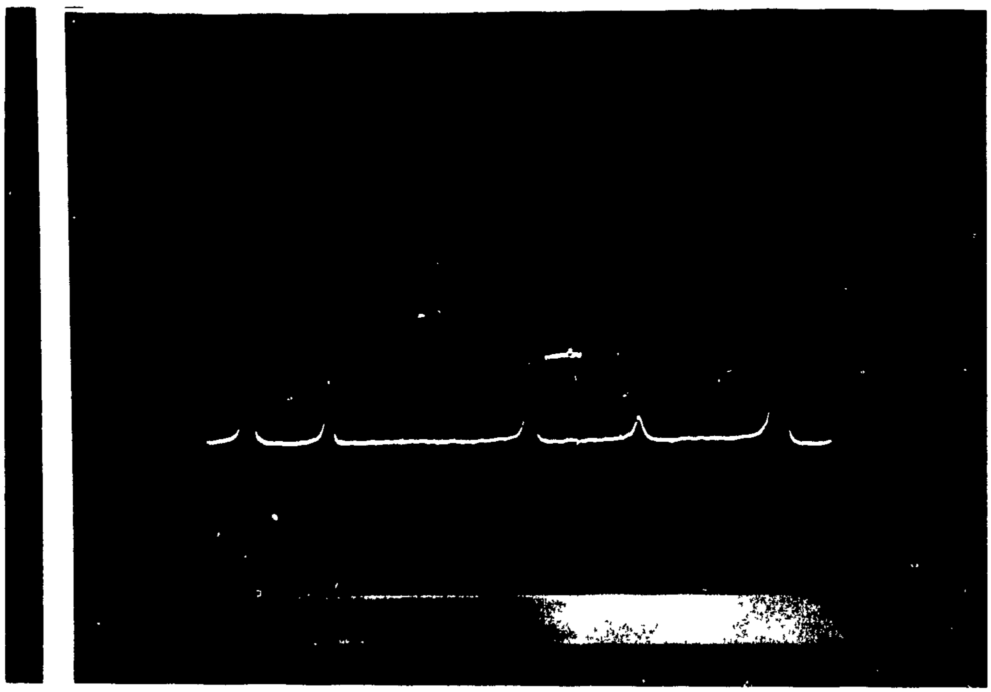

Figure 4-8 Typical signals detected on the oscilloscope. Time is represented on the abscissa and voltage on the ordinate.

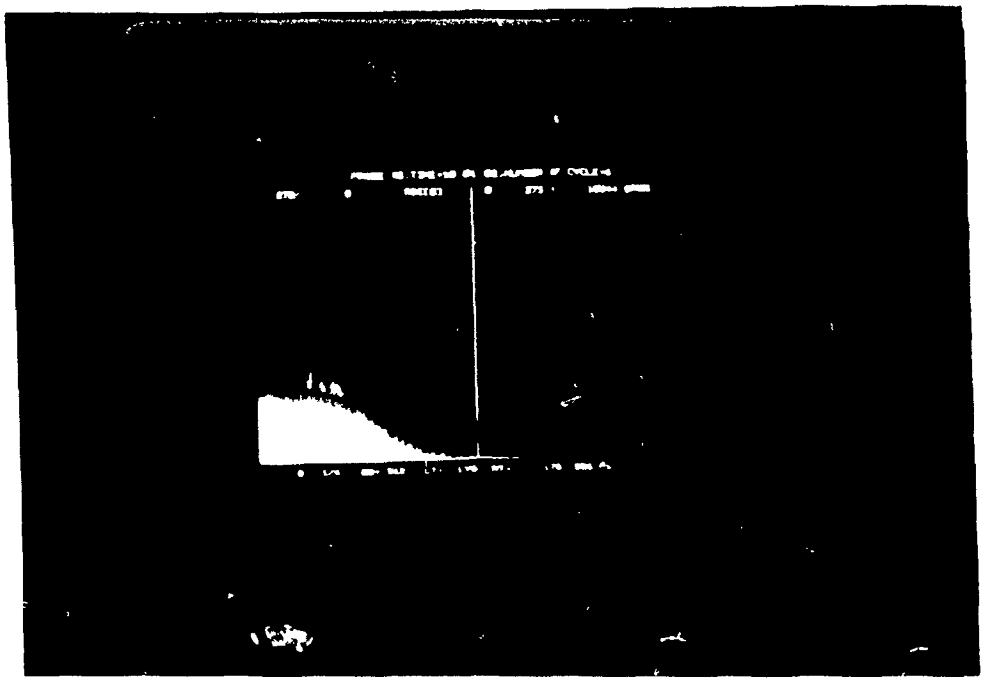

Figure 4-9 A CRT display of particle size distributions aquired over a selected time period The abscissa represents the channel numbers corresponding to particle size, and ordinate the number of particles.

2.2 Measurement of Inclusions

After the water level had been established for steady flow at 1 1 m bath depth, glass bubbles were continuously fed into the tundish through the inlet shroud. The separation behaviour of particles was then measured using the novel E.S.Z. technique just described. (Its novelty versus a Coulter counter lies in the fact that this sensor is 'on-line' and is capable of operating in untreated tap water.)

Alternating sensing of particles over 10 second intervals at the inlet and the outlet nozzles to the tundish was continued, until a total data acquisition time of 60 seconds had been accumulated for each nozzle The data sets thus acquired were transferred to an IBM compatible personal computer and saved on diskettes, using a data acquisition code for the TN-7200 multichannel analyzer developed by F. Dallaire et al[25]. Data on particle population densities were monitored for about 40 minutes. This includes all particles greater than 50 μm in diameter which were counted. The data set transfer time required some five seconds between the PHA monitor and the PC. Table 4-3 provides an example of a typical data set.

Figure 4-10 shows a typical comparison of the PHA recordings of particles frequency distribution curves at inlet and outlet nozzles. Thus, the upper curve provides the number, and size distribution, of particles at the intake to the tundish, while the lower curve gives the number of such particles leaving in the effluent. The relationship between channel number and inclusion diameter is given by[6]:

$$d_p = \frac{10^{\frac{ch.}{640}}}{[100k(T)]^{1/3}} \tag{4-4}$$

where *k(T)* assumes a fixed value when the temperature and amplifier gain are constant. Its value can be obtained by passing particles of known size distribution through the E.S.Z. system.

Figure 4-11 plots the relative number of particles at the intake and outlet ports to the tundish versus time. It can be seen that the particle number feeding rate was constant during the course of an experiment. It is noteworthy that pseudo-steady state was reached after about 25 minutes (i.e. **three mean residence times**) from feeding for the output curve. The details of experimental results will be described in the following chapters for comparison with theoretical predictions.

Table 4-3 **Data acquisition file transfered from the multichannel analyser to a personal computer.**

TN-7200 X01A
* PROBE 41.TIME=11:07:20.NUMBER OF CYCLE=6
** LT= 60 RT= 60
*+ 0 0 512 0 512
# 0 512

< 0>	41	27	46	33	37	38	47	42	40	45	37	36	43	[illegible]
< 14>	51	45	36	27	56	36	37	42	53	46	50	54	50	[illegible]
< 28>	56	45	46	50	50	51	54	48	65	42	40	41	42	44
< 42>	40	52	35	39	52	45	56	55	34	53	54	[illegible]	35	[illegible]
< 56>	42	39	59	56	60	52	45	59	59	67	55	65	40	[illegible]
< 70>	57	43	54	62	48	48	62	56	56	49	59	41	49	55
< 84>	52	35	49	49	31	45	51	56	39	51	45	57	57	54
< 98>	62	72	59	44	54	63	55	45	43	52	39	70	53	46
< 112>	57	59	47	54	51	58	39	58	75	52	48	53	62	[illegible]
< 126>	51	61	46	55	53	56	57	53	61	53	56	57	52	[illegible]
< 140>	65	61	44	49	48	48	67	48	60	44	46	54	55	[illegible]
< 154>	60	52	41	40	42	37	46	41	43	46	38	41	45	[illegible]
< 168>	47	40	37	43	47	38	36	49	46	36	38	[illegible]	[illegible]	[illegible]
< 182>	30	28	41	28	23	32	35	28	24	22	29	[illegible]	[illegible]	[illegible]
< 196>	20	24	23	13	26	14	22	21	19	15	15	24	15	[illegible]
< 210>	12	9	14	19	15	17	14	10	7	15	15	5	9	[illegible]
< 224>	9	12	12	5	9	6	14	5	6	5	[illegible]	5	[illegible]	
< 238>	5	9	5	8	4	7	9	4	4	5	2	2	4	
< 252>	3	3	1	1	1	3	6	4	4	3	1	2	2	
< 266>	1	2	0	1	3	1	[illegible]	0	2	[illegible]		[illegible]		
< 280>	0	4	2	0	0	2	1	0	0	[illegible]	[illegible]	[illegible]	[illegible]	
< 294>	0	2	1	1	1	0	4	0	2	0	[illegible]	[illegible]	[illegible]	
< 308>	1	3	0	0	0	3	0	1	0	1	1	[illegible]	[illegible]	
< 322>	2	0	1	0	0	0	1	0	1	1	0			
< 336>	0	1	0	0	0	0	0	0	0	0	[illegible]		[illegible]	
< 350>	0	0	0	0	0	0	0	0	0	0	0	[illegible]	[illegible]	
< 364>	0	0	0	0	0	0	0	0	0	0	0	[illegible]	0	
< 378>	0	0	0	0	0	0	0	0	0	0	0	[illegible]	0	[illegible]
< 392>	0	0	0	0	0	0	0	0	0	0	0	[illegible]	[illegible]	
< 406>	0	0	0	0	0	0	0	0	0	0	0	[illegible]	[illegible]	
< 420>	0	0	0	0	0	0	0	0	0	0	0	0	0	[illegible]
< 434>	0	0	0	0	0	0	0	0	0	0	0	1	0	[illegible]
< 448>	0	0	0	0	0	0	0	0	0	0	0	0	0	[illegible]
< 462>	0	0	0	0	0	0	0	0	0	0	0	0		[illegible]
< 476>	0	0	0	0	0	0	0	0	0	0	0	0	0	0
< 490>	0	0	0	0	0	0	0	0	0	0	0	0	[illegible]	[illegible]
< 504>	0	0	0	0	0	0	0	0						

END

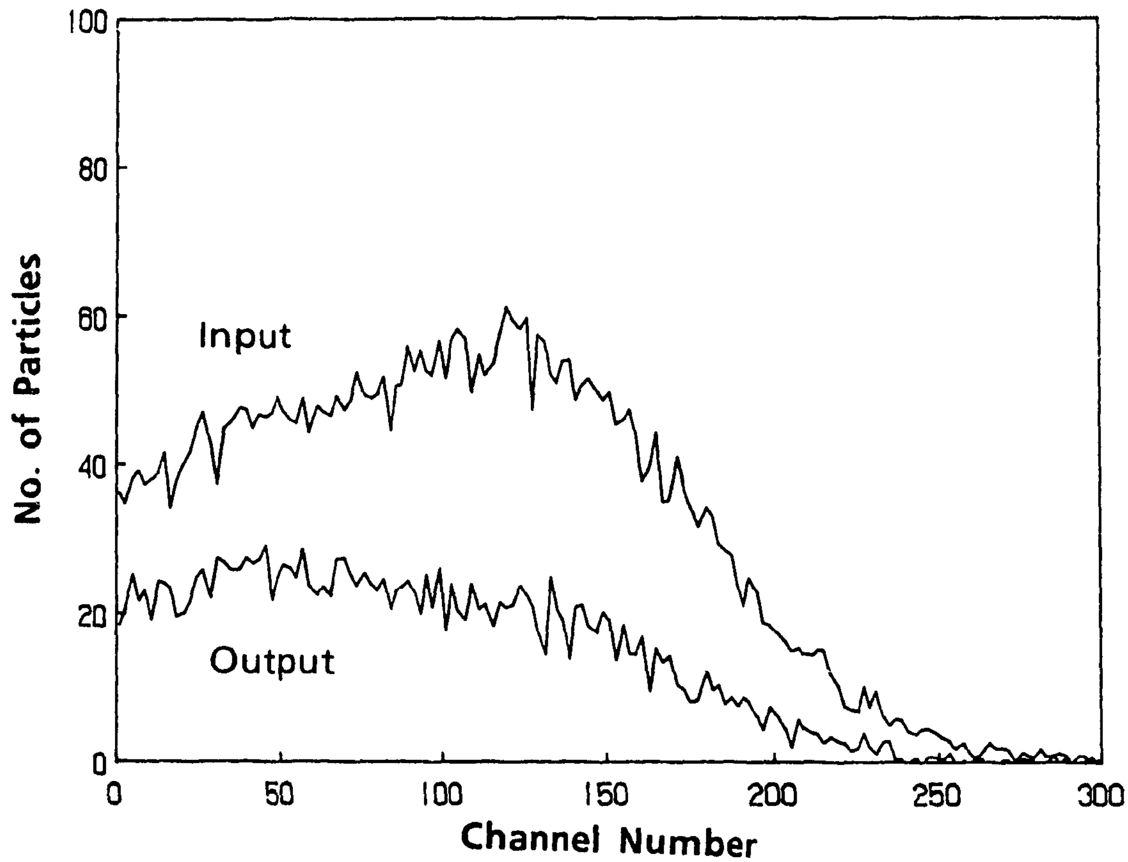

Figure 4-10 Comparison of PHA recordings of particles at an inlet, and at an outlet, nozzle.

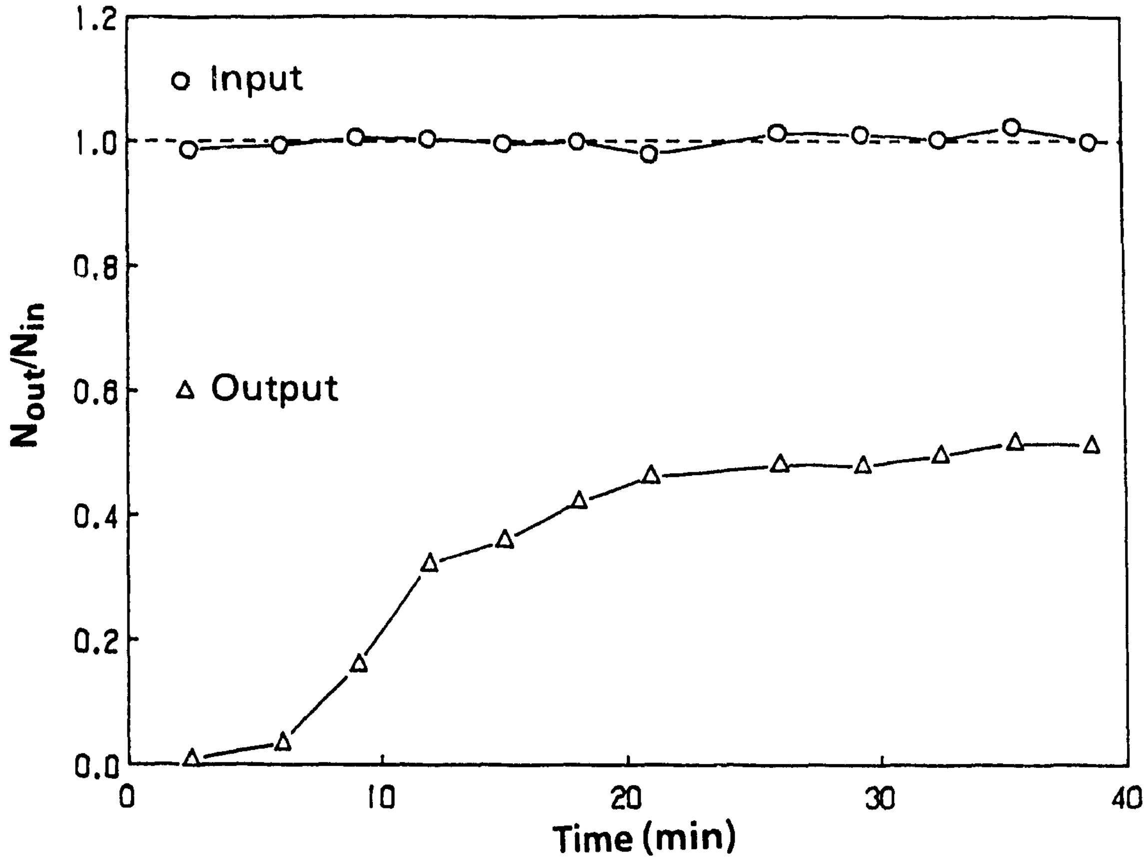

Figure 4-11 Changes in the number density of particles with respect to time, monitored at an inlet (input), and at an outlet (output), port.

Chapter 3

Tank Reactor Model

3.1 Theory

Tank reactor models can be a useful tool for evaluating inclusion separation rates. The technique, in practice, hinges on a quantitative interpretation of C-diagrams. Such models propose that a tundish volume can be divided serially into a well-mixed or back-mix zone, a plug flow zone and a dead volume zone[1,2,5,6] One can choose various levels of complication in choosing these volumes in order to mimic observed residence time distribution curves following a pulse tracer addition to the reactor/tundish.

3 1.1 Definition of Residual Ratio

The entrainment rate of inclusion particles into the mould through the outlet nozzle of a tundish can be represented by the **Residual Ratio** of inclusion particles defined as

$$R = \frac{N_{out}}{N_{in}} = \frac{\text{output number density of inclusion}}{\text{input number density of inclusion}} \qquad (4\text{-}5)$$

where N_{in} and N_{out} denote the number density of inclusions at the inlet and at the outlet nozzles, respectively. For instance, a value of 0.5 in the Residual

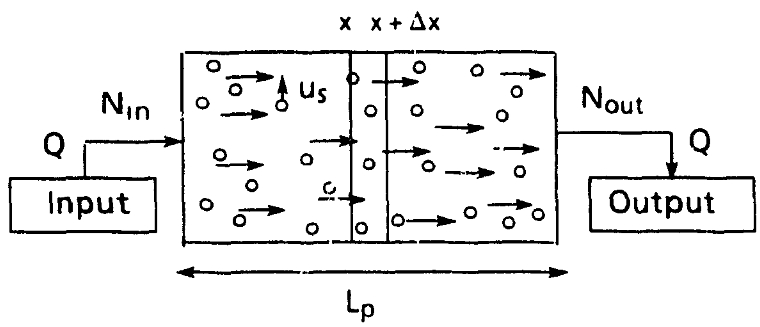

(a) plug flow reactor

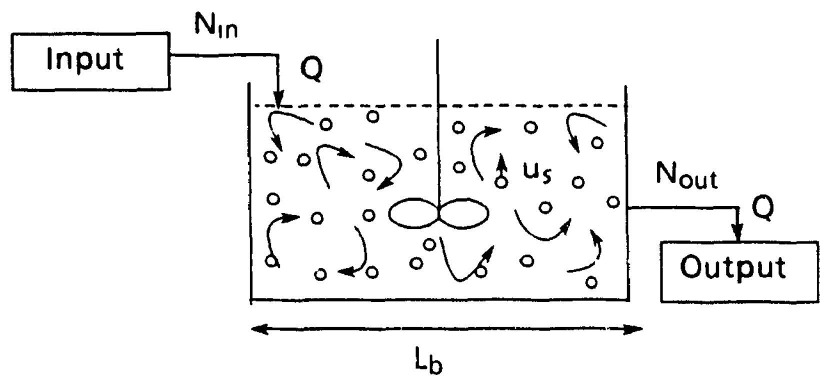

(b) backmix flow reactor

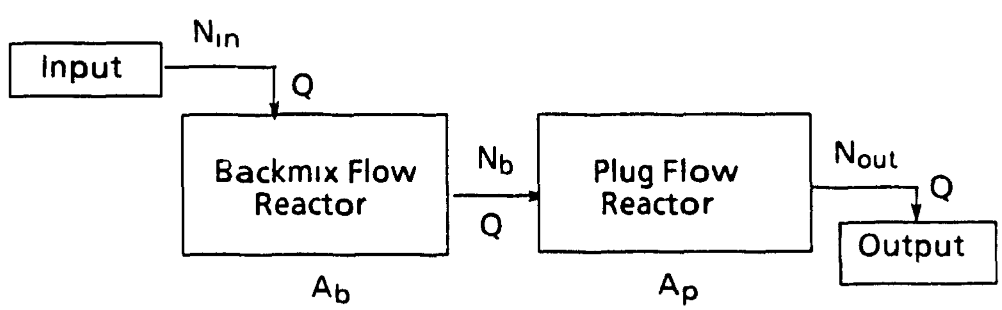

(c) hybrid reactor

Figure 4-12 Schematic of (a) plug flow reactor, (b) well-mixed reactor, (c) a hybrid reactor.

Ratio for a single port tundish implies that 50 % of such inclusions entering the tundish are entrained into the mould through the effluent stream from the outlet nozzle.

3.1.2 Plug flow reactor model

In the plug flow reactor model, flow within a tundish vessel is assumed to be a plug (or linear) flow. Considering a simple plug flow reactor, shown in Figure 4-12 (a), one can establish a number balance on particles of a specific Stokes rising velocity, u_S, over an infinitesimal segment, Δx, as follows.

$$\begin{bmatrix} \textit{number of particles} \\ \textit{flowing into} \\ \textit{the segment} \end{bmatrix} = \begin{bmatrix} \textit{number of particles} \\ \textit{rising out of the} \\ \textit{reactor to surface} \end{bmatrix} + \begin{bmatrix} \textit{number of particles} \\ \textit{flowing out} \\ \textit{from the segment} \end{bmatrix}$$

This can be expressed as

$$QN_x = u_s N_x W \Delta x + QN_{x+\Delta x} \tag{4-6}$$

and

$$N_{x+\Delta x} = N_x + \frac{dN_x}{dx}\Delta x \tag{4-7}$$

where W represents the width of the reactor. The specific Stokes rising velocity of a size of particles, u_S, is expressed as

$$u_s = \frac{\Delta\rho g d^2}{18\mu} \tag{4-8}$$

Substituting Equation 4-7 into Equation 4-6, one obtains

$$\frac{dN_x}{dx} = \frac{u_s W}{Q} N_x \tag{4-9}$$

Applying appropriate boundary conditions ·

at $x = 0$, $N_x = N_{in}$

at $x = L_p$, $N_x = N_{out}$

where L_p is the length of the plug flow reactor, and integrating Equation 4-9 between $x = 0$ and $x = L_p$ gives :

$$R = \frac{N_{out}}{N_{in}} = exp(-\frac{A_p}{Q} u_s) \tag{4-10}$$

where A_p (= WL_p) represents the surface area of the plug flow reactor.

4.1.3 Backmix flow reactor model

A backmix flow reactor is one in which the fluid contents are assumed to be well stirred and thus of uniform composition throughout. Referring to Figure 4-12 (b), the number balance on particles of a specific Stokes rising velocity, u_s, over the backmix flow reactor, is expressed as

$$QN_{in} = u_s A_b N_{bulk} + QN_{out} \tag{4-11}$$

where N_{bulk} represents the number density of particles within the bulk of reactor and A_b is the surface area of the backmix flow component of the reactor. Since N_{bulk} is equal to N_{out} in the backmix flow (well-mixed) reactor, the residual ratio of particles is written by

$$R = \frac{N_{out}}{N_{in}} = \frac{Q}{(A_b u_s + Q)} \qquad (4\text{-}12)$$

3.1.4 Hybrid reactor model

Previous studies(5,6) of mixing in the Stelco tundish showed that this design of tundish gave a flow field approximating a well-mixed zone followed by a plug flow zone Referring to Figure 4-12 (c), one can therefore write :

$$R = \frac{N_{out}}{N_{in}} = \frac{1}{(1 + A_b u_s / Q)} \exp\left(- \frac{A_p u_s}{Q}\right) \qquad (4\text{-}13)$$

or

$$R = \frac{1}{(1 + (1 - \gamma) A u_s / Q)} \exp\left(- \frac{\gamma A u_s}{Q}\right) \qquad (4\text{-}14)$$

assuming no dead volume zone in the reactor. Here, γ represents the volumetric portion of plug flow reactor to backmix flow reactor (i.e. $A_p = \gamma A$ and $A_b = (1\text{-}\gamma)A$).

3.1.5 Reactor volume fractions

For a reactor model, the respective volume fraction of a plug flow zone (V_p), back-mix zone (V_m), and a dead volume zone (V_d) can be evaluated from a C-diagram (or RTD curve)(26) The auxiliary relationships are

$$V_p = \theta_{min} \tag{4-15a}$$

$$V_d = 1 - \theta_{av} \tag{4-15b}$$

$$V_m = 1 / C_{max} \tag{4-15c}$$

or

$$V_m = 1 - V_{dp} - V_d \tag{4-15d}$$

where V is a fractional volume of each reactor and θ is a dimensionless time ($\theta = t / \bar{t}$; $\bar{t}$ = nominal residence time). A typical C-diagram for such a model is illustrated in Figure 4-13

Such a model requires that once the plug volume has been traversed by a tracer addition dispersing from the well mixed zone upstream, an instantaneous increase in tracer concentration to a maximum should then occur, followed by an exponential decay However, actual experiments reveal the minimum residence time to be less than the peak time for the peak in the C-curve. Ahuja and Sahai[27] have, therefore, proposed a modified version of the well-mixed, plug flow, dead zone reactor, by introducing the concept of a *dispersed plug flow volume*, V_{dp}, represented by:

$$V_{dp} = \frac{\theta_{min} + \theta_{peak}}{2} \tag{4-16a}$$

$$V_d = 1 - \theta_{av} \tag{4-16b}$$

and

$$V_m = 1 - V_{dp} - V_d \tag{4-16c}$$

In the present study, this modified model was used for evaluating the characteristic reactor volume fractions of the tundish

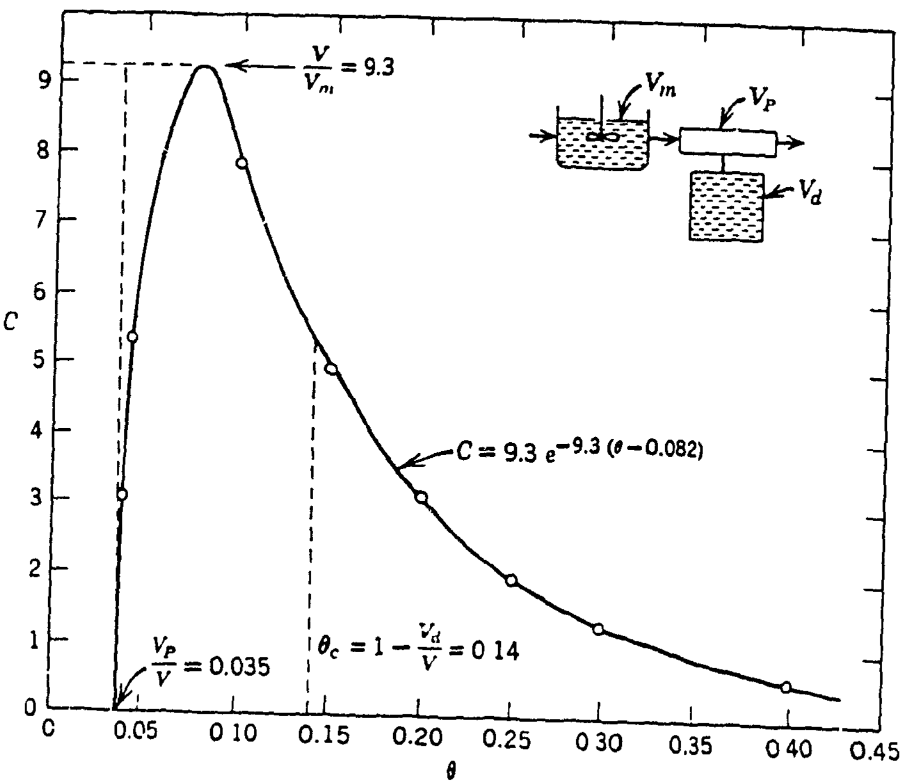

Figure 4-13 A typical analysis of C-curve of reverberatory flow according the mixed model

3.2 Results and Discussions

Equation 4-14 provides significant information on those factors determining particle separation in a reactor Residual ratios shows the following dependencies

(1) Particle size (d): Since the particle diameter is proportional to the square root of the Stokes rising velocity, smaller particles are more likely entrained into the mould (i e residual ratio increases for smaller particles).

(2) Surface area of reactor (A): An increase in the free surface area of the reactor leads to a decrease in the residual ratio of particles because the opportunity for particle float-out increases

(3) Volumetric flow rate (Q): Equation 4-14 shows that as the fluid flow rate increases, the residual number of particles entering the mould increases

(4) Plug flow volume fraction (γ): Figure 4-14 illustrates the change in the residual ratio of particles with respect to a dimensionless flow rate (Au_s/Q). The RR curves were drawn for well-mixed flow ($\gamma = 0$), $\gamma = 0.2$, $\gamma = 0.5$, and pure plug flow ($\gamma = 1$) based on Equation 4-14 As seen, plug flow is preferable to backmix flow for particle separation

In order to evaluate the residual ratio of particles using the hybrid reactor model, reactor volume fractions (or γ) must be determined *a priori* Reactor volume fractions are usually estimated from experimental pulse mixing curves employing Equation 4-16 [5,6,27]. For the other approach, El-

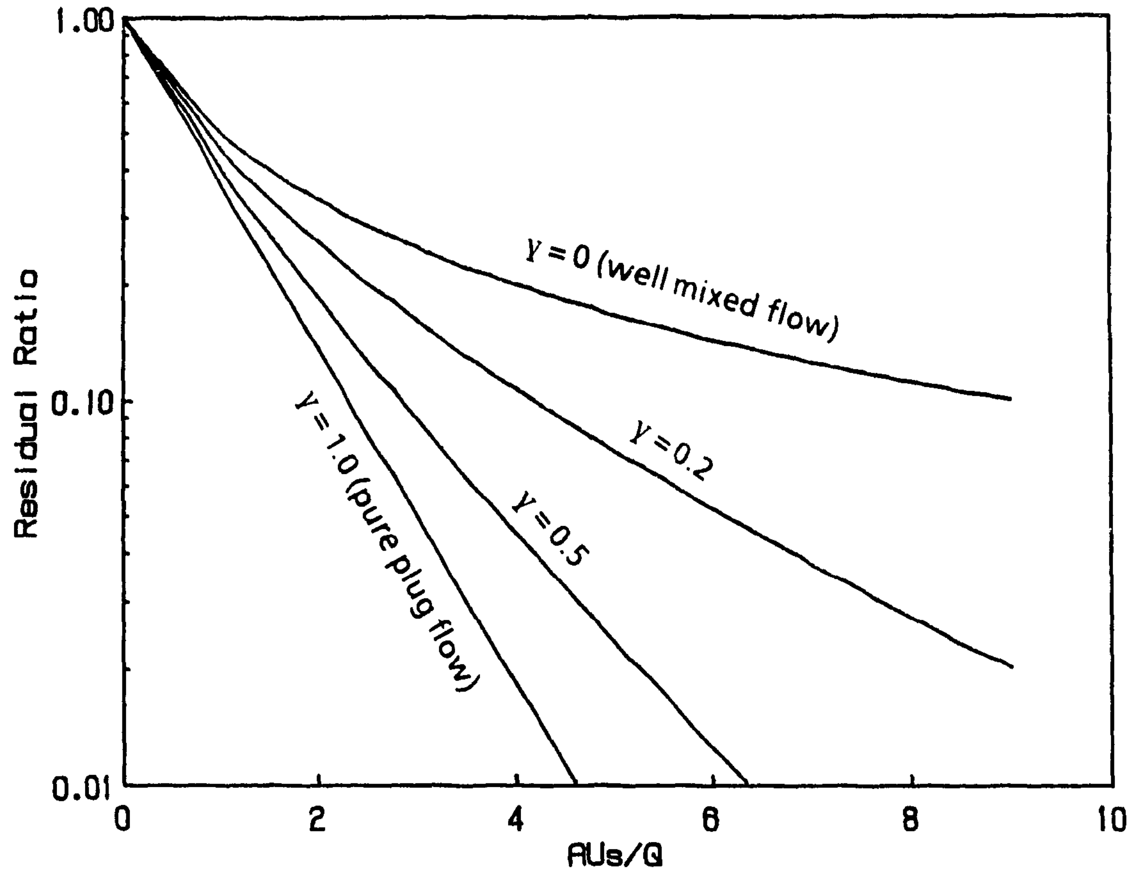

Figure 4-14 Illustration of the effect of plug flow volume fraction to the particle residual ratio.

Kaddah et al. [7] and Sahai [8] proposed that C-diagrams could be predicted by solving a differential mass conservation equation (i.e. Eq. 2-14), having first solved the steady flow field. This concept represents a step backwards, since particle dispersion characteristics are more readily solved by a differential mass transport equation (i.e. Eq. 2-17). (See Chapter 4 and 5)

Figure 4-15 shows plots of the retention time distributions (C-diagrams) with, and without, flow modification, predicted by the mass transport equation. There, a weir and dam arrangement was placed at 1/3 L_c, 1/2 L_c and 2/3 L_c (L_c : distance between inlet and outlet nozzles). Previous researchers[7,10] have reported that their computed RTD curves were in very good agreement with measurements. It is seen from Figure 4-15 that the tundish flows modified by the weir and dam arrangement chosen (F.M.D.'s), lead to somewhat longer minimum retention times, delays in the *peak time* and higher *peak concentrations*.

This implies that the effective dispersed plug flow volume was increasedby using F.M.D.'s, while the backmix and dead volumes were decreased. Assuming that ideal tundish flows correspond to plug flow characteristics, one can conclude that the flow patterns were improved with the flow controls used. As the weir/dam combination was moved closer to the exit nozzle, the peak time becomes further delayed and the peak concentration higher. Characteristic flow volume fractions, calculated on the basis of Figure 4-15, are summarized in Table 4-4. Since the volume fraction of dispersed plug flow was increased with placement at 1/2 L_c, the corresponding separation of particles is anticipated to be improved.

Table 4-4 Volume fractions of the characteristic flows

	V_{dp}	V_m	V_d
no flow modification	0 39	0 56	0 05
flow modification	0 50	0 50	-

Predicted and experimental results for particle separation in the Stelco tundish with a weir/dam arrangement at 1/2 L_{c}, versus those without flow modification are compared in Figure 4-16. As seen, the agreement is good except for large particles (over 3 mm/s Stokes rising velocity). When flow was modified using a weir and dam arrangement, the residual ratios of particles were reduced. Figure 4-16 also confirms that the flow characteristics in this tundish is neither pure plug flow nor well-mixed flow, but a combination of plug and well-mixed flow.

It is clear that these practices of modelling tundishes in terms of well-mixed, plug, and dead flow regions represents a useful, but gross, simplification of real events, and need to be restricted to simple systems. As Nakajima(6) reported, it is difficult to establish such models for complicated tundish geometries. Further, tank reactor model can only evaluate particle separations under steady state conditions. In actual steelmaking practice, a recirculating load of inclusions can build up within the molten steel as it passes through the tundish. Metal temperature distributions within a tundish should also be an important factor, since one can readily demonstrate (see Chapter 5) the magnitude of natural convective velocities is likely to be in the same order as those for mean convective velocities These aspects cannot be covered by such crude types of models. By contrast, a differential equation model can treat such phenomena through solution of the conservation equations for fluid flow, heat, and dispersion of (buoyant) particles.

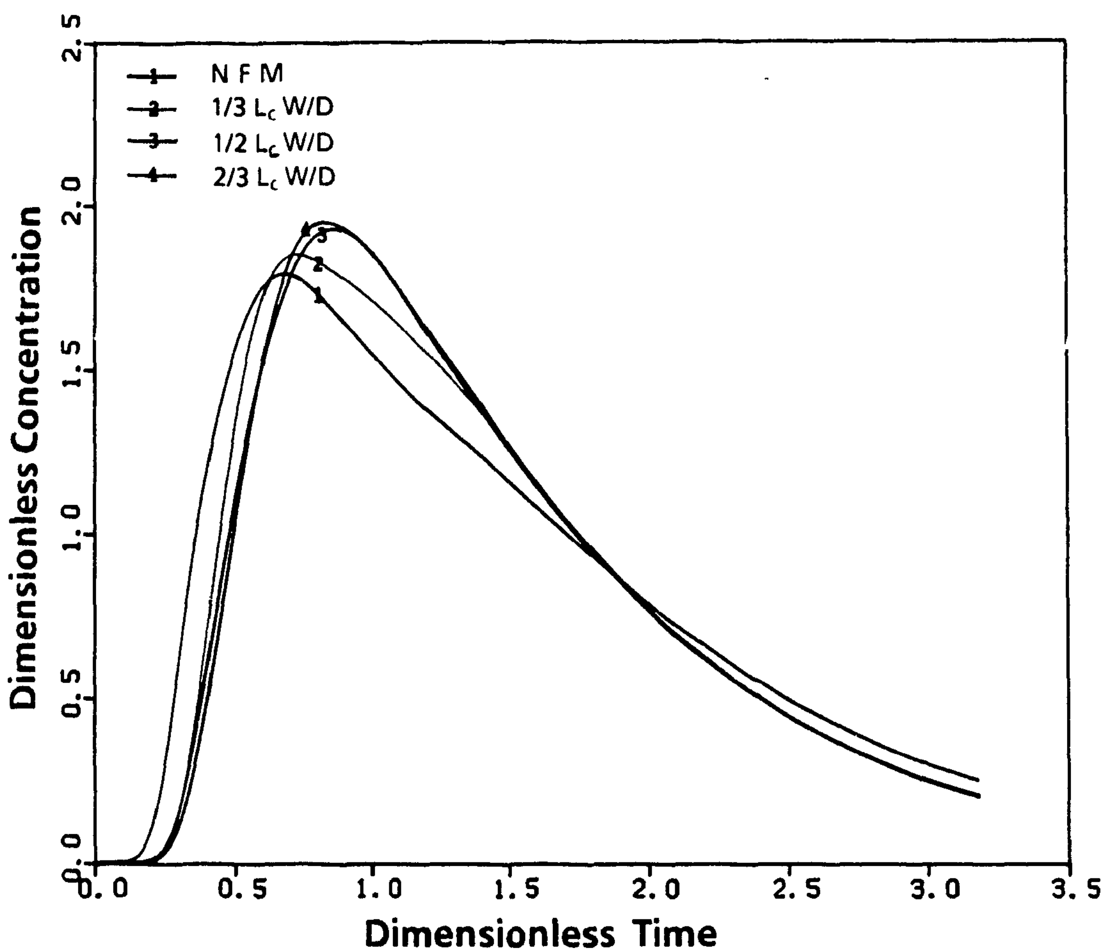

Figure 4-15 Residence time distribution (RTD) curves predicted with, and without flow modifications for Stelco's single port tundish.

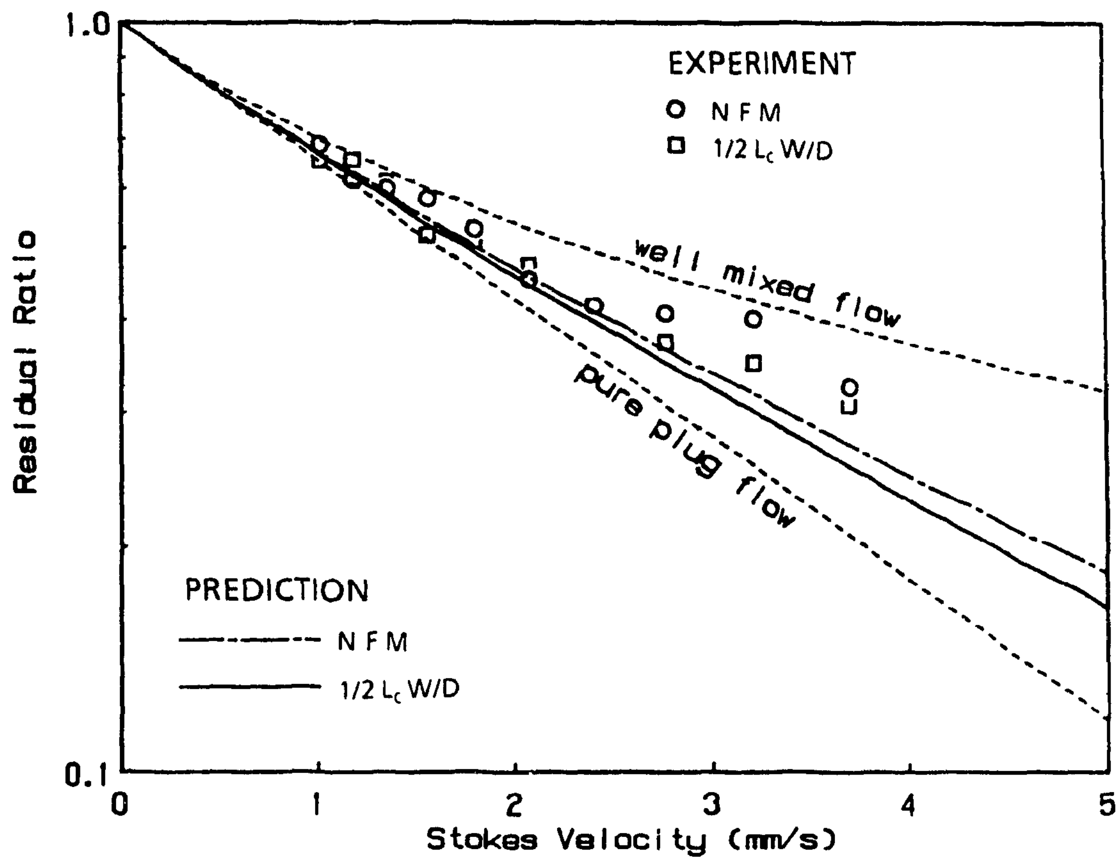

Figure 4-16 Comparisons of experimental measurements and predictions, using a tank reactor model (hybrid reactor model), on particle separation in Stelco's single ported tundish.

Chapter 4

Differential Equation Model I

: Full-Scale Water Model System (Isothermal Conditions)

4.1 Theory

4.1.1 Governing equations

In order to describe fluid flow, heat transfer and inclusion float-out in steelmaking tundishes, the relevant partial differential equations are the equations of continuity (Equation 2-2), momentum (Equations 2-3 to 2-9), energy (Equation 2-18), and fine particle conservation (Equation 2-17) expressed in cartesian form. The k-ε turbulence model (Equations 2-10 to 2-13) was incoporated to calculate turbulent eddy viscosity.

Computations for the full-scale water model tundish were carried out so as to compare with the experimental results of particle separation. In such a situation, it is appropriate to assume that the system is under isothermal conditions.

4.1.2 Numerical treatment of sloping wall

The shape of typical industrial tundishes is normally non-rectangular. For instance, the wall of the 'trough-shaped' tundish at Stelco's

Hilton Work was outwardly inclined at an angle of 10 degrees to the vertical. BHP's Port Kembla No.2 tundish (in Chapter 5) has an irregular wedge-shape, its surfaces being inclined to the horizontal, longitudinal and vertical axes Since the present computations were performed using a standard rectangular coordinate system, it had to be improvised to handle inactive or 'blocked-off' region. Two alternative techniques can be generally used to treat the irregular boundary domain. One is the 'stepped wall' technique(15), for which a sloping, or curved, boundary is approximated by a series of rectangular steps. This method is somewhat expensive, since a fine grid is necessary if the curved boundary is to be accurately modelled. The other is the 'blockage-ratio' method(28), for which the finite difference coefficients for a node of an irregular inert boundary cell are normally calculated and then modified by the blockage ratio. This ratio is defined as the proportion of a cell's face area that is blocked by the solid obstacle.

In the present study, the stepped wall technique was used, since it is convenient to incorporate the wall function equations at the nodes next to the walls and easy to set up heat transfer boundary conditions at side walls. The true boundary and nominal boundary are illustrated in Figure 4-17, where the shaded area represents the inactive control volumes, where velocity components must be set to zero. Any desired value of a variable, ϕ, in the inactive zone can be arranged to be the solution at an internal grid point by setting the source terms as.

$$S_C = 10^{30} \phi_{P,desired} \tag{4-17}$$

and

$$S_P = 10^{30} \tag{4-18}$$

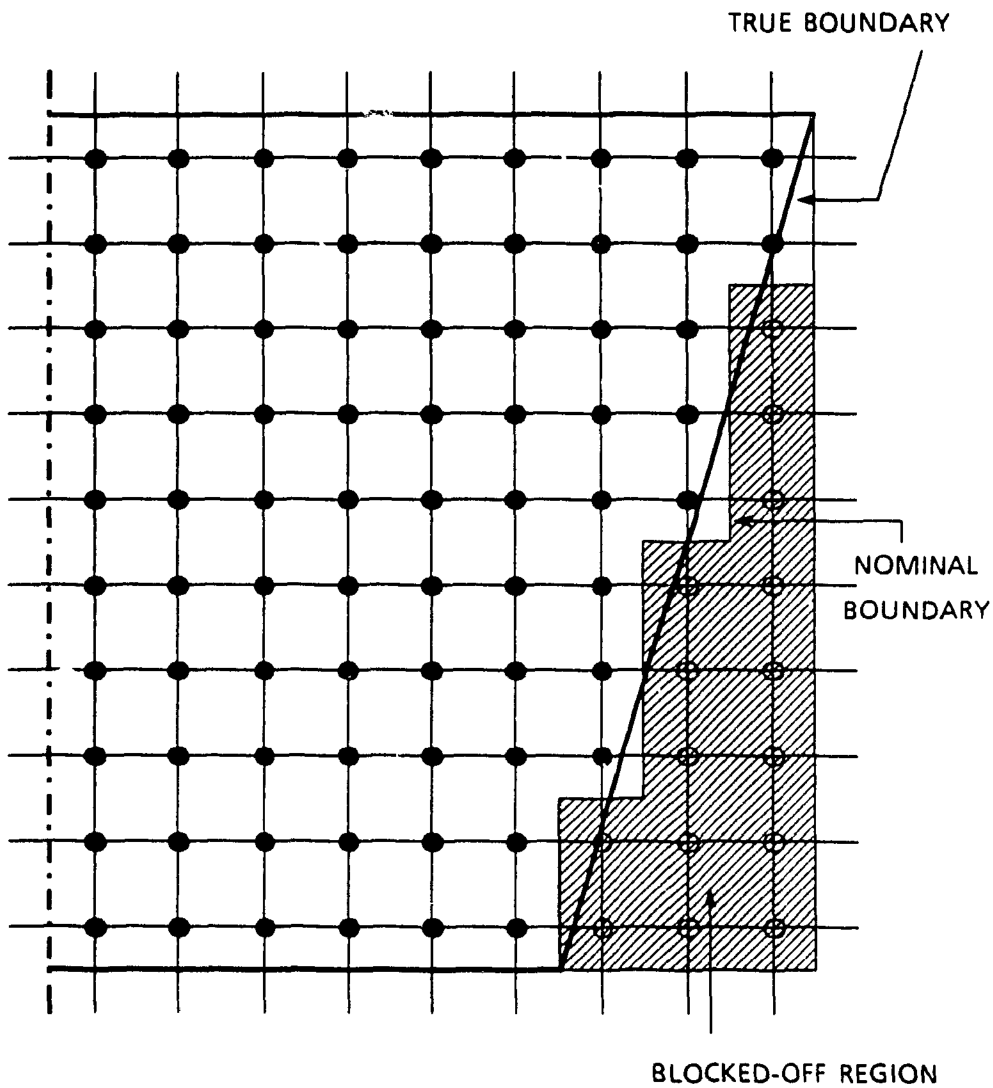

Figure 4-17 Blocked-off regions in the regular grid using *stepped wall* method.

where 10^{30} denotes a number large enough to make the other terms in the discretization equation (Equation 2-21) negligible. The consequence is that Equation 2-21 reduces to

$$S = S_C + S_P \phi_P = 0 \tag{4-19}$$

Hence,

$$\phi_P = S_C / S_P = \phi_{P,desired} \tag{4-20}$$

Using this procedure, the value of the dependent variables can be fixed where needed.

4.1.3 Boundary conditions

(a) fluid flow

For the node next to the tundish wall , the wall function method described in Part II was employed. For velocity components normal to the wall, zero flux was imposed, and for velocity components parallel to the wall, non-slip conditions were imposed

At the symmetry planes and the free surface boundary, which is assumed to be flat, the normal velocity components and normal gradients of all other variables were set equal to zero. At the jet's entry point into the tundish (from the steel contained in the ladle above), the velocity component perpendicular to the free surface was calculated from volumetric flow rate and the area of nozzle as follows:

$$U_{in} = Q / A_{nozzle} \tag{4-21}$$

Similar boundary conditions were imposed at the outlet nozzles.

The inlet values of k, the level of turbulence kinetic energy, and ε, the rate of turbulence energy dissipation, were approximated from the following relationship

$$k_{in} = 0.01 U_{in}^{2} \tag{4-22}$$

and

$$\varepsilon_{in} = k_{in}^{3/2} / R_{nozzle} \tag{4-23}$$

(b) inclusion behaviour

In order to simplify the problem of inclusion flotation, the following assumptions were made in the mathematical formulation:

(1) Particles are spherical, and the surface tension of particles has no effect on float-out velocity.

(2) The motion of inclusions/fine particles (in the range of 20-150 μm in diameter) follows Stokesian behaviour within the whole region of a tundish.

(3) There is no modelling of any interactions and/or agglomeration/ coalescence phenomena between inclusion particles within the tundish.

(4) The side-walls and bottom of the tundish, as well as flow modification devices, are all non-wetting (reflecting) to inclusions within the melt.

(5) Any erosion of refractories is not taken into account.

The particle concentration is normalised to a value of unity at the inlet nozzle. Thus, the resultant concentration at the outlet nozzles represents simultaneously the Residual Ratio of inclusions.

4.1.4 Numerical solution procedures

As aleady described, the relevant differential equations were discretized using the finite integral volume method employing a hybrid differencing scheme[19]. The whole set of equations were solved via a semi-implicit TDMA marching scheme coupled with a Gauss-Siedal routine. The SIMPLE algorithm was used to solve the pressure field through simultaneous satisfaction of the continuity and momentum equations within each volume element.

Only a symmetrical half of the model tundish at Stelco's Hilton Work was considered for the present computations. The domain was divided into a non-uniform grid of 17 (vertical) x 40 (longitudinal) x 16 (transverse) in the three orthogonal directions. Figure 4-18 (a) and (b) illustrate the effect of grid spacing on the accuracy of flow field predictions Thus, 4-18 (a) shows fluid vectors along the vertical axis of the penetrating jet, while 4-18 (b) gives corresponding vectors for liquid within the vertical axis of the exit port to the tundish. Such a test shows that the grid field chosen is sufficiently fine to render flow field computations independent of grid size

The computer runs for the isothermal conditions were carried out on a desk-top microprocessor (IBM-AT) fitted with a Definicon system of 8MB RAM and 20MHz clock speed. Converged solutions were obtained after 700-1000 iterations requiring 12-16 hours with this machine.

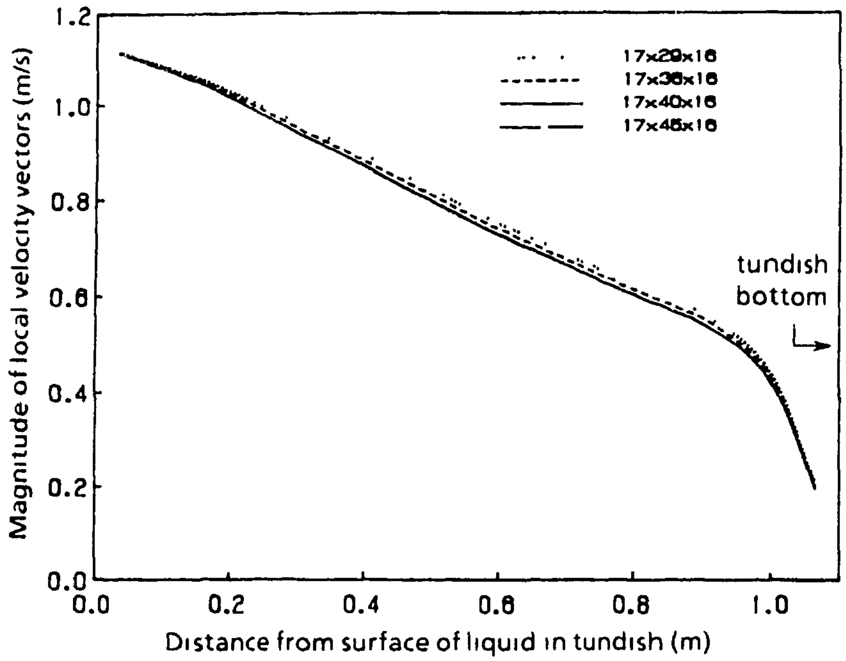

(a) vertical axis of the entry jet

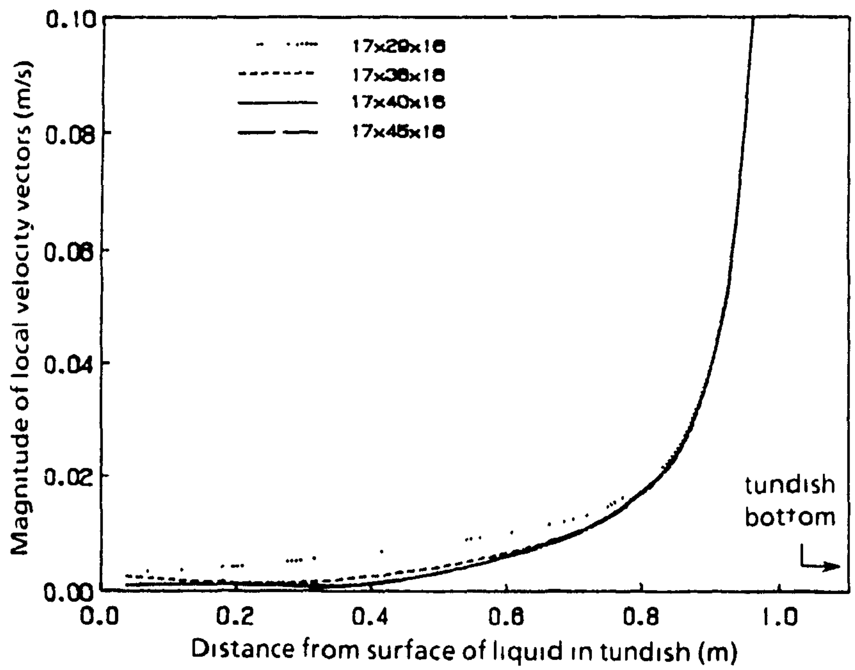

(b) vertical axis of the exit port

Figure 4-18 The effect of grid spacing on the accuracy of flow field predictions

4.2 Application to Single Port Water Model Tundish

4.2.1 Flow fields

General features of the flow field induced in such a water model tundish (isothermal condition), when no flow control devices are employed, are indicated by the predicted vector plots in Figure 4-19 Figure 4-19A presents an isometric view of the flows generated in a half section of the tundish, and these may be interpreted in terms of Figure 4-19B, where a collage of two-dimensional plots of velocity components along selected longitudinal, transverse and horizontal axes of the tundish are given.

As seen , the entering jet hits the bottom of the tundish and then flows downstream or sideways towards the walls of tundish. This rising fluid then moves up the tundish sidewalls to the free surface, part moving downstream in the direction of the exit, while the rest recirculates back towards the incoming jet. It is clear that maximum velocities drop significantly with increasing distance from the incoming jet. Indeed, at the edge, near the exit, the flow becomes practically motionless The incoming jet's velocity through the ladle shroud was 1 13 m/s while local velocities in the tundish varied from 3 to 100 mm/s The average flow speed in this full scale tundish was only 22 mm/s Figure 4-20 also provides a view of flow characteristics within the tundish The incoming jet generates a back-mix flow (recirculating flow) region, and a flow towards the exit nozzle which has plug-flow-like characteristics. This justified the use of the hybrid reactor model introduced in Chapter 3

Weir and dam combinations were next introduced into the tundish, in order to obtain flows that were potentially more conducive to

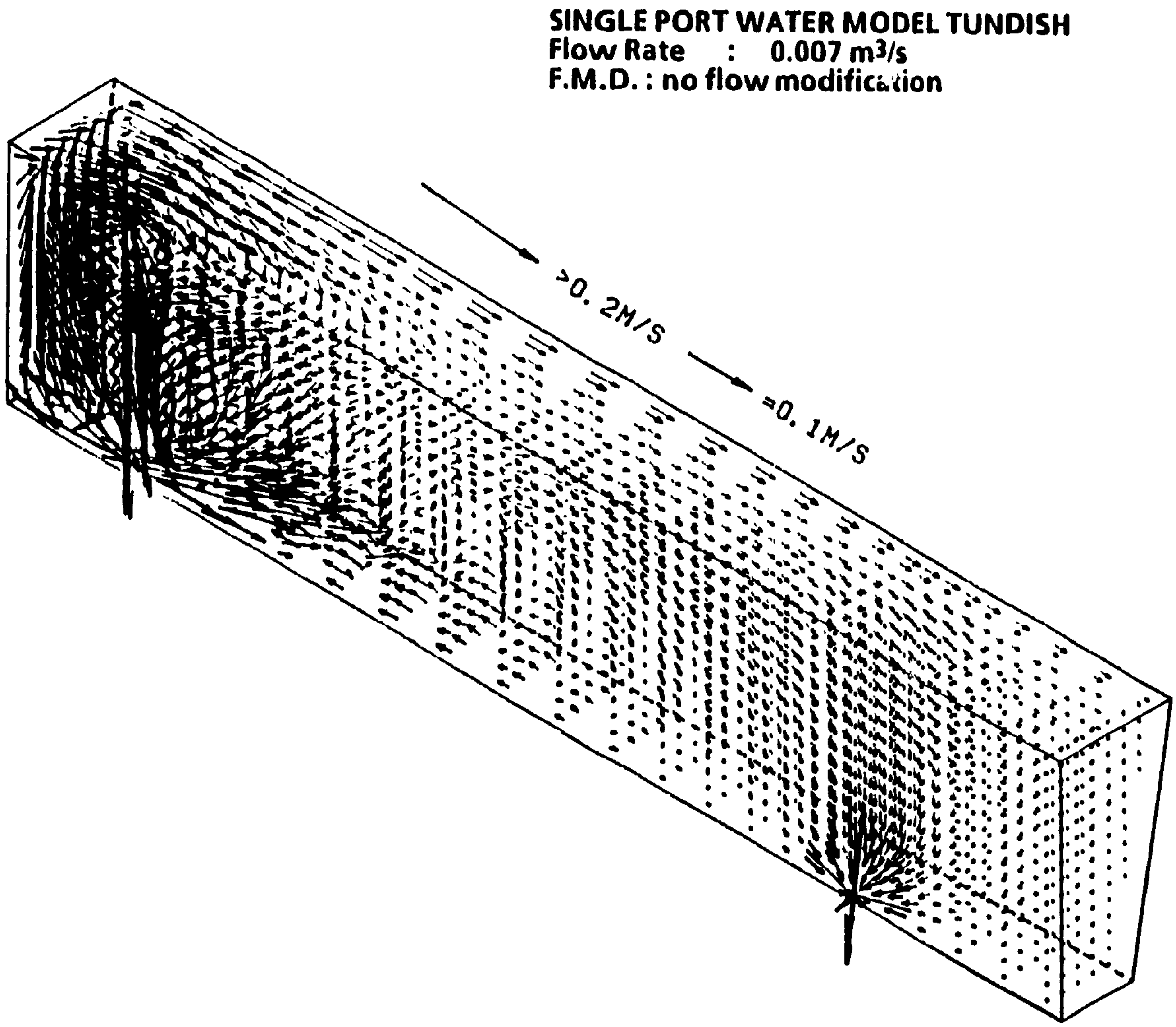

Figure 4-19A An isometric view of flow fields predicted in the longitudinally bisected single strand water model tundish (isothermal conditions) of slab casting without flow modification device.

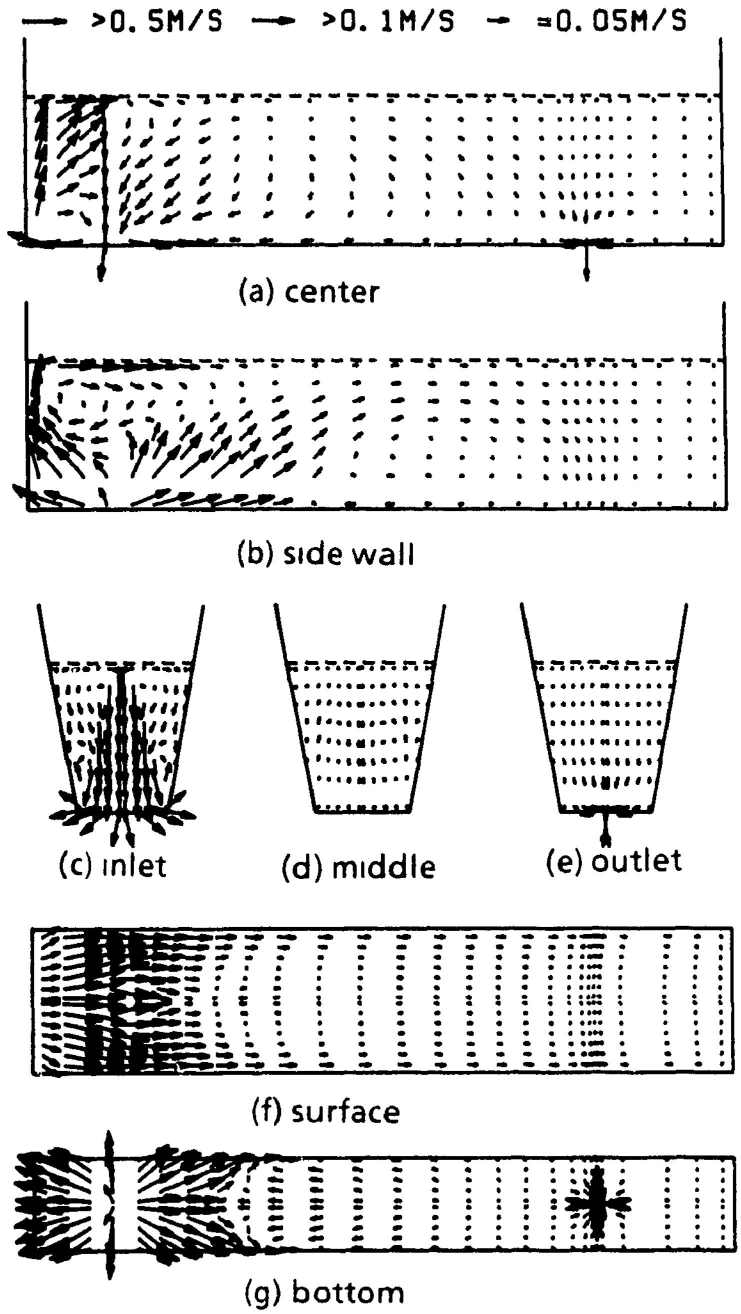

Figure 4-19B Predicted flow fields in some selected longitudinal planes (a, b), transverse planes (c, d, e), and horizontal planes (f, g) for the single strand water model tundish (isothermal conditions) with no flow modification device

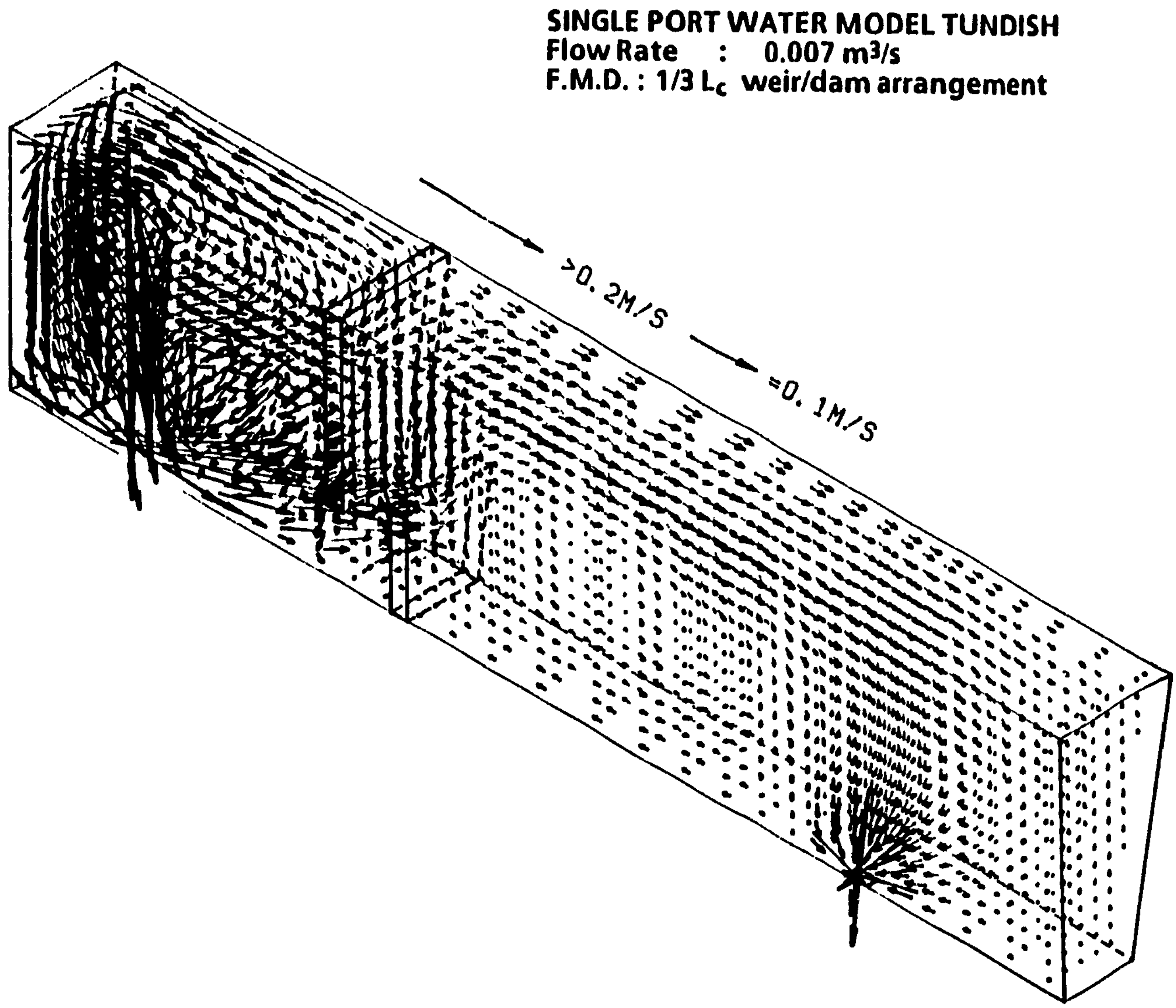

Figure 4-20A An isometric view of flow fields predicted in the longitudinally bisected single strand water model tundish of slab casting with weir/dam arrange:.ient placed at 1/3 L_c.

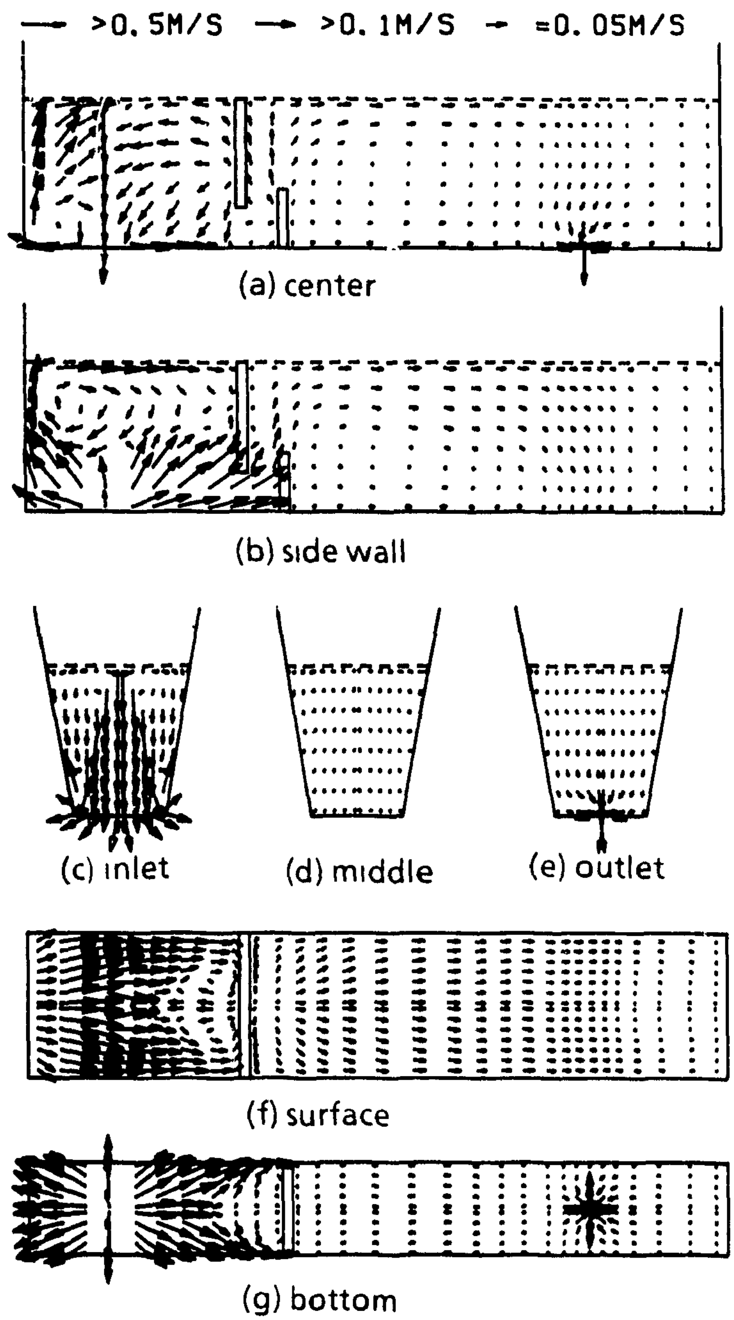

Figure 4-20B Predicted flow fields in some selected longitudinal planes (a, b), transverse planes (c, d, e), and horizontal planes (f, g) for the single strand water model tundish with weir/dam arrangement placed at 1/3 L_c

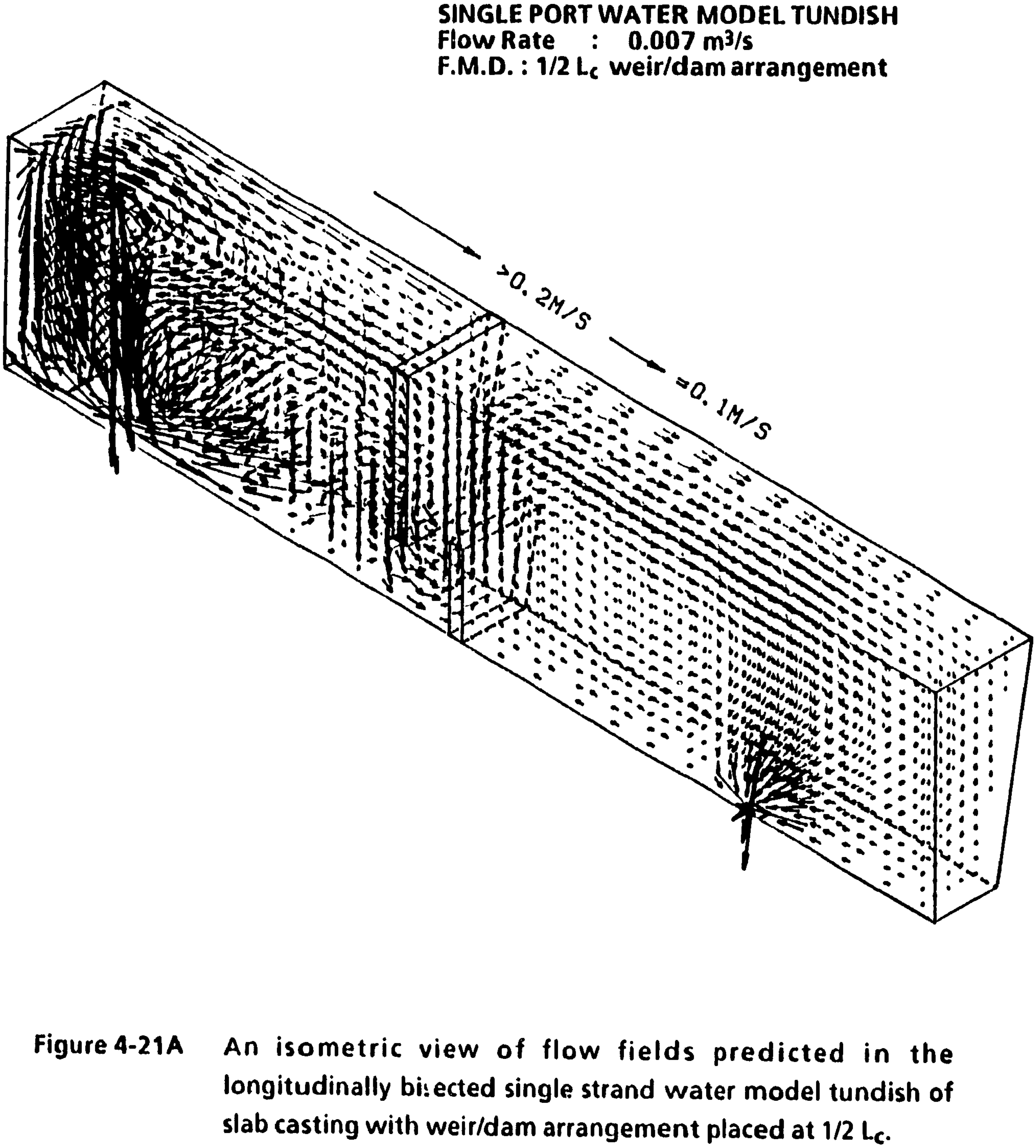

Figure 4-21A An isometric view of flow fields predicted in the longitudinally bisected single strand water model tundish of slab casting with weir/dam arrangement placed at 1/2 L_c.

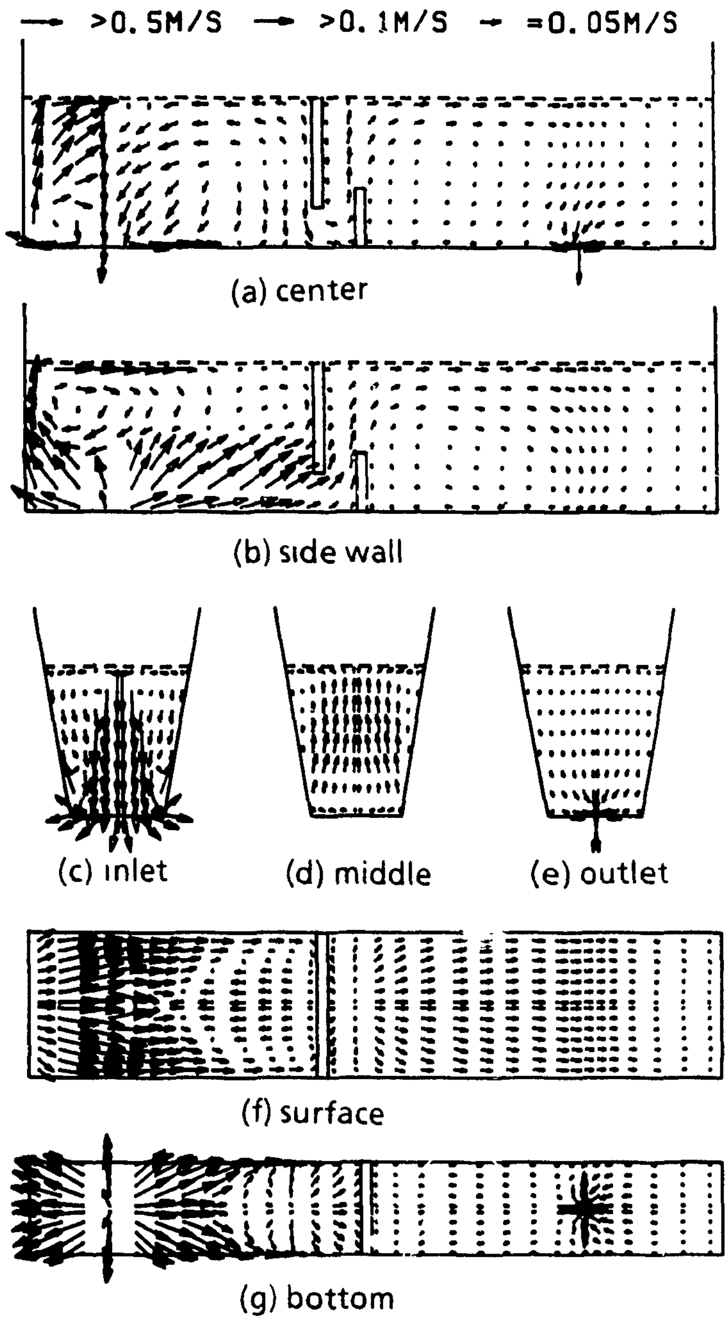

Figure 4-21B Predicted flow fields in some selected longitudinal planes (a, b), transverse planes (c, d, e), and horizontal planes (f, g) for the single strand water model tundish with weir/dam arrangement placed at 1/2 L_C.

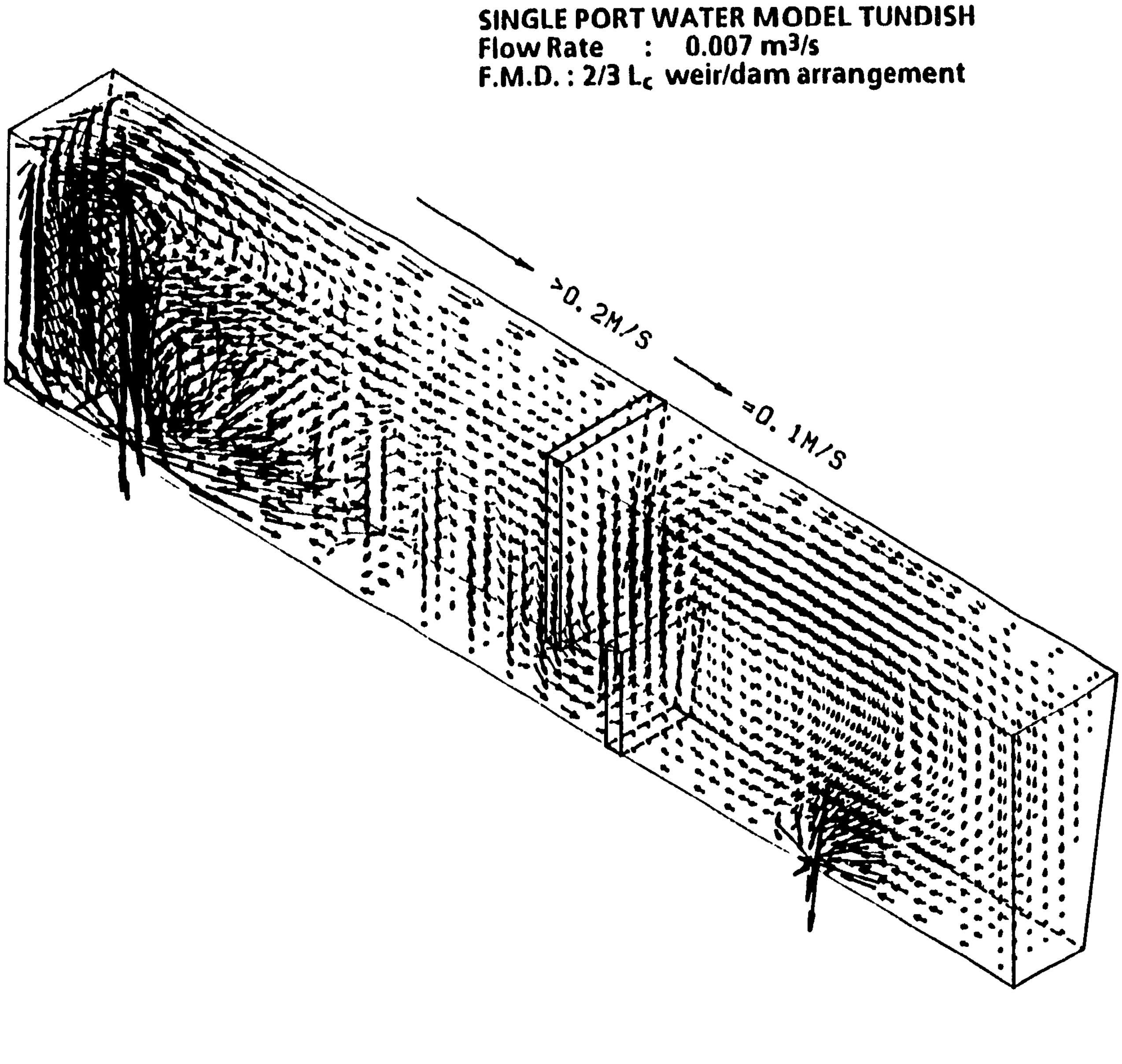

Figure 4-22A An isometric view of flow fields predicted in the longitudinally bisected single strand water model tundish of slab casting with weir/dam arrangement placed at 2/3 L_c.

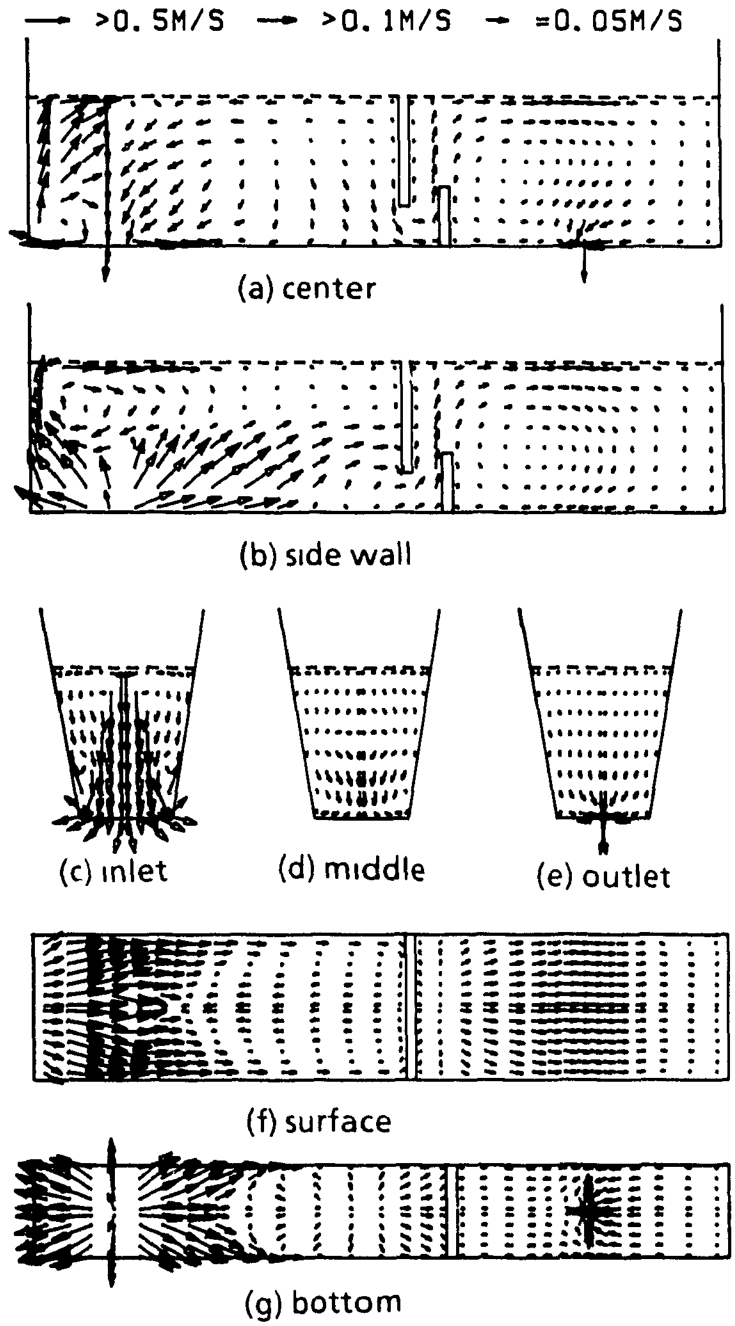

Figure 4-22B Predicted flow fields in some selected longitudinal planes (a, b), transverse planes (c, d, e), and horizontal planes (f, g) for the single strand water model tundish with weir/dam arrangement placed at 2/3 L_C.

inclusion float-out. The length of weir chosen penetrated to 0.8 m below the free surface, while the height of dam chosen was 0.45 m from the bottom The separation distance between the weir and dam was 0.3 m. These weir and dam combinations were used at $1/3L_C$, $1/2L_C$, and $2/3L_C$, so that their optimum placement could be determined (L_C represents the distance between inlet and outlet nozzle, 3.37 m).

Figure 4-20 shows the velocity fields given a $1/3L_C$ placement of the weir and dam arrangements. The flow pattern predicted for the region of the entering jet was similar to that for no flow modifications. As seen, once liquid reaches the weir, part of it generates an ascending flow up the weir's vertical face, swirling backwards to the inlet jet. Some of the liquid flows underneath the weir, and then vertically upwards towards the free surface between the weir and the dam. This flow then moves downstream towards the exit nozzle. The flow downstream of the dam/weir arrangements tends to exhibit more stable plug flow characteristics *vis a vis* the no flow modification flows. However, since the level of turbulence and shearing is high at the bounding surfaces of the weir and dam, their erosion and subsequent contamination of the melt refractory inclusions would be likely in practice.

Flow patterns at the $1/2L_C$ placement are shown in Figure 4-21. As seen, turbulence is predicted to diminish at the weir and dam location. Similarly, Figure 4-22 illustrates the velocity vectors for the case of $2/3L_C$ placement. It is appropriate to note that as the location of weir/dam combinations is moved away from the inlet nozzle, the plug-like-flow characteristic zone tends to be reduced.

4.2.2 Particle dispersion and separation

A comparison of inclusion residual ratios (i.e. those inclusions still present in the effluent stream expressed as a fraction of those entering) with water model experiment is provided in Figure 4-23 (a) and (b). As seen, while good agreement was achieved between predicted and measured R.R. values during the transient stage, predictions somewhat overestimate measured residual ratios at quasi steady state. As described previously, the model assumed that particles and solid walls were non-wetting to each other in the present study. This may not entirely correct and may be the cause for the slightly high values of particle residual ratios predicted at quasi steady state.

It is emphasized that this data refers to *quasi steady state* conditions, following the continuous injection of inclusions into the tundish. This is typically achieved after about three mean residence times (25 minutes), and corresponds to those conditions wherein inclusions within the recirculating flow zones have accumulated to steady levels, while those in stagnant zones continue to accumulate. This slow approach to steady state does not seem to have been recognised or appreciated in earlier work on tundishes (e.g. Ref. 1, 2, and 4)

Corresponding particle/inclusion separation curves at quasi steady state (30 minutes after feeding) for the dam and weir arrangements set up for the water model are shown in Figure 4-24. As seen, the residual ratio of very small inclusions is close to unity at all dam/weir combinations, and zero for all large inclusions. This is to expected, since very small particles will have minimal Stokes rising velocities and are therefore unable to separate, while particles with rising velocities in the order of 5-6 mm/sec. will have an adequate opportunity to accumulate in the top regions of the tundish.

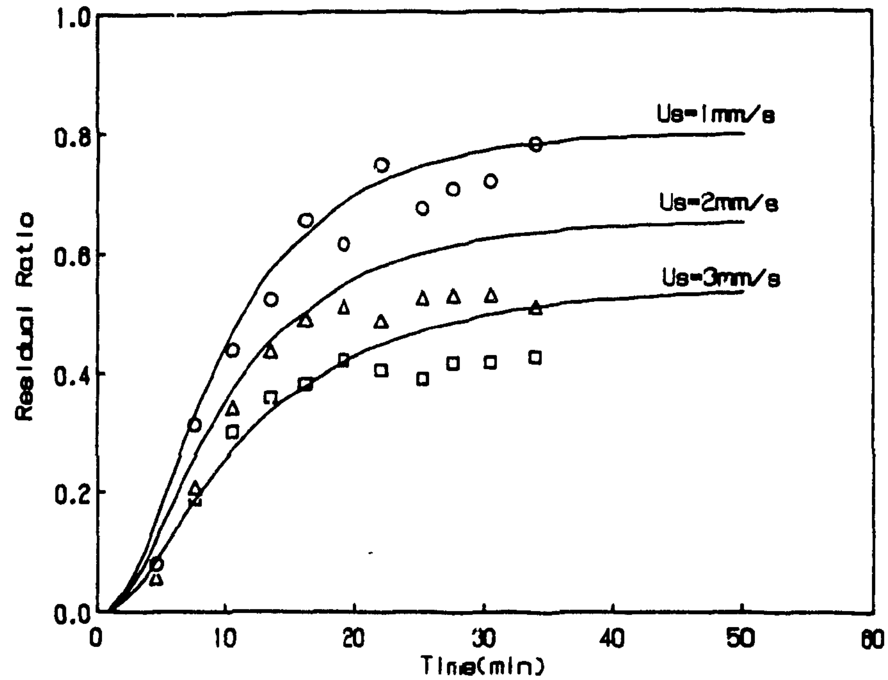

(a) no flow modification

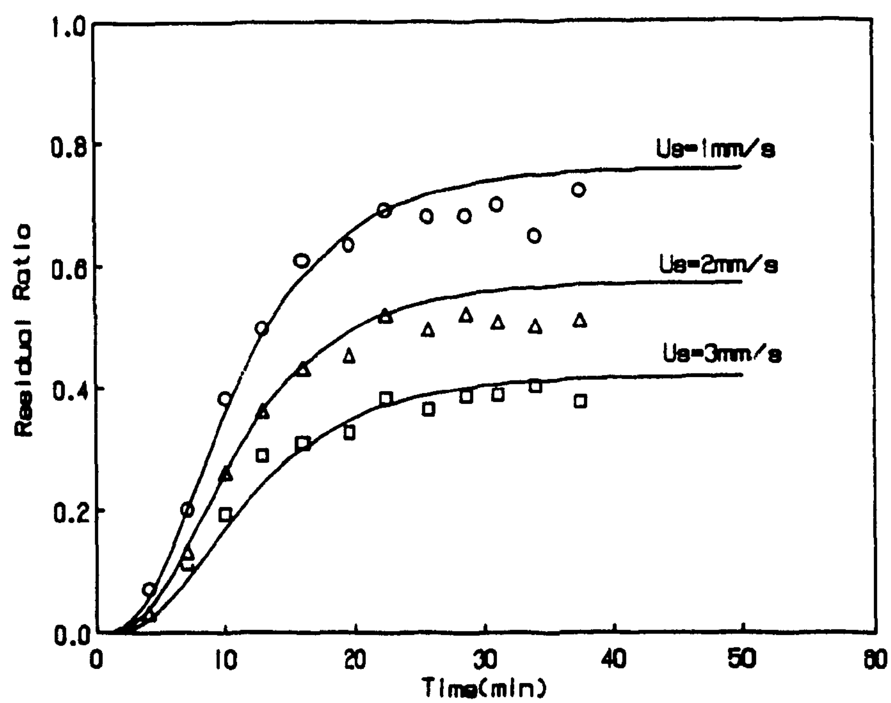

(b) flow modification

Figure 4-23 Comparison of experimentally measured and predicted particle separation ratio versus time of casting for the single strand water model tundish with (a) no flow modification and (b) flow modification (weir/dam arrangement placed at 1/2 L_c).

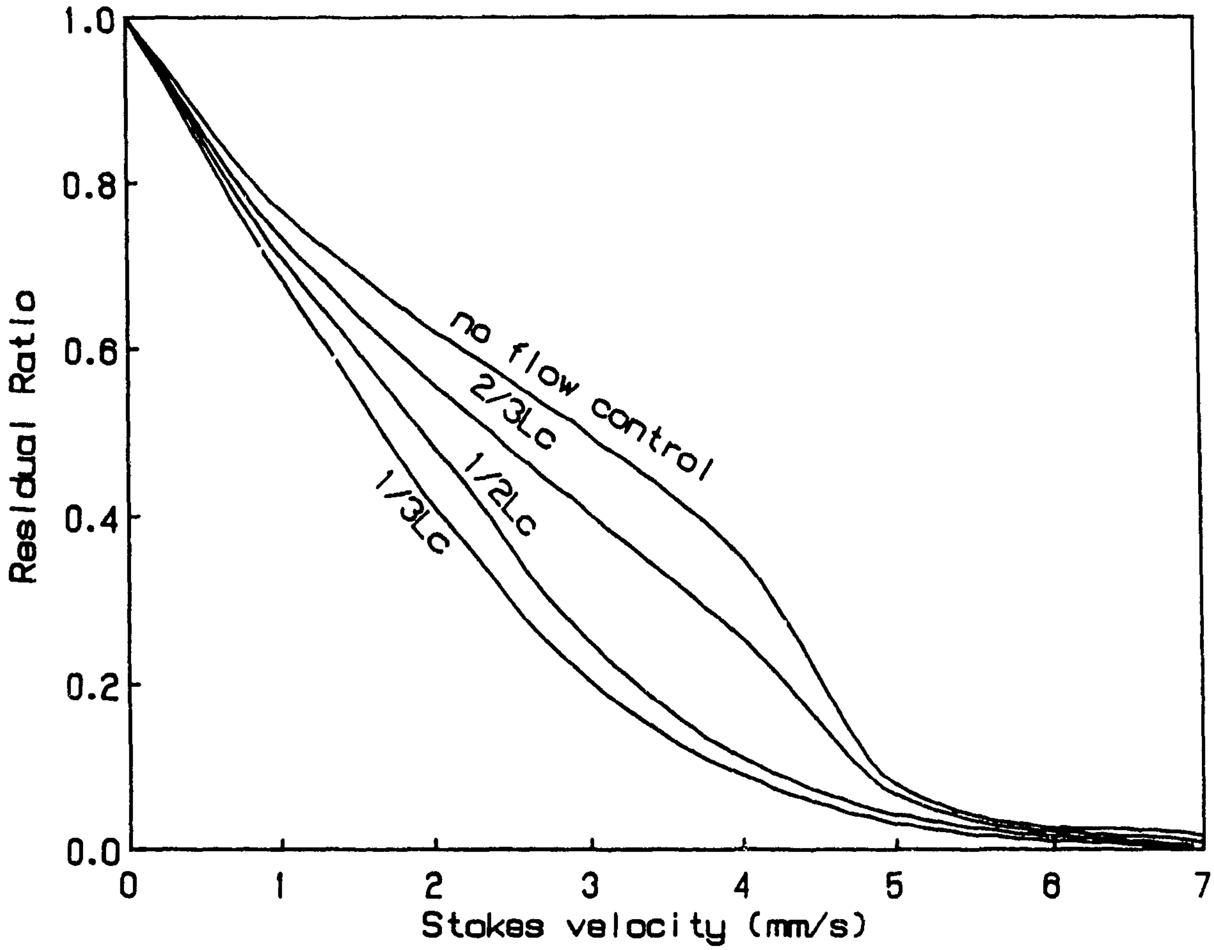

Figure 4-24 Relationship between the residual ratios of inclusion particles and Stokes rising velocities predicted for a full scale water model of slab casting tundish.

4.3 Application to Double Ported Water Model Tundish

Computations were also carried out for a tundish set up for twin bloom casting. The geometry and boundary conditions were taken to be exactly the same as those for single slab casting, but at a volumetric flow rate of 0.005 m^3/s.versus 0.0069 m^3/s.

Figures 4-25 and 4-26 provide computed velocity vectors of the flows developed within a full-scale water model tundish for no flow modification and for flow modification, respectively The flow patterns within the tundish are similar to those for the single ported slab casting arrangement except the effluent occurs at two outlet nozzles. It can be seen that the flows become weaker than those for slab casting, owing to the smaller volumetric flow rate at the inlet nozzle.

Figure 4-27 and Figure 4-28 present comparisons of the prediction and the experimental measurement of particle entrainment (a) at the inside port (nozzle A) and (b) at the far port (nozzle B) with no flow modification, and with flow modification, respectively. It can also be seen that predictions tend to over-evaluate particle residual ratios versus those measured experimentally. Nonetheless, the transient effects on R.R. are seen to be real and unmistakable.

Similarly, Figure 4-29 illustrates the relationship between inclusion residual ratios and Stokes rising velocity at both outlet nozzles with, and without, weir/dam arrangements under isothermal conditions. Since the outlet ports of this tundish are serially arranged, it is supposed that the quality of steel exiting the inside port should be poorer than that exiting the far port, there being less time for float-out with no flow control. Figure 4-29 (a) illustrates this point, while particle entrainment amounts at both outlet ports becomes approximately identical when a weir/dam arrangement is employed, as seen in Figure 4-29 (b).

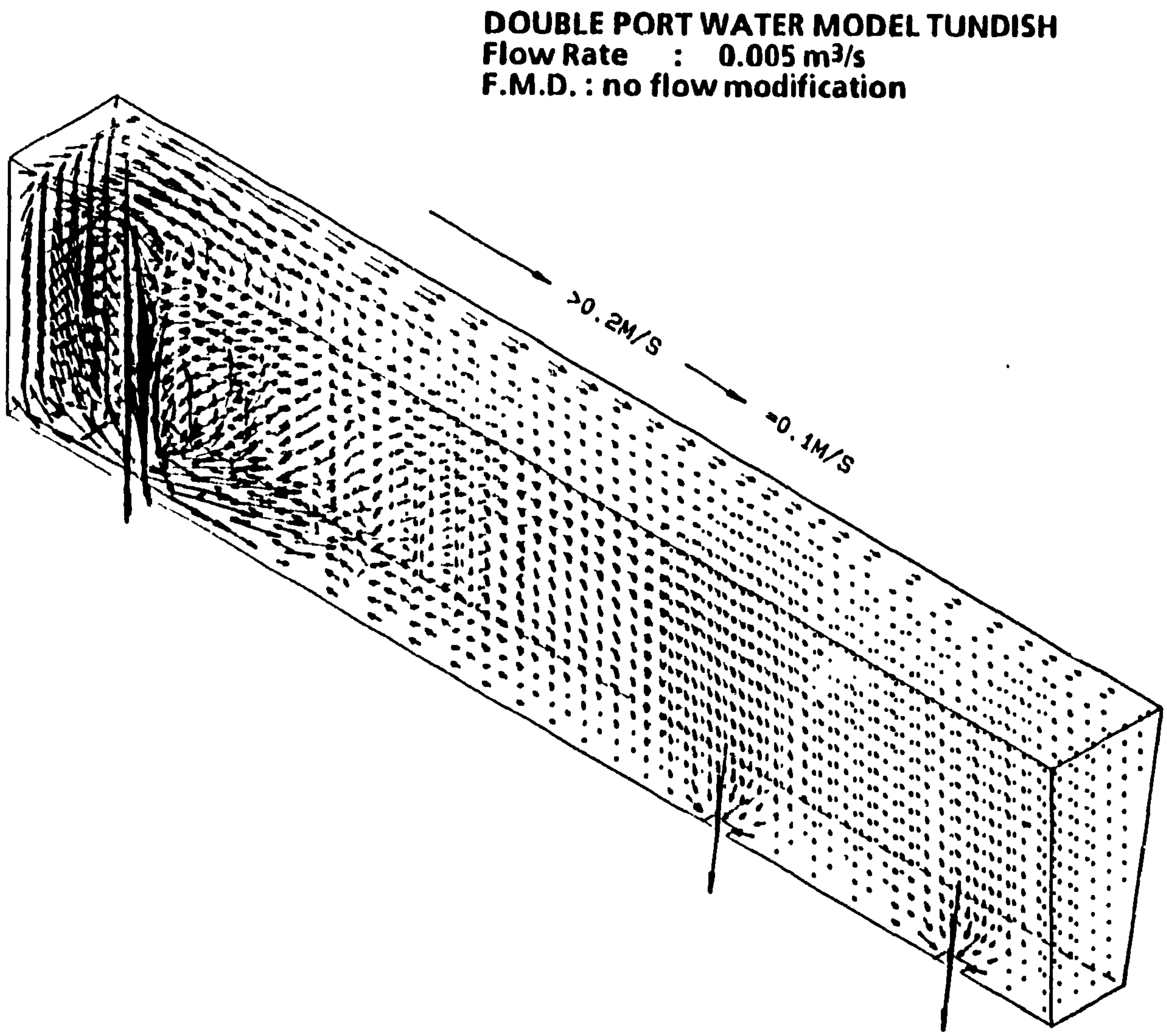

Figure 4-25A An isometric view of flow fields predicted for a half volume of the water model tundish (isothermal conditions) set up for twin bloom casting with no flow modification device.

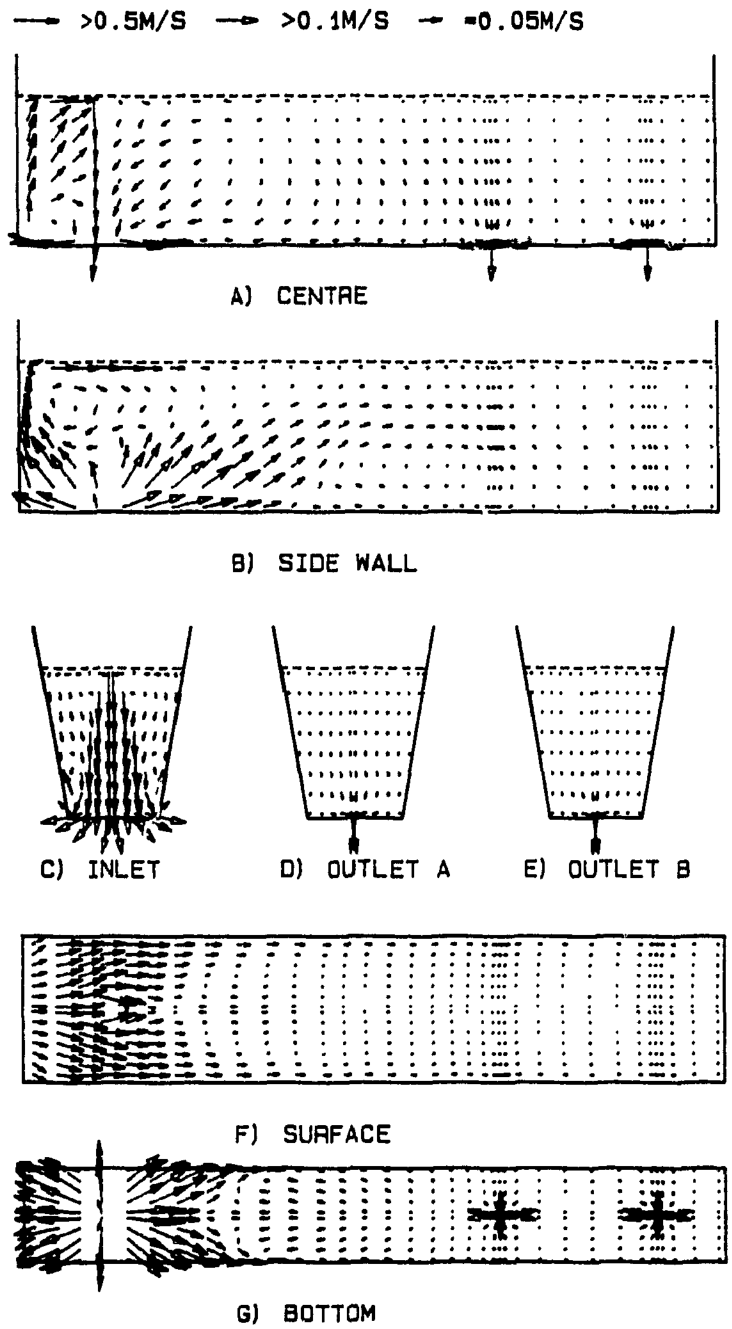

Figure 4-25B Predicted flow fields in some selected two-dimensional planes for the double strand water model tundish (isothermal conditions) with no flow modification device.

DOUBLE PORT WATER MODEL TUNDISH
Flow Rate : 0.005 m³/s
F.M.D. : flow modification (weir/dam)

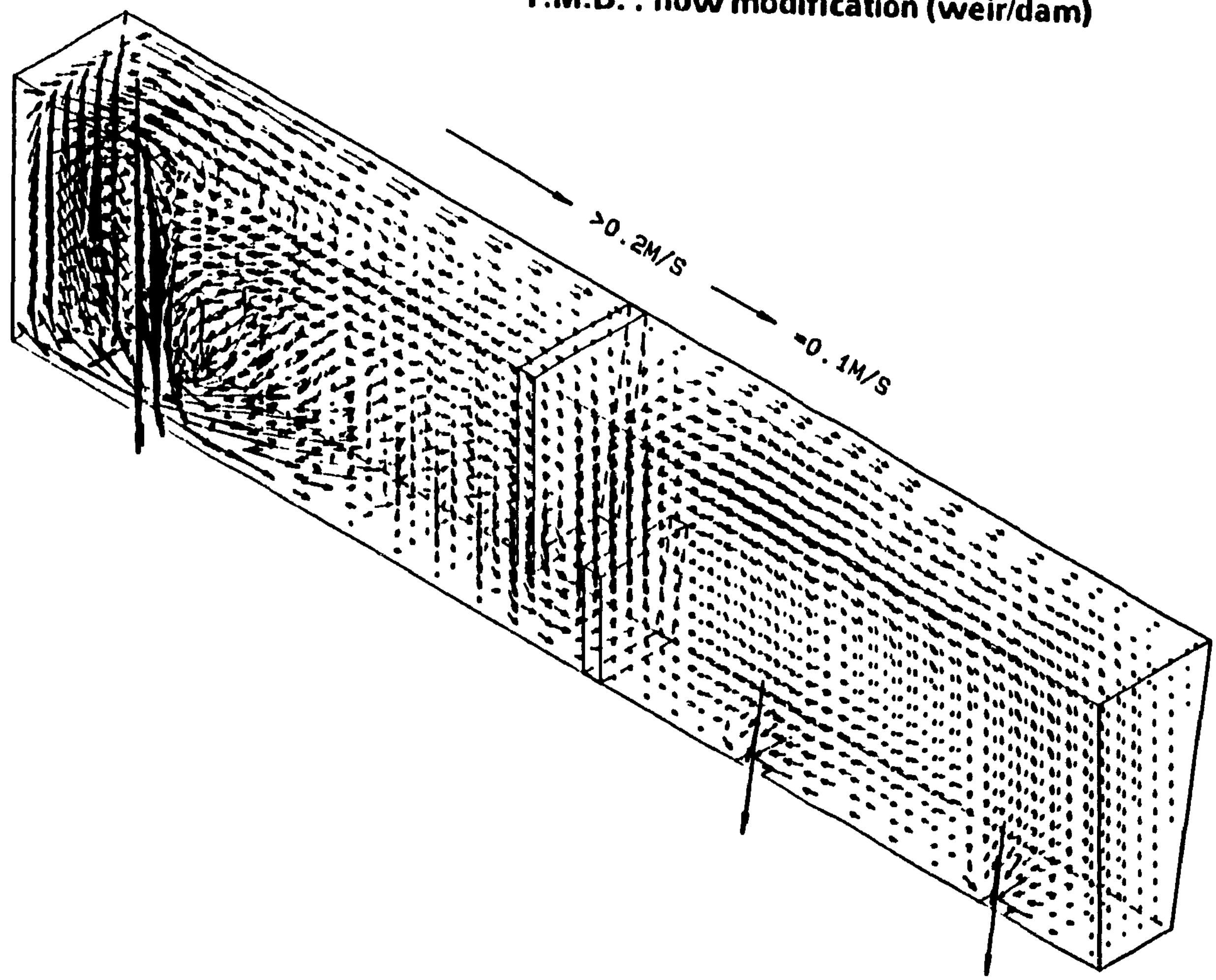

Figure 4-26A An isometric view of flow fields predicted for a half volume of the water model tundish (isothermal conditions) set up for twin bloom casting with flow modification.

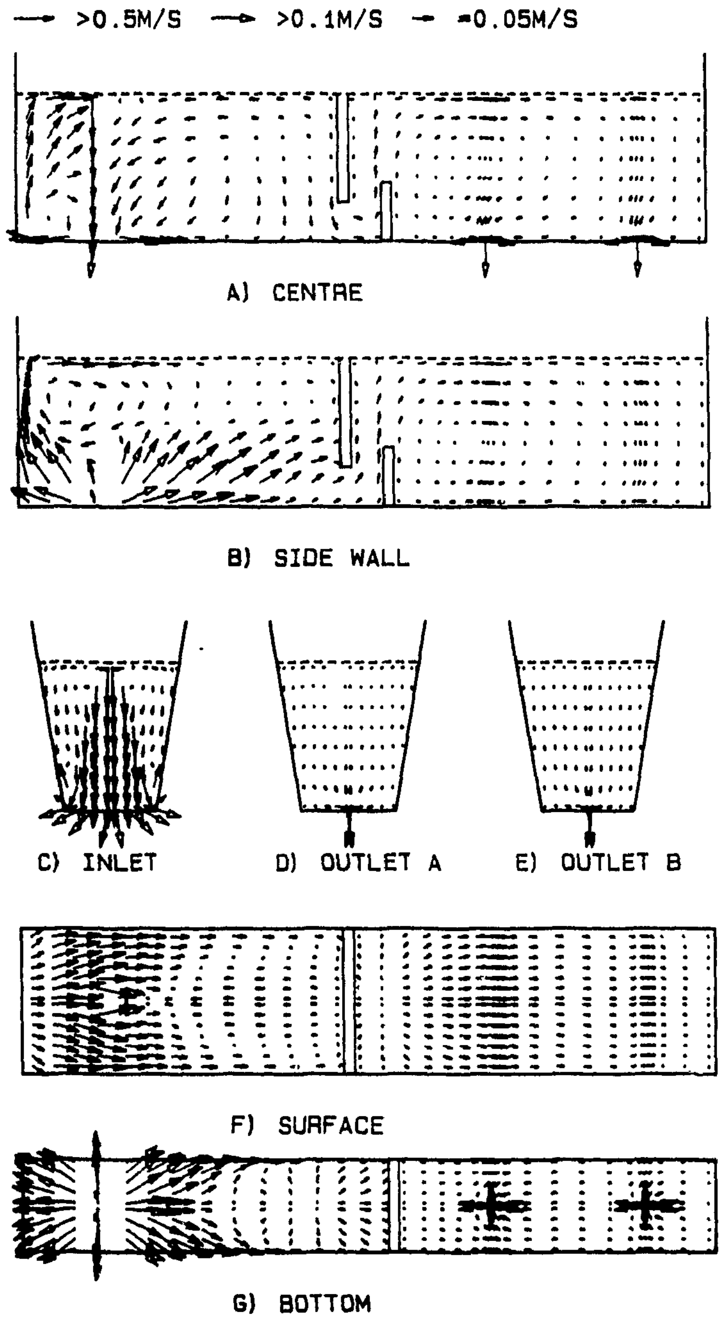

Figure 4-26B Predicted flow fields in some selected two-dimensional planes for the double strand water model tundish (isothermal conditions) with flow modification.

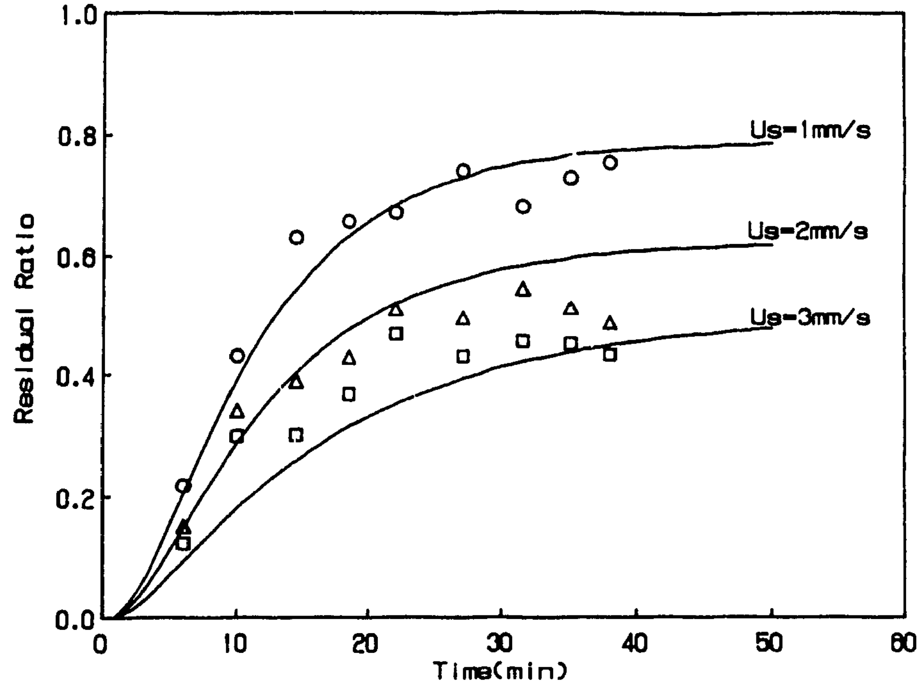

(a) the inside port

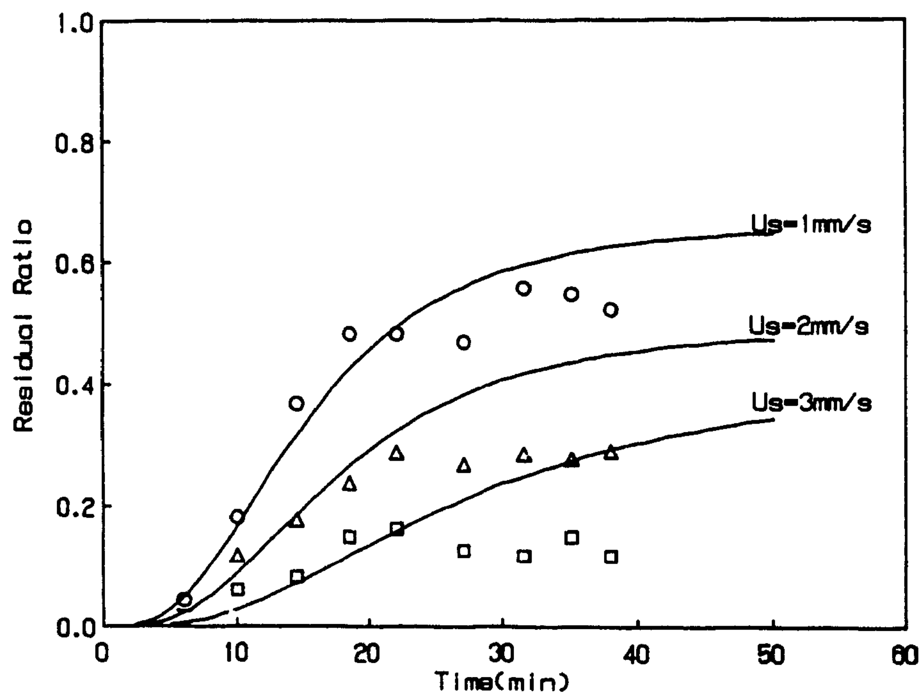

(b) the outside port

Figure 4-27 Comparison of experimentally measured and predicted particle separation ratio versus time of casting at (a) the inside port (nozzle A) and (b) the far port (nozzle B) of a full scale water model tundish for twin bloom casting arrangement without flow modification device

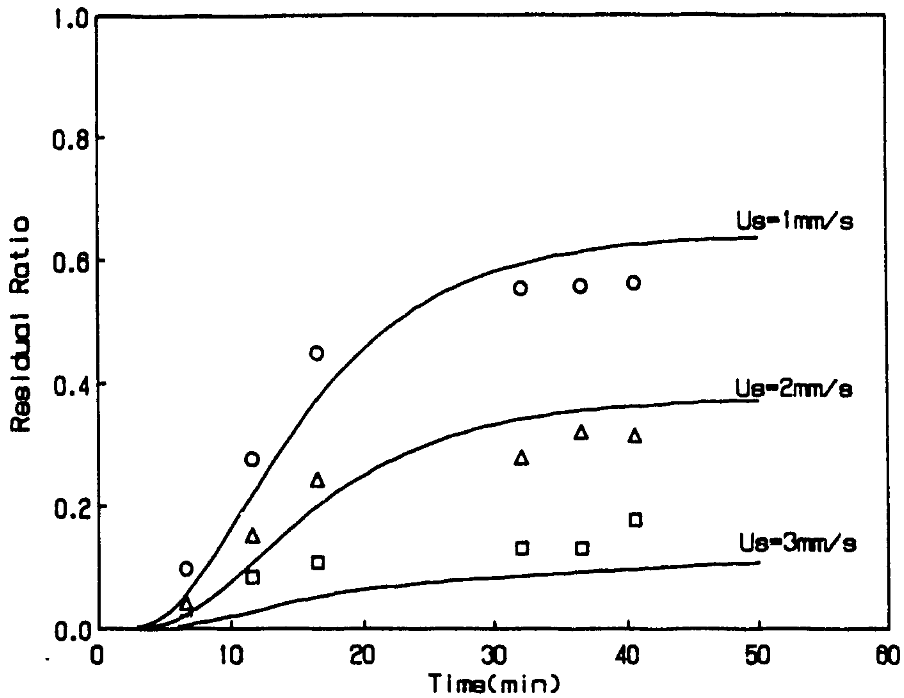

(a) the inside port

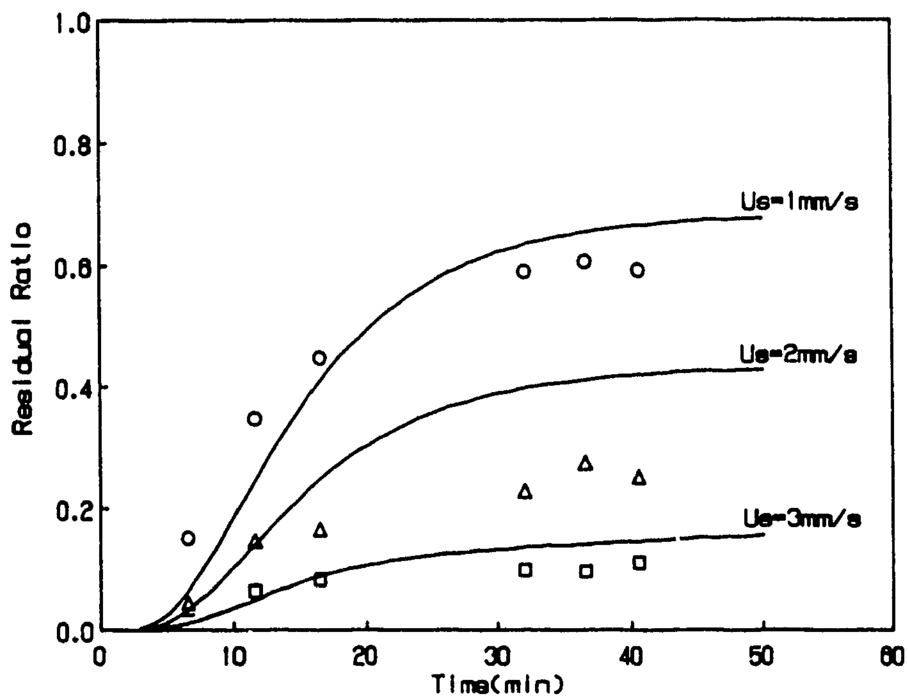

(b) the outside port

Figure 4-28 Comparison of experimentally measured and predicted particle separation ratio versus time of casting at (a) the inside port (nozzle A) and (b) the far port (nozzle B) of a full scale water model tundish for twin bloom casting arrangement with weir/dam arrangement.

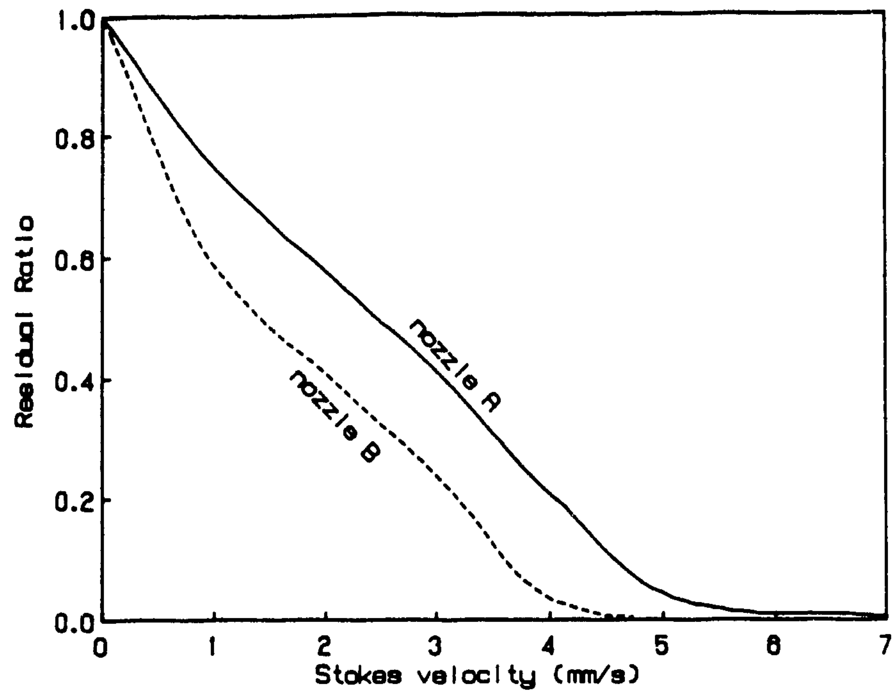

(a) no flow modification

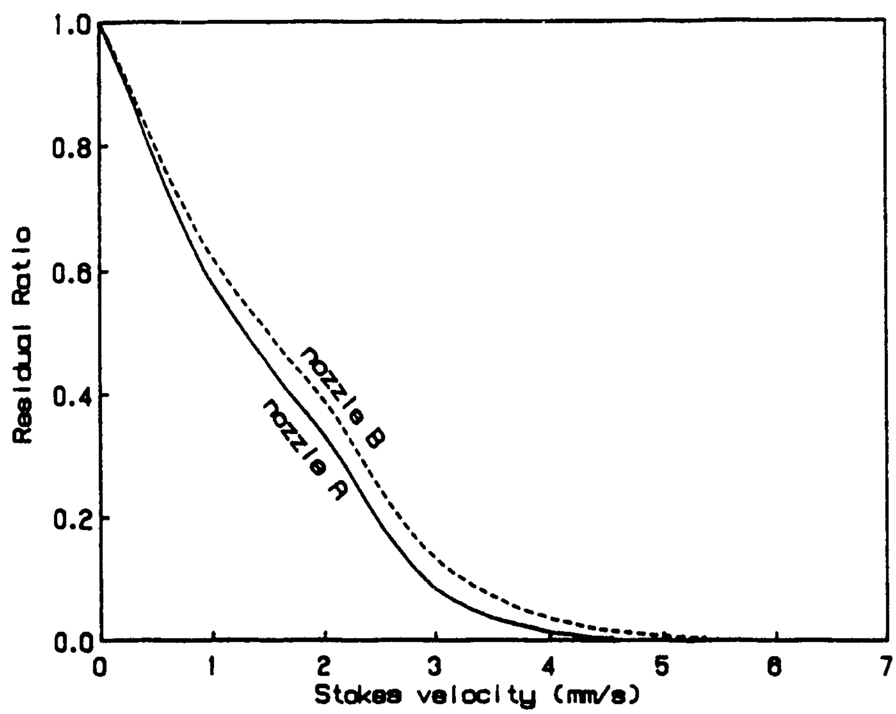

(b) flow modification

Figure 4-29 Relationship between the residual ratios of inclusions and Stokes rising velocities at exit nozzles of the tundish set for twin bloom casting with (a) no flow modification and (b) flow modification.

Chapter 5

Differential Equation Model II

: Application to Industrial Systems (Non-isothermal Conditions)

5.1 Theory

5.1.1 Role of thermal natural convection

The computational work described in Chapter 4 was performed under isothermal conditions for comparison with water model data However, in real tundish operations , significant drops in metal temperature can occur between entry and exit points[20]. Consequently, the probability of thermal natural convection currents modifying flow patterns and inclusion float-out deserves more careful attention than that received to date by process metallurgists.

In estimating the likely importance of natural convection, the dimensionless parameter, Gr/Re^2 is a measure of its relative magnitude in relation to forced convection. When $Gr/Re^2 = 1$, natural convection fluxes are of same order of magnitude as forced convective fluxes, so that both must be considered. Mathematically,

$$\frac{Gr}{Re^2} = \frac{g\beta\Delta TL}{u^2} \tag{4-24}$$

where β is the volumetric expansion coefficient, defined as

$$\beta = -\frac{1}{\rho}\left(\frac{d\rho}{dT}\right)_p \tag{4-25}$$

The relationship between the density of steel and melt temperature is represented by(19)

$$\rho = 8523 - 0\ 8358T \qquad (kg/m^3) \tag{4-26}$$

Combining Equations 4-24, 4-25 and 4-26 gives

$$\frac{Gr}{Re^2} = \frac{0\ 8358g\Delta TL}{\rho u^2} \tag{4-27}$$

Introducing $\rho = 7000$ kg/m3, $g = 9.81$ m/s2, $L = 1.1$ m (height of the tundish) and $u = 0.022$ m/s (average flow velocity within the tundish) into Equation 4-27, the factor Gr/Re^2 reduces to

$$\frac{Gr}{Re^2} \simeq 2\ 66\Delta T \tag{4-28}$$

As seen from this equation, even a small temperature drop (of say 1°C) would make natural convection currents significant in such a large tundish. One can anticipate that any natural convection effects will be particularly important at the end walls of tundishes owing to small flow velocities and larger heat losses in those regions.

5.1.2 Numerical procedures

In this work, the *METFLO* code was extended to take into account the role of thermal natural convection. This has typically been neglected in previous computational models presented by the authors and others engaged in tundish studies (8,9,11,28). In order to describe fluid flow, heat transfer and particle (inclusion) float-out in industrial tundishes, the relevant partial differential equations requiring (numerical) solution are the equations of continuity, momentum, energy and species conservation, expressed in cartesian form.

In the discretisation of these equations for numerical solution, a rectangular grid of elemental fluid volumes, or cells, was again used. In order to allow for curved, or inclined surfaces, cell blockage procedures were adopted once more. Only a symmetrical volume of each tundish was taken into consideration for computation (i.e. a symmetrical half volume for Stelco tundishes and BHP wedge-shaped tundish, and a symmetrical quadrant for Dofasco and BHP's trough-shaped tundishes). In order to ensure that the results were independent of grid size, relatively fine grids of 18 (vertical) × 40 (longitudinal) × 18 (transverse) were chosen. Particuarly, for the visualization of metallurgical transport phenomena by a graphic video movie (section 5.8), the tundish elements in the No. 2 BHP tundish occupied a finer grid of 40 × 80 × 40 matrix, for the x, y and z vectors. Computations were carried out on a family of CRAY computers, including the CRAY-1S machine at the Dorval Weather Center, Montreal, Canada, and the CRA- YMP machine at CRAY RESEARCH, Mendota Heights, Minnesota, U.S.A. About 3000 iterations were required to achieve fully converged results, this taking 1 hour machine time with the Cray-1S supercomputer. The finer grids (40 × 80 × 40 matrix) required four hours of machine time for converged solutions using the CRAY-YMP machine

5.1.3 Boundary conditions

In extending the *METFLO* code to include thermal natural convection phenomena, a set of typical boundary conditions was chosen. These included steady state flows and heat losses, and an overlaying slag wetting to inclusions.

(a) heat transfer

In modelling heat losses through the side-walls and surface of steel in the tundish, steady state heat conduction was, as noted, assumed. Various constant heat flux conditions for the upper, side and bottom surfaces were specified Figure 4-30 shows the profile of insulating material for BHP operations: a 20 mm layer of Catoleum K411 gunning material, in contact with liquid steel, is followed by a 115 mm thick wearing lining, and a 50 mm thick safety lining of pyrophyllite adjacent to a 12 mm thick lining of steel.

The boundary heat flux from the exterior side walls was obtained according to

$$q_w'' = h_w(T_w - T_a) + \varepsilon_w \sigma(T_w^4 - T_a^4) \tag{4-29}$$

where the first and the second terms on the right side of the equation represent heat loss by natural convection and by radiation, respectively. The values of important parameters and heat loss from the side walls, were based on thermocouple implant tests, and are listed in Table 4-5.

For estimating surface heat losses from the steel, it was assumed that these were radiative in nature with an absorbent slag. The slag was assumed to be liquid, 30 mm thick, and motionless, with a thermal conductivity of 4.0 W/m°K. The resulting heat fluxes and temperatures at the free surface of the tundish were deduced as part of the overall iterative procedures already described. The input temperature of the melt at the inlet nozzle was taken to be 1575 °C. Mean heat flux through the slag was estimated to be $\simeq$28 kW/m2. Table 4-6 gives the relevent thermal properties taken for these calculations.

Table 4-5 Important parameters and heat loss from the side walls

h_w(W/m^2°K)	σ(W/m^2°K^4)	ε_w	T_w(°K)	T_a(°K)	q_w(kW/m^2)
6.738	5.67x10^{-8}	0.9	448	298	2.6

Table 4-6 Thermal data for slag and side-walls.

Material	Value (W/mK)
Safety Lining -Pyrophyllite Brick	0.95
Wearing Lining - ZAP75 or KALA	2.10
Gunning Material - Catoleum K411	0.15
Molten layer of slag	4.0
Emissivity of slag	0.9

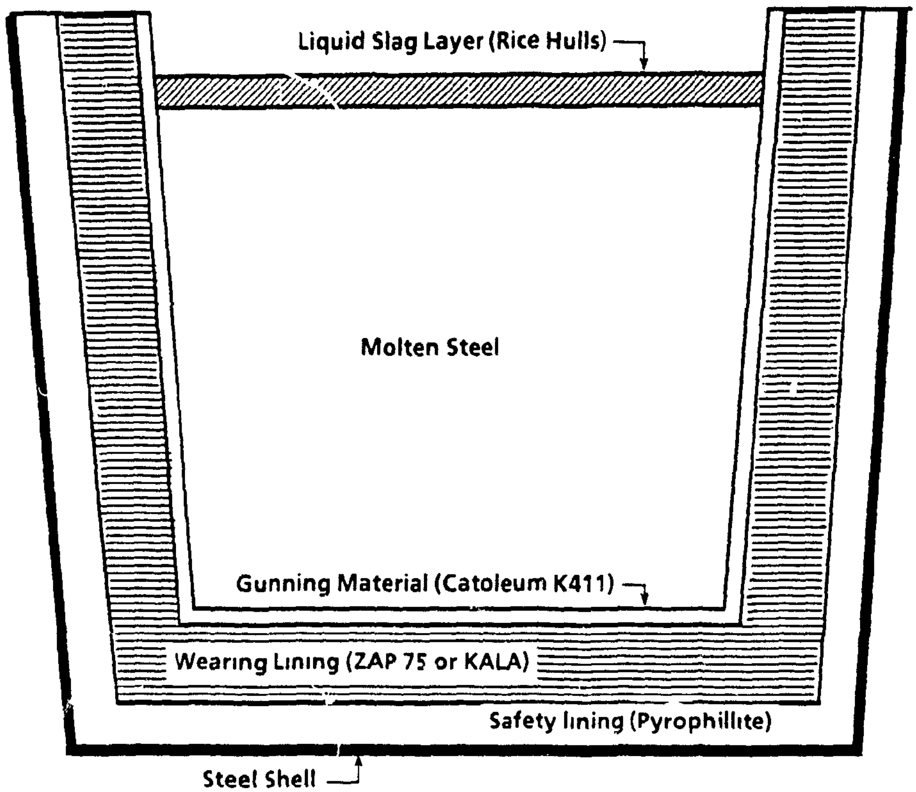

Figure 4-30 Tundish refractory practices at BHP Port Kembla works.

(b) inclusion behaviour

For particle/inclusion float-out, the number of particles separating to the surface of the melt was assumed to follow Stokesian behaviour, wherein the inclusions, being wetting with respect to the overlaying slag, were totally absorbed at the slag/metal interface. This leads to the inclusion flux equation:

$$\dot{n} = u_s C^* \tag{4-30}$$

where C* represents the stagnant boundary layer number density of mono-sized inclusions with a Stokes rising velocity of u_s. The analysis further assumed that the side-walls, and bottom of the tundish were non-wetting (reflecting) to inclusions. Similarly, potential agglomeration/coalescence phenomena within the tundish were not modelled.

5.2 Stelco's Single Port Tundish

5.2.1 Fluid flow and temperature distributions

Figures 4-31A and B present computed flow patterns for no flow control, wherein both forced and natural convection of liquid steel (non-isothermal conditions) were taken into account. In these computations, an input temperature of 1580 °C and an overlaying slag thickness of 30 mm were considered together with side wall heat losses corresponding to steady state conduction through the insulating side boards and brick work of a typical tundish ($q'' = 2.6 \text{kW/m}^2$).

One can immediately see that the flow patterns are markedly different to those in Figure 4-19 for isothermal conditions. The main difference is a much stronger flow down the side and particularly end walls of the tundish, coupled with a strong flow along the bottom surface. Furthermore computations suggest that the average flow speed in Stelco's real tundish was increased to 40 mm/sec., twice that in the full scale water model tundish.

Figures 4-32, 4-33, and 4-34 illustrate how flow patterns are modified when weir and dam (W/D) arrangements are introduced. In order to study the effect of the F.M.D. position, W/D arrangements were placed at $1/3L_c$, $1/2L_c$ and $2/3L_c$, respectively. It can again be seen from the figures that heat loss through the sidewalls and slag surface leads to much stronger downflows at the side and end walls, and a much stronger zone of recirculation to the right of the W/D arrangement.

Figure 4-35 provides the corresponding isotherms within the molten steel at longitudinal vertical planes located at the axisymmetrical center line for no flow modification (NFM) and for flow modification (FM). As seen, the net drop in temperature for the conditions modelled was about 14°C, the jet entering at 1580 °C and exiting at 1566 °C. Temperature drops were not significantly improved using W/D arrangements, but relatively more uniform temperature distributions were predicted. The mean bulk temperature of molten steel was predicted to be about 1570 °C.

STELCO'S HILTON WORK SLAB CASTING TUNDISH

Casting Rate : 3 ton/min (0.007 m^3/s)

F.M.D. : no flow modification

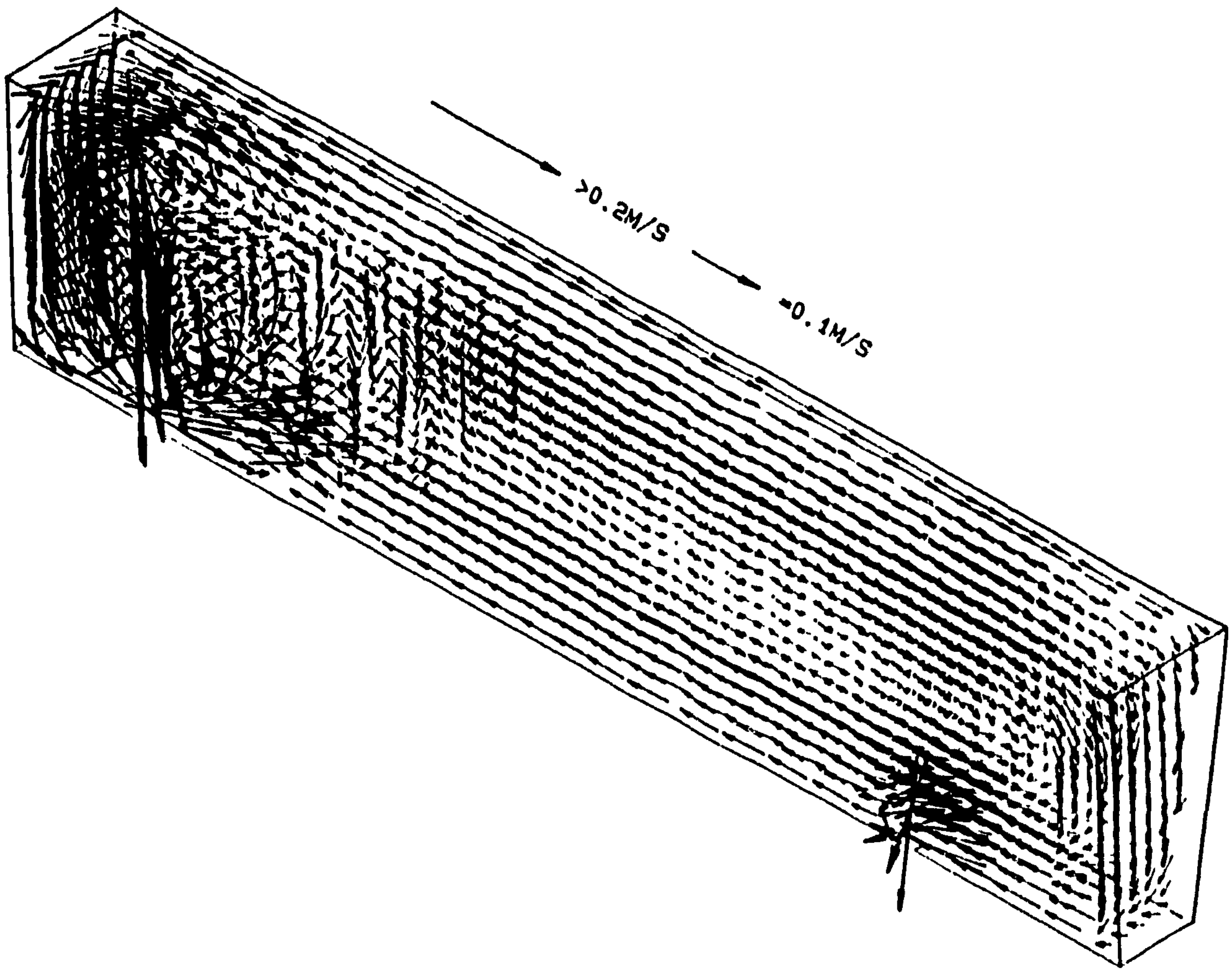

Figure 4-31A An isometric view of molten steel flow fields (non-isothermal conditions) predicted in the longitudinally bisected single port tundish of slab casting Stelco's Hilton Works without flow modification device.

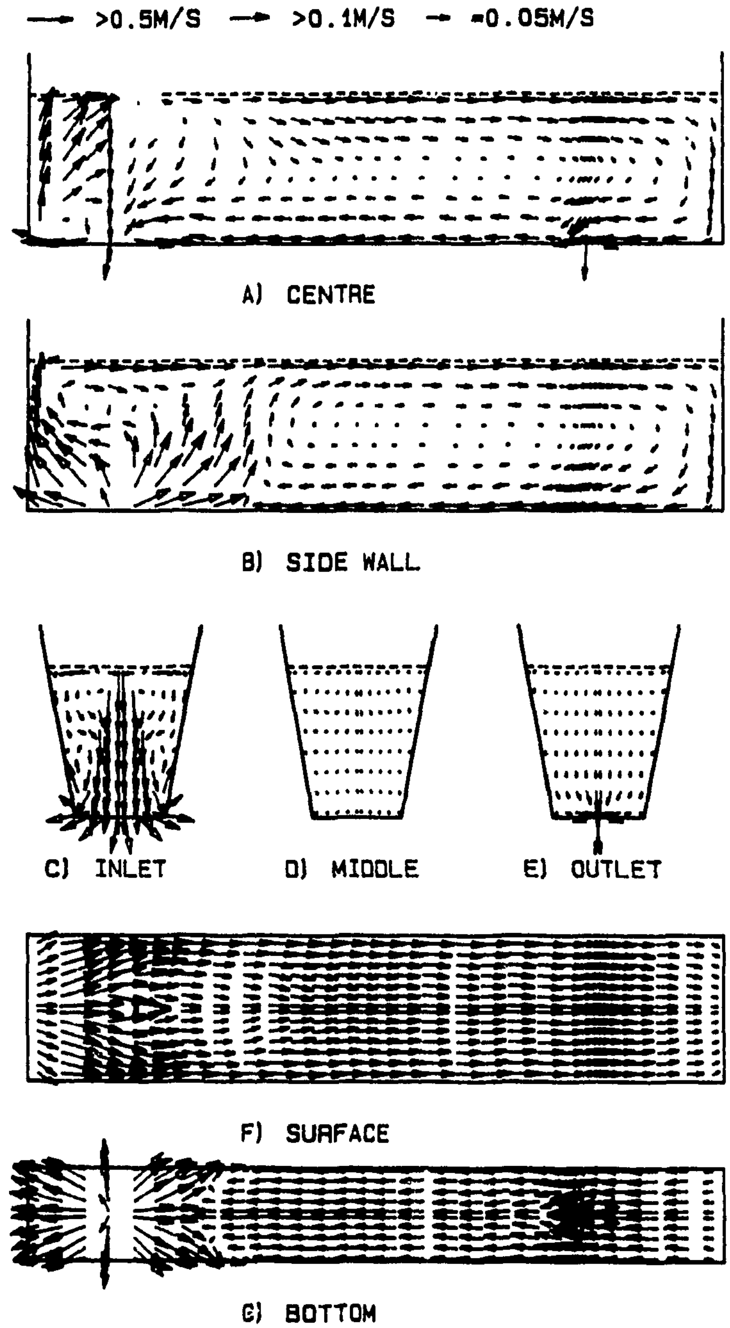

Figure 4-31B Predicted flow fields of molten steel in some selected longitudinal planes (a, b), transverse planes (c, d, e), and horizontal planes (f, g) for the single port tundish without flow modification device.

STELCO'S HILTON WORK SLAB CASTING TUNDISH

Casting Rate : 3 ton/min (0.007 m^3/s)

F.M.D. : 1/3 L_c weir/dam arrangement

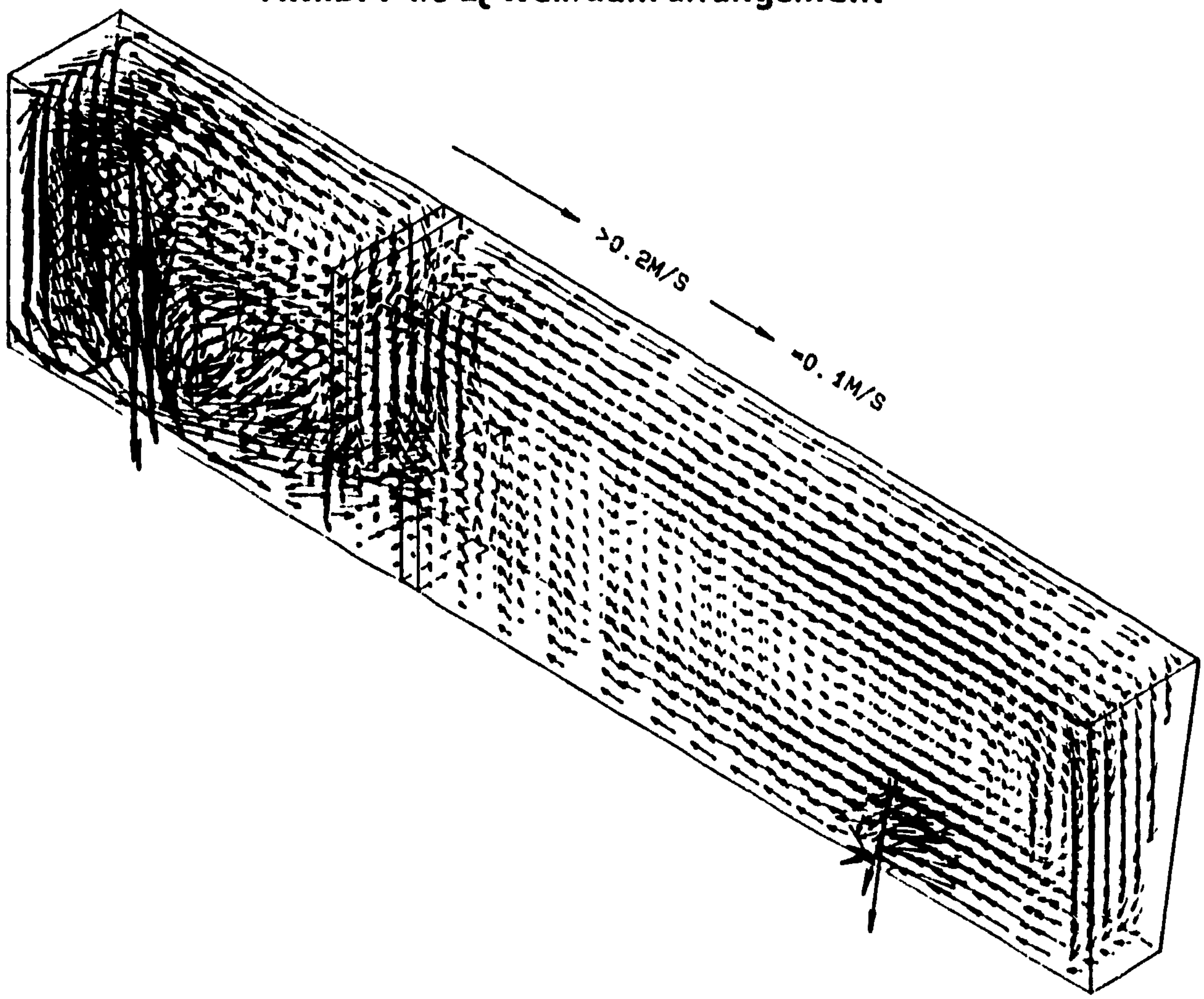

Figure 4-32A An isometric view of molten steel flow fields predicted in the longitudinally bisected single port tundish of slab casting Stelco's Hilton Works with weir and dam arrangements placed at 1/3 L_c.

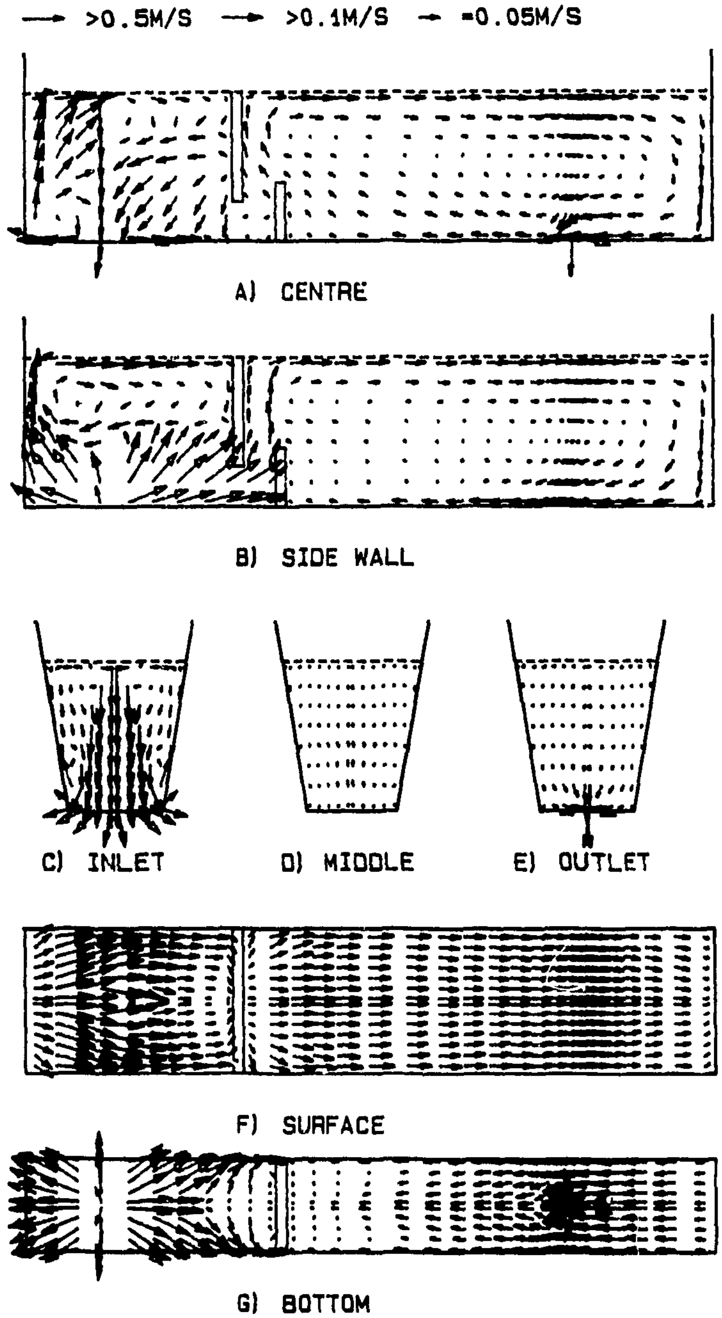

Figure 4-32B Predicted flow fields of molten steel in some selected two-dimensional planes for the single port tundish with weir and dam arrangements placed at 1/3 L_c.

STELCO'S HILTON WORK SLAB CASTING TUNDISH

Casting Rate : 3 ton/min (0.007 m^3/s)

F.M.D. : 1/2 L_c weir/dam arrangement

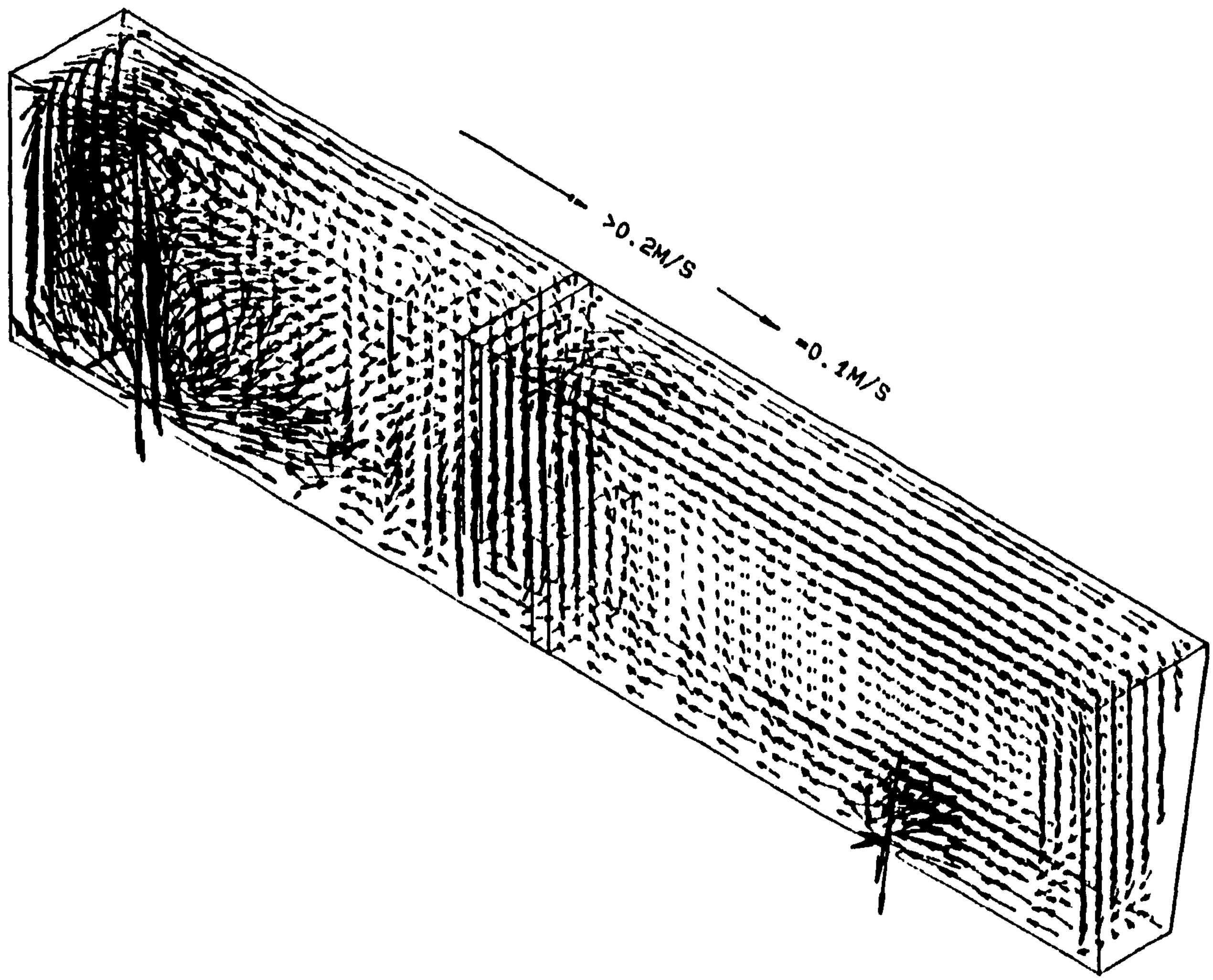

Figure 4-33A An isometric view of molten steel flow fields predicted in the longitudinally bisected single port tundish of slab casting Stelco's Hilton Works with weir and dam arrangements placed at 1/2 L_c.

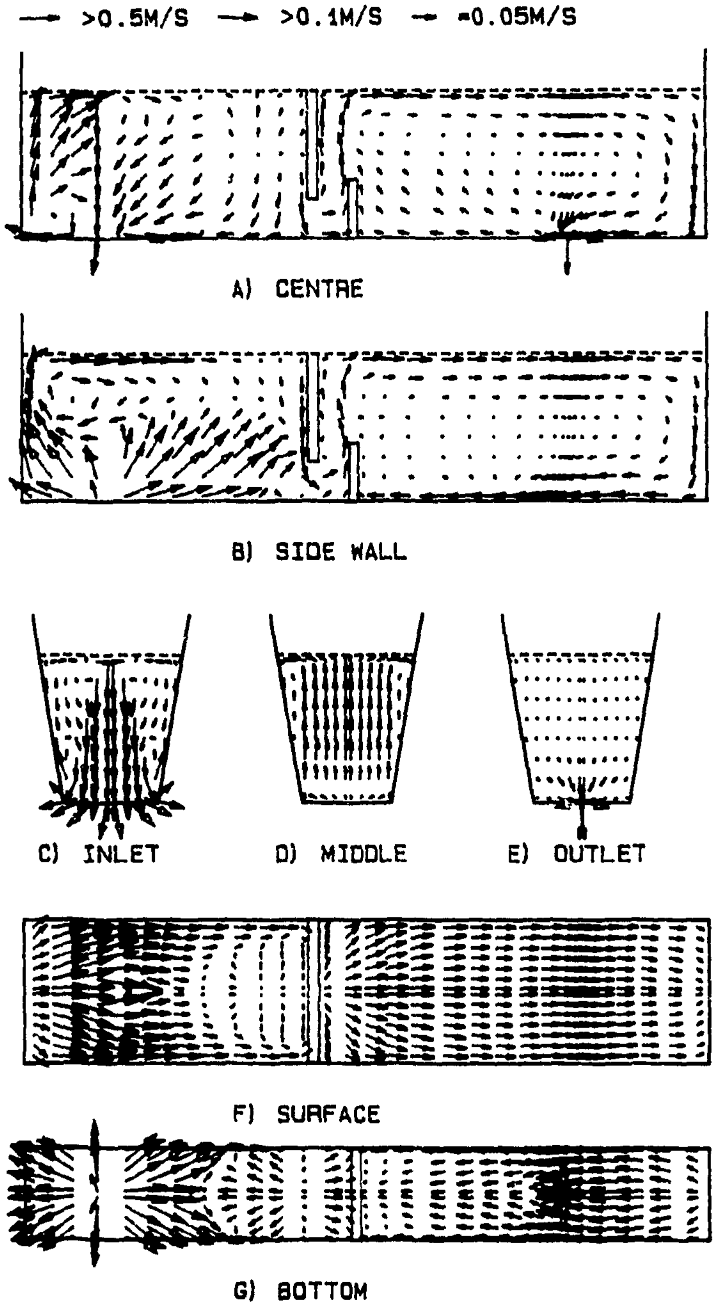

Figure 4-33B Predicted flow fields of molten steel in some selected two-dimensional planes for the single port tundish with weir and dam arrangements placed at 1/2 L_c.

STELCO'S HILTON WORK SLAB CASTING TUNDISH

Casting Rate : 3 ton/min (0.007 m^3/s)

F.M.D. : 2/3 L_c weir/dam arrangement

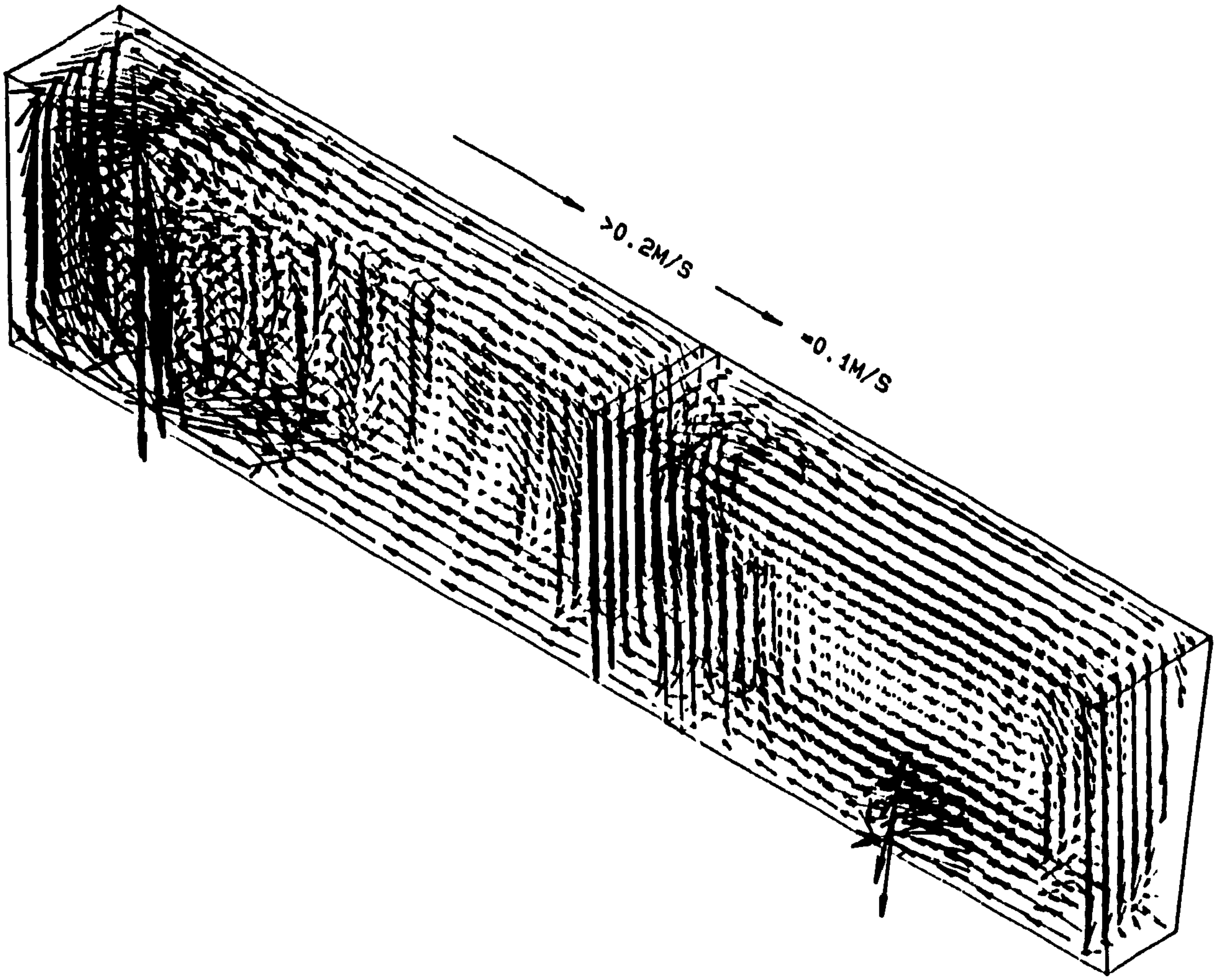

Figure 4-34A An isometric view of molten steel flow fields predicted in the longitudinally bisected single port tundish of slab casting Stelco's Hilton Works with weir and dam arrangements placed at 2/3 L_c.

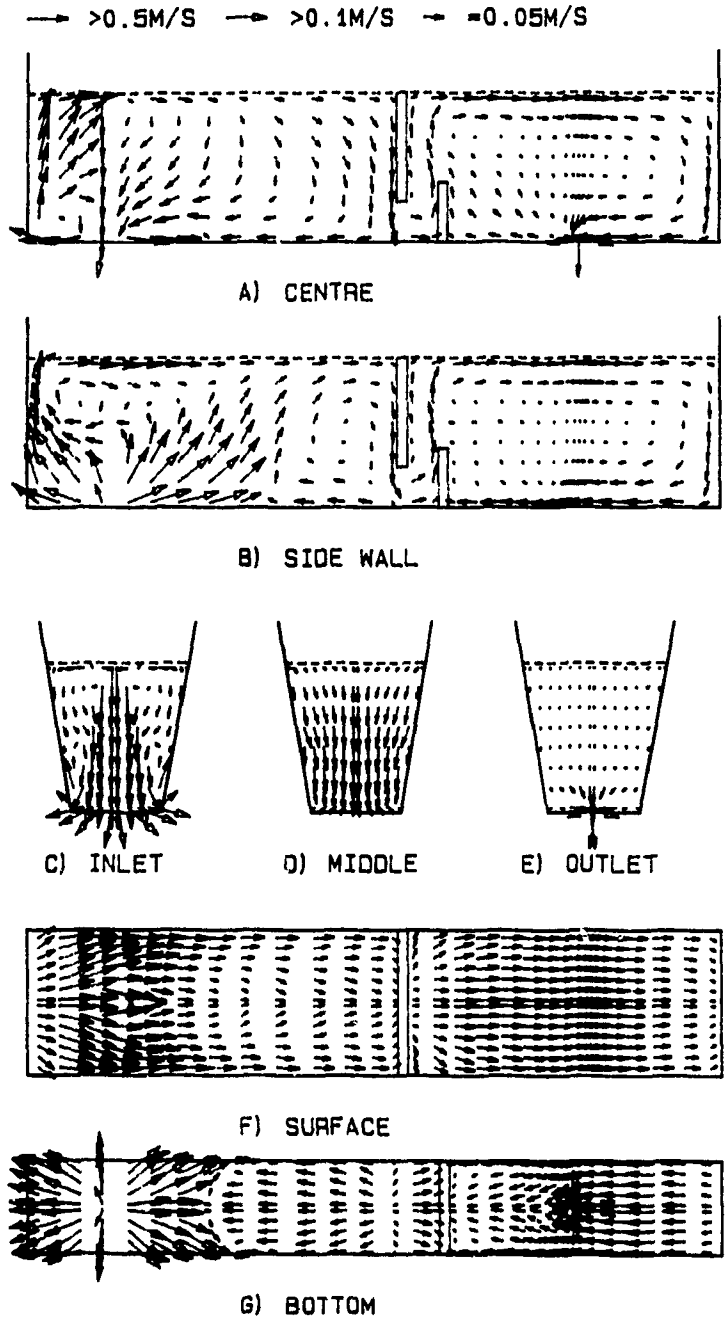

Figure 4-34B Predicted flow fields of molten steel in some selected two-dimensional planes for the single port tundish with weir and dam arrangements placed at 2/3 L_C.

TEMPERATURE DISTRIBUTIONS
Input temperature : 1580°C

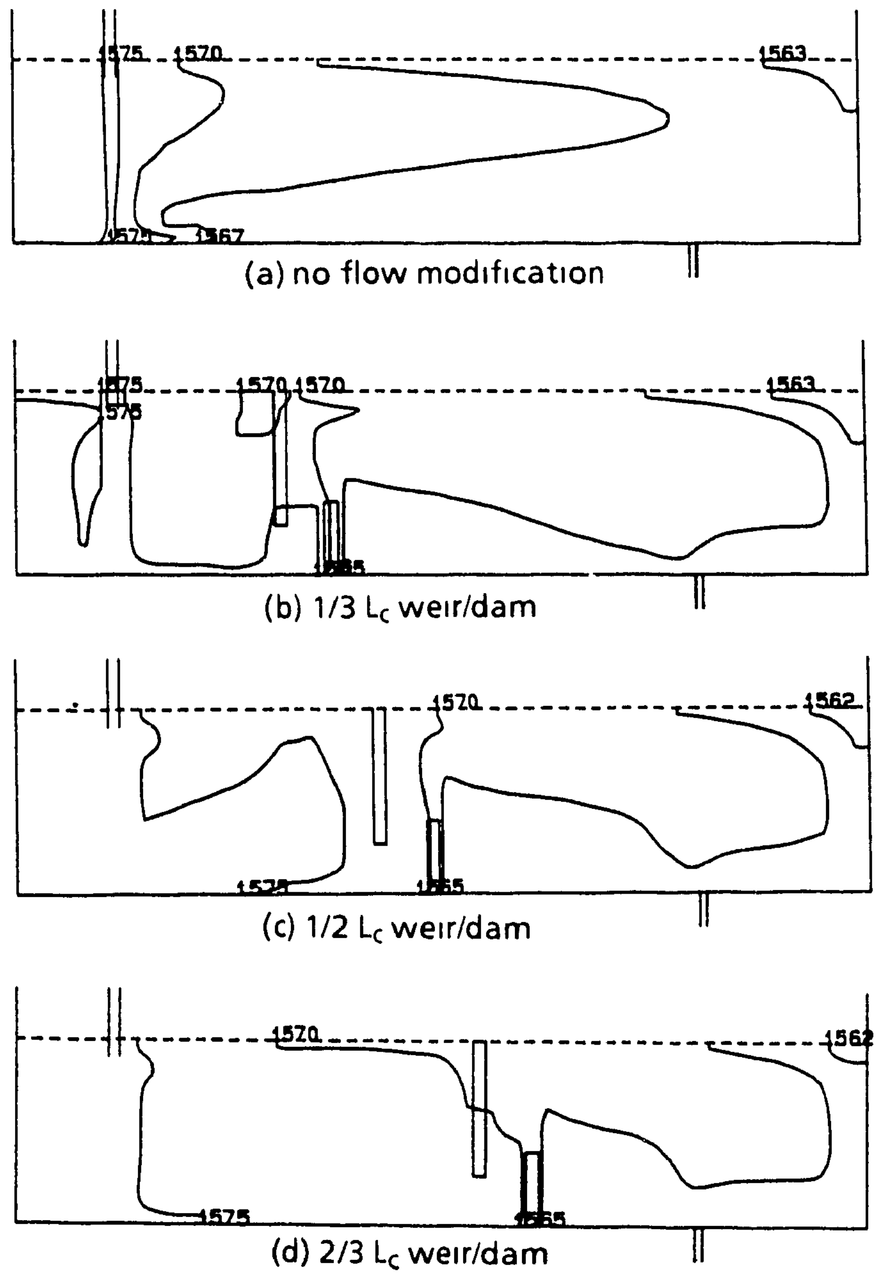

(a) no flow modification

(b) 1/3 L_c weir/dam

(c) 1/2 L_c weir/dam

(d) 2/3 L_c weir/dam

Figure 4-35 Predicted temperature isotherms withinin the single port slab caster at Stelco's Hilton Works assuming radiation from an overlaying slag thickness of 30 mm, and steady state side wall heat losses to the environment with various placements of weir and dam arrangements. (Isotherms only in the logitudinally central planes of the tundish are shown.)

5.2.2 Inclusion dispersion and separation

In real tundishes, those thermal natural convection current which arise owing to temperature variations within the molten steel are predicted to result in different flow patterns and inclusion dispersion characteristics versus those observed for isothermal systems (e.g. water models). A comparison of residual ratio values for real tundishes and for the full-scale water model, when a W/D combination is placed at $1/2L_C$, is illustrated in Figure 4-36. As seen, particle separations in steel baths are dramatically changed compared to those observed and predicted from water modelling. For the no slag situation, where no sink is assumed to be present (i.e. a reflective free surface), residual ratios are increased at each increment in particle size (i.e. more inclusions are entrained into product). On the other hand, when an overlaying slag cover of liquid phase is taken into acount, they are significantly decreased owing to inclusion absorption into the slag.

Figure 4-37 predicts the inclusion separation curves at *quasi steady state* (30 minutes after feeding) for various placements of W/D arrangements in molten steel with a slag cover of 30 mm thickness. When these flow modification devices were used, the residual ratio of inclusions was decreased. However, it was found that the particle separation rate is not very sensitive to the location of a W/D arrangement, contrary to the results of water modelling (see Figure 4-24). Under isothermal conditions, flow patterns in regions to the right of W/D arrangements were affected by their placement since flows were largely parabolic. These parabolic flow condition raises the possibility of increasing the plug flow volume by locating a W/D combination as near to the inlet nozzle as possible. On the other hand, Figures 4-31 ~ 4-34 show that flow patterns to the right side of a W/D arrangement is dominated by flow induced by thermal natural convection (i.e. elliptic flow). This should cause the particle separation behaviour to become less sensitive to the location of a W/D arrangement.

Inclusion dispersion behaviour at *quasi steady state* is illustrated in terms of dimensionless iso-concentration contours in Figure 4-38 There, the dimensionless values are particle number densities normalized with respect to the input particle number density. Figure 4-38 (a) provides dispersion patterns of relatively fine inclusion particles (i.e. 0.5 mm/s Stokes rising velocity/40 μm Al_2O_3 in molten steel). It can be seen that the fine particles are highly concentrated in the left side region of W/D arrangement, with about 75% of particles passing through the weir/dam arrangement. The right bottom of the dam is relatively less polluted, and finally 57% of particle are entrained into the mould. For the relatively coarse particles (i.e. 4.5 mm/s Stokes rising velocity/120 μm Al_2O_3 in molten steel) shown in Figure 4-38 (d), half of them floated up and were captured into the overlaying slag cover, while the other half recirculates in the steel flow before the flow passes through the W/D arrangement. Hence few particles have opportunity to be entrained into the mould.

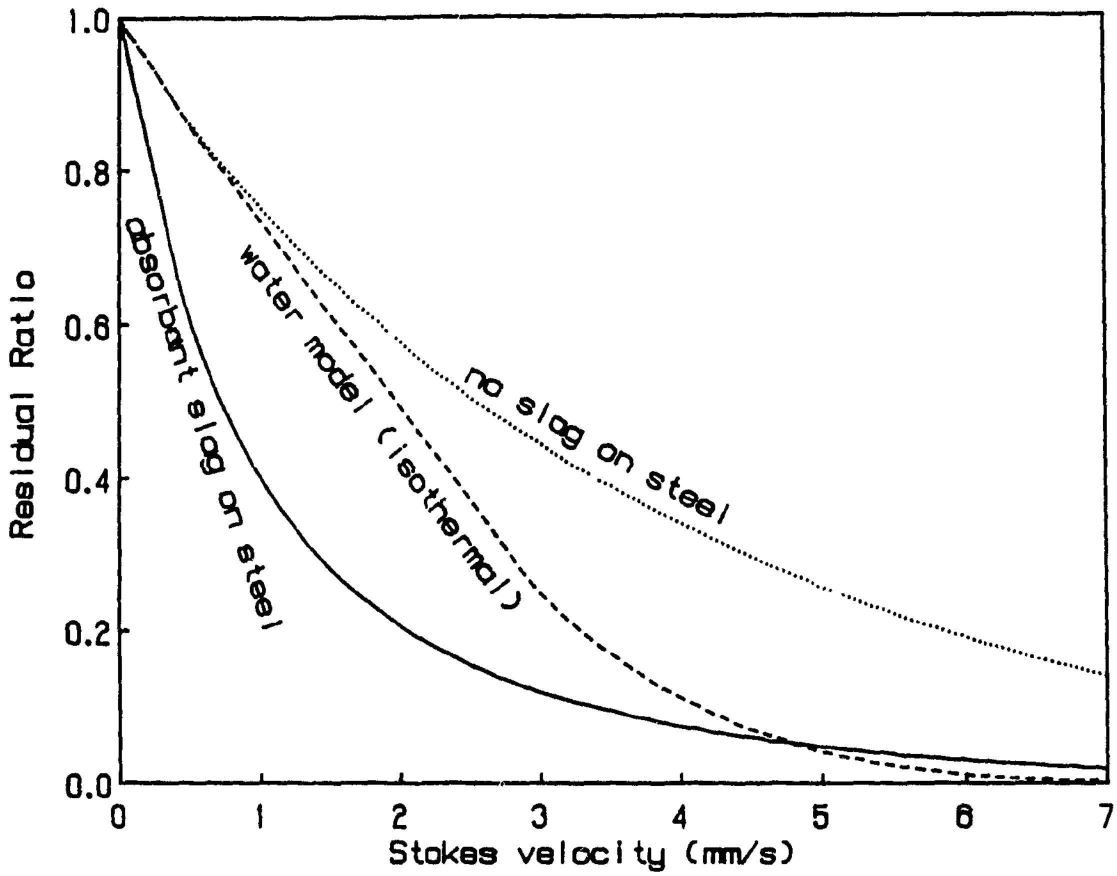

Figure 4-36 Comparison of the residual ratios versus Stokes rising velocities for molten steel and for water model systems. (Note that when an overlaying slag cover was taken into account, the ideal absorption of inclusions into the slag was assumed.)

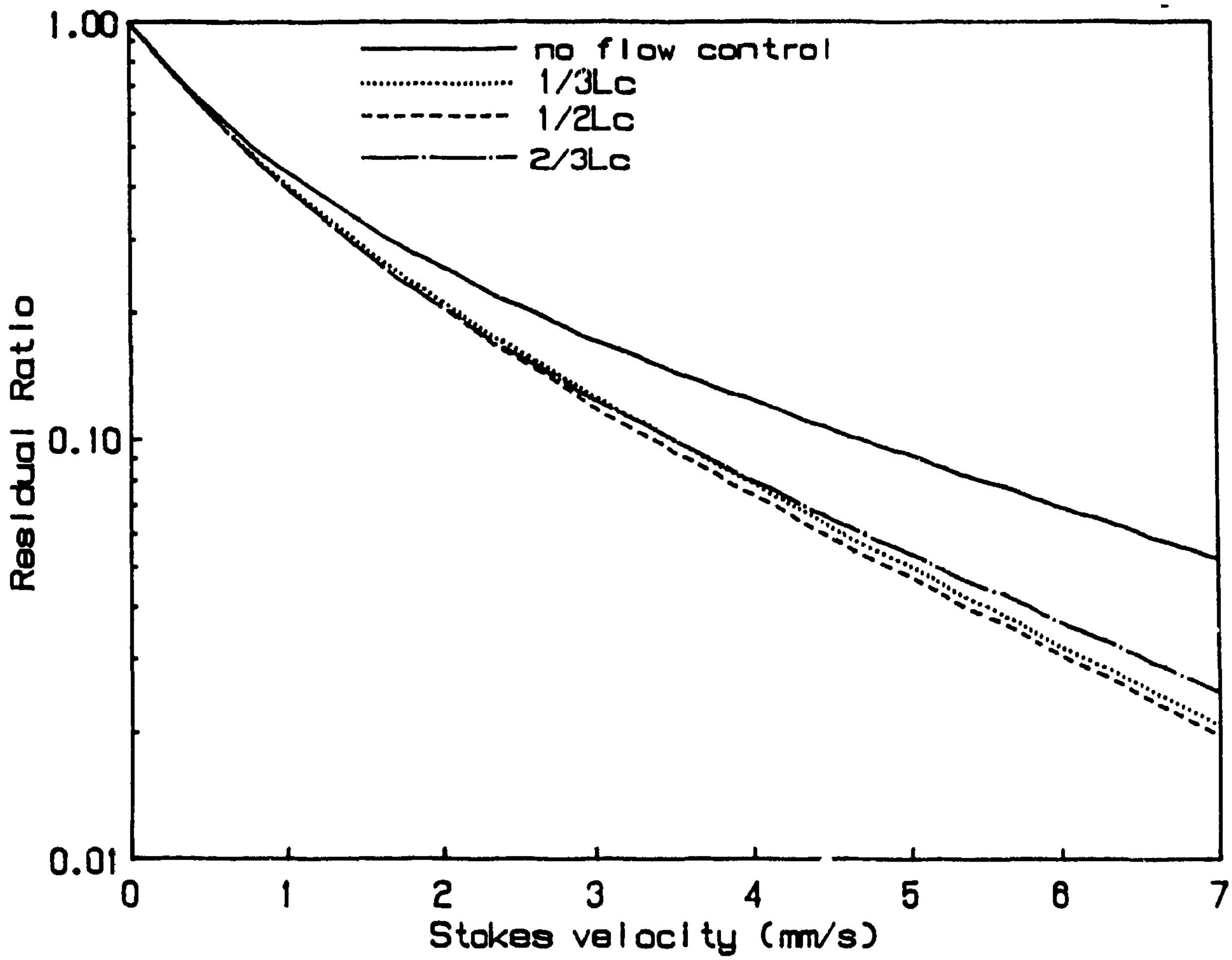

Figure 4-37 Relationship between the residual ratios of inclusions and Stokes rising velocities predicted for the molten steel system of Stelco's Hilton Works tundish.

PARTICLE DISPERSION

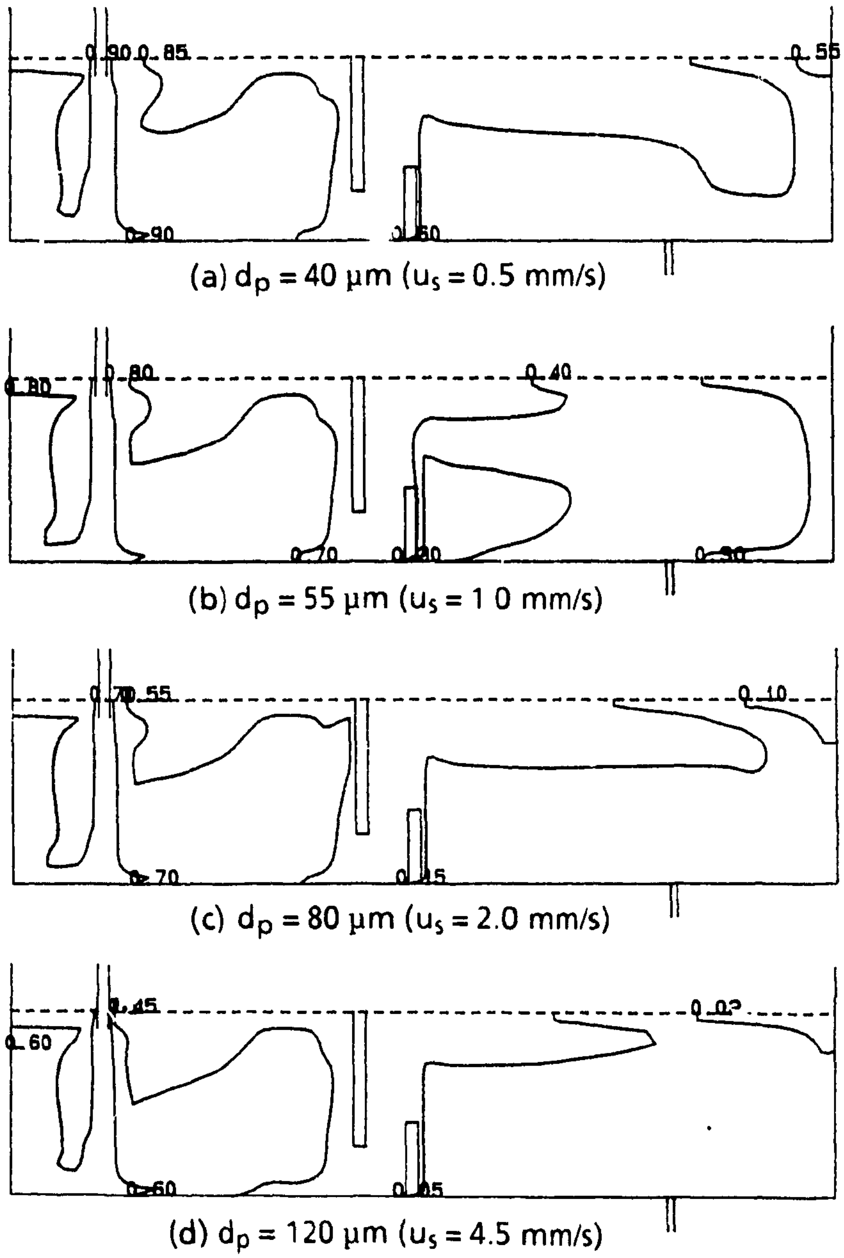

Figure 4-38 Normalized iso-concentrations in the longitudinally central plane of the tundish, predicted for various size of inclusions at *quasi-steady state* (i.e. 30 minutes after feeding).

5.3 Stelco's Double Port Tundish

Figures 4-39 and 4-40 provide velocity vectors of flows predicted for the twin bloom caster tundish arrangement where natural convection is taken into account. One should observe a much stronger recirculating flow along the metal surface, the wall and bottom edges of the tundish than that for water modelling. These stronger recirculating flows are caused by the thermal natural convection induced at the side and end walls of the tundish. The corresponding predicted temperature distributions within the steel bulk are shown in Figure 4-41.

Figure 4-42 shows residual ratio values versus Stokes rising velocities under non-isothermal conditions. When a W/D combination is employed, it is predicted that inclusion particle separation should be improved, as do water model studies. However, it is noteworthy that the quality of steel should be similar at both outlet ports even for NFM. This is contrary to the results of the water modelling study and presumably result from the thermal natural convection currents which generate sweeping flows along the metal surface, the end walls and bottom surface (see Figure 4-39) However, these predictions have yet to be confirmed in practice

STELCO'S HILTON WORK BLOOM CASTING TUNDISH

Casting Rate : 2 ton/min (0.005 m^3/s)

F.M.D. : no flow modification

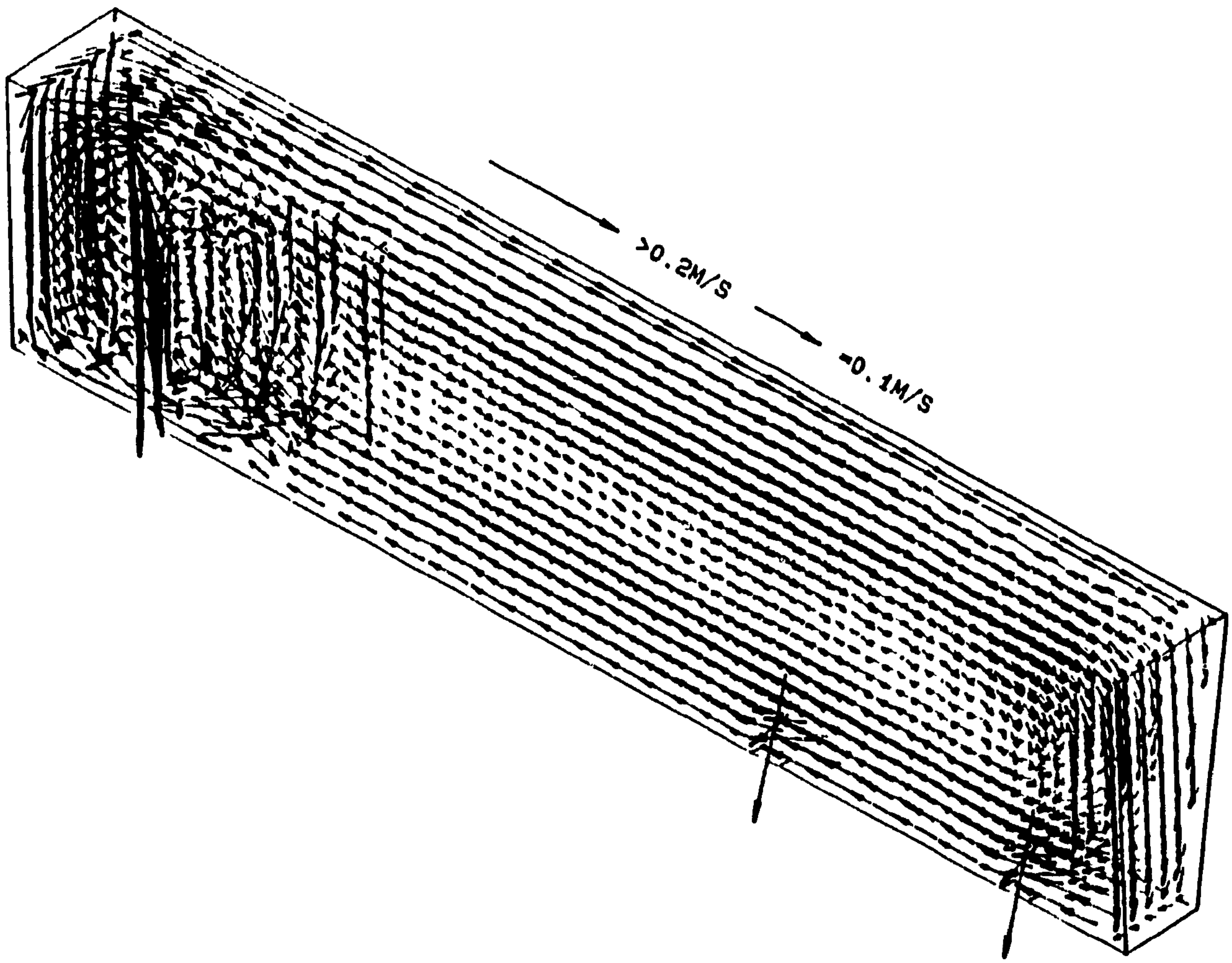

Figure 4-39A An isometric view of flow fields of molten steel (non-isothermal conditions) predicted for a half volume of the tundish set for twin bloom casting without flow modification device.

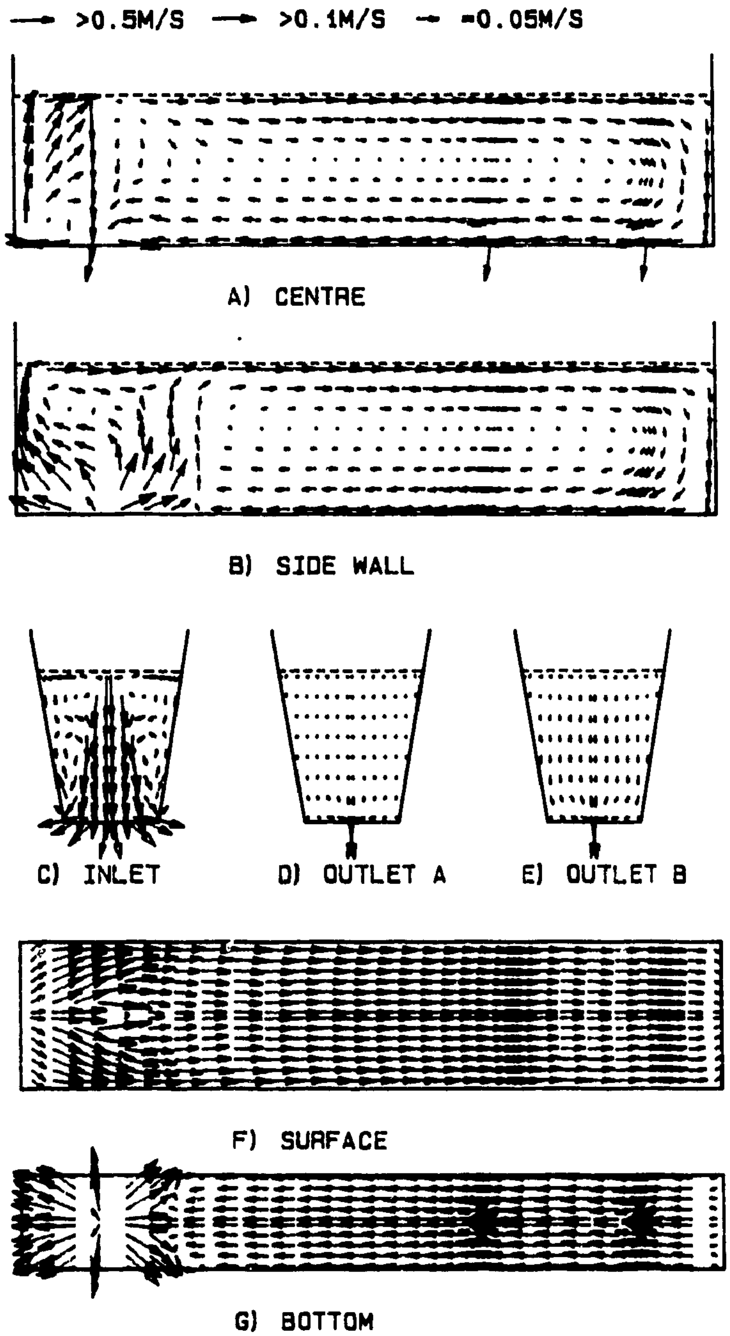

Figure 4-39B Predicted flow fields of molten steel (non-isothermal conditions) in some selected two-dimensional planes for the double port tundish without flow modification device.

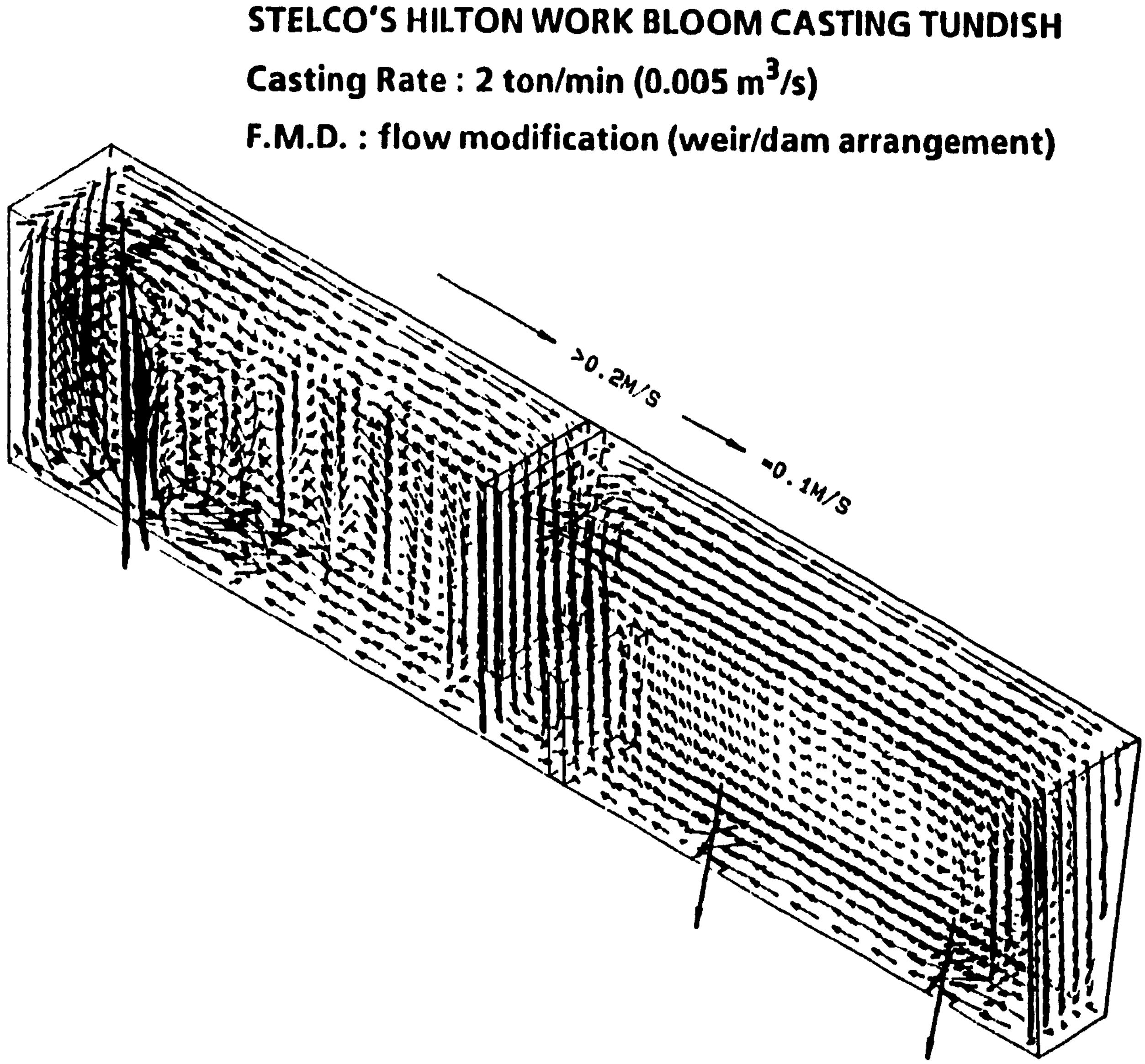

Figure 4-40A An isometric view of flow fields of molten steel (non-isothermal conditions) predicted for a half volume of the tundish set for twin bloom casting with weir and dam arrangements.

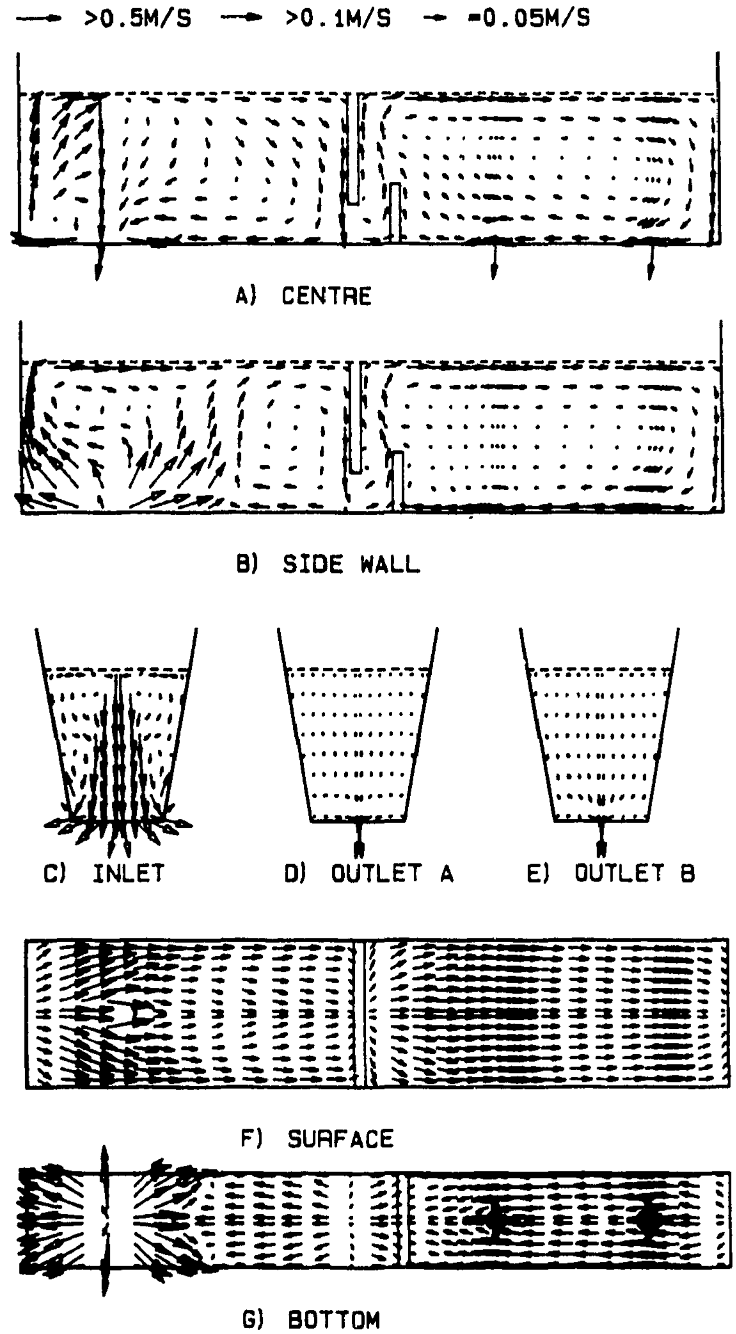

Figure 4-40B Predicted flow fields of molten steel (non-isothermal conditions) in some selected two-dimensional planes for the double port tundish with weir and dam arrangements

TEMPERATURE DISTRIBUTIONS
Input temperature : 1580°C

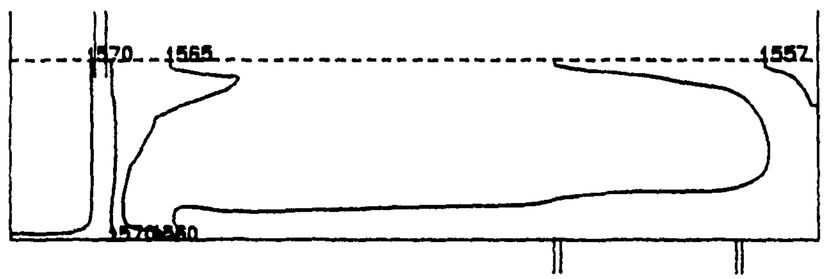

(a) no flow modification

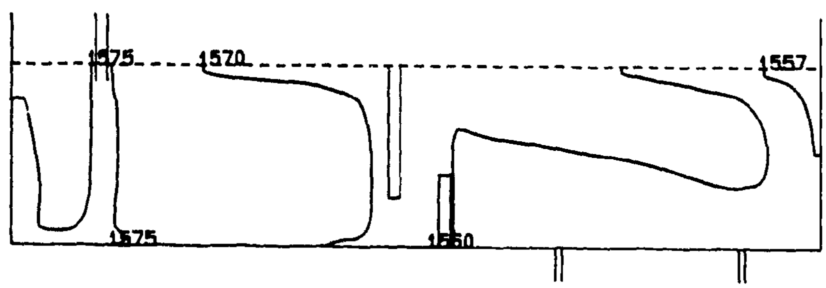

(b) flow modification

Figure 4-41 Predicted temperature isotherms in longitudinally central planes of the tundish set for twin bloom casting arrangement with, and witout, flow modifications.

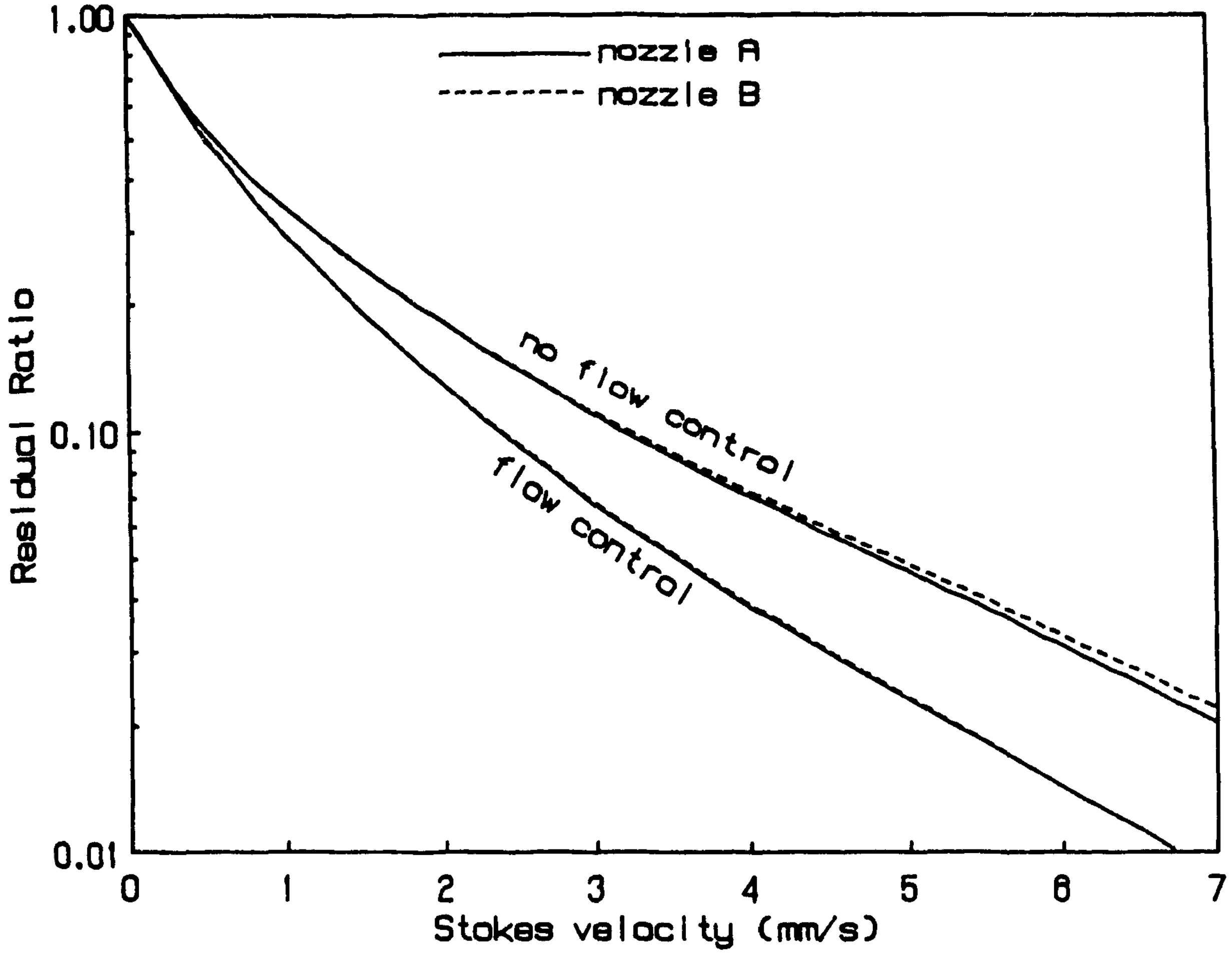

Figure 4-42 Relationship between the residual ratios of inclusions and Stokes rising velocities at exit nozzles of tundish set for twin bloom casting in the molten steel system.

5.4 Dofasco's Twin Ported Tundish

Computations were also carried out for an axisymmetric twin port tundish at Dofasco's Hamilton Work. In this work, the respective role of a weir, a dam, and W/D arrangements was studied. The effect of wall sloping angle on inclusion separation ratios was also examined.

Figure 4-43 (a), (b), (c), and (d) illustrate flow patterns developed by employing NFM, a weir, a dam, and a W/D arrangement, respectively. There, the side-walls are outwardly inclined at an angle of 10 degrees to the vertical. It can be seen that a weir (Figure 4-43 (b)) would not significantly modify flow patterns versus NFM. Only upper downstream to the outlet is blocked by the weir and a small recirculating flow can be seen to the right side of the weir. By contrast, a dam (Figure 4-43 (c)) leads to an upwardly flowing stream directed towards the metal surface, this improving the potential for inclusion separation into molten slag from liquid steel. Figure 4-44 supports those aspects of inclusion separation behaviour that can be deduced from study of flow patterns. There, residual ratios for the twin port tundish illustrate the critical importance of a well-placed dam. By comparison, the role of a weir is seen to be of secondary importance for inclusion float-out. It is interesting to note that a weir reduces residual ratios (i.e. improves inclusion removal) for small-size inclusions of less than 50 microns (u_s<1 mm/s), whereas a dam works effectively for relatively larger inclusions (u_s>1 mm/s). Consequently, when a W/D arrangement is used, the improvement in metal quality is markedly better than NFM for inclusions of 40 μm-150 μm in diameter.

Figure 4-45 illustrates the effect of sloping walls on flow patterns within tundishes of identical fluid volume. Figure 4-45 (a) shows flow vectors predicted for vertical side-walls to bottom wall (i e. zero degree slope), and (b) for 30 degree sloping side-walls. As seen, strong recirculating flows along the side-walls and bottom wall become less pronounced with increase in angle. Figure 4-46 demonstrates, in a quantitative way, the beneficial effects of inclined side-walls for removing inclusions. Four curves, corresponding to four different slopes of tundish side-wall, show that the lowest residual ratios are obtained by using more steeply inclined side-walls. This can be readily appreciated from Equation 4-16, in Chapter 3. Since less steeply inclined side-walls leads to a larger metal/slag interface area (i.e. increase of A in Eq. 4-16) and smaller recirculating zones (i.e. increase of γ in Eq.4-16), residual ratios for inclusions can be expected to be reduced.

However, this improvement will take place at the expense of increased heat losses due to a higher surface area/volume ratio with increasing angle. This results in a lower,mean metal temperature within the tundish, and a higher temperature drop between the inlet and outlet nozzles, as demonstrated (computed) in Figure 4-47. There, for the standard 10 degrees slope of side-walls, the net temperature drop was predicted to be 9 °C, which agrees with the industrial measurements [30] It should be noted that when flow modifiers were in place, the effect of side-wall slope became much less marked on inclusion separation ratios.

Computations were also performed by introducing a second W/D arrangement. Flows of liquid steel within the tundish for this case is provided in Figure 4-48. It was predicted that a second W/D arrangement might not significantly contribute to any improvement in metal quality, this being illustrated in Figure 4-49.

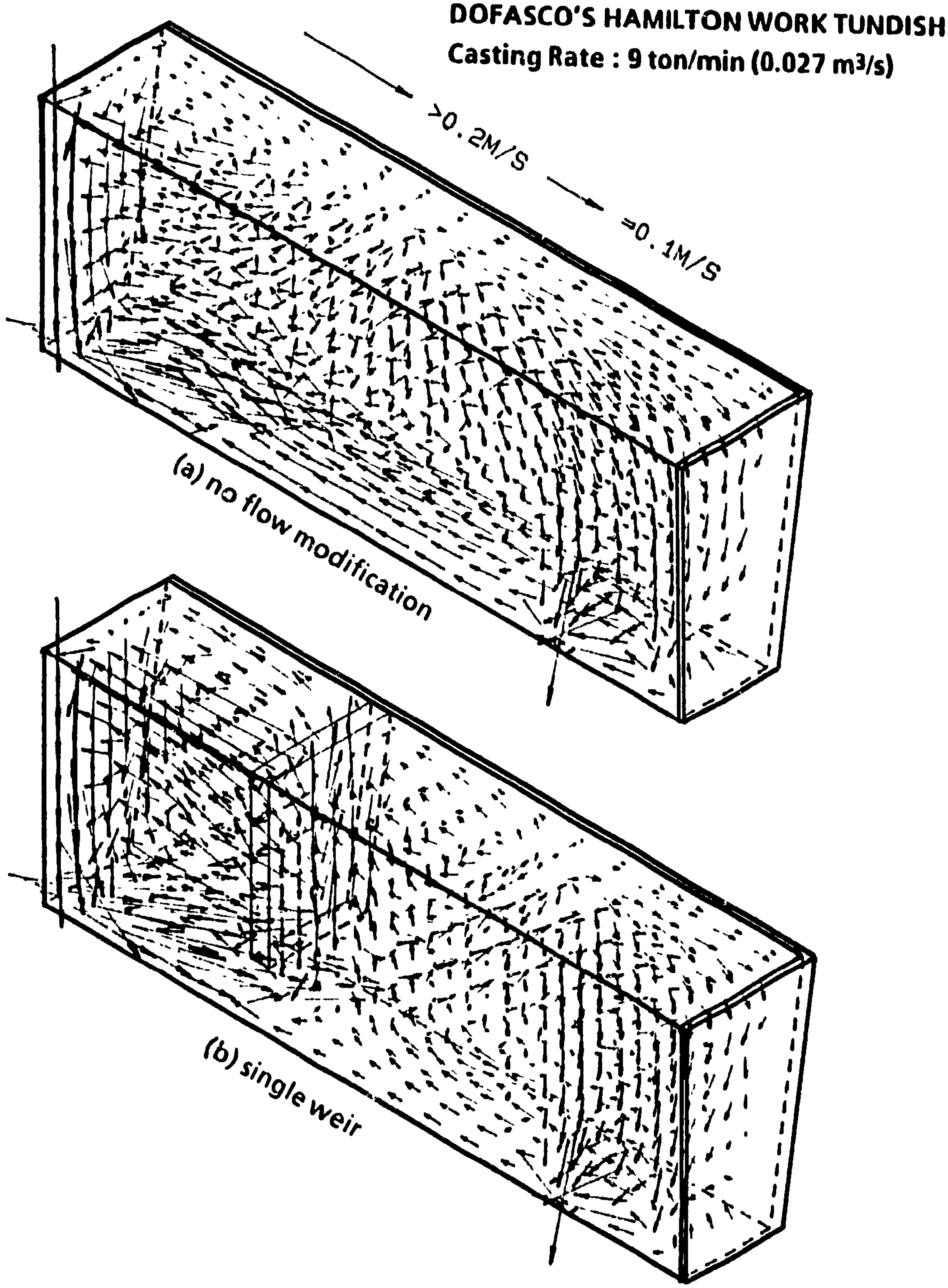

Figure 4-43 Isometric view of the flows developed in quadrant of Dofasco's twin port tundish with (a) no flow modification, (b) a dam.

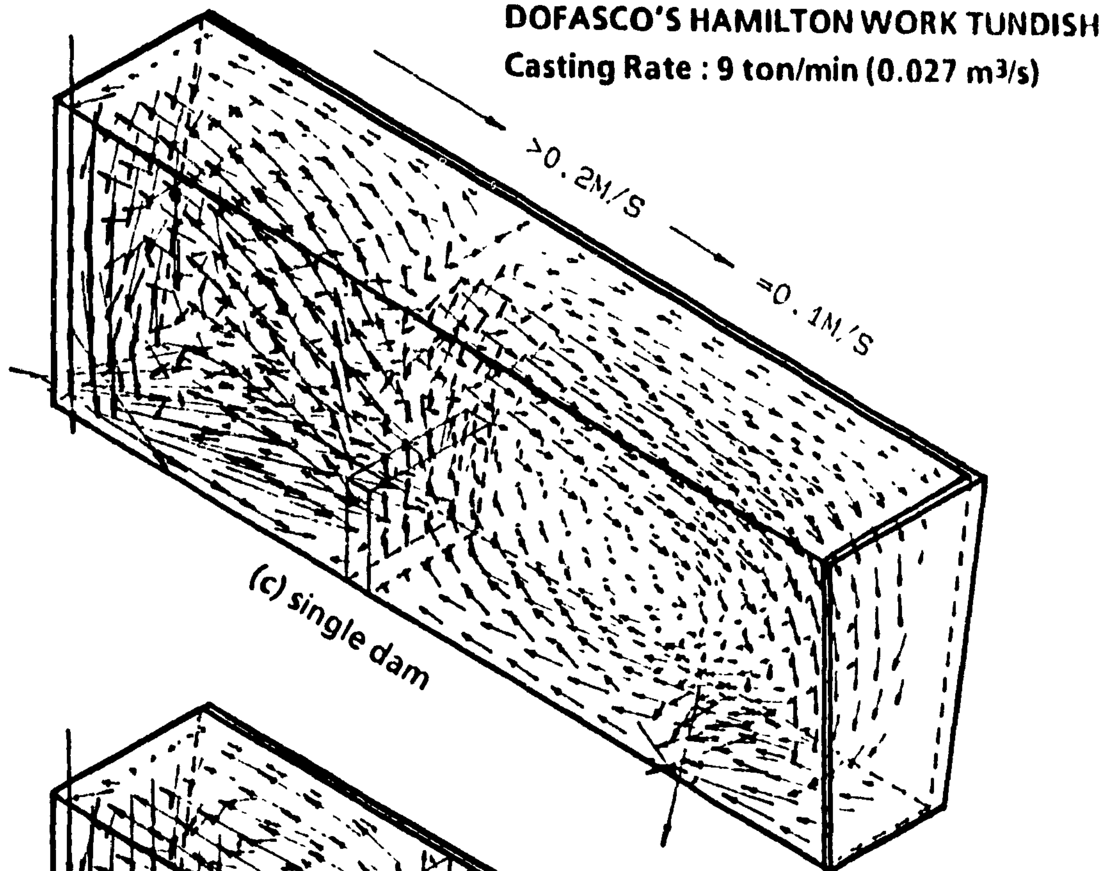

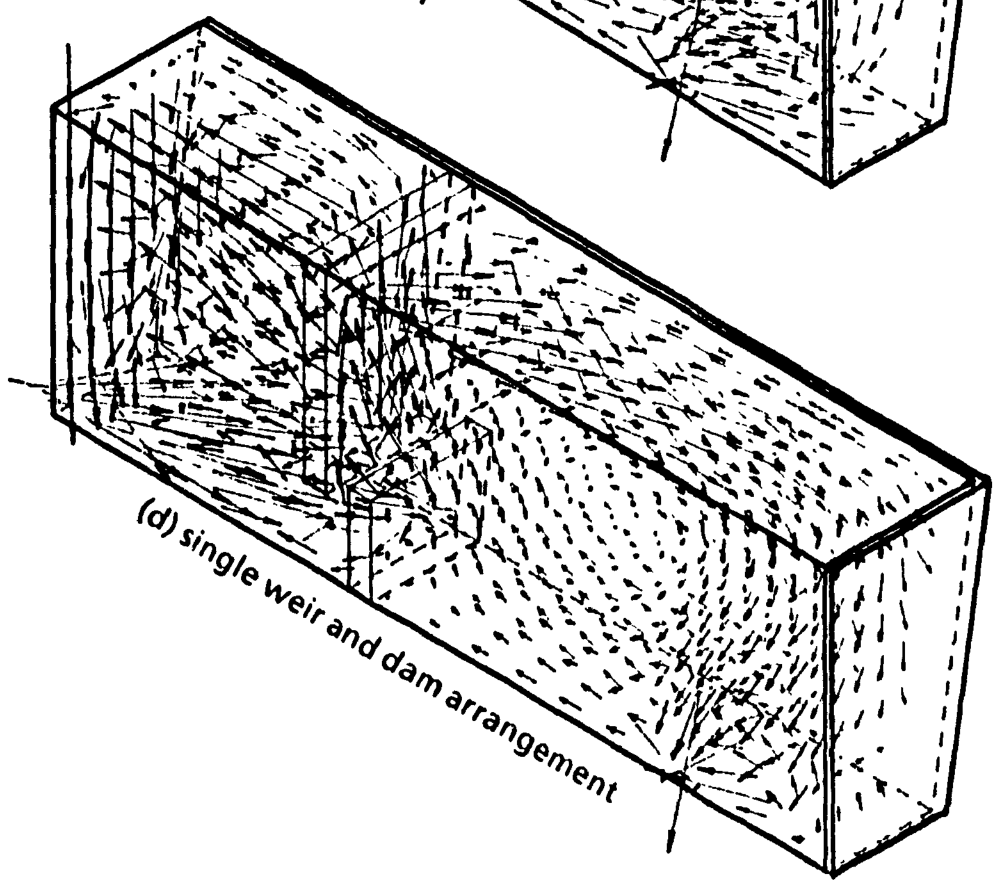

Figure 4-43 Isometric view of the flows developed in quadrant of Dofasco's twin port tundish with (c) a weir, and (d) a weir/dam arrangement.

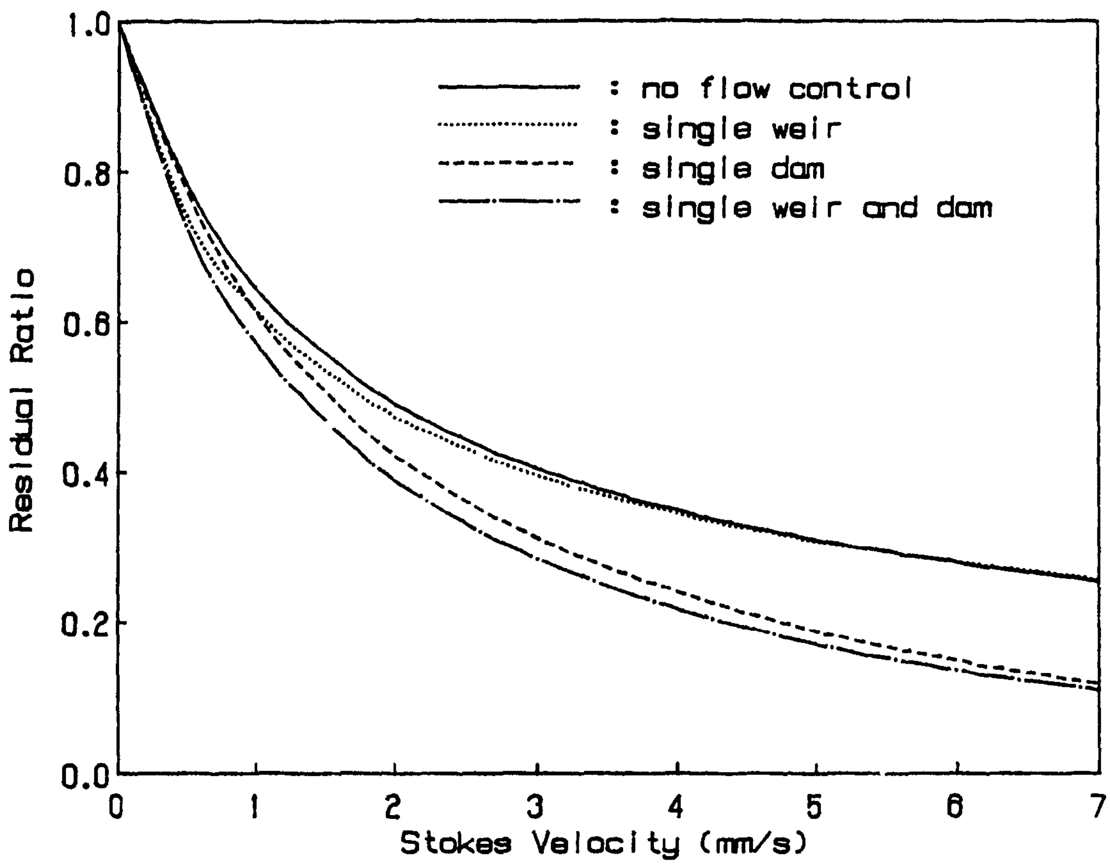

Figure 4-44 Plot of residual ratios for a Dofasco's twin port tundish fitted with (a) no flow modification, (b) a dam, (c) a weir, and (d) weir/dam arrangement.

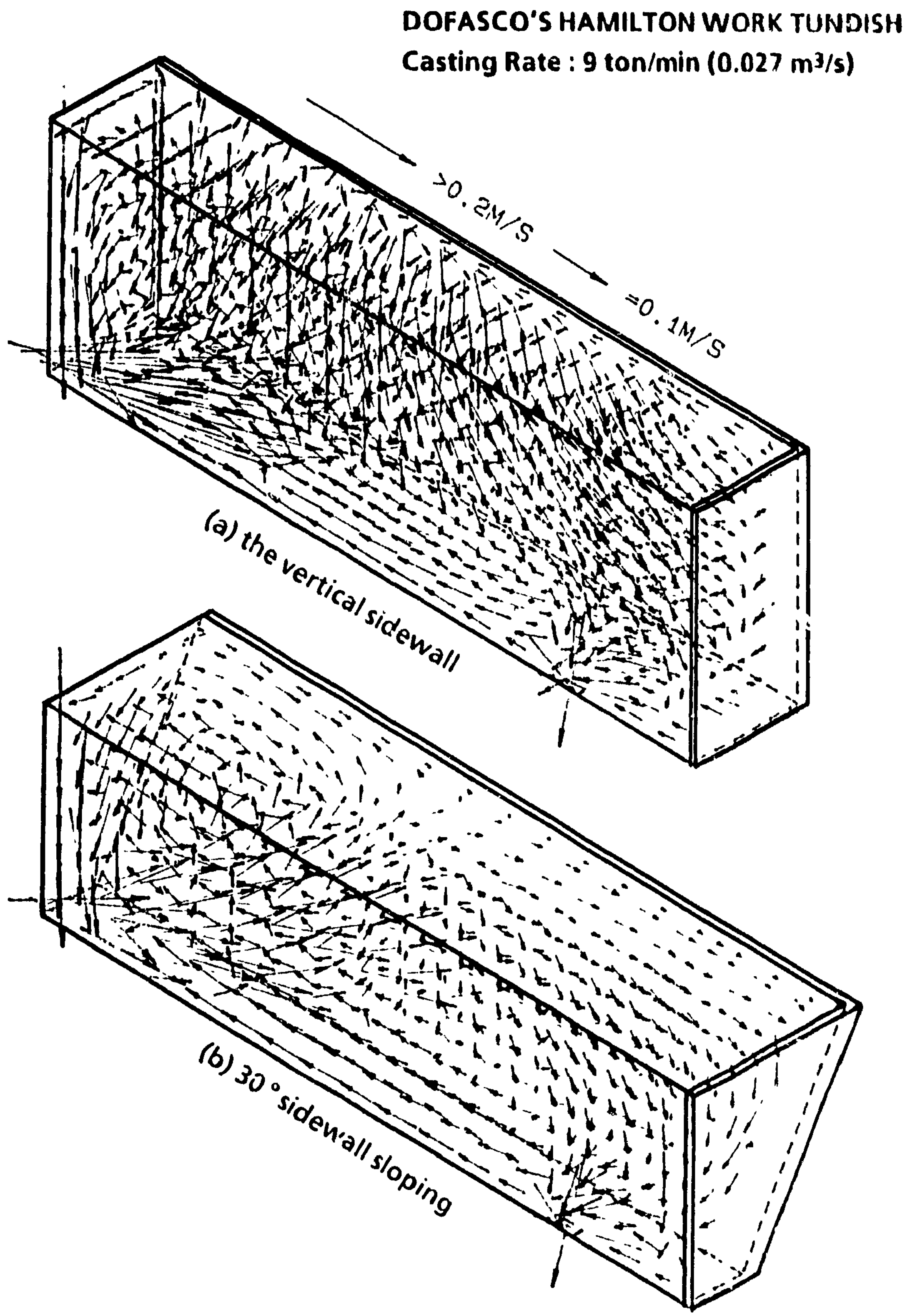

Figure 4-45 Isometric view of the flows developed in quadrant of Dofasco's twin port tundish with (a) no side-wall sloping (vertical side-walls), (b) 30° side-wall slope.

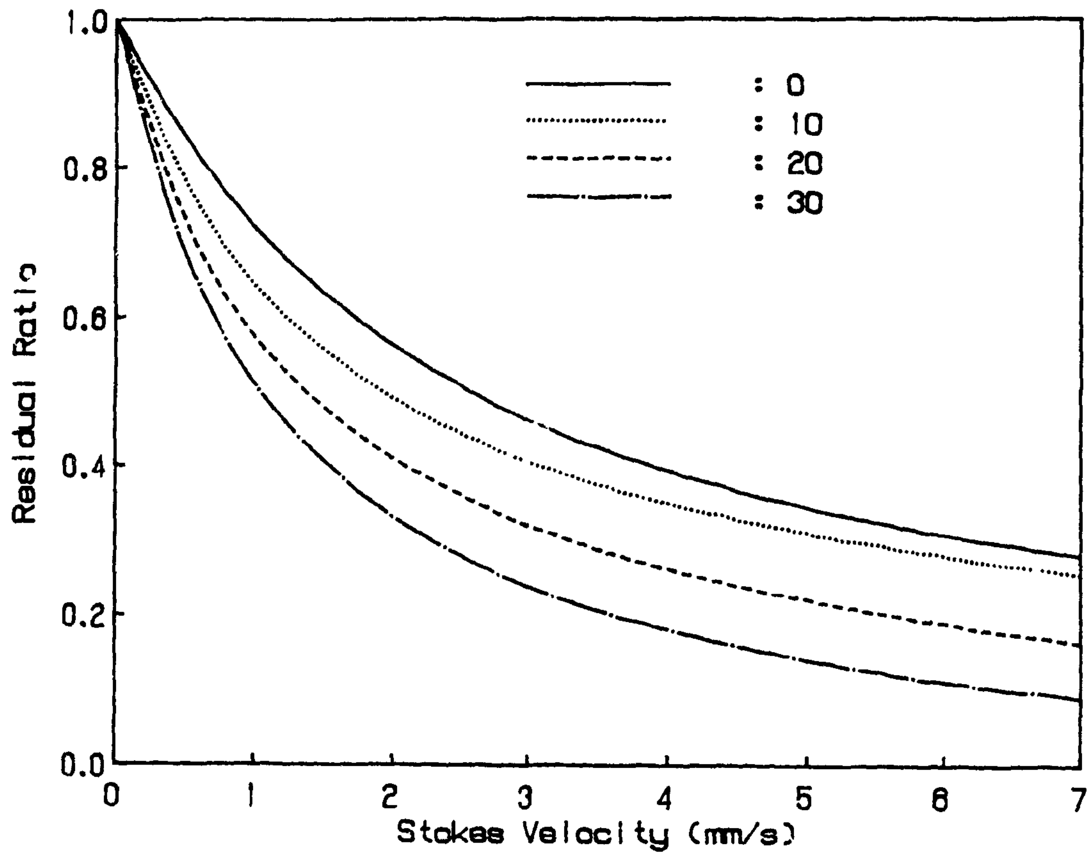

Figure 4-46 Residual ratios of inclusions versus specific Stokes rising velocities for different slopes of side-wall of twin slab caster without flow modification device

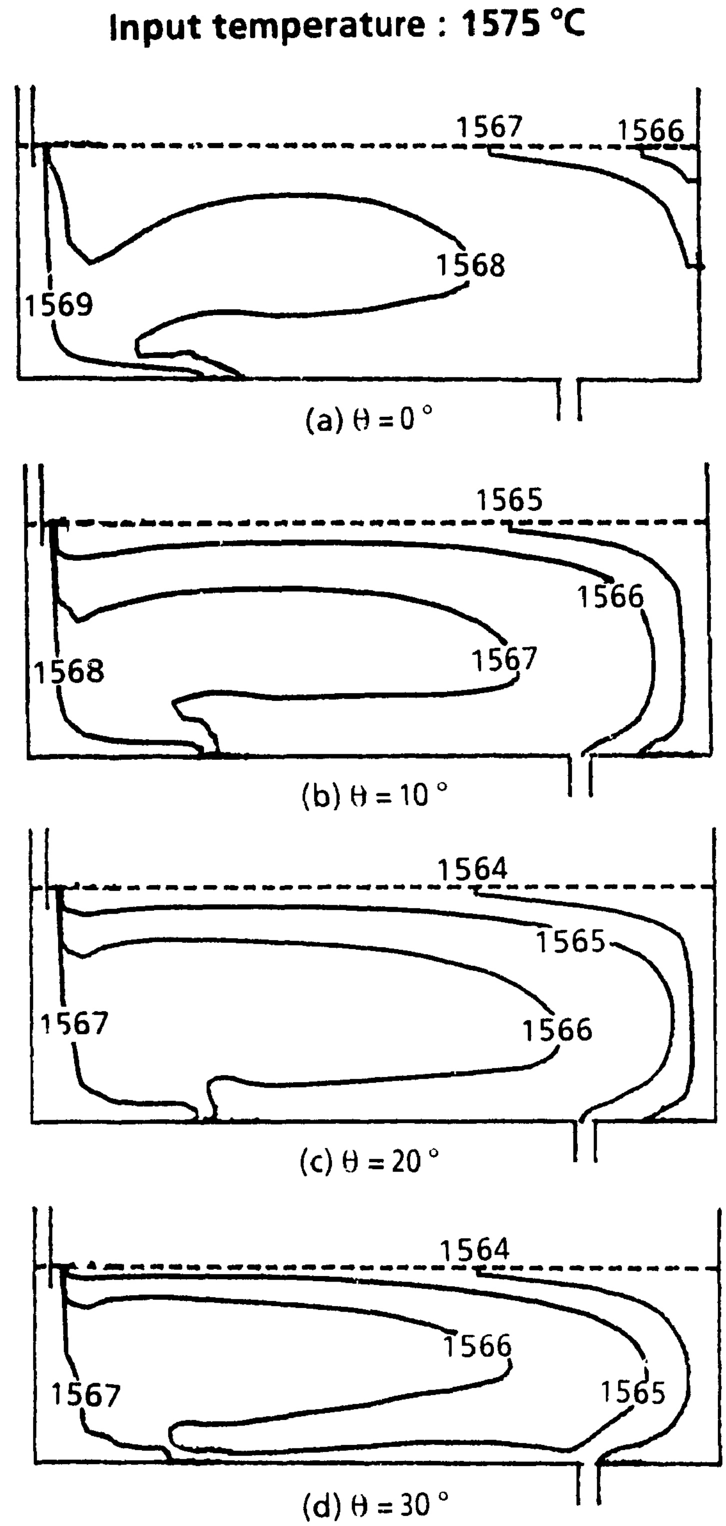

Figure 4-47 Isothermal curves for different slopes of side-walls of tundish without flow modification device.

DOFASCO'S HAMILTON WORK TUNDISH
Casting Rate : 9 ton/min (0.027 m³/s)
F.M.D. : Double weir/dam arrangements

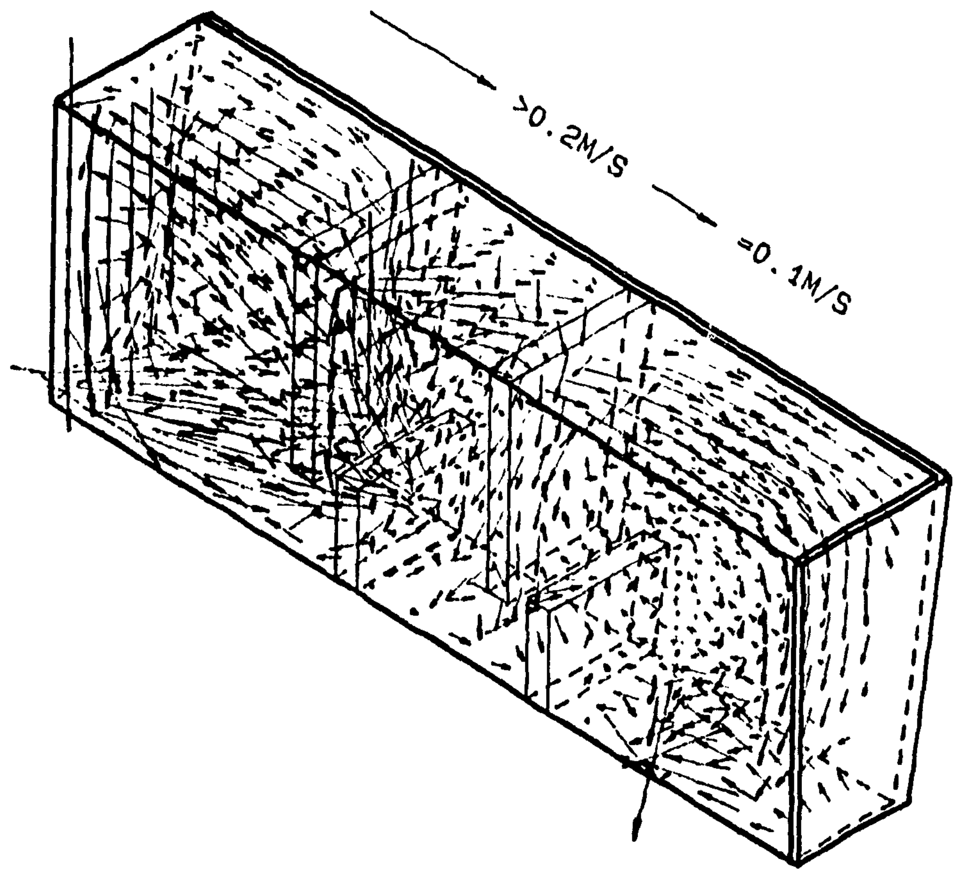

Figure 4-48 Isometric view of the flows developed in quadrant of Dofasco's twin port tundish employing double weir/dam arrangements.

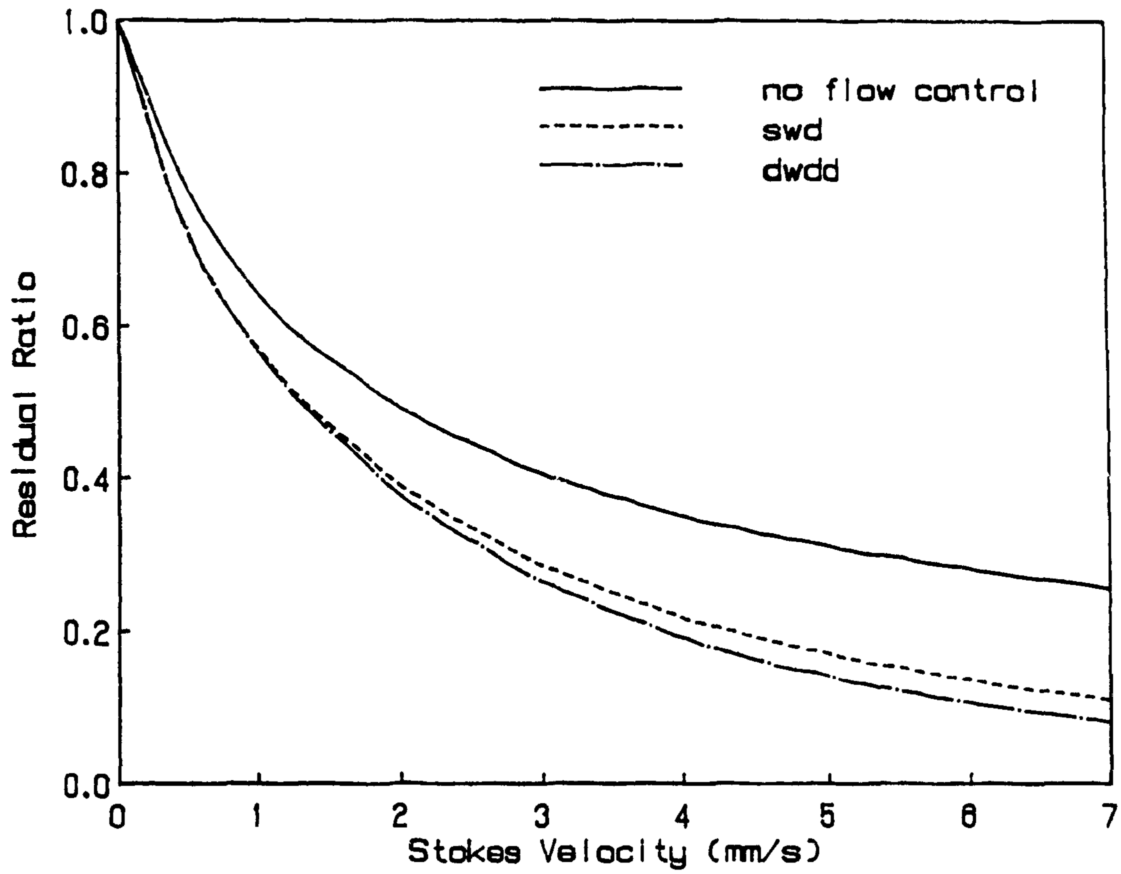

Figure 4-49 The effect of double weir/dam arrangements to inclusion separation intundish.

5.5 BHP's Trough-Shaped Tundish

Figures 4-50 (a) and (b) show computed flows without and with a flow modification device (F.M.D.). As seen, symmetry considerations required only one quadrant of this tundish to be modelled. Both flow fields suggest that the stagnant conditions typically observed at the end-walls of tundishes under isothermal conditions, can be greatly influenced by natural convection phenomena. Thus, for the boundary conditions noted, it is seen that the heat losses to the refractory end-walls and side-walls lead to strong downflows at side-wall surfaces. Consequently, the velocity vector data given as an isometric view in Figure 4-50 (a) shows an entry region of turbulent recirculatory flow, followed by a strong, secondary recirculating flow in the outer regions of the tundish. This flow is quite different from the isothermal case, for which an outflow jet along the base of the tundish leads to short-circuiting. Figure 4-50 (b) shows how flow patterns are modified when a dam and weir F.M.D. of the type shown, is introduced.

Figure 4-51 provides associated temperature maps (isotherms) along the central longitudinal plane, for an input steel bath temperature of 1575 °C to the tundish. The effluent temperatures to the mould, with and without flow modification, were essentially independent of F.M.D. studied. Temperature drops of about 20 °C compared well with those observed in practice.

Figures 4-52A and 4-52B illustrate the fractional concentrations of 40 micron inclusions ($u_S = 0.5$ mm/s) between tundish entry and exit. Computations suggest that the Residual Ratio of inclusions entering the mould should be in the order of 48 % of those entering the tundish in the absence of flow controls, and less than 45 % with flow controls. Figure 4-52B shows that the larger inclusions of 120 microns ($u_S = 4.5$ mm/s) separate far more strongly, such that the residual ratios reporting to the mould are ~0 05 (N.F.M.) and ~0.02 (W.F.M), or 5 % and 2 % of the number density of 120 micron particles entering. In terms of a percentage improvement in metal quality between entry and exit, these figures suggest an improvement of about 3 %.

Figure 4-53 illustrates the time needed for the level of effluent inclusions to become steady, following their (sudden but then constant and continuous) introduction into the tundish via the ladle shroud. It shows that concentration transients within the tundish amounted to some 20 minutes, or about three nominal holding times (t_n = ~7 mins), before small inclusions ($u_S \leqq 0.5$ mm/s), passing into the mould, reached steady state levels Larger particles, rising more rapidly, became distributed within the tundish more quickly As a result, steady state effluent levels were achieved within about one nominal holding time.

Figure 4-54 shows the predicted advantages of the flow modification arrangement studied, illustrating the very marked decrease in absolute residual ratios for larger particles, as well as the nearly complete elimination of particles with Stokes rising velocities in excess of 5 5 mm/s If steel quality improvements are quoted in terms of the ratio of inclusions in steel entering the mould, with and without flow modification devices, then very significant quality improvements would be observed For instance, a quality increase of some 20 % for 50 μm particles (u_S = 1 mm/s), and some 60 % for 120 μm inclusions (u_S = 4 5 mm/s), is indicated This argument rests on the assumption that there is a direct correlation between the number density of critically sized inclusions, and final steel quality

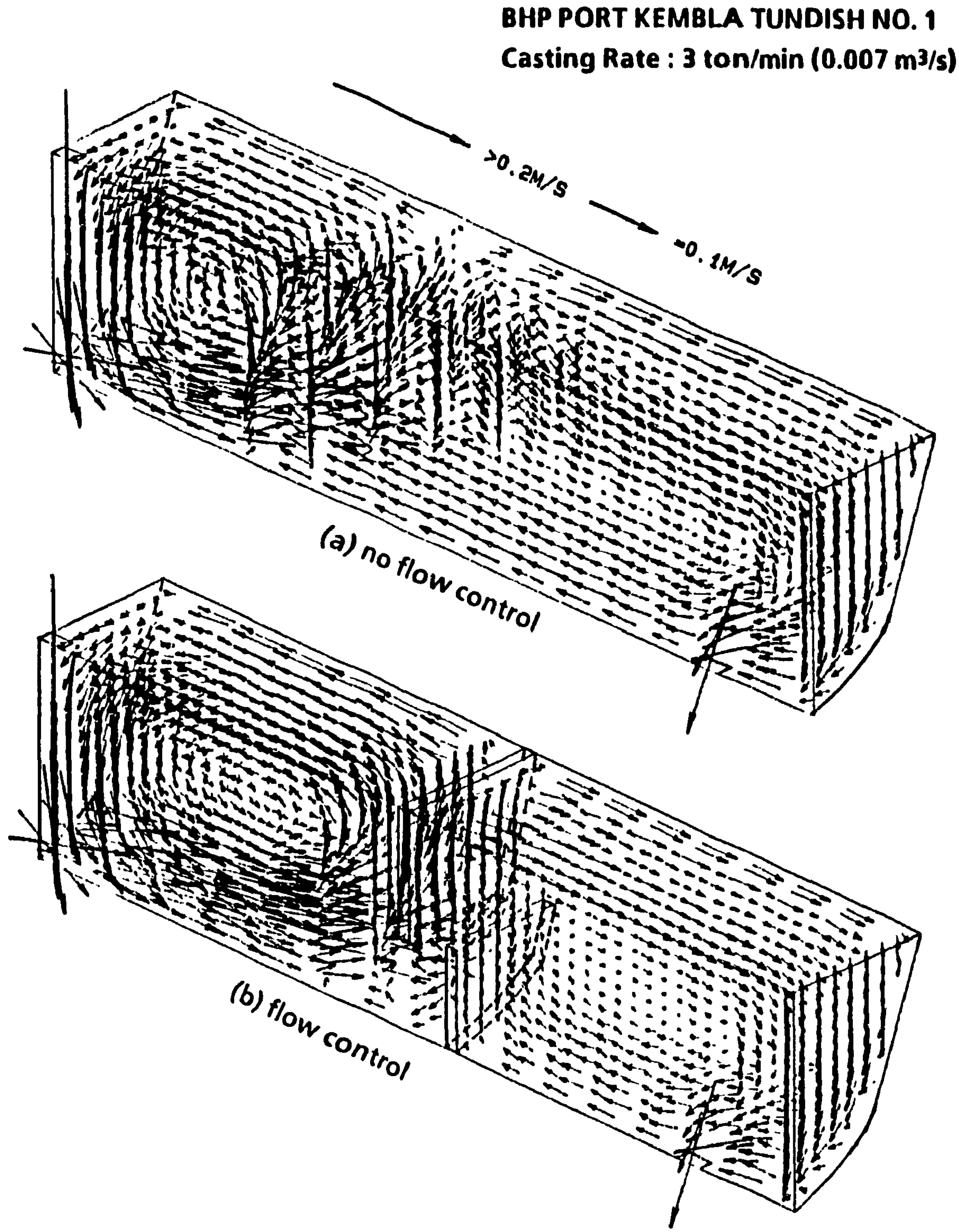

Figure 4-50 Computed flows in BHP's trough-shaped tundish, taking into account natural convection.

TEMPERATURE DISTRIBUTIONS
Input temperature : 1575°C

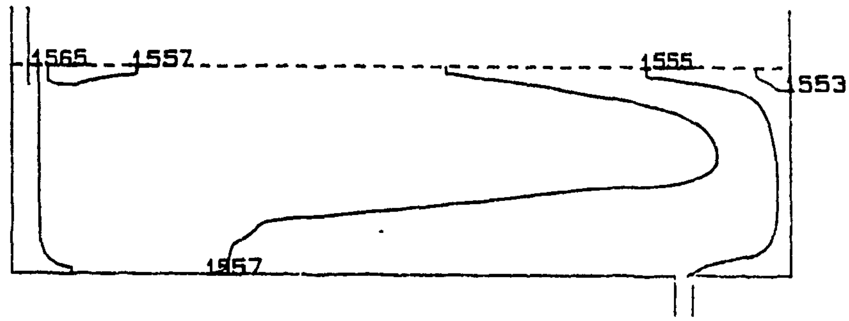

(a) no flow modification

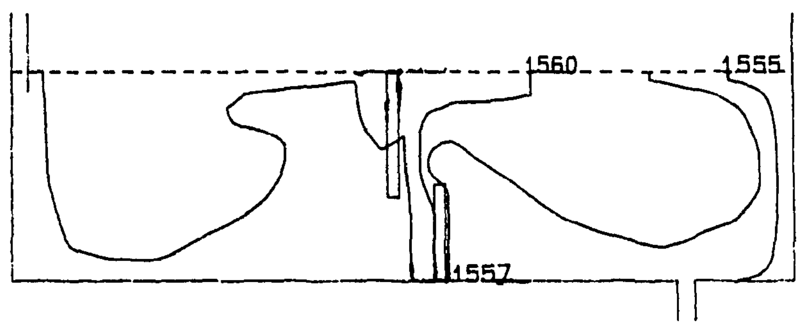

(b) flow modification

Figure 4-51 Computed isotherms along central longitudinal plane of half section of BHP's trough-shaped tundish.

PARTICLE DISPERSION

Particle size : 40 microns ($u_s = 0.5$ mm/s)

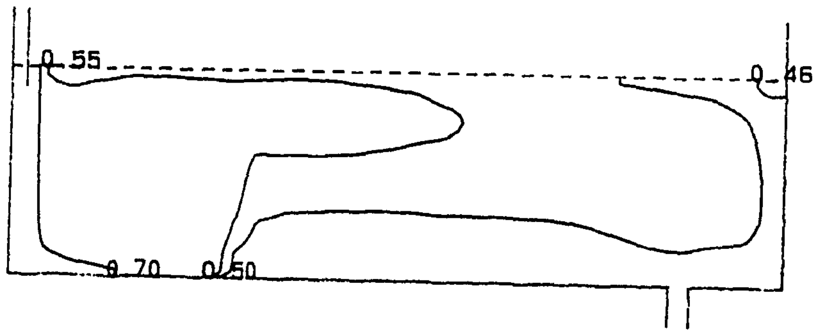

(a) no flow modification

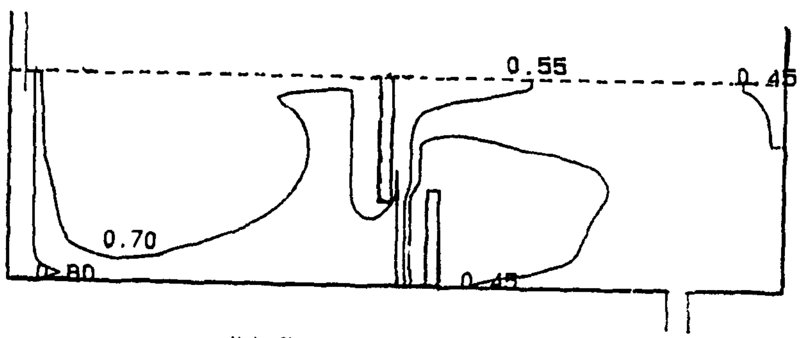

(b) flow modification

Figure 4-52A Computed iso-density levels of inclusions with, and without flow modifications for 40 microns inclusions ($u_s = 0.5$mm/s) Ordinate scale normalized with respect to entering levels of inclusions

PARTICLE DISPERSION

Particle size : 120 microns ($u_s = 4.5$ mm/s)

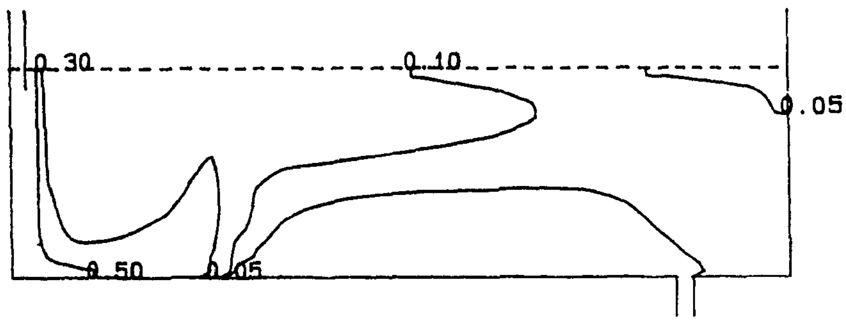

(a) no flow modification

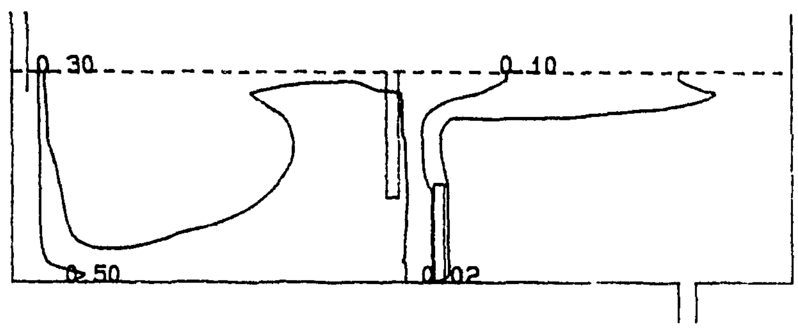

(b) flow modification

Figure 4-52B Computed iso-density levels of inclusions with, and without flow modifications for 120 microns inclusions ($u_s = 4.5$mm/s)

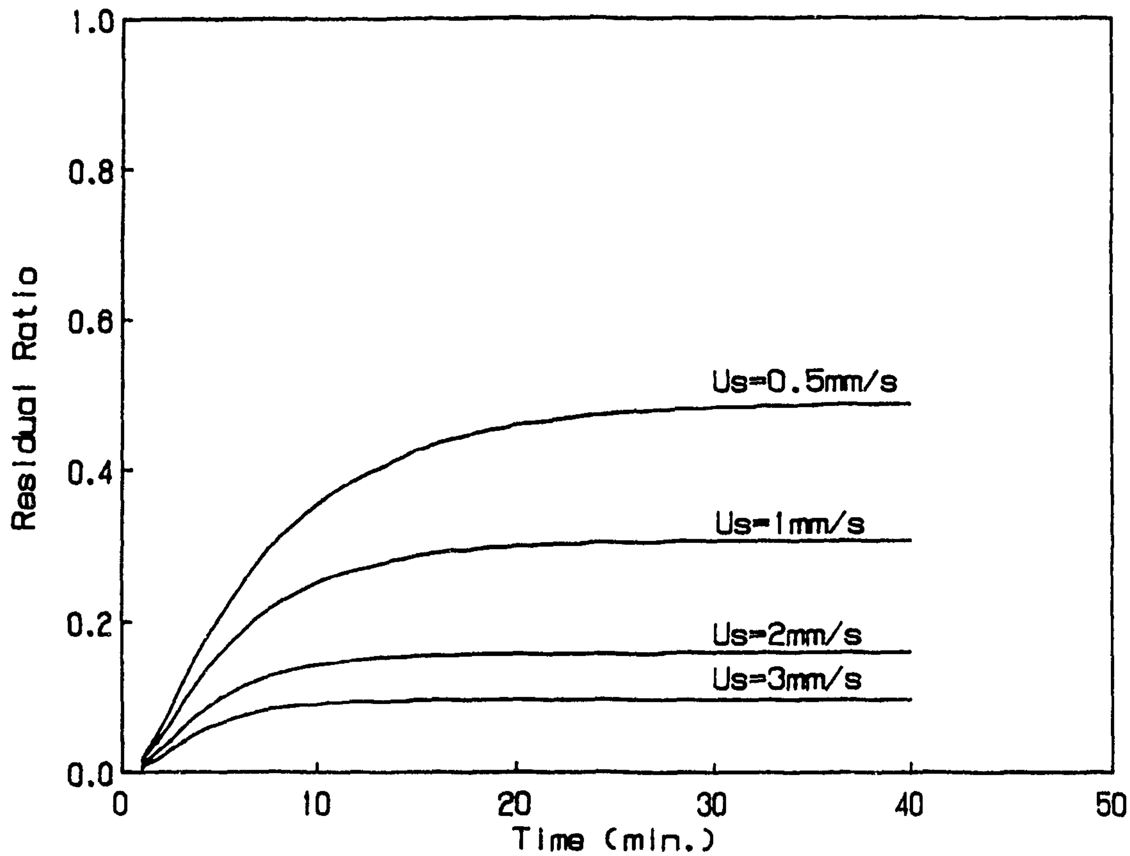

Figure 4-53 Residual ratios of inclusions entering mould flowing their introduction into the tundish, for various float-out velocities. Ordinate scale normalized with respect to entering levels of inclusions.

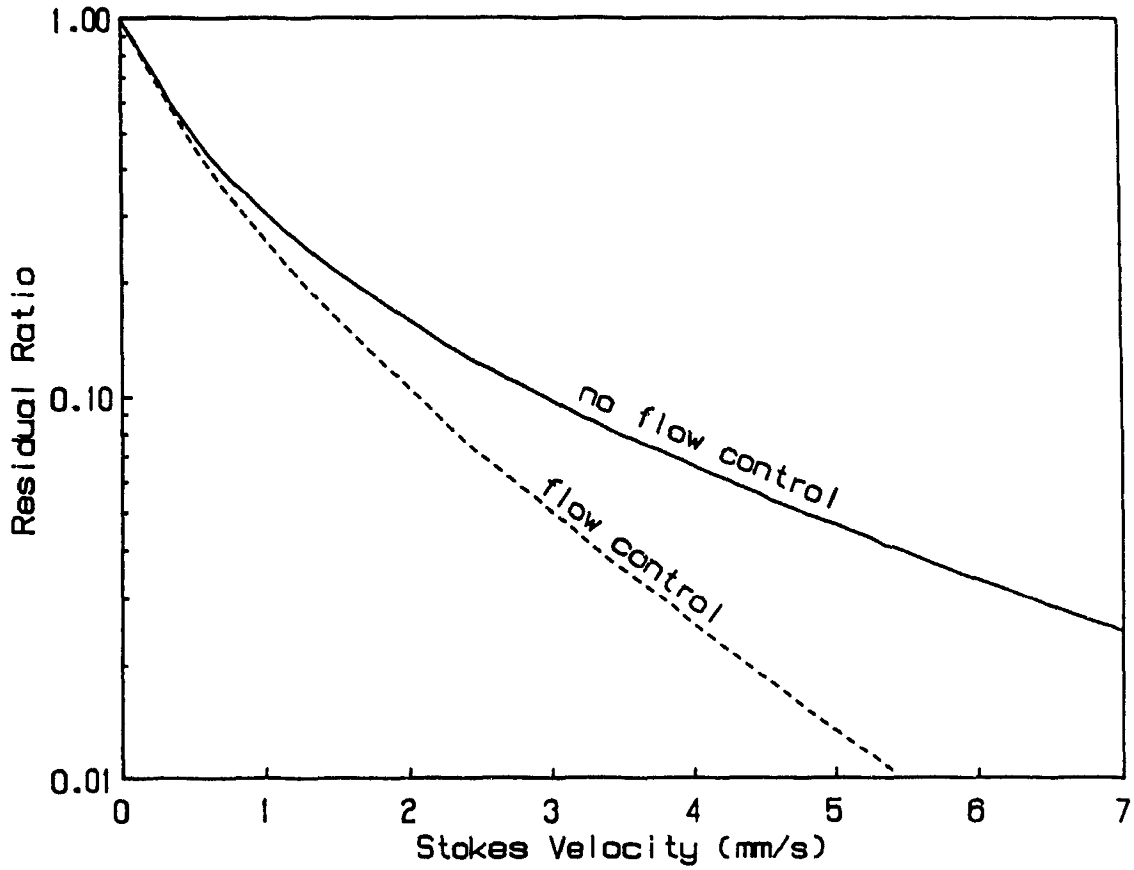

Figure 4-54 Semi-logarithmic plot of residual ratio of inclusions entering mould versus their Stokes rising velocity, for BHP trough-shaped tundish.

5.6 BHP's Wedge-Shaped Tundish

Computed flows for the BHP Port Kembla No.2 tundish are shown in Figures 4-55 (a) and 4-55 (b). These again illustrate the effects of flow modification devices and thermal natural convection In this case, a half segment of the tundish has been modelled, the central longitudinal plane being a plane of symmetry Once again, the importance of natural convection with large, deep tundishes is illustrated, in that the stagnant regions at the corners and end-faces observed for isothermal conditions are replaced with downflows adjacent to walls, and a recirculating flow back towards the entrance, across the exit port. Temperature fields shown in Figure 4-56 illustrate the boundary of the hot plume, entering at 1570 °C, and the cool steel adjacent to the outside end-wall near to the surface, at 1562 °C. The temperature drops of 14 °C and 12 °C, with and without flow modification devices, again correspond well with those typically observed.

Figure 4-57 provides information on residual ratios versus time for the wedge-shaped tundish (N F.M), following the continuous input of inclusions at time zero The results are similar to those presented in Figure 4-53 for the trough-tundish, except that the longer mean residence time leads to longer absolute time transients.

Figure 4-58 summarises the effectiveness of the flow control device. It is seen to be ineffective for small inclusions with $u_S \cong 0.5$ mm/s, but very effective for inclusions of 120 µm ($u_S = 4.5$ mm/s,) where a 70% improvement in effluent quality for that size would be expected.

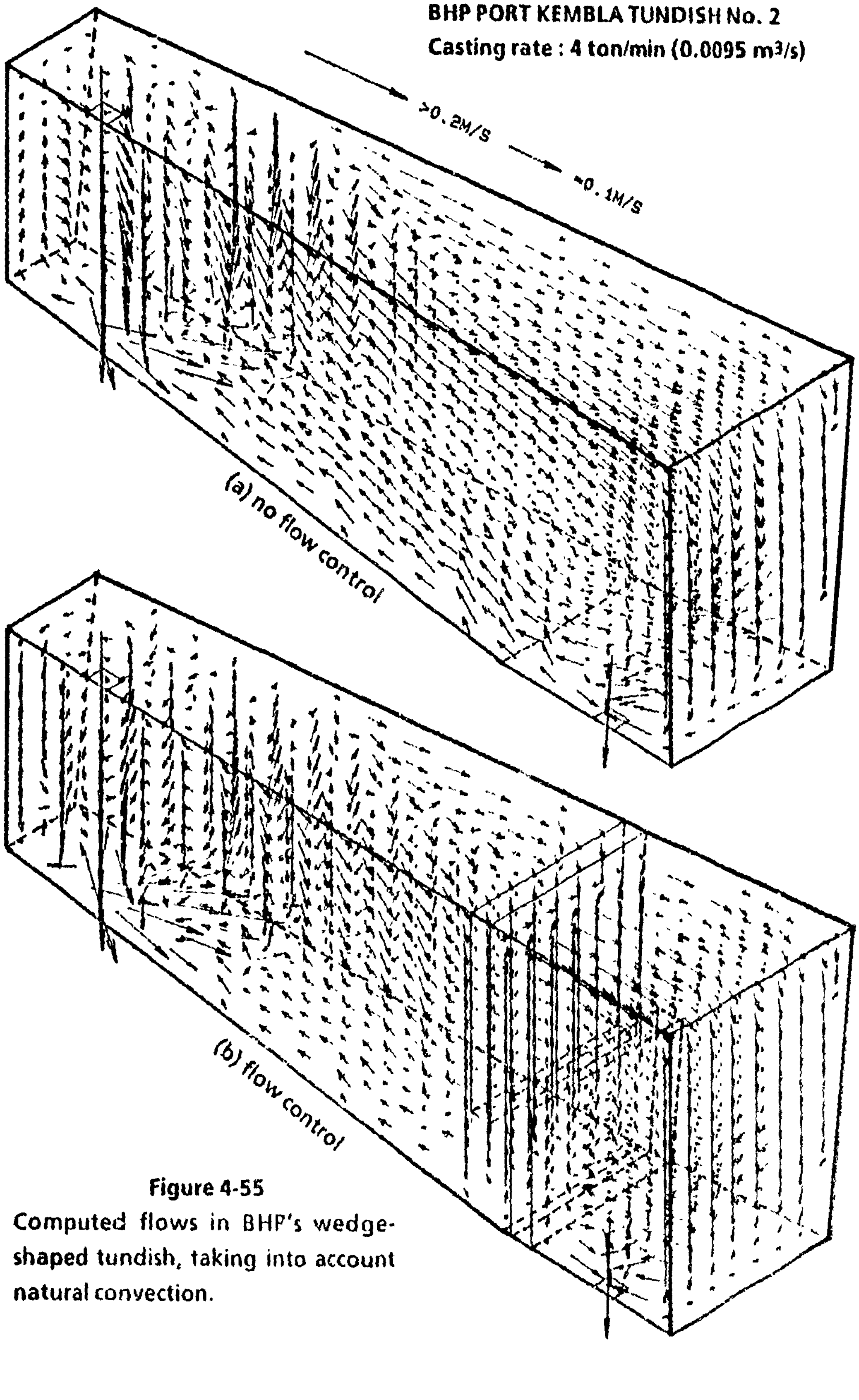

Figure 4-55
Computed flows in BHP's wedge-shaped tundish, taking into account natural convection.

TEMPERATURE DISTRIBUTIONS
Input temperature : 1575°C

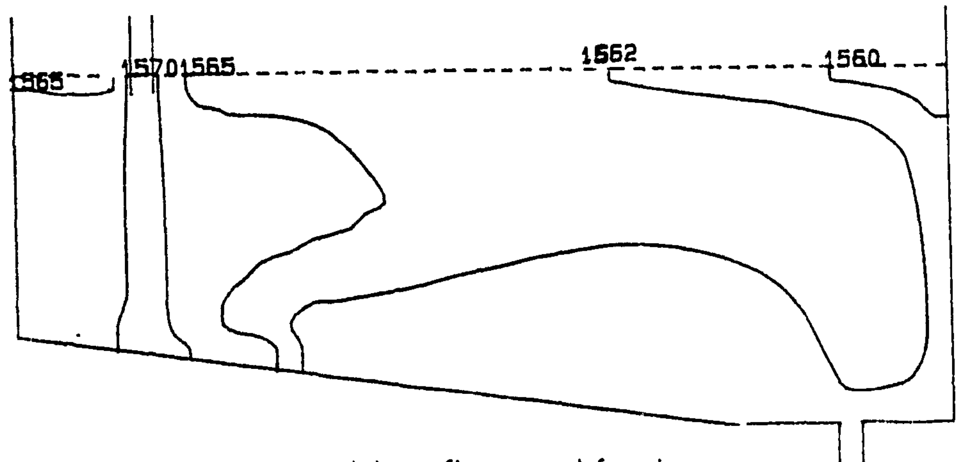

(a) no flow modification

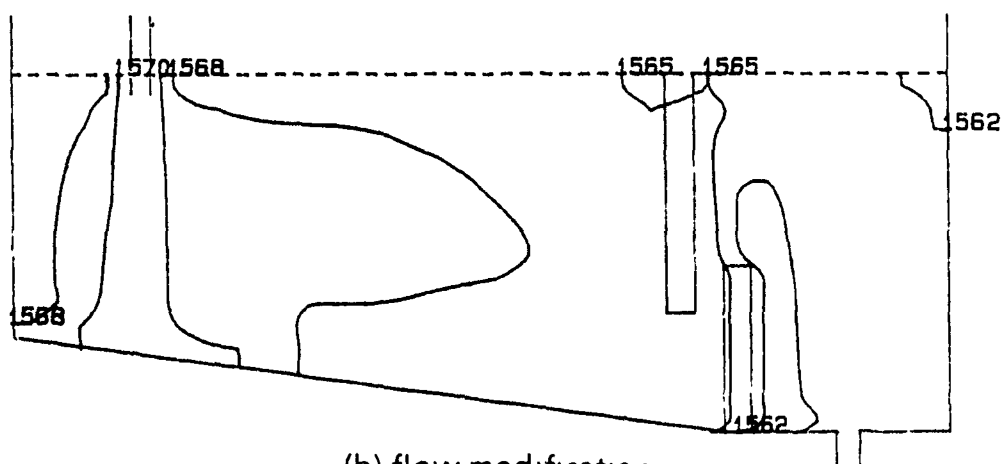

(b) flow modification

Figure 4-56 Computed isotherms along central logitudinal plane of BHP's wedge-shaped tundish.

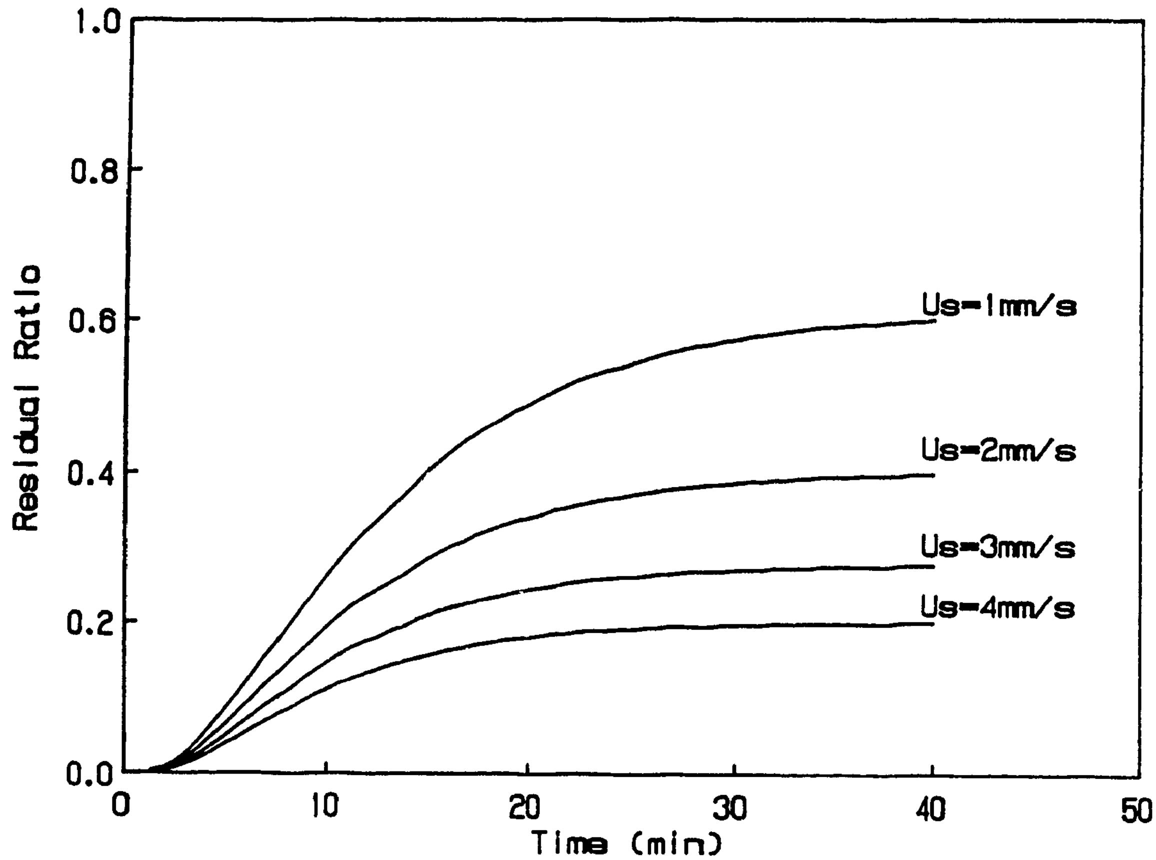

Figure 4-57 Residual ratios of inclusions entering mould, following their introduction into wedge-shaped tundish, for various float-out velocities.

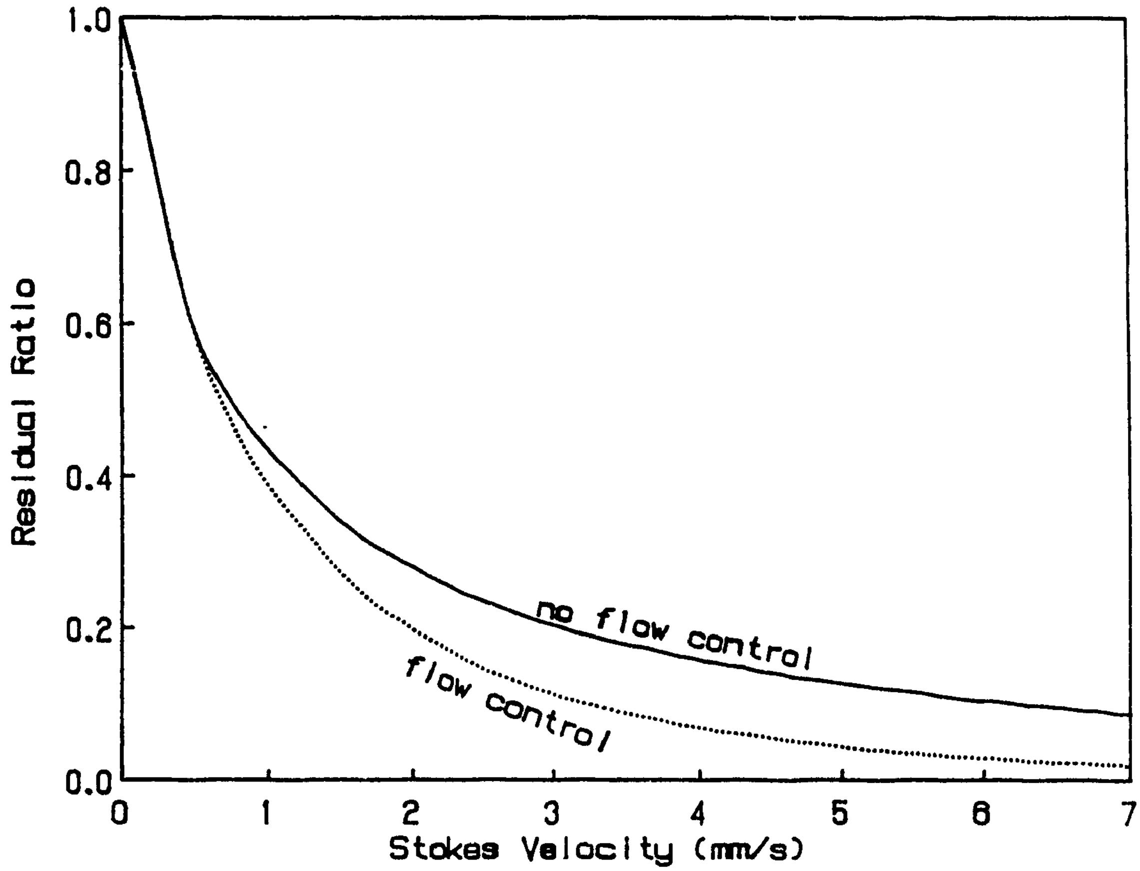

Figure 4-58 Plot of residual ratio of inclusions entering mould from BHP's wedge-shaped tundish versus Stokes rising velocity, with and without a flow modification device.

5.7 Industrial Tests

In order to evaluate casting equipment and practices, Hille testing was conducted on non-critical tinplate grades.[31] This testing procedure employs a ball diameter of 75 mm, which was used to deform a sample sheet, 0.21 mm thick, into the form of a deepening cup, up to the point of fracture. The inclusion-related splits surrounding the major tear were counted and visually rated as light, medium or heavy. Depending on sheet width, either 5 or 6 cups were pressed across its width. A trial was conducted on the BHP No. 1 tundish, in which a twin weir and dam arrangement of the type shown in Figure 4-50 was compared against a twin dam arrangement. Results[32] indicated that no significant improvement was discernible. Figure 4-44 supports this finding There, residual ratios for a trough-shaped tundish, illustrate the critical importance of a well-placed dam. By comparison, the role of a weir is seen to be of secondary importance for inclusion float-out.

In other tests with the wedge-shaped tundish at the BHP No. 2 slab caster, 145 casts were produced using a 0.5m high dam set one metre from the tundish end-wall adjacent to the inlet pouring stream. Under steady state casting operations on tinplate grades, the following results were obtained[32]:

Body skelps	Tested	Failed	Fraction failed	% failed
with dam	100	25	0.25000	25
with no dam	211	45	0.21327	21

while for transition skelps ladle changes :

Body skelps	Tested	Failed	Fraction failed	% failed
with dam	393	15	0 03817	3.8
with no dam	920	66	0.07174	7.17

The results under steady state conditions are significant, and suggest that there is about a 50% reduction in the number of failures. Referring to Figure 4-58, similar flow modification devices modelled in the present study, lead to improved, (i.e lower) residual ratios, varying between 30 % for inclusions with Stokes rising velocities of 2 mm/s (~60 μm) to 60 % for the larger inclusions rising at 4.5 mm/s (120 μm). While the size distribution of inclusions was not measured, it is reasonable to estimate that inclusion densities of critical size in the final product and deriving from the tundish will be reduced by about 50 %, and that this should translate into an equivalent quality improvement, in the order of that actually measured At the time of writing, the wedge-shaped tundish is being operated with a ported dam arrangement.

5.8 Scientific Visualization

In conjunction with the work just described, a graphic video movie was prepared to visualize the massive amounts of data produced in collaboration with Cray Software Reaserch Group [33] For this, a distributed processing system consisting of an I R.I.S. graphic workstation and a CRAY-2S supercomputer was used to provide the hardware platform. The Multi-Purpose Graphic System (MPGS) software package, which consists of two parts, a CRAY resident portion and workstation resident portion provided the necessary control

Certain calculations, such as multiple particle traces, required extensive computing. The MPGS essentially used the CRAY-2S for these operations, while the workstation was used for local graphic manipulations and control. The communication between the workstation and the CRAY uses TCP/IP over the Network System Corporation's Hyperchannel (Figure 4-59). One of the feature of MPGS is its ability to record commands for a sequence of images. This in turn can be played back and an animation sequence viewed. Once an animation sequence is properly prepared, a standard analog video signal can be directly generated from the workstation onto a video recording system The video segments of the graphic movie were produced in this fashion.

Using this equipment, thermal profiles within the tundish were colour-coded according to appropriate temperature scale, while streak lines were used to illustrate the transient passage of massless particles between the entry and exit ports. What had not been appreciated prior to this visualization was the complex rotational features present within the flow This lead to a stochastic spiraling, and looping back of particles. Similarly, the film simulation package allowed the development of a transient scalar field (envelope of iso-density inclusion levels) to be viewed three-dimensionally. The simulations graphically illustrated the value of flow modification devices in reducing the number of larger inclusions entering the effluent steel from the tundish into the slab caster mould.

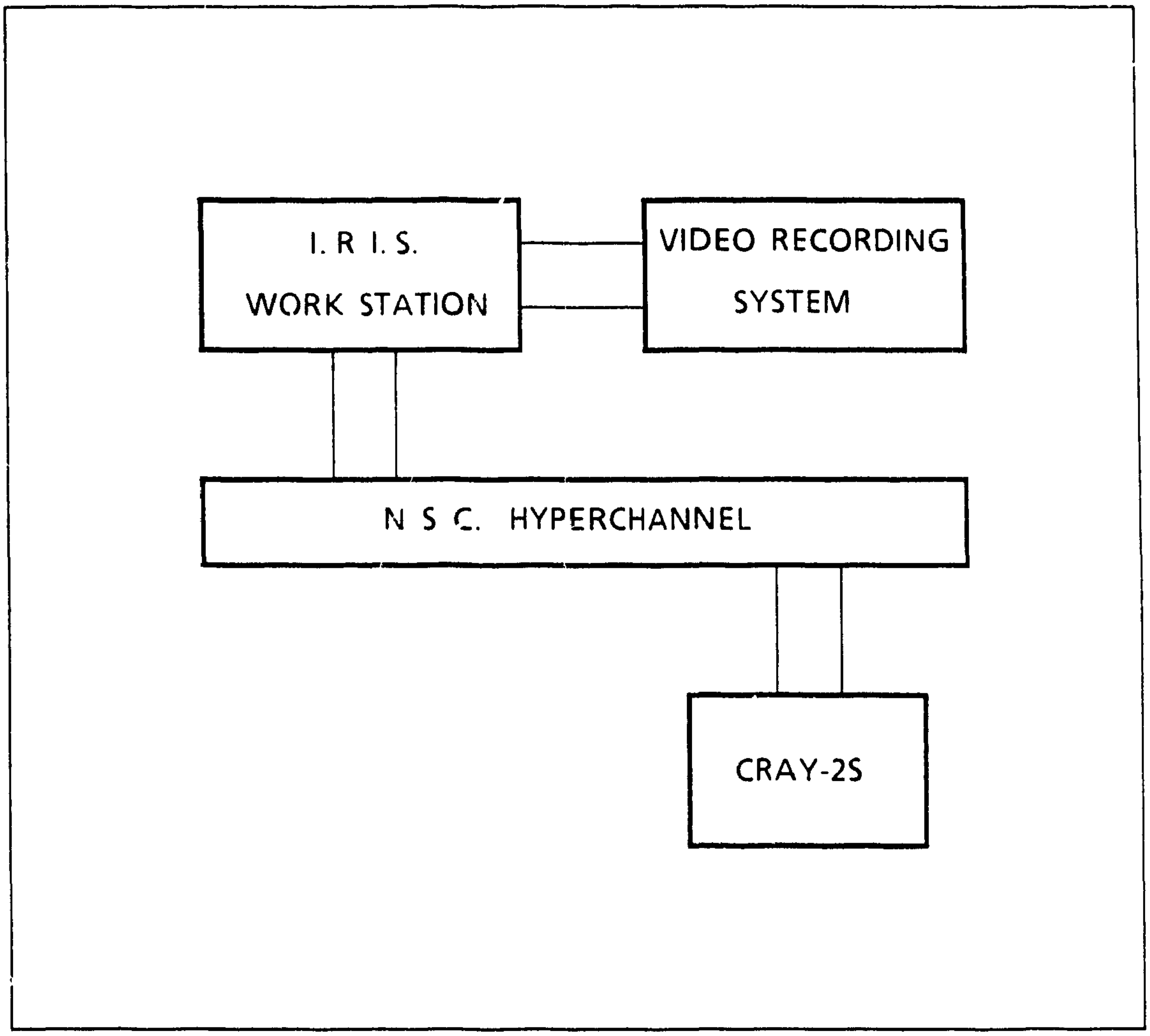

Figure 4-59 Scientific visualization using distributed processing

Chapter 6

Conclusions

Fluid flow, heat transfer, and inclusion separation behaviour have been studied for several types of industrial tundishes using mathematical and physical models. It was concluded that :

1. A novel technique for the on-line measurement of particle concentrations in aqueous systems has been developed which allows local concentrations of particles (hollow glass microspheres) to be monitored on-line in full-scale water models of metallurgical flow systems.

2. It is shown that a fully three dimensional description of the flow field, and of buoyant particle dispersion and separation was capable of matching corresponding experimental data.

3. Transport phenomena in molten steel in real tundish systems will be significantly different from those in water model tundishes since thermal natural convection modifies flow patterns within a large tundish quite substantially.

4. Thermal convection can generate secondary recirculating flows and increased fluid motion near tundish exit ports. These flows reduce separation efficiencies for inclusions, but also reduce thermal cold spots.

5. Flow modification devices (weir/dam arrangements) can lead to significant improvements in steel quality for the intermediate (50 µm) and larger inclusions (120 µm), effluent inclusion ratios typically exhibiting 50% improvements in metal cleanliness over non-modified tundishes.

6. With using a weir/dam arrangement, temperature drops between inlet and oulet nozzles were not signicantly improved, but relatively more uniform temperature distributions were predicted.

7. The dam is the critical component of a dam and weir arrangement for enhancing inclusion separation.

8 Wall sloping gives the beneficial effects for removing inclusions, but at the expense of increasing heat losses.

9 Both experiments and predictions show that concentration transients of small inclusions within tundishes reach pseudo-steady state level at about three nominal holding times.

10. Mathematical modelling can provide quantitative information on flows, temperatures and inclusion concentrations, for the optimisation of tundish designs and metal handling procedures.

Since such metallurgical transport phenomena associated with heat transfer phenomena cannot be readily modelled with physical models[34], mathematical models present the most reasonable alternative to adequate tundish design, if the importance of ladle covers, slag covers, bubbling, etc., on the design and operation of such vessels are to be properly predicted and understood.

REFERENCES

1) F.L. Kemeney, D J. Harris, A. McLean et al , 2nd Process Technology Conference, Chicago, ISS-AIME, 1981, pp. 232-245

2) D.J. Harris and J.D. Young, Continous Casting Vol 1, ISS-AIME 1983, pp. 99-112.

3) M. Hashio, M. Tokuda et al., 2nd Process Technology Conference Chicago, ISS-AIME, 1981, pp. 65-73.

4) D.O. Wilshynsky, D.J. Harris and L.J. Heaslip, Proc. of CIM 23rd Conference, August, 1984

5) S. Tanaka and R.I L. Guthrie, Proc. of the 111th ISIJ Spring Meeting, Tokyo, April, 1986.

6) H. Nakajima, Ph D. Thesis, McGill University, 1987

7) N. El-Kaddah and J. Szekely, 114th AIME Annual Technical Meeting, New York, 1985.

8) K. Lai, M. Salcudean, S. Tanaka and R.I.L. Guthrie, Metal Trans. 17B, 1986, pp. 449-459.

9) Y. He and Y. Sahai, Metal. Trans. 18B, 1987, pp. 81-92.

10) Y. Sahai, Metal. Trans. 18B, Sept. 1987.

11) K.H. Tacke and J.C. Ludwig, Process Metallurgy, Steel research, Vol. 58, No.6, 1987, pp262-269.

12) R.I.L. Guthrie, S. Joo and H. Nakajima, Int'n. Sym. on Direct Rolling & Charging of Strand Cast Billet, Montreal, 1988, Paper 51-5.

13) D.A. Doutre and R.I.L. Guthrie, Int. Seminar on Refining and Ferro-alloy, Ed. T.A. Engh et al, Aluminium-Verlag Dusseldorf, 1985, pp. 147-161.

14) F. Sebo, F. Dallaire, S. Joo and R.I L. Guthrie, Int'n. Sym. of Production and Processing of Fine Particles, Montreal, 1988, Paper 12-3.

15) S.V. Patankar, "Numerical Heat Transfer and Fluid Flow", McGraw Hill, 1980.

16) W.P. Jones and B.E. Launder, Int. J. Heat & Mass Transfer, Vol. 15, 1972, pp. 301-303.

17) B.E. Launder and D.B. Spalding, Comp. Math. Appl. Mech. Eng., Vol. 3, 1974, pp. 269-289.

18) D.B. Spalding, Int. J. Num. Math. Eng., Vol. 4, 1972, pp. 551-559.

19) Kirshenbaum and Cahill, Trans. AIME, Vol. 224, 1962, p816.

20) Y. Maruki, S. Shima and K. Tanaka, "Effect of Continuous Measurement Technology of Temperature in Continuous Casting Tundish", Trans. ISIJ, Vol 28, 1988.

21) W.H. Coulter, U S. Patent No 112819, Octorber 20, 1953.

22) S. Kuyucak, Ph.D Thesis, McGill University, Montreal, Canada, 1989.

23) H.C. Lee, Unpublished Research, Mcgill Univrsity, Montreal, Canada.

24) R.W. DeBlois, C.P. Bean and R.K.A. Wesley, J. Colloid & Interface Science, Vol. 61, 1977, pp323-335

25) F. Dallaire, "Data Aquisition Software for Limca Experiment using TN-7200 Multichannel Analyser", Internal Report, McGill University, 1987

26) J. Szekely and N.J. Themelis, "Rate Phenomena in Process Metallurgy", Wiley-Interscience, 1971.

27) R. Ahuja and Y Sahai, Proceedings of International Symposium on the Continuous Casting of Steel Billets, Vancouver, B C., CIM, 1985, pp73-87.

28) O.J. Illegbushi and J. Szekely, Mathematical Modelling of Materials Processing Operations, Ed. by J Szekely et al., TMS-AIME, 1987, pp409-429.

29) A. Moult, D.B. Spalding and N C.G. Markatos, Trans. Inst. Chem. Eng., Vol. 57, 1979, pp200-204.

30) D. Curry, Internal Report, Dofasco Steel Center, 1988.

31) I. Simpson, R. Serje, K. Kuit, Z. Tritsiniotis and D. Porteous, Proceedings of the Third International Conference on Clean Steel. The Institute of Metals, 1987, pp85-91.

32) K. Kuit, I. Simpson, "Performance and Non-metallic Inclusion Content", Internal Technical Note, BHP steel, July 1988.

33) H. Greiss, K. Misergade, S. Joo and R.I.L. Guthrie, Int. Symp. of Supercomputer, Toronto, Jun, 1989.

34) J.W. Hlinka and T.W. Miller, Iron & Steel Engineer, August 1970, pp123-133.

THESIS CONCLUSION - CLAIM TO ORIGINALITY

A general purpose computer code, *METFLO*, has been developed in order to numerically predict three-dimensional turbulent flow, heat and mass transfer in metallurgical processing vessels. Through the use of both physical and mathematical models, mixing behaviour during off-center and multi-plug gas bubbling operations in steelmaking ladles, and nonmetallic inclusion dispersion/separation and temperature distributions during tundish processing operations, have quantitatively been analysed.

Experience has shown that physical and mathematical models need to be meshed in a complementary manner, when tackling new events, or phenomena. Given the power and speed of today's computers, many industrial problems are now amenable for study at reasonable cost using complex mathematical models.

This thesis has many aspects of originality. It is the first time that :

1. Three-dimensional turbulent recirculation flows in a ladle have been predicted for off-center and double-plug gas bubbling. These have been visualised isometrically with the aid of a computer graphic program written by the author.

2. Transient mixing processes have been predicted and illustrated for the various conditions of bubbler positions and tracer injection points.

3. Plume distortion and wall effects on mixing time have been demonstrated.

4. Equipment was assembled so that the particle size distribution data, acquired using an on-line measurement technique of particle concentrations in aqueous systems, could be transferred to a personal computer from a multichannel analyser and saved on floppy diskettes for further analysis.

5. Experimental measurements and numerical predictions of particle /inclusion separation for a full-scale water model tundish have been performed and compared to one and another.

6. The importance of thermal natural convection has been demonstrated for the flow of molten steel in industrial steelmaking tundishes. (Thus, flow patterns and inclusion separation behaviour within real industrial tundishes have been demonstrated to be significantly different from those pertaining to isothermal water models.)

7. Numerical predictions have been performed for various types of industrial tundishes, such as single port, double port, symmetrical twin port, rectangular-shaped, trough-shaped, and wedge-shaped tundishes.

8. Flow patterns, temperature distributions, and inclusion dispersion/ separation behaviour in tundish processing operations have been visualized through a graphic video movie, generated in collaboration with Cray Software Research Group.